



HAL
open science

Modeling of water sprays effects on premixed hydrogen-air explosion, turbulence and shock waves

Guodong Gai

► **To cite this version:**

Guodong Gai. Modeling of water sprays effects on premixed hydrogen-air explosion, turbulence and shock waves. Thermics [physics.class-ph]. Normandie Université, 2020. English. NNT : 2020NORMIR14 . tel-03222614

HAL Id: tel-03222614

<https://theses.hal.science/tel-03222614>

Submitted on 10 May 2021

HAL is a multi-disciplinary open access archive for the deposit and dissemination of scientific research documents, whether they are published or not. The documents may come from teaching and research institutions in France or abroad, or from public or private research centers.

L'archive ouverte pluridisciplinaire **HAL**, est destinée au dépôt et à la diffusion de documents scientifiques de niveau recherche, publiés ou non, émanant des établissements d'enseignement et de recherche français ou étrangers, des laboratoires publics ou privés.



Normandie Université

THÈSE

Pour obtenir le diplôme de doctorat

Spécialité Énergie

Préparée au sein de l'Institut National des Sciences Appliquées Rouen Normandie

Modeling of water sprays effects on premixed hydrogen-air explosion, turbulence and shock waves

Présentée par
Guodong GAI

Thèse soutenue publiquement le 2 Novembre 2020
devant le jury composé de

Nabiha CHAUMEIX	Directrice de Recherches CNRS, Laboratoire ICARE	Rapportrice
Jean-Michel GHIDAGLIA	Professeur à l'ENS Cachan	Rapporteur
Ashwin CHINNAYYA	Professeur à l'ENSMA Poitiers, Institut Pprime	Examineur
Stéphane MIMOUNI	Ingénieur de Recherches Expert R&D Chatou, EDF	Examineur
Vincent MOUREAU	Chargé de Recherches au CNRS, Laboratoire CORIA	Examineur
Olivier THOMINE	Ingénieur-Chercheur CEA Saclay	Examineur
Sergey KOUDRIAKOV	Ingénieur-Chercheur CEA Saclay	Co-encadrant
Abdellah HADJADJ	Professeur à l'INSA de Rouen, Laboratoire CORIA	Directeur de thèse

Thèse dirigée par Abdellah HADJADJ et co-encadrée par Sergey KOUDRIAKOV



Acknowledgement

This thesis work was performed in the CORIA laboratory of the Institut National des Sciences Appliquées (INSA Rouen) as well as the LATF laboratory in the Commissariat à l’Energie Atomique et aux Energies Alternatives (CEA Saclay). I would like to take this opportunity to express my sincere gratitude to all the people who have ever helped me during this Ph.D project.

Firstly, I want to express my great thanks to my thesis director, Prof. Abdellah Hadjadj, professor of laboratory CORIA in INSA Rouen, for his advice and suggestions during the research. We had many important discussions which gave me good inspiration. With great patience, Abdellah gave me indispensable advice in the editing of this thesis. My gratitude to him knows no bounds.

My sincere and hearty thanks and appreciations go to my supervisor Dr. Sergey Koudriakov, research engineer at CEA, for welcoming me to his laboratory and giving me the golden opportunity to work on the topic of interaction between premixed hydrogen flame and water droplets, and also for his patience, motivation, enthusiasm, and immense knowledge. His guidance helped me in all the time of my research and redaction of this thesis. I could not have imagined having a better advisor and mentor for my study.

I want to express my special regards to Dr. Olivier Thomine, researcher at Aix-Marseille University, for his technical and scientific supports, his availability, and his valuable comments on my research.

Then, I gratefully acknowledge Dr. Etienne Studer, research engineer at CEA, for his friendly reception when I came to the laboratory of LATF, for his guide and inspiration. I would like to express my sincere acknowledgments to Dr. Stephane Mimouni, research engineer at EDF, for his generous advice and help. At the same time, I want to give my hearty thanks to Dr. Clotaire Geffray, Mr. Laurent Salmon, Mrs. Véronique Lechopied, as well as many other colleagues in the laboratory LATF for their kindness and availability during my work at CEA.

I would like to thank Mr. Jean-Marie Bourgeois-Demersay and Prof. Bertrand Mercier for their help during my stay in Paris. They have given me precious advice and generous guidance both in my study and in my life since I became a student of IFCEN.

My thanks also go to Dr. Yanshu Wang and Dr. Qinjun Fu my best friends ever, we have and will continue to explore the world together. I would like to thank Dr. Yang Li and Dr. Yanjun Wang for teaching me how to ski and for giving me courage to chase my dreams. Also, I want to thank my friends: Nan Jiang, Chufa Qiu, Chengming Shang, Xuan Wang, Jingyi Wang, Hanchen Li, Yazhe Lu and Dr. Ziqiang Zou.

Especially, I want to give my most sincere thanks to Dr. Xiaocui Wu for everyday care and for feeding me well. She taught me not to fear failure and gave me support through my darkest times. Hope that she can finally realize her dream of being a professor shortly.

Finally, I must express my very profound gratitude to my parents for providing me with unfailing support and continuous encouragement throughout my years of study and through the process of researching and writing this thesis.

The author gratefully acknowledges the financial support from Electricité de France (EDF) within the framework of the generation II & III reactor research and development program.

Abstract

This PhD dissertation is dedicated to develop simple models to investigate the effect of water spray system on the premixed hydrogen-air combustion in the nuclear power plants. Specific simple models are developed to describe the water droplet evaporation in the flame, particle cloud dispersion after the shock wave passage, and turbulence length scale evolution with the presence of a water spray. A methodology is proposed to evaluate the spray evaporation effects on the propagation of the turbulent hydrogen flame inside a closed volume and a simple model is developed for the quantification of the laminar velocity deceleration with the droplets evaporation inside the flame. An analytical model is proposed for the prediction of particle cloud dispersion after the shock passage in the one-way formalism and another analytical model is dedicated to describe the spray-shock interaction mechanism and predict the appearance of a particle number density peak using the two-way formalism. A review of the important criteria and physical modelings related to the particle-induced turbulence modulation is given and a mechanistic model is used for the estimation of the turbulent integral length scales induced by the injection of particle clouds. These developed numerical models can be coupled to implement in the large-scale numerical simulations of the spray system effects on the accidental hydrogen explosions in the nuclear power plants.

Key words: Hydrogen Explosion, Nuclear Spray System, Particle-laden Flow, Shock-wave

Resumé

Cette thèse de doctorat est dédiée au développement de modèles physiques pour l'étude des systèmes d'aspersion de gouttelettes d'eau en milieu réactif d'hydrogène-air pré-mélangée dans les centrales nucléaires. Des modèles d'ordre réduit sont développés pour décrire l'évaporation des gouttelettes d'eau dans la flamme, la dispersion des nuages de particules après le passage des ondes de choc et l'évolution de l'échelle caractéristique de turbulence avec la présence d'un jet d'eau. Une nouvelle méthodologie est proposée pour évaluer les effets de l'évaporation par l'aspersion sur la propagation de la flamme d'hydrogène turbulente à l'intérieur d'un volume fermé et un modèle simple est développé pour la quantification de la décélération de la vitesse laminaire avec l'évaporation des gouttelettes à l'intérieur de la flamme. Egalement, un modèle analytique est proposé pour la prédiction de la dispersion de nuage de particules après le passage d'une onde de choc en s'appuyant sur le one-way formalisme avec une extension afin de prédire l'apparition d'un pic de densité du nombre de particules en utilisant le two-way formalisme. En ce qui concerne la modulation de la turbulence induite par les particules, un modèle simple est utilisé pour l'estimation des échelles intégrales de la turbulence induites par l'injection de nuage des particules. Ces modèles numériques développés peuvent être couplés pour être mis en œuvre dans les simulations numériques à grande échelle de l'effet du système d'aspersion sur les explosions accidentelles d'hydrogène dans les centrales nucléaires.

Mots clés: Explosion d'hydrogène, Système d'aspersion Nucléaire, Ecoulement Chargé de Particules, Onde de Choc

Contents

Contents	v
List of abbreviations and symbols	vii
List of Figures	xv
List of Tables	xvii
1 Introduction	1
1.1 General context	1
1.2 Scientific issues	2
1.2.1 PWR containment spray system	3
1.3 Combustion phenomena during severe accidents	5
1.3.1 Flame acceleration and DDT	5
1.3.2 Premixed hydrogen-air combustion	7
1.3.3 Flame thickness, velocity and length scales	9
1.4 Flame-spray interaction mechanisms	12
1.4.1 Droplet evaporation	14
1.4.2 Droplet breakup	19
1.5 Spray-shock interaction	23
1.5.1 Planar shock waves	25
1.5.2 Spray characteristics	25
1.5.3 Two-way interactions	27
1.6 Spray-induced turbulence	30
1.7 Overview of large-scale simulation codes	30
1.7.1 FLACS code	31
1.7.2 FLUENT code	32
1.8 Spray-flame interaction experiments	33
1.8.1 Small-scale experiments	34

1.8.2	Medium-scale experiments	37
1.8.3	Large-scale experiments	40
1.9	Scope of the current study	42
1.9.1	Outline of dissertation	43
2	Lumped parameter study	45
2.1	Fundamental assumptions	45
2.2	Model development and conservation laws	46
2.2.1	Conservation of mass	47
2.2.2	Conservation of energy	48
2.2.3	Modeling assessment	51
2.3	Results and discussions	51
2.3.1	Case I	52
2.3.2	Case II	52
2.3.3	Case III	53
2.3.4	Case IV	54
3	Spray-flame Interaction	57
4	Spray-shock Interaction	91
5	Spray-induced Turbulence	125
6	Conclusions and Perspectives	159
A	Appendix of spray flame interaction	I
A.1	Combustion length scales	I
A.2	Cosilab code	II
B	Appendix of spray shock interaction	V
B.1	Asphodele code	V
B.1.1	WENO scheme	V
B.1.2	Minimal storage time-advancement scheme	VII
C	Appendix of spray turbulence interaction	XI
C.1	Numerical modelling Neptune_CFD	XI
C.2	Turbulence modeling	XII
C.2.1	Standard $k - \epsilon$ model	XIII
C.2.2	$R_{ij} - \epsilon$ SSG model	XIV
C.2.3	Turbulence scaling	XV
C.3	Mean inter-particle distance	XVI

List of abbreviations and symbols

C.3.1	Cubic case	XVI
C.3.2	Regular tetrahedron case	XVIII

Bibliography		XXIX
---------------------	--	-------------

List of Abbreviations

AIBC	Adiabatic IsoBaric complete Combustion
AICC	Adiabatic Isochoric Complete Combustion
CEA	French Alternative Energies and Atomic Energy Commission
CFD	Computational Fluid Dynamics
DDT	Deflagration to Detonation Transition
DEN	Nuclear Energy Direction
DM2S	Department of System and Structures
DNS	Direct Numerical Simulation
DOE	Design of Experiments
DynAsp	Dynamique de l'Aspersion
EDF	Electricité de France
ENACCEF	ENceinte d'ACCElération de Flamme
EPR	European Pressurized-water Reactor
FA	Flame Acceleration
FEM	Finite Element Method
IAEA	International Atomic Energy Agency

LDV	Laser Doppler Velocimeter
LES	Large-Eddy Simulation
LMN	Low Mach Number
LVDEM	Laminar Flame Velocity under Droplet Evaporation Model
NPP	Nuclear Power Plant
NP	Not Provided
PIV	Particle Image Velocimetry
PWR	Pressurized Water Reactor
RANS	Reynolds-averaged Navier-Stokes equations
SWACER	Shock Wave Amplification by Coherent Energy Release
TKE	Turbulent Kinetic Energy
UDPM	Unresolved Discrete Particle Model
WENO	Weighted Essentially Non-Oscillatory

Nomenclature

α	Liquid volumetric fraction, dimensionless
α_g	Thermal diffusivity, [m^2/s]
Δx	Average cell size, [cm]
δ	Flame thickness, [m]
$\dot{\alpha}$	Volumetric evaporation rate, [s^{-1}]
$\dot{\omega}$	Chemical reaction rate, [s^{-1}]
\dot{m}	Evaporation rate of droplets, [kg/s]
η	Kolmogorov length scale, [m]

List of abbreviations and symbols

γ	Specific heat ratio, dimensionless
κ	Distribution coefficient, dimensionless
λ	Inter-particle distance, dimensionless
λ	Thermal conductivity, $[W/m/K]$
Λ_f	Eulerian integral length scale, $[m]$
\mathcal{M}	Turbulence modulation, dimensionless
\mathcal{R}	Universal gas constant, $[J/K/mol]$
μ_g	Dynamic viscosity of gas, $[Pa \cdot s]$
Ω	Fuel-Free Oxygen fractions, dimensionless
ϕ	Equivalence ratio, dimensionless
Ψ	Criterion function for the ignition, dimensionless
ρ	Mass density, $[kg/m^3]$
Σ	Flame surface, $[m^2]$
σ	Expansion ratio between density of unburnt and burnt gases, dimensionless
σ_s	Surface tension, $[N/m]$
σ_w	Surface tension of droplets, dimensionless
τ_k	Kolmogorov time scale, $[s]$
τ_p	Particle response time, $[s]$
τ_v	Load rate, dimensionless
ε	Parameter in the criterion function of the CREBCOM model, dimensionless
A_0	Area of the burner mouth, $[m^2]$
A_f	Area of the flame front, $[m^2]$
$a_{0.5}$	Averaged heat flux, $[W/cm^2]$
B_M	Spalding mass transfer number, dimensionless

B_T	Spalding temperature transfer number, dimensionless
C_D	Drag coefficient, dimensionless
$c_{p,g}$	Gas heat capacity at constant pressure, $[J/K/kg]$
c_p	Constant pressure specific heat, $[J/kg/K]$
c_{sp}	Sound speed in the combustion products, $[m/s]$
c_v	Constant volume specific heat, $[J/kg/K]$
D	Diameter of the droplet, $[\mu m]$
D_a	Damkohler number, dimensionless
D_p	Diameter of the droplet, $[m]$
$D_{3,2}$	Sauter mean diameter, $[m]$
$D_{c,1}$	First critical droplet diameter, $[\mu m]$
$D_{c,2}$	Second critical droplet diameter, $[\mu m]$
e	Specific energy, $[J/kg]$
E_a	Global activation energy, $[kcal/mol]$
F	Correction factor in evaporation model, dimensionless
H	Volumetric heat transfer coefficient, $[W/m^3/K]$
h	Specific enthalpy, $[J/kg]$
I	Static pressure impulse, $[bar \cdot s]$
k	Turbulent kinetic energy, $[m^2/s^2]$
K_0	Parameter related to flame velocity in CREBCOM model, $[m/s]$
K_a	Karlovitz number, dimensionless
K_f	Reaction-rate constant
L	Length of the experimental tube, $[m]$
l	Latent heat of evaporation, $[kJ/kg]$

List of abbreviations and symbols

L_h	Hybrid length scale, [m]
L_T	Integral length scale, [m]
L_w	Effective length of the wake, [μm]
Le	Lewis number, dimensionless
M_s	Shock Mach number, dimensionless
M_{H_2}	Molar weight of hydrogen, [kg/mol]
N	Ratio of the flame surface to the tube cross-section area, dimensionless
n_{vol}	Number of droplets per volume, [m^{-3}]
Nu	Nusselt number, dimensionless
O_n	Onhesorge number, dimensionless
P_0	Initial pressure, [bar]
p_{max}	Maximum pressure, [bar]
Pa_{S_i}	Particle momentum number, dimensionless
Pe	Peclet number, dimensionless
Pr	Prandtl number, dimensionless
Q	Surface heat transfer coefficient, [$\text{kW}/\text{m}^2/\text{K}$]
Q_w	Supply flow rate, [l/s]
R	Universal gas constant, [$\text{J}/\text{K}/\text{mol}$]
r_0	Initial radius of the droplet, [μm]
$R_{i,j}$	Reynolds stress tensor, [m^2/s^2]
Re	Reynolds number, dimensionless
Re_p	Particle Reynolds number, dimensionless
Re_t	Turbulent Reynolds number, dimensionless
S_L	Laminar flame velocity, [m/s]

S_t	Stokes number, dimensionless
s_T	Turbulent flame velocity, [m/s]
Sc	Schmidt number, dimensionless
Sh	Sherwood number, dimensionless
T_0	Initial temperature, [K]
t_c	Chemical reaction time, [s]
t_q	Quenching time, [s]
t_{max}	Time needed for the flame to reach the maximum pressure, [s]
u'	Turbulence intensity, [m/s]
u_R	Particle relative velocity, [m/s]
u_{rms}	Root-mean-square velocity, [m/s]
v_0	Average flow velocity in the burner, [m/s]
V_b	Burnt gas velocity, [m/s]
V_f	Fresh gas velocity, [m/s]
V_r	Reflected shock velocity, [m/s]
V_s	Shock velocity, [m/s]
V_t	Transmitted shock velocity, [m/s]
v_t	Visible turbulent flame velocity, [m/s]
W	Molar mass, [kg/mol]
We	Weber number, dimensionless
X_{H_2}	Molar fraction of hydrogen, dimensionless
y	Coordinates in the Cosilab code, [mm]
Y_{H_2}	Mass fraction of hydrogen, dimensionless
Ze	Zel'dovich number, dimensionless

List of Figures

- 1.1 Spray rings and envelopes in a French PWR (not to scale) [1]. 4
- 1.2 (a) Spray nozzle SPRACO 1713A (Lechler 373.084.17.BN) (b) drop size distribution at 6 m from the nozzle under different relative injection pressure [1]. 4
- 1.3 Regimes of flame propagation leading to DDT (SWACER = Shock Wave Amplification by Coherent Energy Release) [2]. 6
- 1.4 Sketch of a nuclear reactor building with an ignition taking place at the dome part (a) and at the obstructed lower part (b). 7
- 1.5 Experimental P-T diagram for H_2-O_2 reaction [3]. 8
- 1.6 (a) Mallard-Le Chatelier description of the temperature in a laminar flame [4]. (b) Temperature and concentration profiles, schematically for a lean mixture in thermal flame theory [5]. . . 11
- 1.7 Graphical determination of the flame thickness from the temperature profile. 12
- 1.8 Interaction mechanism between the flame and water droplets with flame propagating from left to right; (a) slow flame with small droplets, (b) slow flame with big droplets, (c) fast flame following pressure wave. 13
- 1.9 Droplet vaporization time as a function of droplet size and relative velocity: $T = 2051\text{ K}$, relative velocity of 0 m/s (—●—), 10 m/s (—▲—), 50 m/s (—▼—), 100 m/s (—◆—), 200 m/s (—■—) [6]. 17
- 1.10 (a) Influence of ambient temperature on the mass evaporation rate: $d_p = 500\ \mu\text{m}$, 900 K (—), 1200 K (—), 1547 K (—) and 1885 K (—). (b) Influence of ambient pressure on the mass evaporation rate: $d_p = 350\ \mu\text{m}$, 1 bar (—), 3 bar (—), 5 bar (—) and 6 bar (—). 19
- 1.11 Droplet breakup mechanisms [7]. 20
- 1.12 Drop size normal distribution (a) and size distribution after secondary breakup (b). 22
- 1.13 Droplet fragment size distribution after the interaction with gas flow of velocity $v_g = 50\text{ m/s}$; the original spray a droplet size distribution of 3.9 bar SPRACO nozzle at 6 m from the nozzle [8]; (a) model of Pilch (b) model of Rosin. 23
- 1.14 Shock waves from a hydrogen oxygen explosion. Schlieren photography of an explosion of $H_2 - O_2$ gas inside a bubble detonated with an electrical spark [9]. 24

1.15	Shock wave generation in a piston tube.	25
1.16	Spatial distribution of the source term of an evaporating droplet [10], the coordinates give the relative position of the nodes in gas phase.	27
1.17	(a) Evolutions of the gas mass (—), droplet mass(—) and total mass (—) of the biphasic system; (b) Evolution of the gas momentum (—), droplet momentum (—) and total momentum (—) of the biphasic system; (c) Evolution of two-way gas velocity (—) and droplet velocity (—) without evaporation, the one-way gas velocity (---) and droplet velocity (---) are given as references; (d) Evolution of the gas enthalpy (—), droplet enthalpy(—) and total enthalpy (—) of the biphasic system; (e) Evolution of the droplet temperature (—) and the gas temperature (—) during the evaporation.	29
1.18	The burner and mist generation system. Scanned from [11].	35
1.19	Schlieren images of hydrogen flame cones for (a) typical stable rich mixture and for (b) $\Phi = 0.6$ with 143 mg/l of water mist. Scanned from [11].	36
1.20	Variation of burning velocity with equivalence ratio, $\Omega = 0.21$. Scanned from [11].	36
1.21	Comparison between the domes corresponding to ENACCEF (left) and ENACCEFII (right). Scanned from [12].	37
1.22	Spacial distribution of droplets generated by spray. Scanned from [12].	39
1.23	Spacial distribution of droplets generated by spray. Scanned from [12].	39
1.24	THAI test vessel configuration for HD-tests. Scanned from [13].	41
2.1	Lumped-parameter study: equilibrium solution of the simplified system	46
2.2	(a) Evolution of equilibrium pressure as a function of H_2 molar fraction, model results (—) are compared with Cast3M operator (—) and CHEMKIN code (—). (b) Evolution of equilibrium temperature as a function of H_2 molar fraction. Model results (—), Cast3M (—) and CHEMKIN (—); The model results are fully super-imposed with the results of Cast3M.	53
2.3	Limit volume fraction of liquid droplets as a function of H_2 molar fraction.	54
2.4	(a) Evolution of pressure as a function of H_2 molar fraction, results of $\alpha = 2 \times 10^{-4}$ (—) are compared with results of $\alpha = 3 \times 10^{-4}$ (—) and $\alpha = 4 \times 10^{-4}$ (—). (b) Evolution of equilibrium temperature as a function of H_2 molar fraction, $\alpha = 2 \times 10^{-4}$ (—), $\alpha = 3 \times 10^{-4}$ (—), $\alpha = 4 \times 10^{-4}$ (—).	55
2.5	(a) Evolution of equilibrium pressure as a function of H_2 molar fraction, results of $\alpha = 2 \times 10^{-4}$ (—) are compared with results of $\alpha = 3 \times 10^{-4}$ (—) and $\alpha = 4 \times 10^{-4}$ (—). (b) Evolution of temperature as a function of H_2 molar fraction, $\alpha = 2 \times 10^{-4}$ (—), $\alpha = 3 \times 10^{-4}$ (—), $\alpha = 4 \times 10^{-4}$ (—).	56
C.1	(a) Regular cubic arrangement of particles in space (b) Regular tetrahedron arrangement of particles.	XVII

List of Tables

- 1.1 Reactions and rate coefficients in Arrhenius law for a detail hydrogen combustion mechanism [14]. 10
- 1.2 Important parameters related to the slow flame interactions. 15
- 1.3 Important parameters related to the rapid flame interactions. 16
- 1.4 Droplet breakup regimes for different Weber numbers. 21
- 1.5 Simplified models and assessment codes. 33
- 1.6 Overview of the experimental conditions corresponding to hydrogen flame-spray interaction experiments. NP = “Not Provided”, NA - a burner was used for laminar flame velocity measurements. 34
- 1.7 Photomultiplier tubes positions along the facility. 38
- 1.8 Initial test conditions specified and measured [15]. 40

- 2.1 Initial conditions for different cases. 52

- C.1 Different turbulent models in Neptune_CFD code [16]. XIII

Chapter 1

Introduction

1.1 General context

Energy is essential for meeting basic human needs and improving human welfare. In terms of the global warming mitigation, nuclear energy provides a clean, reliable and affordable option to keep sustainable economic growth. As a significant part of the world energy production, the nuclear energy is expected to grow in the coming decades. According to the annual report of international atomic energy agency, the world's 450 operational nuclear power reactors provide a generation capacity of 396.4 gigawatts (electrical) (GW(e)), or 10% of global electricity supply, at the end of 2018 [17]. After Fukushima accidents, even facing an uncertain future in many countries, nuclear still obtained an annual growth of 3.3% in 2018 as a result of new additions in China and the restart of four reactors in Japan [18]. Currently, lifetime extensions of old nuclear power plants are crucial for worldwide energy transition. New insights are also recommended by IAEA experts, that nuclear hydrogen production can play important roles in the future hydrogen economy. Security has always been a core issue in the field of nuclear engineering. Many researches have focused on hydrogen-related safety issues in order to prevent severe accidents [19; 20; 21].

The hydrogen generation and the risk of hydrogen explosion, combined with other phenomena leading to containment over-pressurization in the case of severe accidents, can solicit complicated safety issues related to accident management [22]. In the case of a severe accident in a nuclear power plant (NPP), hydrogen can be released from the oxydation of the fuel cladding leading to the formation of combustible mixtures of hydrogen with air [23; 24; 25; 26]. The dry hydrogen concentration can be estimated to be between 12% and 21% in American plant designs, under the assumption that all the Zircaloy of the fuel-cladding are oxidized by water (except for the in-vessel Zr or structure steel) [27]. Similarly, for the operating and future European Pressurized-water Reactor (EPR) designs, the dry hydrogen concentration can reach between 17% and 20%. Even though the typical steam concentration can vary from 20% to 70%, the premixed hydrogen-air-steam mixture can be still ignited in different scenarios, leading to a flame propagating through different regimes such as slow deflagration, fast deflagration or even detonation regimes [20]. The explosion-induced

overpressure can represent a great threat to the integrity of the confinement of nuclear radiological materials. A set of mitigation devices is installed inside an NPP reactor building, such as spray systems, recombiners and wall condensers, etc. These sprays can limit overpressure from explosion and also they are aimed to enhance the gas mixing, avoid hydrogen accumulation, and wash out fission products and structure materials that may be released into the reactor building [1].

Depending on accident scenario evolutions, ignition might occur after the activation of the spray system, thus the understandings of : *a*) the dynamics of water spray exposed to explosion-induced flow field, and *b*) the ability of spray on pressure mitigation are needed. If premixed combustion takes place during the spray activation, the spray droplets can have two opposite effects on the flame propagation [6; 28]: either mitigate the hydrogen combustion or aggravate the consequences of combustion due to enhancement of the turbulence of the gas mixture. Droplet diameters and the relative velocities are reported to be main parameters affecting the global effects [29].

It has been indicated in various experiments that spray systems can have a mitigation effect on explosions as a result of droplet evaporation inside the flame [28]. The droplets generated by industrial water-spray systems are relatively large, having diameters of the order of $O(100 - 1000 \mu m)$. Break-up may occur when the droplets are exposed to a high velocity flow due to flame acceleration or explosion-induced shock waves. The most effective explosion-mitigating water-spray systems are those generating either very small droplets (less than $10 \mu m$), which are favorable to evaporate, or large droplets (larger than $200 \mu m$), which are easier to break up [29]. On the contrary, an explosion-enhancing effect could not be neglected. As established in experiments, the main reason for explosion enhancement is turbulence generation in the gas mixture by the water sprays, in particular of large droplets [6].

1.2 Scientific issues

The effects of the spray system on the hydrogen explosion can be divided into two aspects: mitigation and enhancement. The physical phenomena related to the spray-explosion interaction are numerous and closely related. Several important scientific issues rise while modeling spray-explosion interaction for industrial applications:

Issue 1 : How to identify the dominant phenomena and what kind of modeling approaches to choose for large-scale simulations?

Issue 2 : How to quantify the mitigation effect of a spray on flame burning velocity?

Issue 3 : What are the consequences of the interaction between the spray cloud and the explosion-generated shock wave and how to evaluate them?

Issue 4 : How to quantify the spray-induced turbulence and its effect on the flame propagation?

In this manuscript, we are interested in the phenomenology and modeling issues related to the interaction between a premixed hydrogen-air flame, resulting from an accidental explosion, and a water spray, activated

to prevent an over-pressurization inside the building. Now we briefly describe the spray system in the PWR containment buildings in Section 1.2.1 and the combustion explosion phenomena associated in Section 1.3. Section 1.4-1.6 provide an introduction the general concepts and important phenomena related to the spray-flame, spray-shock interactions and spray-induced turbulence, respectively.

1.2.1 PWR containment spray system

In a nuclear Pressurized Water Reactor (PWR), the containment spray system, consisting of a spray subsystem and an additive subsystem, serves to mitigate the consequences of a loss of coolant accident by injecting a water spray into the containment building. The containment spray system may be used for one or more of the following purposes: *a*) containment post-accident pressure suppression; *b*) containment heat removal; *c*) containment atmosphere fission products removal; *d*) mixing of containment atmosphere; and *e*) containment sump chemistry control [30].

The efficiency of the spray system depends on the droplet size, velocity distributions, droplet volume fraction and their variations in the confinement building [31]. Several phenomena related to droplets such as condensation [32], collision [31; 33], breakup [34] and dispersion [35] are of particular importance and usually coupled in real accident scenarios. Accurate and complete input data related to the spray droplets are required for the large-scale numerical simulations.

Generally, the French PWR containment buildings have two series of nozzles placed in circular rows at the dome of the building [36]. For the 900 MWe PWR, a total of 506 nozzles are installed evenly on the four rings at a height of 51 – 55 *m*. The schematic views of these spray rings and the associated spray envelopes are given in Fig. 1.1. Under the spray nozzles, two spray regions can be distinguished from the Fig. 1.1: the near nozzle region and the quasi-homogenous region. The nozzle type used in many French 900 MWe PWRs is the SPRACO 1713A, distributed by Lechler under Reference No. 373.084.17.BN, Fig. 1.2a. This nozzle is generally used with water at a relative pressure of 3.5 *bar*, producing a flow rate of approximately 1 *l/s*, with an outlet orifice size of the nozzle of 9.5 *mm*. The temperature of the water injected during the hypothetical accident is either 20°C or between 60°C and 100°C, depending on the mode chosen (the 60°C to 100°C process is called the recirculation mode).

The industrial spray nozzles generate droplets in the sizes ranging from a few micrometers to around 1000 μm , following a non-uniform distribution centered on a mean value [34]. The droplet size distribution can vary with different parameters such as relative injection pressure, orifice diameter and water temperature, etc. An example of the drop size distribution under different relative pressure is depicted in Fig. 1.2b. Some spray characteristics in the region just below a single spray nozzle can be drawn from experimental measurements. At a distance of 20 *cm*, the spray droplets have a geometric mean diameter D_{10} varying from 280 to 340 μm . The Sauter mean diameter D_{32} varies from 430 to 520 μm and the mean axial velocity varies from 14 to 20 *m/s*. The radial velocity is around 7 *m/s*, whereas in contrast, the ortho-radial velocity is almost equal to zero [1].

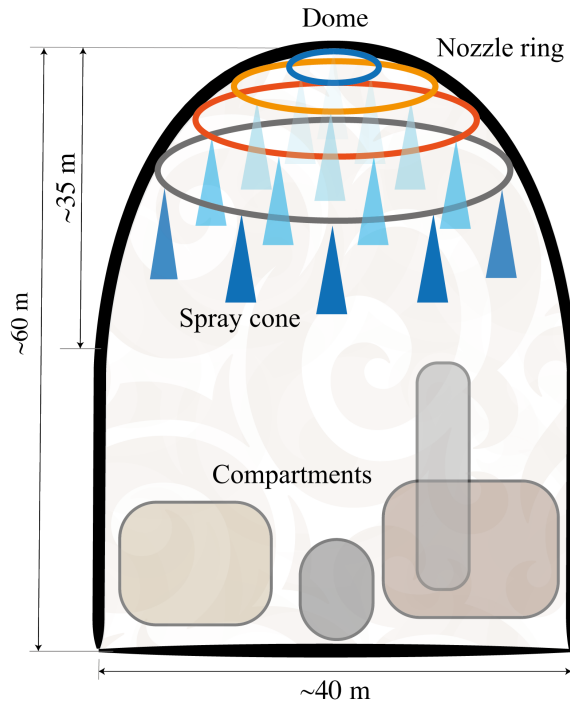


Figure 1.1: Spray rings and envelopes in a French PWR (not to scale) [1].

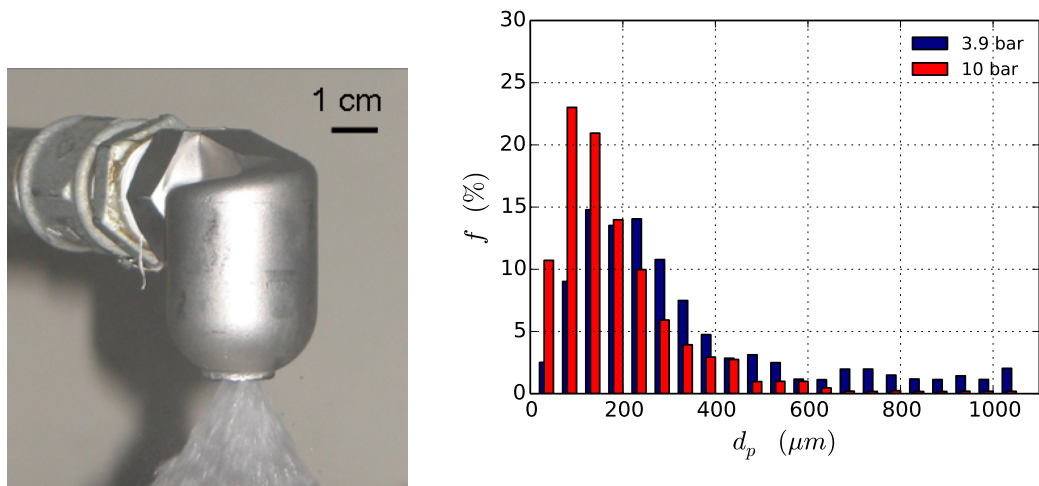


Figure 1.2: (a) Spray nozzle SPRACO 1713A (Lechler 373.084.17.BN) (b) drop size distribution at 6 m from the nozzle under different relative injection pressure [1].

1.3 Combustion phenomena during severe accidents

Several nuclear accidents in the history led to severe core melt down, such as the Three Mile Island disaster and the Fukushima Daiichi accident. An accumulation of hydrogen in the containment building can occur due to the oxydation of fuel cladding and other reactions. In case of these severe accidents, the premixed combustion of hydrogen-air mixture can result in different flame propagation regimes. Among them, two fundamental processes emerge: Flame Acceleration (FA) and Deflagration to Detonation Transition (DDT). Different combustion regimes of the combustible gaseous mixtures are involved such as deflagration, fast deflagration, or even detonation [24].

1.3.1 Flame acceleration and DDT

As a result of the Darrieus–Landau and thermal-diffusion instabilities, the free expanding of a premixed flame is intrinsically unstable due to the thermal expansion of the gas produced by the combustion process. Both in laboratory-scale and large-scale experiments, it is demonstrated that the obstacles located along the flame expanding path can lead to rapid flame acceleration [37; 38; 39]. The burnt products of combustion produce movement in the unburnt gas by thermal expansion. Under some specific initial and geometry conditions, the flame acceleration can result in DDT process [40].

Depending on the fuel gas composition and geometry conditions, the flame acceleration may progress through a series of regimes, as shown in Fig. 1.3. In case of mild ignition, a laminar flame propagates at the velocity s_L and it is much affected by the density ratio across the flame front. According to the thermal flame theory, the un-stretched laminar flame speed depends on two parameters: the thermal diffusivity and the reaction rate through the flame zone [4]. The laminar flame is relatively short-lived and can be soon replaced by the *wrinkled* flame regime or cellular regime. The hydrodynamic or Darrieus–Landau instability is considered to play an important role in the flame wrinkling. For most of the accidental explosions, the wrinkled flame regime can persist over a large flame propagation distance. As a result of the increase in flame area, the burning rate, the flame propagation velocity can be several times higher than the un-stretched flame velocity.

Affected by the obstacles or boundary layers induced turbulence, the wrinkled flame can be eventually transformed to a turbulent flame brush, which is an ensemble of discrete, laminar flames, called flamelets. The increase in surface area of the laminar flamelets can lead to a further flame acceleration. In case of sufficient turbulence levels, the flamelets can be destroyed and replaced by a reaction zone structure [41].

Through shock ignition or the shock wave amplification by coherent energy release (SWACER) amplification mechanism, the flame acceleration can eventually lead to DDT [42]. For geometries containing repeated obstacles, as a result of the feedback mechanism of the flame velocity and turbulence, generated by fluid motion across the obstacles, flame can have significant acceleration. The turbulent flame acceleration process can be influenced by several parameters: the mixture composition, the shape of the obstacles and the enclosure dimension [2].

In severe accident scenarios during which the spray system activated before or during the hydro-

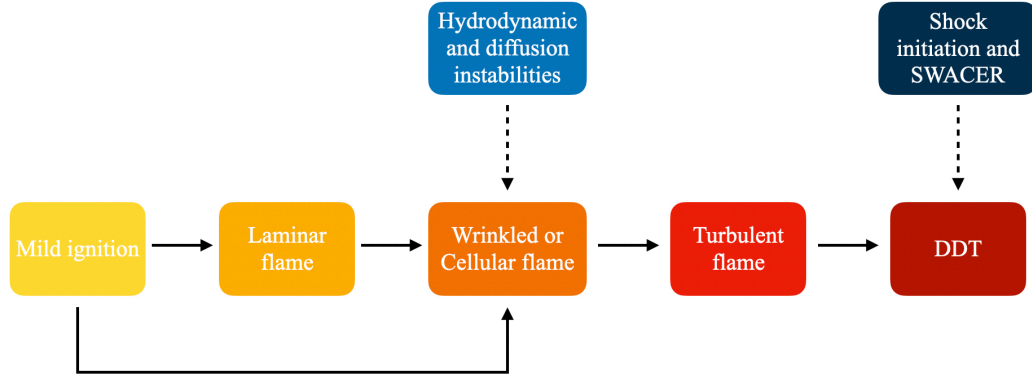


Figure 1.3: Regimes of flame propagation leading to DDT (SWACER = Shock Wave Amplification by Coherent Energy Release) [2].

gen/air/steam mixture explosion, one can have two possibilities of the ignition point as shown in Fig. 1.4. First, the ignition takes place at the upper part of the reactor building, which has a low volumetric blockage ratio as shown in Fig. 1.4a. In this case, the resulting flame would start to interact with the spray soon after ignition. The spray-induced turbulence is the main reason for the combustion flame acceleration. Second, the ignition takes place at the lower, obstructed part of the building where liquid water can hardly penetrate as depicted in Fig. 1.4b. Resulting flame will accelerate in the obstructed part before emerging into the upper part with possibly high velocity (several hundred meters per second). In this case, the high velocity gas flow can lead to the secondary breakup of the spray droplets and change the spray topology as well as the spatial distribution of the droplet volume fraction. For both cases, the interaction between the laminar flame and spray droplets plays important roles. The evaporation of small droplets within the flame reaction zone is considered to be the main reason for the reduction of flame velocity by water spray. Therefore, we should pay attention in our study to these essential phenomena: laminar flame-droplet interaction, spray topology modification, spray droplet breakup and the spray-induced turbulence.

In large-scale modeling, the effects of the phenomena discussed above on flame acceleration process are usually described through the variation of the turbulent burning velocity s_T . For example, one possible expression for the turbulent velocity s_T can be as following [43]:

$$s_T = f(s_L, \delta_L, Le, \dots) \times u'^\alpha \times L_t^\beta, \quad (1.1)$$

where $f(s_L, \delta_L, Le, \dots)$ is a function of chemical properties of the gas mixture such as, laminar flame velocity s_L , laminar flame thickness δ_L , Lewis number Le , etc., u' is the turbulence intensity, and L_t is the integral turbulence length scale. This function has different forms with different turbulent flame velocities models but

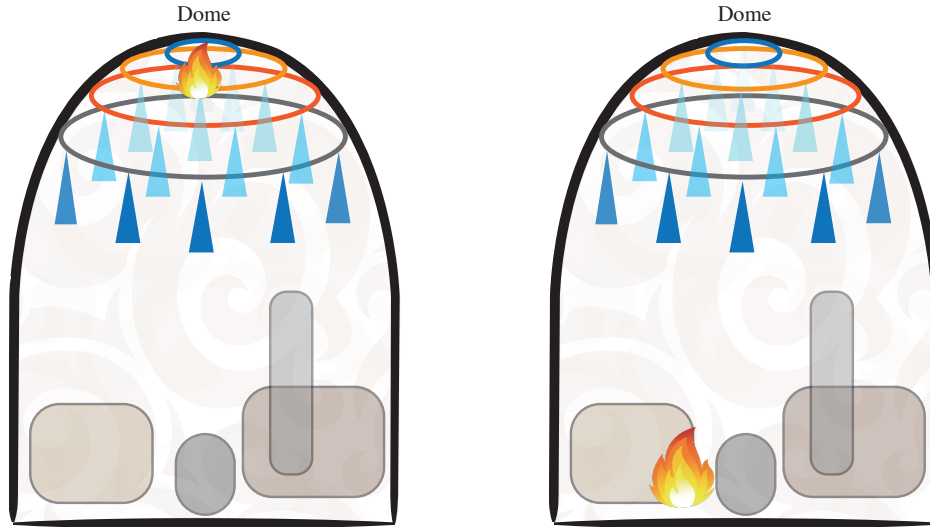
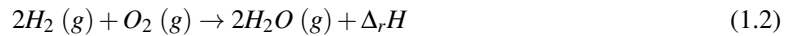


Figure 1.4: Sketch of a nuclear reactor building with an ignition taking place at the dome part (a) and at the obstructed lower part (b).

the main idea keeps the same. The spray mitigation effects can be described through the modification of s_L , as a result of droplet evaporation. While the flame acceleration is determined by turbulent properties such as u' and L_t . Many other expressions for the turbulent flame modeling also exist [44; 45; 46].

1.3.2 Premixed hydrogen-air combustion

In a flame of premixed hydrogen-air mixture, the hydrogen (H_2) reacts with oxygen (O_2) to form water steam (H_2O) and releases energy ($\Delta_r H$). The overall reaction is well-known and can be written as:



The combustion reaction rate of the overall reaction can be given by the fitting formula:

$$\frac{d[H_2]}{dt} = -K_f [H_2]^n [O_2]^m \quad (1.3)$$

where K_f is the reaction-rate constant. This reaction is exothermic, with a global order of reaction $m + n$ depending on pressure and gas mixture compositions. The equation (1.2) is only applicable as a simple chemistry assumption for the hydrogen combustion. It is used in the lumped parameter study in the Chapter 2. In fact, the mechanism of hydrogen-air combustion consists of several elementary reactions in which one or more chemical species or radicals react directly to form products in a single reaction step and with a single

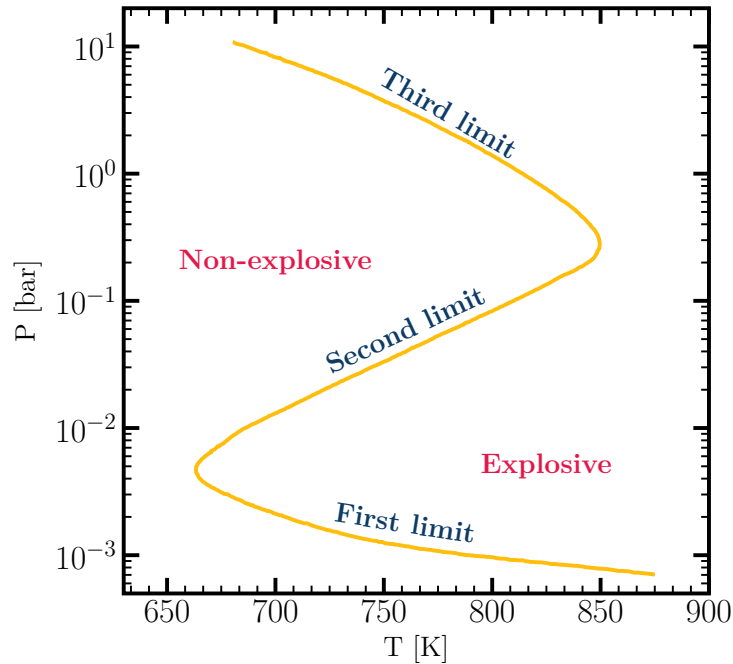


Figure 1.5: Experimental P-T diagram for H_2-O_2 reaction [3].

transition state. More precisely, the combustion mechanism can be divided into several kinds of elementary reactions such as chain initiation reactions, chain branching/propagating reactions and chain termination reactions [47].

The explosion limits of $H_2 - O_2$ mixtures are usually presented in temperature–pressure ($P - T$) boundaries that divide the overall chemistry of hydrogen combustion into slow-burning and explosive regimes. An example is given in Fig. 1.5. In the explosive region the chain branching reaction rates are more important than the chain breaking reactions. On the contrary, in the non-explosive region, the relation of these reaction rates is reversed, and the two rates are equal at the limit. The explosion limit curve has a shape of reversed S-curve, of which three branches are marked as first, second, and third explosion limit, respectively, as depicted in Fig. 1.5. An increase of pressure along the first and third limits can lead from no explosive region to explosion, whereas along the second limit it behaves inversely. As for the temperature, when it is increased, the first and third limits shift to lower pressures and the second limit shifts to higher pressures. The second explosion limit exists as a result of the balancing of chain-branching and chain-breaking reaction rates. And the third explosion limit is closely related to the fact that the radical HO_2 becomes very reactive in high pressure conditions. The first and third explosion limit is diffusion-dependent and can be much affected by the reaction vessel (size, wall surface, surface to volume ratio, etc). The explanations of these three explosion limits and more quantitative details can be found in [3].

The detailed chemistry of combustion is reported to be important for the phenomena understanding and

numerical simulation [48]. Various available detailed mechanisms exist for describing hydrogen combustion in air or pure oxygen [49; 14; 50]. The detail mechanism used in the following numerical simulations is the San Diego mechanism [14] implemented in the Cosilab code [51] (see Appendix A.2). This mechanism has been reported to give satisfactory predictions for laminar flame velocities for most initial conditions. Consisting of 21 reversible elementary reactions, this mechanism involves 8 reacting species H_2 , O_2 , H_2O , H , O , OH , HO_2 and H_2O_2 . The elementary reaction rate constant can be described by the Arrhenius law:

$$k = AT^n \exp\left(\frac{E_a}{R_0T}\right) \quad (1.4)$$

where A is the pre-exponential factor, a constant for each reaction; E_a is the activation energy of the reaction; R_0 is the universal gas constant. A summary of the elementary reactions in the detailed hydrogen combustion mechanism and the associated constants are given in the Tab. 1.1. More information on the combustion mechanisms can be found in the works [14; 52].

1.3.3 Flame thickness, velocity and length scales

The exact solution of laminar flame propagation requires the resolution of complicated fluid dynamics and complex chemical reactions. By using proper physical assumptions and mathematical techniques, many simplified formulations have been proposed. Among various interpretations of the laminar premixed flame velocity and thickness, two theories are of vital importance: the simple approach of Mallard-Le Chatelier [4] and the thermal flame theory of Zeldovich and Frank-Kamenetzki [53].

Mallard and Le Chatelier developed a two zones theory of a laminar premixed flame which has a historical significance. This simple analysis allows to establish important parameters in laminar flame propagation that are more difficult to interpret in complex analyses. In this theory, the flame consists of a preheated zone I and a burning zone II. The heat conducted from the combustion in the zone II is supposed to raise the unburnt gas to the ignition temperature T_i . It is assumed that the temperature slope is linear of slope $(T_f - T_i)/\delta$, where T_f is the flame temperature and δ is the thickness of the reaction zone, as shown in Figure 1.6a. The enthalpy balance gives:

$$\dot{m}c_p(T_i - T_0) = \lambda \frac{T_f - T_i}{\delta} A \quad (1.5)$$

where λ is the thermal conductivity, \dot{m} is the mass rate of the fresh gas mixture, T_0 is the unburnt gas temperature and A is the cross-sectional area.

Generally, when the unburnt gas flow direction is normal to the flame front, the laminar flame velocity s_L is defined equal to the unburnt gas velocity u . Thus, one can obtain from Eq. (1.5) for the expression of the flame velocity:

$$s_L = \frac{\lambda(T_f - T_i)}{\rho c_p(T_i - T_0)} \frac{1}{\delta} \quad (1.6)$$

The major drawback of this model is the indefiniteness of the ‘‘ignition temperature’’. Moreover, the thickness of the flame δ is usually unknown. An approximative expression could be [54]:

$$s_L \approx \frac{\alpha}{\delta} \quad (1.7)$$

TABLE 1.1: Reactions and rate coefficients in Arrhenius law for a detail hydrogen combustion mechanism [14].

Elementary reaction		$A [s^{-1}]$	n	$E_a [kJ/mol]$
$H + O_2 \rightleftharpoons OH + O$		3.52×10^{16}	-0.7	71.42
$H_2 + O \rightleftharpoons OH + H$		5.06×10^4	2.67	26.32
$H_2 + OH \rightleftharpoons H_2O + H$		1.17×10^9	1.3	15.21
$H_2O + O \rightleftharpoons 2OH$		7.00×10^5	2.33	60.9
$2H + M^{(1)} \rightleftharpoons H_2 + M^{(1)}$		1.30×10^{18}	-1.0	0.0
$H + OH + M^{(2)} \rightleftharpoons H_2O + M^{(2)}$		4.00×10^{22}	-2.0	0.0
$2O + M^{(3)} \rightleftharpoons O_2 + M^{(3)}$		6.17×10^{15}	-0.5	0.0
$H + O + M^{(4)} \rightleftharpoons OH + M^{(4)}$		4.71×10^{18}	-1.0	0.0
$O + OH + M^{(4)} \rightleftharpoons HO_2 + M^{(4)}$		8.0×10^{18}	0.0	0.0
$H + O_2 + M^{(5)} \rightleftharpoons HO_2 + M^{(5)}$	k_0	5.75×10^{19}	-1.4	0.0
	k_∞	4.65×10^{12}	0.44	0.0
$HO_2 + H \rightleftharpoons 2OH$		7.08×10^{13}	0.0	1.23
$HO_2 + H \rightleftharpoons H_2 + O_2$		1.66×10^{13}	0.0	3.44
$HO_2 + H \rightleftharpoons H_2O + O$		3.10×10^{13}	0.0	7.20
$HO_2 + O \rightleftharpoons OH + O_2$		2.00×10^{13}	0.0	0.0
$HO_2 + OH + M \rightleftharpoons H_2O + O_2 + M$	k_0	7.0×10^{12}	0.0	-4.58
	k_∞	4.5×10^{14}	0.0	45.7
$2OH + M^{(6)} \rightleftharpoons H_2O_2 + M^{(6)}$	k_0	2.76×10^{25}	-3.20	0.0
	k_∞	9.55×10^{13}	-0.27	0.0
$2HO_2 \rightleftharpoons H_2O_2 + O_2$	k_0	1.030×10^{14}	0.0	46.2
	k_∞	1.940×10^{11}	0.0	-5.89
$H_2O_2 + H \rightleftharpoons HO_2 + H_2$		2.3×10^{13}	0.0	33.3
$H_2O_2 + H \rightleftharpoons H_2O + OH$		1.00×10^{13}	0.0	15.0
$H_2O_2 + OH \rightleftharpoons H_2O + HO_2$	k_0	1.74×10^{12}	0.0	6.0
	k_∞	7.59×10^{13}	0.0	30.4
$H_2O_2 + O \rightleftharpoons HO_2 + OH$		9.63×10^6	2.0	16.7

Third-body efficiencies are:

$$[M^{(1,2,3,4)}] = 2.5 [\text{H}_2] + 12 [\text{H}_2\text{O}] + 1 [\text{other}].$$

$$[M^{(5)}] = 2.5 [\text{H}_2] + 16 [\text{H}_2\text{O}] + 1 [\text{other}].$$

$$[M] = 1 [\text{other}].$$

$$[M^{(6)}] = 2.5 [\text{H}_2] + 6 [\text{H}_2\text{O}] + 6 [\text{H}_2\text{O}_2] + 1 [\text{other}].$$

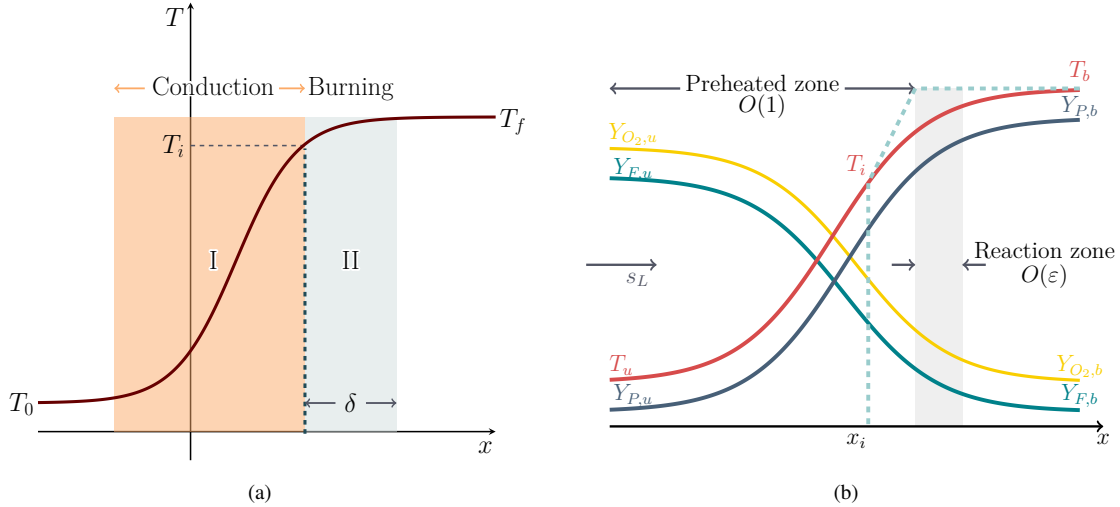


Figure 1.6: (a) Mallard-Le Chatelier description of the temperature in a laminar flame [4]. (b) Temperature and concentration profiles, schematically for a lean mixture in thermal flame theory [5].

where α is the thermal diffusivity. This expression is very useful in estimating the laminar flame properties such as s_L in various physical and chemical conditions. However, the estimated values may differ from the exact values [55].

The thermal flame theory of Frank-Kamenetzki is the first theoretical treatment which places the combustion science on a mathematical basis [53]. Assuming a one step global reaction with high activation energy, the classical mathematical description of the premixed gas combustion is provided on stationary one-dimensional flames. Compared to the approach of Mallard, the definition of the preheat zone is larger and reaction zone determined by the intersection of the temperature slope tangent line and the flame temperature, as depicted in Fig. 1.6b.

In terms of the burning velocity, the thermal flame theory links the thermal diffusivity D_T and the chemical time t_c and obtains [56]:

$$s_L = \sqrt{D_T/t_c} \quad (1.8)$$

with

$$D_T = \frac{\lambda_b}{\rho_u c_{p,u}}, \quad t_c = \frac{\rho_u E^2 (T_b - T_u)^2}{2B\rho_b^2 (RT_b^2)^2 S} \exp\left(\frac{E_a}{RT_b}\right) \quad (1.9)$$

where B and S are parameters determined by the gas compositions, the subscript u and b denote the properties of the unburnt and burnt gas, respectively.

Many ways exist to determine the thickness of the premixed flame for simple chemistry approaches. An expression of flame thickness can be proposed using scaling laws [57]:

$$\delta = \frac{\lambda_b}{\rho_u c_{p,u} s_L}. \quad (1.10)$$

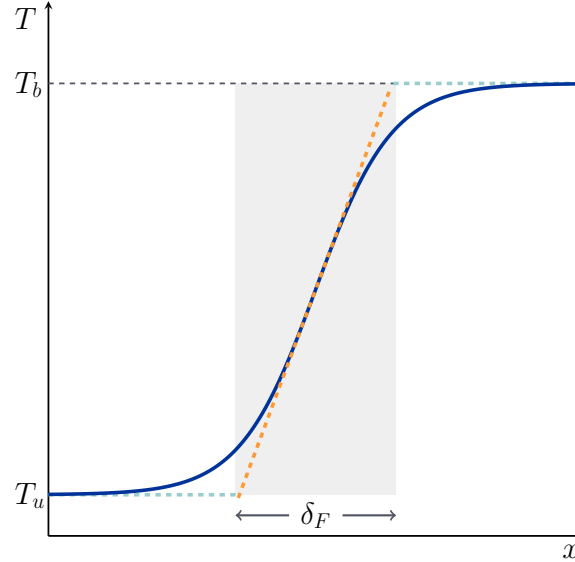


Figure 1.7: Graphical determination of the flame thickness from the temperature profile.

where δ is called *diffusive* thickness, which can be determined as soon as the flame velocity is known, before a computation.

In another way, the flame thickness can be descriptively constructed from the temperature profile as shown in Fig. 1.7. Placing tangent in the turning point of the profile, the flame thickness δ_F is taken as the intersections of the tangent with the horizontal lines at T_u and T_b on the abscissa. The flame thickness can be computed using the temperature profile:

$$\delta_F = \frac{T_2 - T_1}{\max\left(\left|\frac{\partial T}{\partial x}\right|\right)} \quad (1.11)$$

The graphical definition of the flame thickness is considered to be the best definition. However, one can only get this thickness after a computation of the flame propagation [57; 58].

1.4 Flame-spray interaction mechanisms

As indicated in some experimental works, the water spray systems have a mitigating effect on the flame propagation. Early small scale experiments using methane and hydrogen have revealed that sprays can be effective against premixed combustion [59; 60; 61]. Meanwhile, sometimes an explosion-enhancing effect cannot be neglected [28; 6]. A sketch of premixed flame propagating through an unburnt mixture containing water droplets is presented in Fig. 1.8. Two different flame propagation regimes are presented: slow flame and fast flame interacting with spray droplets. A slow flame, usually subsonic, interacts directly with the spray

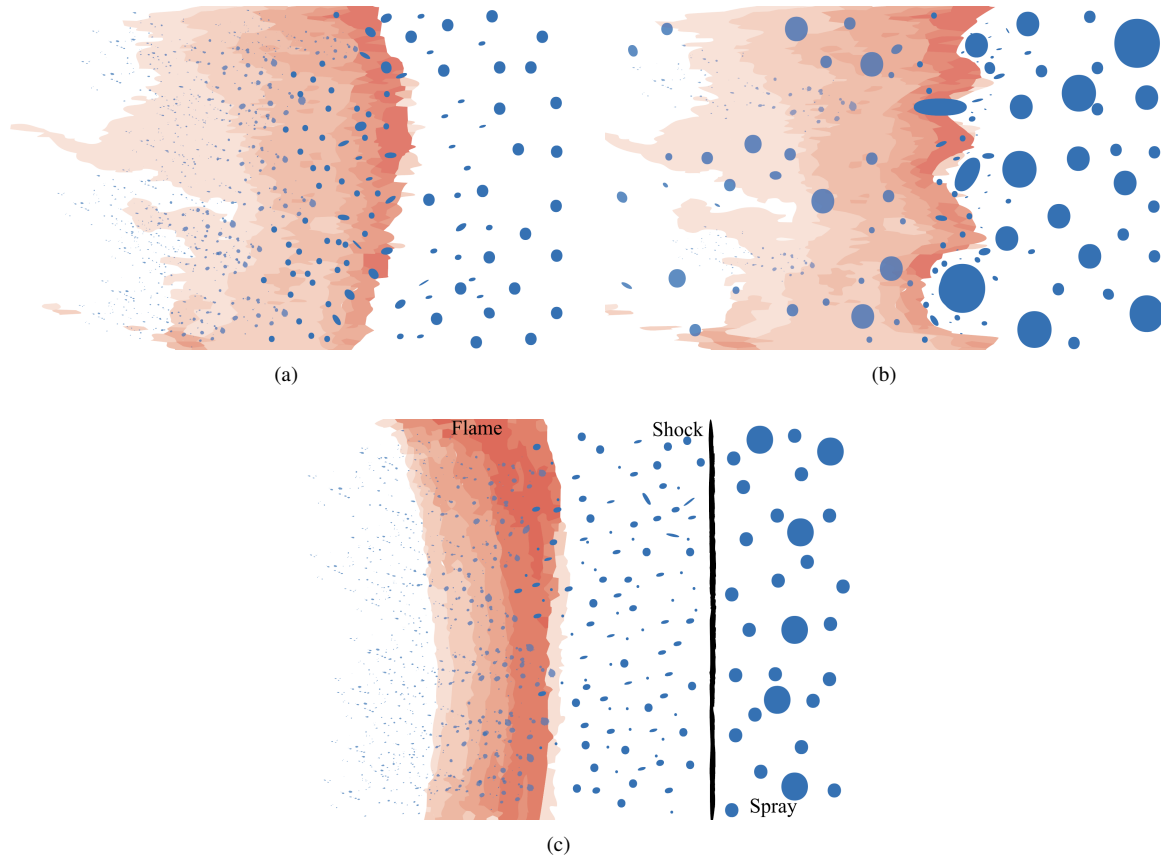


Figure 1.8: Interaction mechanism between the flame and water droplets with flame propagating from left to right; (a) slow flame with small droplets, (b) slow flame with big droplets, (c) fast flame following pressure wave.

droplets, of which the flame front can be stretched by the penetration of droplets. A fast flame propagates closely following a compression pressure wave (such as detonation), or a shock wave as depicted in Fig. 1.8c. The pressure wave interacts with the spray droplets, before the spray-flame interaction.

Figure 1.8a shows the interaction process between a slow flame and the spray droplets. Penetrating the slow flame front, the droplets are evaporated as a result of high temperature of the ambient gas. The evaporation of the droplets inside the flame thickness can lead to a direct mitigation effect on the flame propagation. Interactions of a slow flame and the spray of big droplets are depicted in Fig. 1.8b, where one can see that the big droplets can behave as obstacles in the gas flow and increase the flame surface. The flame velocity is also affected by the turbulence generated from the spray droplets movement. For the rapid deflagration, the flame front is close to the expansion pressure wave or shock wave as presented in Fig. 1.8c. In this regime, the flame propagates in the post-shock gas and thus is directly affected by the shock wave.

The pressure wave can lead to the breakup of the droplets, change the droplets size and the spray dispersion before flame-spray interaction takes place.

Main phenomena and parameters related to spray-explosion interactions are overviewed in Tabs. 1.2 and 1.3. A variety of parameters involved can be noted and different modeling approaches exist for different specific interactions. One can see that a single code cannot model all the phenomena with necessary precisions.

Several possible flame mitigation mechanisms by water sprays are proposed in the literature [62; 29; 61]:

- Both liquid droplet and the steam generated from evaporation can serve as a heat sink. The former can be more effective in quenching flames as a result of the high latent heat.
- The presence of droplets in the gas flow can dissipate acoustic and shock waves.
- Droplets punch holes in the flame surface which can cause an extinction, since flames cannot propagate through a too narrow path separating the droplet. A separation path of 0.3 mm is noted to be critical for propagation of stoichiometric hydrogen-air flames.

Among all these mitigation mechanisms, the most important is believed to be the water droplet evaporation, which results in considerable heat losses and mixture dilution.

Taking an example of a 23% hydrogen-air mixture, the corresponding laminar flame thickness is approximately 0.04 mm . Assuming that the flame speed relative to the droplet is similar to the burning velocity $s_L = 1.045\text{ m/s}$, the residence time of the droplet is equal to 0.04 ms . From Fig. 1.9, it can be noted that only droplets smaller than $2\text{ }\mu\text{m}$ can evaporate completely within the flame.

Droplets generated directly from the industrial nozzles of spray systems are relatively large, of which the diameters can have a range of $O(100 - 1000\text{ }\mu\text{m})$. Even though these large droplets can hardly evaporate through a premixed flame, a significant reduction in explosion overpressure has been observed [63; 28; 61]. As a result of aerodynamic interactions between the droplets and the explosion-induced flow, large droplets can break up into small ones leading to the mitigation of the flame propagation. On the contrary, the presence of spray droplets bulk flow can also generate turbulence, which can cause the flame propagation to accelerate [6]. Both these two opposite effects should be considered in real accidental scenarios in order to quantify the effects of spray on the premixed hydrogen explosion.

1.4.1 Droplet evaporation

The droplet evaporation modeling has been an active research field for decades. Spalding *et al.* [64] gave a classical quiescent droplet evaporation model. Kunary *et al.* [65] took into consideration of the effect of the gas velocity in his evaporation correlations. These are the basis of many following works [66]. Sirignano [67] summarizes several former researches and classifies six types of droplet evaporation models, in order of increasing complexity:

- constant-droplet-temperature model, which yields the d^2 -law [68; 69]
- infinite-liquid-conductivity model, droplet temperature uniform but time-varying [70]

TABLE 1.2: Important parameters related to the slow flame interactions.

Physical phenomena	Main characteristic parameters	Symbols and expressions
Spray-laminar flame interaction	Laminar flame velocity	s_L
	Equivalence ratio	ϕ
	Laminar flame thickness	$\delta_F = \frac{\lambda_p}{\rho_u c_p s_L}$
	Droplet volume fraction	$\alpha_p = \frac{V_p}{V_p + V_g}$
	Droplet diameter	d_p
	Droplet evaporation rate	\dot{m}
	Inter-particle distance	$\lambda/d_p = \left(\frac{\tau_c}{\alpha_d}\right)^{\frac{1}{3}} - 1$
Zel'dovich number	$Ze = \frac{E_a}{RT_b} \frac{T_b - T_u}{T_b}$	
Flame-turbulence interaction	Turbulent flame velocity	s_T
	Integral length scale	L
	Damkohler number	Da
	Karlovitz number	Ka
	Laminar flame passage time	t_L
	Turn-over time of largest eddies	t_T
	Turn-over time of smallest eddies	t_K
Turbulent Reynolds number	$Re_t = \frac{\rho v L}{\mu}$	
Spray-induced turbulence	Integral length scale	L
	Inter-particle distance	$\lambda/d_p = \left(\frac{\tau_c}{\alpha_d}\right)^{\frac{1}{3}} - 1$
	Kolmogorov length scale	$\eta = \left(\frac{\nu^3}{\varepsilon}\right)^{1/4}$
	Length-scale ratio	d_p/L
	Stokes number	$St = \frac{\tau_p}{\tau_f}$
	Particle Reynolds number	$Re_p = \frac{\rho u-v d_p}{\mu}$
	Particle momentum number	Pa_s
Particle response time	$\tau_p = \frac{\rho_p d_p^2 \nu}{18\mu}$	

The phenomena mainly investigated in this study are shown yellow background.
 The definitions of the parameters can be referred to Chapter 3-Chapter 5.

TABLE 1.3: Important parameters related to the rapid flame interactions.

Physical phenomena	Main characteristic parameters	Available modeling approach
Shock-spray interaction : droplet breakup	Weber number	$We = \frac{\rho_g v^2 L}{\sigma_w}$
	Ohnesorge number	$On = \frac{\mu_d}{\sqrt{\rho_d d_p \sigma_w}}$
	Maximal stable diameter	d_p^{max}
	Droplet diameter	d_p
	Particle response time	τ_p
	Fragments size distribution	
Shock-spray interaction : spray dispersion	Shock mach number	$M_s = \frac{v_s}{c}$
	Particle volume fraction	$\alpha_p = \frac{V_p}{V_p + V_g}$
	Particle Reynolds number	$Re_p = \frac{\rho u-v d_p}{\mu}$
	Drag coefficient	$C_D = \frac{24}{Re}$
	Reflected shock velocity	v_r
	Transmitted shock velocity	v_t

The phenomena mainly investigated in this study are shown yellow background.
The definitions of the parameters can be referred to Chapter 3-Chapter 5.

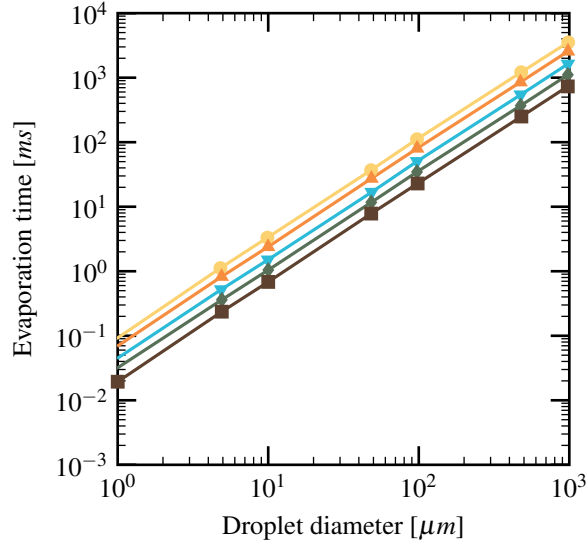


Figure 1.9: Droplet vaporization time as a function of droplet size and relative velocity: $T = 2051$ K, relative velocity of 0 m/s (—○—), 10 m/s (—▲—), 50 m/s (—▼—), 100 m/s (—◆—), 200 m/s (—■—) [6].

- spherically symmetric transient droplet-heat model, conduction limit model [71]
- effective-conductivity model [72]
- vortex model of droplet heating [73; 74]
- direct Navier-Stokes solution [75]

Various differences exist among these methods, and they all have their limits of application. The essential issue is the treatment of droplet heating, which is usually the controlling factor of droplet evaporation rate.

As a direct quantification of the spray effect, the description of mass evaporation rate \dot{m} is vital for the estimation of laminar flame velocity s_L and the laminar flame thickness δ . Starting from the spherically symmetric droplet model, the evaporation rate can be given by [64]:

$$\dot{m} = 4\pi\rho_g D_g r_s \log(1+B) \quad (1.12)$$

where ρ_g and D_g are respectively the mass density and mass diffusivity of the gas film, B is the Spalding transfer constant. The Lewis number is assumed to be unit $Le = 1$.

Kanury has considered the effect of gas velocity to the increase of the vaporization rate [65]:

$$\dot{m} = 4\pi r_s \frac{k_g}{c_{p,g}} \log(1+B) \left(1 + 0.25 Re_D^{0.5}\right) \quad (1.13)$$

An ad hoc method for developing a more robust model has been presented by Abramzon *et al.* [72]. The model extends the classical droplet evaporation model and contains more physical effects such as: variable physical properties, non-unitary Lewis number in the gas phase, influence of Stefan flow etc.,. The gas phase calculation is based on the 1D 'stagnant film theory', incorporating the Stefan flow effect on the thickness of films. The transient liquid heating in the droplet uses the 'effective conductivity model'.

First, the gas properties can be determined by the empirical '1/3' rule:

$$\bar{T}_g = T_s + A_r(T_\infty - T_s); \bar{Y}_g = Y_s + A_r(Y_\infty - Y_s) \quad (1.14)$$

with $A_r = 1/3$ and the subscript s denotes the droplet surface properties.

Coupling the properties of these two phases, the calculation of evaporation rate is given by:

$$\dot{m} = 2\pi\rho_g D_g r_s \tilde{Sh} \ln(1 + B_M) \quad (1.15)$$

where for $Re \leq 5$, D_g is the mass diffusivity of the gas,

$$\tilde{Sh} = 2 + \frac{(1 + 2RePr)^{1/3} \max[1, (2Re)^{0.077}] - 1}{F(B_M)} \quad (1.16)$$

and for $B_M \leq 20$, $Pr \geq 1$, $Sc \leq 3$, $B_H \geq 0$

$$F(B) = (1 + B)^{0.7} \frac{\ln(1 + B)}{B} \quad (1.17)$$

With the estimation of the evaporation rate, the droplet temperature evolution can be obtained by the non-dimensional energy equation for the 'effective thermal conductivity model' [72]:

$$(\phi)^2 \frac{\partial Z}{\partial \tau} = \beta \eta \frac{\partial Z}{\partial \eta} + \frac{1}{\eta^2} \frac{\partial}{\partial \eta} \left(\eta^2 \frac{\partial Z}{\partial \eta} \right) \quad (1.18)$$

where:

$Z = (T - T_0)/T_0$ is the non-dimensional temperature of the droplet;

$\phi = r_s/r_0$ is the non-dimensional radius of the droplet;

$\eta = r/r_s$ is the non-dimensional coordinate;

$\tau = \alpha_L t/r_0^2$ is the non-dimensional time;

α_L is the liquid thermal diffusivity;

β is proportional to the regression rate of the droplet surfaces, which can be estimated by:

$$\beta = -\frac{1}{4\pi\alpha_L\rho_L r_s} \left[\dot{m} + \frac{1}{\rho_L C_{p,L}} Q_L \right] \quad (1.19)$$

From Eq. (1.15), one can deduce the evolution of the droplet surface S_p as a function of time:

$$\frac{dS_p}{dt} = -\frac{\pi d_p^2}{\tau_{ev}} \quad (1.20)$$

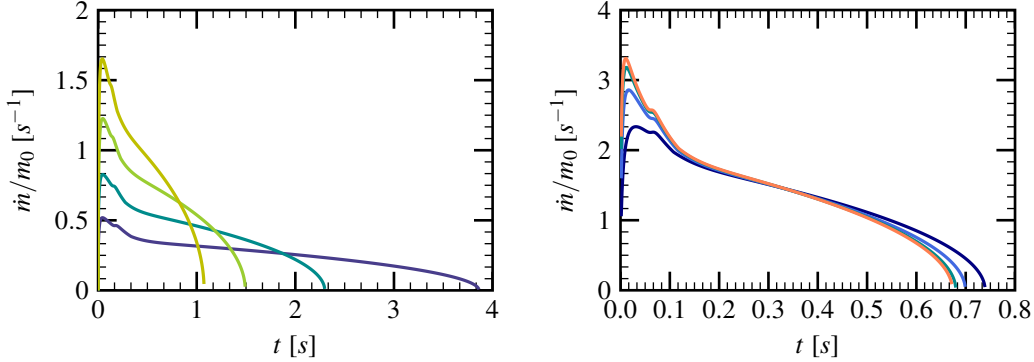


Figure 1.10: (a) Influence of ambient temperature on the mass evaporation rate: $d_p = 500 \mu\text{m}$, 900 K (—), 1200 K (—), 1547 K (—) and 1885 K (—). (b) Influence of ambient pressure on the mass evaporation rate: $d_p = 350 \mu\text{m}$, 1 bar (—), 3 bar (—), 5 bar (—) and 6 bar (—).

where τ_{ev} is called the characteristic time of evaporation, which has an expression in d^2 law:

$$\tau_{ev} = \frac{\rho_d Sc d_p^2}{4 \tilde{S} h \mu_g \ln(1 + B_M)} \quad (1.21)$$

where Sc denotes the Schmidt number, μ_g is the gas dynamic viscosity.

The ambient pressure and temperature can have direct effects on the mass evaporation rate as depicted in Fig. 1.10. Intuitively, the high gas temperature can increase the droplet evaporation rate. High pressure can also affect the evaporation rate as in Fig. 1.10b, but the influence is much less than the temperature.

This effective conductivity model has been implemented during our development as shown in Chapter 3, as well as in the code Cosilab [51]. Easy to implement, this model provides reliable estimation for single droplet evaporation rate, in different ambient conditions [67]. By considering its simplicity, it has the potential capacity to serve for large-scale simulations. The model assessment can be performed using Cosilab code.

1.4.2 Droplet breakup

As mentioned above, the droplet break-up is possible when exposed to aerodynamic forces due to strong gas flows. During primary breakup, the liquid jet out of the nozzle shows coherent structures that interact with the gas-phase and breaks into fragments of different sizes. Then during secondary breakup, these drops break up into much smaller ones. The secondary breakup is more important for the spray-flame interaction since the small fragments formed have better capacity of evaporation.

The Weber number We is a dimensionless number in fluid mechanics that is often useful in analyzing fluid flows where there is an interface between two different fluids, which is defined as [34]:

$$We = \frac{\rho_g l v_s^2}{\sigma_w} \quad (1.22)$$

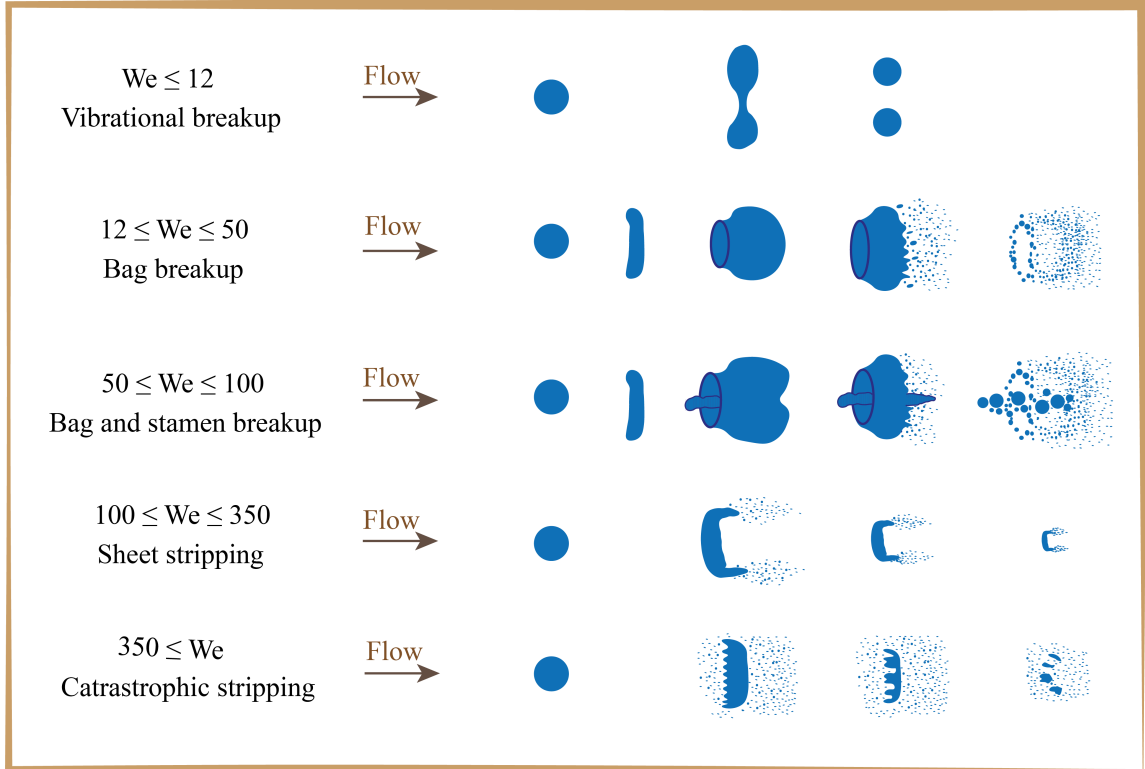


Figure 1.11: Droplet breakup mechanisms [7].

where ρ_g is the density of the carrier fluid, $v_s = ||u_g - u_p||$ is the slip velocity between the two phases, l is its characteristic length, typically the droplet diameter and σ represents the droplet surface tension. Traditionally, there exists five distinct regimes well established in the literature, in order of increasing We as shown in Tab. 1.4.

Vibrational breakup can occur when the Weber number is small, as a result of the oscillations developed at the natural frequency of the droplet. Bag breakup is similar to the soap bubbles blown from a film attached to a ring. This regime is much investigated in both numerical [76; 77] and experimental [78; 79] studies. Bag and stamen breakup is a transition mechanism that has several features in common with the bag breakup regime. For higher Weber numbers, no bags are formed in the sheet stripping and catastrophic breakup regimes. Catastrophic breakup leads to a multistage process in which the fragments are subject to further break-ups, until all the fragments reach a critical Weber number [34]. During accidental hydrogen explosions the visible flame velocity can reach $O(100) m/s$. All the above mentioned droplet breaking regimes can be present during spray-flame interactions.

TABLE 1.4: Droplet breakup regimes for different Weber numbers.

breakup regime	We range
vibrational breakup	$We \leq 20$
bag breakup	$12 < We \leq 50$
bag & stamen breakup	$50 < We \leq 100$
wave crest stripping	$100 < We \leq 350$
catastrophic breakup	$We > 350$

Critical Weber number

The critical Weber number We_c has been investigated experimentally for various types of fluids [80; 79; 81; 82]. In order to account for the influence of liquid viscosity and surface tension, Brodkey *et al.* [83] have proposed an empirical correlation for the critical Weber number:

$$We_c = 12 \left(1 + 1.077 O_n^{0.6} \right) \quad (1.23)$$

where the Ohnesorge number O_n is defined as:

$$O_n = \frac{\mu_d}{\sqrt{\rho_d d_p \sigma_w}} \quad (1.24)$$

where μ_g , ρ_d and σ_w are the dynamic viscosity, the density and the surface tension of the droplet. For the industrial application of the spray breakup, the leading order of $We_c = 12$ is widely accepted and used.

Droplet size distribution

The industrial spray atomizers generate drops in the size range from a few micrometers up to around 1000 μm [34]. The droplets generated by an industrial nozzle follow a non-uniform distribution centered on a mean value as depicted in Fig. 1.12a. After the interaction between the spray droplets and the gas flow (such as spray-shock interaction), the secondary breakup can lead to the change of the fragment drop size distribution, as presented in Fig. 1.12b. As discussed above, the drop size data is crucial to estimate heat and mass transfer during spray-flame interaction.

The fundamental mechanisms involved in droplet atomization are not clearly understood and no single distribution model can predict all drop size data [34]. It is noted that the direct experimental counting for droplet fragment size distribution is hardly possible under high Weber conditions [84]. Several models have been proposed, based on either probability or purely empirical considerations. The general used ones are normal, log-normal, Nukiyama–Tanasawa [85], Rosin–Rammler [86; 87], and upper-limit distributions [88].

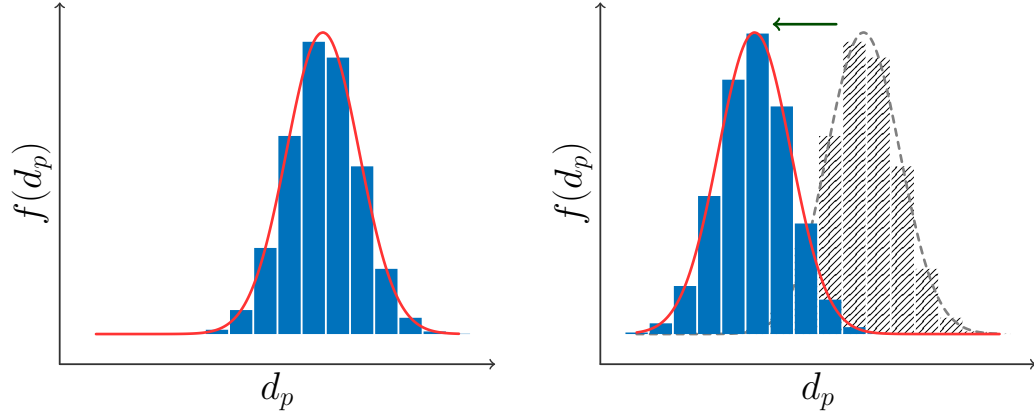


Figure 1.12: Drop size normal distribution (a) and size distribution after secondary breakup (b).

The empirical expression for drop size distribution after break-up developed by Rosin *et al.* [86] is widely used [89]. This distribution function is also known as the Weibull distribution. It may be expressed in the form:

$$1 - Q = \exp \left[-0.693 \left(\frac{d_p}{1.2 d_{32}} \right)^q \right] \quad (1.25)$$

where Q is the volume fraction of droplets of diameter less than d_p , q is constant chosen between 1.5 and 4, d_{32} is the Sauter mean diameter of the spray.

The method of Pilch [7] is specially dedicated to characterize the size distribution of the drop fragments after secondary breakup. The breakup of large accelerated droplets is considered as a cascade process until the fragment Weber number becomes lower than the critical Weber number. After the completeness of the breakup up process, all the droplets fragments are assumed to be smaller than a critical size, which is referred to be the maximal stable diameter given by:

$$d_p^{max} = We_c \frac{\sigma}{\rho v_g^2} \left(1 - \frac{v_p}{v_g} \right)^{-2} \quad (1.26)$$

where v_g is the gas velocity and v_p is the velocity of the fragment cloud after breakup process. This expression is reported to be valid for $We < 10^5$. The velocity of the fragment cloud is calculated using empirical correlation:

$$\frac{v_d}{v_g \sqrt{\rho_g / \rho_p}} = \frac{3}{4} C_D T + 3BT^2. \quad (1.27)$$

where T is the dimensionless total breakup time based on initial Weber number We and defined as the time when the drop and all its fragments no longer undergo further breakup:

$$T = \frac{v_g \sqrt{\rho_g / \rho_p}}{d_p} t \quad (1.28)$$

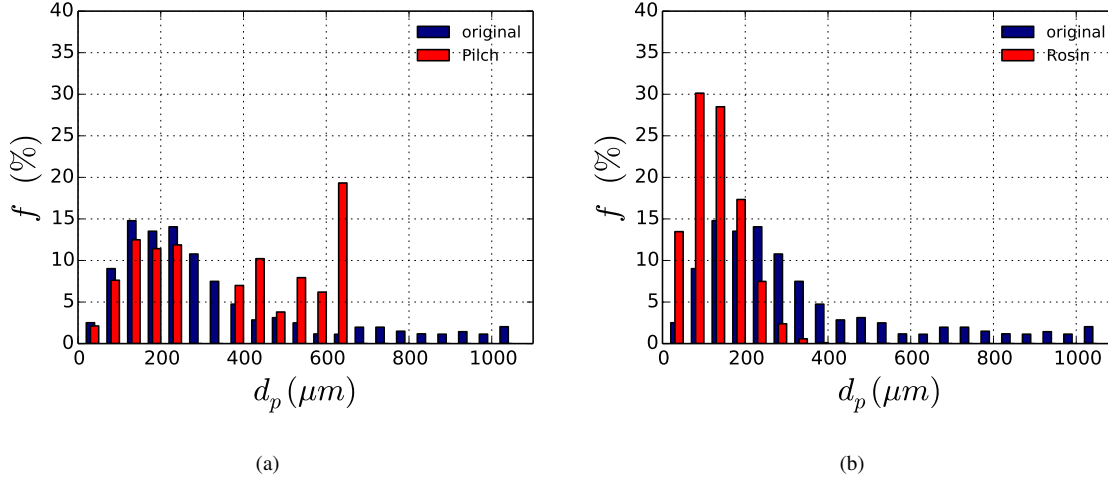


Figure 1.13: Droplet fragment size distribution after the interaction with gas flow of velocity $v_g = 50 \text{ m/s}$; the original spray a droplet size distribution of 3.9 bar SPRACO nozzle at 6 m from the nozzle [8]; (a) model of Pilch (b) model of Rosin.

The empirical correlations for the dimensionless breakup up time T are given by [7]:

$$\begin{aligned}
 T &= 6(We - 12)^{-0.25} & 12 \leq We \leq 18 \\
 T &= 2.45(We - 12)^{0.25} & 18 \leq We \leq 45 \\
 T &= 14.1(We - 12)^{-0.25} & 45 \leq We \leq 351 \\
 T &= 0.766(We - 12)^{0.25} & 351 \leq We \leq 2670 \\
 T &= 5.5 & We \geq 2670
 \end{aligned} \tag{1.29}$$

The droplets coalescence is not taken into account in the model of Pilch.

Figure 1.13 shows the application of the two models mentioned above on an industrial nozzle spray. The fragment size distribution obtained from the two models have different shapes. In order to have a better coincidence with experimental data, several size distribution models should be consulted together [34].

1.5 Spray-shock interaction

A blast wave is a pressure area expanding supersonically outward from an explosive core. The flow field can be approximatively separated by a leading shock front of compressed gases and a following self-similar subsonic flow field [90]. Confined explosions that detonate can generate blast waves which are extremely harmful for the internal structures and human lives. An example of the explosion-induced shock wave is

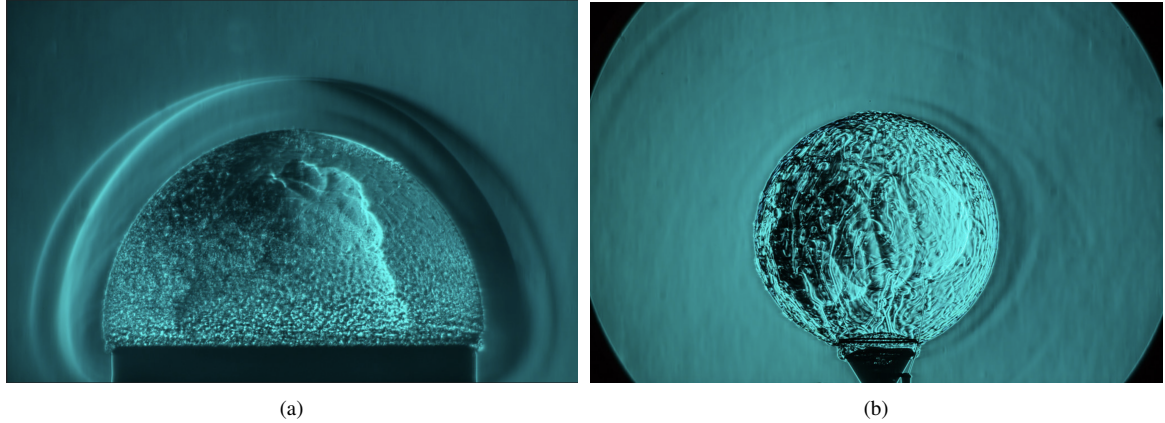


Figure 1.14: Shock waves from a hydrogen oxygen explosion. Schlieren photography of an explosion of $H_2 - O_2$ gas inside a bubble detonated with an electrical spark [9].

given in Fig. 1.14. The density variation of a hydrogen-oxygen explosion is presented by the Schlieren photography, where the pressure waves ahead of the flame front can be clearly noted. The pressure waves can propagate much faster than the flame front, which can interact with the droplets before flames, in the presence of water spray.

Many theoretical and experimental investigations have been carried out on the spray-shock or particle-shock interactions since it is present and of major importance in various industrial applications [91; 92; 93; 94; 95; 96]. Considering the interaction between a planar shock wave and a spray cloud, two main phenomena can be drawn: spray/particle dispersion and secondary droplets breakup [97; 98]. Once a shock wave hits the droplet-laden field, the shocked gas accelerates the droplets and the spray dispersion can be much altered. The local increase of the droplet volume fraction can lead to the change of the mitigation capacity of the spray system [99; 100; 101]. On the contrary, the particles decelerate the post-shock gas and thus the spray cloud can also mitigate the propagation of the shock waves [102]. In case of a water spray in high-speed gas flow, a secondary droplets atomization may occur for Weber number $We > 12$ which leads to the formation of a fine droplet spray that enhances the shock energy dissipation [103; 104; 105]. The spray breakup can contribute to increase the transfer surface and improve both the heat (evaporation) and the mass transfer [106]. Such transfer processes primarily influence the post-shock gas thermo-equilibrium conditions and can alter the cloud dispersion topology. The shock-wave mitigation can be further reinforced and a flame extinction can be encountered in case of reacting flows [98; 99; 100].

For simplicity, small rigid particles are often considered in various studies in place of water droplets. The particles of diameter $O(1 \mu m)$ to $O(10 \mu m)$ are investigated in the current development for several reasons. First, the particle dispersion due to dynamic interaction can be isolated without considering the droplet breakup processes. The droplet diameters of a real industrial spray have an order of magnitude $O(100 \mu m)$,

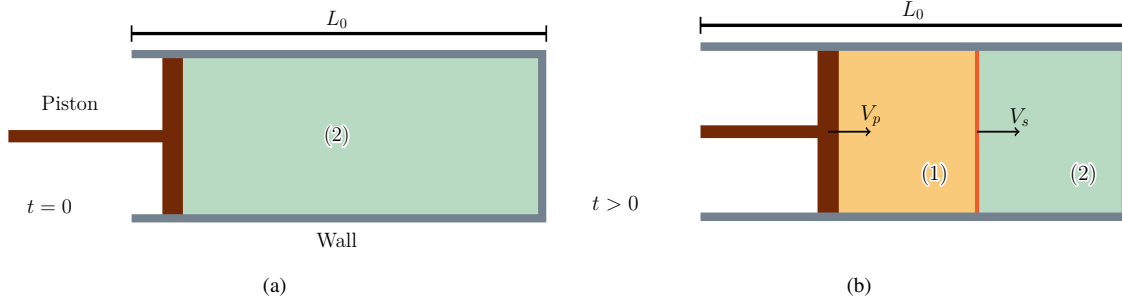


Figure 1.15: Shock wave generation in a piston tube.

small particles of $O(10 \mu m)$ can represent the droplet fragment after atomization.

1.5.1 Planar shock waves

When the shock wave is perpendicular to the gas flow direction it is called a normal shock. Across the shock, the static pressure, temperature and gas density increase almost instantaneously. A planar shock wave can be generated by a piston as shown in Fig. 1.15. The piston starts moving at $t = 0$ with a velocity V_p , generating a shock wave with a velocity V_s . Two areas are divided by the shock wave: the post- (1) and the pre-shock area (2). Given the sound speed in the pre-shock area, c_2 , one can obtain the piston velocity V_p by the following relation:

$$\frac{2}{\gamma+1} \frac{M_s^2 - 1}{M_s} = \frac{V_p}{c_2}, \quad V_s = M_s c_2, \quad (1.30)$$

where M_s is the shock Mach number, γ is the heat capacity ratio is constant which equals to 7/5 for air. The post-shock gaseous flow is assumed to have the same velocity as the piston. Analytical solutions are available for the relation of the pre- and the post-shock thermodynamic quantities [107]:

$$\frac{p_1}{p_2} = \Gamma_1(M_s, \gamma), \quad \frac{T_1}{T_2} = \frac{\Gamma_1(M_s, \gamma)\Gamma_2(M_s, \gamma)}{M_s^2}, \quad \frac{\rho_1}{\rho_2} = \frac{p_1 T_2}{p_2 T_1}, \quad (1.31)$$

where:

$$\Gamma_1(M_s, \gamma) = \frac{2}{\gamma+1} \left(\gamma M_s^2 - \frac{\gamma-1}{2} \right), \quad \Gamma_2(M_s, \gamma) = \frac{2}{\gamma+1} \left(1 + \frac{\gamma-1}{2} M_s^2 \right). \quad (1.32)$$

One can note that the thermodynamic quantity ratios (p_1/p_2 , ρ_1/ρ_2 , T_1/T_2) depend only on the free stream Mach number M_s . Thus, knowing the Mach number, one can determine all the physical conditions across the normal shock.

1.5.2 Spray characteristics

The following assumptions are made in the numerical simulations for spray-shock interactions: *i*) the gas is considered as inviscid and obeys a perfect-gas law; *ii*) the droplets are considered as spherical, rigid particles

of uniform diameter with a uniform temperature distribution; *iii*) the particle volume fractions are small so that the collisions between particles can be neglected [108]; *iv*) only the viscous drag forces are considered to act on the particles. The Basset force can be neglected as a result of high particle-to-gas density ratio [10] and the Magnus force is neglected under no-spin conditions. The gravity is much smaller than the drag force for the range of parameters in this study; *v*) the heat transfer between gas and particles is not considered at present.

In the numerical simulations, the drag force is computed as a result of the gas flow of velocity $\mathbf{u}(\mathbf{x}, t)$. For a particle with a velocity $\mathbf{V}(t)$ located at \mathbf{x} the general motion equation gives:

$$m_p \frac{d\mathbf{V}(t)}{dt} = \sum \mathbf{F}, \quad (1.33)$$

where $m_p = \pi \rho_p d_p^3 / 6$ is the particle mass and ρ_p is the particle density. The viscous drag force reads:

$$\mathbf{F} = \frac{\pi}{8} \rho_g d_p^2 C_D |\mathbf{u}(\mathbf{x}, t) - \mathbf{V}(t)| (\mathbf{u}(\mathbf{x}, t) - \mathbf{V}(t)), \quad (1.34)$$

where C_D is the drag coefficient defined as:

$$C_D = \frac{24}{Re_p} \left(1 + \frac{Re_p^{2/3}}{6} \right) \text{ with } Re_p = \frac{\rho_g |\mathbf{u}(\mathbf{x}, t) - \mathbf{V}(t)| D}{\mu_g}. \quad (1.35)$$

Re_p is the particular Reynolds number related to the flow around the particle and μ_g is the dynamic viscosity of the gas. A correction of the drag coefficient is used since the diameters of the particles considered vary from 1 μm to 20 μm . For each particle, one can obtain the motion equation:

$$\frac{d\mathbf{V}(t)}{dt} = \frac{1}{\tau_p} (\mathbf{u}(\mathbf{x}, t) - \mathbf{V}(t)), \text{ with } \tau_p = \frac{\rho_p d_p^2}{18\mu_g}, \quad (1.36)$$

In case of a two-way formalism, the momentum transfer is considered in order to estimate the effect of the particles on the gas. For a gas volume \mathcal{V} containing one particle with a velocity variation $\frac{d\mathbf{V}}{dt}$, the particle can decelerate the gas by:

$$\frac{d\mathbf{u}}{dt} = -\frac{m_p}{\rho_g \mathcal{V}} \frac{d\mathbf{V}(t)}{dt}. \quad (1.37)$$

More details and the numerical realization of the two-way formalism can be found in [10].

The shock-spray interaction is studied through direct-numerical simulations with a compressible Navier-stokes solver, named Asphodele, developed in CORIA Rouen to simulate the two-phase dispersed fluid flows [10]. The Eulerian-Lagrangian approach is used with an Unresolved Discrete Particle Model (UDPM) which relies on a larger computation cell with regard to the particle sizes and uses a drag force model to describe the gas-particle interactions. A 5-order WENO scheme is implemented with a global Lax-Friedrichs splitting for space discretization which is widely used in shock descriptions. Adaptive stencils are used in the reconstruction procedure based on the local smoothness of the numerical solution to achieve high order accuracy and non-oscillatory property near discontinuities [109]. The time resolution employs a fourth-order Runge-Kutta method, with a minimal storage time-advancement scheme of [110]. The governing equations are presented in Appendix B.1.

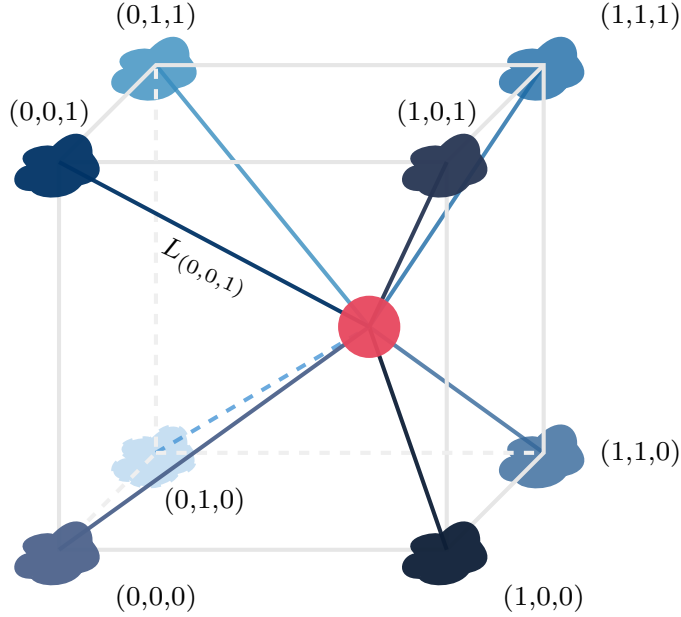


Figure 1.16: Spatial distribution of the source term of an evaporating droplet [10], the coordinates give the relative position of the nodes in gas phase.

1.5.3 Two-way interactions

The typical value of the spray volume fraction in nuclear spray systems during accidental scenarios is reported to be $\alpha_p = O(10^{-4})$ [111]. In this volume fraction range, the two-way formalism has to be considered in the shock-spray interactions [112]. Apart from the droplet acceleration due to the gas movement, the droplets can also effectively act on the gas flow, for instance leading to a mitigation of the shock propagation. The retroaction of the droplets on the flow field consists of mass, momentum and energy transfer. Especially when the droplet evaporation is involved in the interaction process.

The method used in Asphodele consists in the distribution of the source terms on the Eulerian nodes close to the droplet i as shown in Fig. 1.16. The distribution coefficient $\kappa_i^{(n)}$ is positive and inversely proportional to the distance between the droplet i and the numerical node n , which follows the relation:

$$\sum_N \kappa_i^{(n)} = 1 \quad \text{with } \kappa_i^{(n)} \in [0, 1]^3 \quad (1.38)$$

where N is the number of nodes around the target droplet i .

Considering the two-way interaction the gas flow with a droplet of relative velocity V_i , the droplet evaporation can bring evaporated mass into the gas phase. According to the evaporation rate expression in Eq.

(1.15), one can easily obtain the mass of species s transferred from the droplet i to the node n :

$$\frac{dm_s^{(n)}}{dt} = -\sum_I \kappa_i^{(n)} \dot{m}_i, \quad (1.39)$$

where I denotes the number of droplets around the node n .

Concerning the momentum transfer \mathbf{p}_i during the evaporation, both the mass and the velocity change of the droplet i should be considered:

$$\frac{d\mathbf{p}_i}{dt} = m_{p,i} \frac{d\mathbf{V}_i}{dt} + \mathbf{V}_i \frac{dm_{p,i}}{dt} \quad (1.40)$$

One can have the distribution of momentum from the droplets to the node n :

$$\frac{d(\rho\mathbf{u})^{(n)}}{dt} = -\sum_I \kappa_i \left(\frac{m_{p,i}}{\mathcal{V}_i} \frac{d\mathbf{V}_i}{dt} + \frac{\mathbf{V}_i}{\mathcal{V}_i} \frac{dm_{p,i}}{dt} \right), \quad (1.41)$$

where \mathcal{V}_i is the volume of the mesh cell containing the droplet i .

Finally, the energy transfer from the droplet to the node n in gas phase can be described by:

$$\frac{d(\rho e_i)^{(n)}}{dt} = -\frac{1}{\mathcal{V}_i} \sum_I \kappa_i \frac{m_{p,i}(c_p T_i + l_v)}{dt} \quad (1.42)$$

where c_p is the heat capacity, T_i the temperature of the droplet i and l_v is the latent heat of the droplet at T_i .

Some typical phenomena and property evolutions during the interaction between the spray droplets and a gas flow with or without evaporation are depicted in Fig. 1.17.

Figure 1.17a gives the evolution of no dimensional mass of two different phases and the total mass, where m_0 denotes the initial mass of each phase. One can notice that, during the evaporation, the total mass of the biphasic system keeps constant. Similar to the mass conservation, the momentum evolution of two single phases and the total momentum in Fig. 1.17b.

The variation of the gas velocity and droplet velocity under two-way interaction without evaporation is shown in Fig. 1.17c. For comparison, the evolution of velocities of these two phases are also given under the one-way assumption. The deceleration effect of the droplets on gas flow of the two-way formalism is clearly presented.

The evolution of enthalpy of the gas and the liquid phase is depicted in Fig. 1.17d. It can be seen that the enthalpy of the droplet phase increases at first then decreases to a lower value, in the contrary to the gas phase. The increase of the droplet enthalpy can be due to the heat transfer from the gas phase to the liquid phase. The sum of these two enthalpies gives the total enthalpy which keeps a constant value during the evaporation. During the evaporation, there are two competing effects: the energy transfer as latent heat, and the mass injection from the liquid phase to the gas phase. During the first stage, the heat transfer dominates due to the high ambient temperature. Afterwards, the steam evaporated from the droplets brings energy to the gas phase leading to an increase of the gas enthalpy.

Figure 1.17e shows the temperature evolutions of the gas phase and the droplets during the evaporation. At the first stage, the temperature of the gas phase decreases and the droplets temperature increases. The heat transfer from the gas to the liquid phase dominates. After that, an increase of the gas temperature is noticed, which can be due to the mass transfer of the steam evaporated from the water droplets.

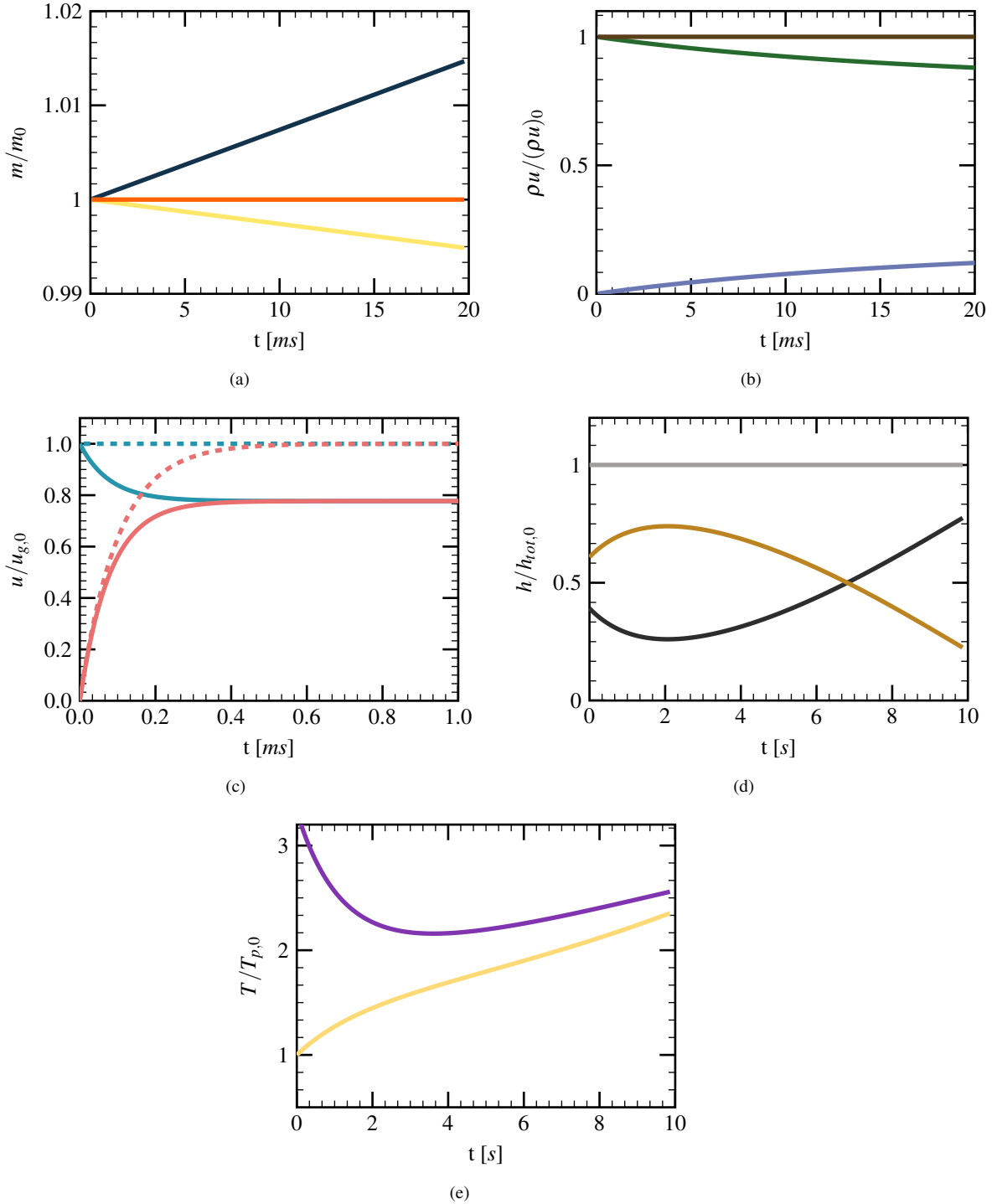


Figure 1.17: (a) Evolutions of the gas mass (—), droplet mass(—) and total mass (—) of the biphasic system; (b) Evolution of the gas momentum (—), droplet momentum (—) and total momentum (—) of the biphasic system; (c) Evolution of two-way gas velocity (—) and droplet velocity (—) without evaporation, the one-way gas velocity (---) and droplet velocity (---) are given as references; (d) Evolution of the gas enthalpy (—), droplet enthalpy(—) and total enthalpy (—) of the biphasic system; (e) Evolution of the droplet temperature (—) and the gas temperature (—) during the evaporation.

1.6 Spray-induced turbulence

Particle-laden flow is a type of two-phase fluid flow, in which one phase is continuous (carrier phase) and the other is made up of small and dilute particles (dispersed phase). Water spray in air is an example of a particle-laden flow, the droplets are the dispersed phase, and the air is the carrier phase. The presence of a second phase in the carrier phase can change the intrinsic turbulence topology and intensity, which is known as turbulence modulation [113]. For several decades, the spray- or particle-induced turbulence modulation has been investigated since it has various engineering and scientific applications: pollution dispersion in the atmosphere, combustion processes, aerosol deposition in spray medication, etc. [114; 115; 116; 117; 112; 118; 119]. Several factors are supposed to contribute to the turbulence modulation such as: the distortion of the carrier phase velocity gradient, the streamline curvatures, the vortex shedding of the particles or the damping of turbulence motion by particles-induced drag forces [113]. Two major effects can be brought by the particles motions to the carrier phase turbulence: either attenuation or enhancement. For example, experimental investigations have shown that the spray systems can mitigate the flame propagation during hydrogen explosions [28; 29]. The evaporation of small-size water droplets inside the flame is thought to be the main reason for the flame attenuation [55]. On the contrary, several experiments resulted in explosion enhancement in the presence of water sprays, which is believed to be due to the movements of large droplets [6]. Therefore, in order to determine the overall spray effects on the explosion, one has to quantify the turbulence characteristics resulting from a spray-gas interaction.

Experimental investigations on particle-laden flow focused on the measurements of the mean flow velocity, Reynolds stresses of the carrier phase flow as well as higher-order statistics such as Lagrangian particle velocity correlations [120]. Many physical parameters are taken as criteria to distinguish between the attenuation and the enhancement effects of the particle cloud on the carrier flow. The most widely discussed are the length scale ratio [121], the Stokes number S_t , the particle Reynolds number Re_p and the particle momentum number Pa [118], etc.

However, no universal criteria is found to be able to correctly predict the turbulence modulation for the currently existing experiments. In our development, we concentrate on the quantification of the turbulence scale induced by the presence of spray droplet inside a confinement geometry without initial gas turbulence. The main object is to find and assess the capacities of the simple or reduced-order models on the turbulence intensity prediction. Coupled with the evaporation modeling, the turbulence scale prediction model can be used to determine the overall effect of water spray on the premixed hydrogen-air explosion.

1.7 Overview of large-scale simulation codes

As a result of a large range of physical length scales and sophisticated interaction phenomena, the current numerical codes and physical models show poor predictive capacities in large-scale simulations for many hydrogen safety applications [44]. In this study, we are interested in the combustion modeling in the presence of sprays with typical grid sizes of the order of 20 – 40 *cm*. Obviously, the flame propagation and

flame-droplets interaction cannot be described in details on such numerical grid sizes. This inevitably leads to introduction of simplified models and of related modeling constants. Several codes exist for industrial applications which imply a capability to deal with large-scale geometries such as FLACS, EUROPLEXUS, AVBP, FLUENT, etc. The flame-spray interaction models are available in some of the codes. Here, we present the models implemented in FLACS and FLUENT.

1.7.1 FLACS code

FLACS is a specialized computational fluid dynamics (CFD) tool for safety applications such as gas explosion, hydrogen safety, dust explosion and blast wave propagation, etc [46]. A simple water spray model is implemented, where a number of regions containing water spray are characterized by the water droplet size (d_p) and the water volume fraction (α_p). These characteristic parameters are determined according to nozzle types, temperature and pressure conditions.

As discussed in the previous works, the presence of water in the turbulent combustion can have two opposite effects: either attenuate the flame propagation by droplet evaporation, or enhance the flame velocity by inducing turbulence in the gas flow [28; 6]. Both these two effects are related to the droplet size d_p distribution and droplet volume fractions α_p . Thus the droplet breakup process is necessary to implement for spray-explosion interaction simulations. In FLACS code, the droplet break-up is determined by the critical Weber number, where break-up occurs for $We > 12$. As for the spray-induced flame acceleration, a factor F_1 is used to increase the burning rate if any water sprays are present. On the contrary, a quenching factor, denoted F_2 , is used to reduce the burning rate if the conditions for droplet break-up are satisfied. These two non-dimensional parameters are combined in the determination of the effective burning velocity using an empirical correlation:

$$s_{eff} = (s_T + F_1 \times s_L) \times F_2 \quad (1.43)$$

where s_T and s_L denote the turbulent and laminar flame velocity, respectively. The dimensionless factor F_1 and F_2 are calculated as:

$$F_1 = \frac{\alpha_p U_z}{U_{ref}}, \quad U_{ref} = 0.07 \text{ m/s}, \quad (1.44)$$

and

$$F_2 = \frac{d_{ref}}{\alpha_p d_{32,p}}, \quad d_{ref} = 0.03 \text{ mm}. \quad (1.45)$$

where U_{ref} and d_{ref} are two reference parameters, U_z is the average droplet vertical velocity, α_p is the droplet volume fraction and $d_{32,p}$ denotes the Sauter mean diameter of the droplets. Unfortunately, the chosen values for U_{ref} and d_{ref} are not justified in [122]. Since the transportation of water droplets is not taken into account, the volume fraction and size distribution in the space should be provided. Moreover, the determination of the two dimensionless factors are case-dependent. The computational results obtained using the model show high sensitivity to the choice of a spray nozzle and to the geometrical configurations [122].

1.7.2 FLUENT code

ANSYS FLUENT is an industrial fluid simulation software designed for the modeling of multi-phase fluid flow, turbulence, heat and mass transfer, combustion and other related phenomena. Known for delivering the reliable solutions, FLUENT is well known and widely used in industrial applications. A premixed turbulent combustion model has been implemented in FLUENT, based on the reaction-progress variable approach [123].

The key parameter for the modeling of premixed combustion model is the turbulent flame velocity normal to the flame front u_t , which is influenced by the following factors:

- laminar flame velocity, fuel concentration, ambient temperature, chemical kinetics and molecular diffusivity;
- flame front wrinkling and stretching by large eddies, and flame thickening by small eddies;

Various turbulent flame velocity models exist in FLUENT code. One of the models on the turbulent flame velocity computation is given by Zimont *et al.* [45]:

$$u_t = A(u')^{3/4} s_L^{1/2} \alpha^{-1/4} L_t^{1/4} = A \left(\frac{\tau_t}{\tau_c} \right)^{1/4}. \quad (1.46)$$

where A is the model constant, u' is the RMS (root-mean-square) velocity, s_L is the laminar flame velocity, $\alpha = k/\rho c_p$ molecular thermal diffusivity, $\tau_t = L_t/u'$ is the turbulence time scale and τ_c is the chemical time scale. L_t is the turbulence length scale defined as:

$$L_t = C_D \frac{(u')^3}{\varepsilon}. \quad (1.47)$$

This model assumes an equilibrium of small-scale turbulence inside the laminar flame, which results in a turbulent flame speed expression dependent on the large-scale turbulent parameters such as integral length scale L_t , etc. The default values of 0.52 for A and 0.37 for C_D are recommended by Zimont *et al.* [45]. This turbulent combustion model is applicable when the Kolmogorov scales are smaller than the flame thickness, which can be quantified by Karlovitz numbers, Ka , greater than unity:

$$Ka = \frac{t_l}{t_\eta} = \frac{v_\eta^2}{s_L^2}. \quad (1.48)$$

where characteristic flame time scale, t_η is the smallest (Kolmogorov) turbulence time scale, $v_\eta = (v\varepsilon)^{1/4}$ is the Kolmogorov velocity and v is the kinetic viscosity.

One can note from Eq. (1.46) that the determination of the turbulent flame velocity depends on the estimation of the large-scale turbulent properties such as u' and L_t . However, these two parameters can not be obtained directly as a result of high computational costs. Thus, modeling of these turbulent kinetic properties with presence of water droplets is crucial for the description of the large-scale turbulent combustion. Other models can be implemented by users for the turbulent flame velocity u_t .

TABLE 1.5: Simplified models and assessment codes.

Simplified model	Main parameter	Assessment code
Evaporation rate model	\dot{m}	Cosilab code
Laminar flame velocity model	s_L	Cosilab code
One-way spray dispersion model	α_p	Asphodele code
Two-way spray dispersion model	α_p	Asphodele code
Kenning's turbulent length-scale model	L_t	Neptune_CFD

In this study, our strategy is to determine the parameters as shown in Table 1.5, using simplified or empirical models in order to implement the water spray model for future developments. Several codes in order to assess these simple analytical or empirical models are used to investigate several important parameters of the spray-explosion interaction. The developed simplified models and different codes used for the assessment of these models are listed in Tab. 1.5. Concretely, we pay attention to the description of the spray properties α_p , \dot{m} , laminar flame velocity s_L and turbulent integral length scales L_t . Kenning's model is found in the open literature to evaluate the integral length scale of turbulence [124]. The developments of each simple models are discussed in the Chapter 3-5.

1.8 Spray-flame interaction experiments

In this section, we present the experimental researches devoted to premixed hydrogen flame interaction with a water spray. The purposes are twofolds: presenting the important experiments of different geometry sizes in the literature and providing experimental data for code validation. This section is divided into three subsections, devoted to: *a*) small-scale, *b*) medium-scale and *c*) large-scale experiments, depending on the order of magnitude of the corresponding combustion chamber.

A number of small-scale experiments have been performed in volumes of the order of 10 L. Medium-scale experiments were performed in volumes of the order of 1 m³. Several experiments were carried out at large scales [125; 126]. Gupta *et al.* [13] have performed tests with the objective to provide additional knowledge and experimental data regarding the influence of water spray on hydrogen combustion in a large-scale test facility by use of experimental conditions typical for severe accidents.

A brief overview of the experiments and the information related to nuclear containment applications is described in Table 1.6). The maximal dry hydrogen concentration corresponds to globally well-mixed air with maximal theoretical amount of hydrogen gas.

Firstly, one can see that certain important pieces of data are missing in some researches, such as an

TABLE 1.6: Overview of the experimental conditions corresponding to hydrogen flame-spray interaction experiments. NP = “Not Provided”, NA - a burner was used for laminar flame velocity measurements.

Source	Chamber volume (m ³)	Droplet size (μm)	X_{H_2} (dry, % vol)	Water vol. fraction ($\times 10^{-4}$)	Flame velocity (m/s)
[11]	NA	5.0	20.0 – 56.0	1.0 – 2.5	0.2 – 3
[127]	5.5×10^{-2}	5.0	7.8 – 65	0.9 – 2.5	$O(10^{-1} - 10^0)$
[60]	1.8×10^{-2}	20.6 – 115.0	4.3 – 8.5	0.8 – 11.0	$O(10^{-1})$
[63]	1.58	≈ 500	4.0 – 16.0	5.0	NP
[128]	6.3	NP	6.1 – 6.8	0.5 – 9.0	NP
[12]	0.7	158 or 270	10.5 – 13.2	NP	$O(10^2)$
[125]	2100	NP	7.1 or 10.0	NP	NP
[126]	56.7	850 or 500	13.5 – 29.7	NP	$O(10^0)$
[13]	60	600	7.5 – 11.7	1.04	$O(10^1)$
NPP	≈ 30000	≈ 500	≤ 19	$O(10^0)$	$O(10^0 - 10^2)$

NPP denotes the nuclear power plant containment buildings.

average flame velocity or water volume fraction. Many authors perform experiments in order to observe the effect of spray, related to a particular spray nozzle, solely on overpressure evolution, without considering other parameters. Secondly, the experiments performed at large scale either dealt with rather poor mixtures or resulted on very low flame velocities. There is no large-scale experiment which is devoted to high-speed flame ($O(10^2)$ m/s) interacting with a spray in which a droplet breakup process is quantified.

In the following, one example of each scale of experiment is presented.

1.8.1 Small-scale experiments

For small-scale experiments, the works of Ingram *et al.* [11] show the effects of small droplets evaporation ($O(10 \mu\text{m})$) on the reduction of laminar flame velocity of the premixed hydrogen-air mixtures.

A work programme has been undertaken at London South Bank University to investigate the practical viability of using fine water mists to mitigate or suppress hydrogen explosions during nuclear decommissioning operations. The measurements of hydrogen burning velocity, required primarily for the development of explosion modeling, are performed. Burning velocity measurements were made with the introduction of ultrasonically generated fine water mists. A diagram of the burner and mist generation system is given in Fig. 1.18. The production of the water mist was accomplished using commercial ultrasonic fogger units. These were individually comprised of 5 piezoelectric discs driven by a high frequency power supply operating at 1.65 MHz. In operation, these elements are situated beneath a column of water. At a suitable depth (below the surface) the high frequency vibration of the piezoelectric discs generates violent cavitation and capillary waves at the water surface. This results in the formation of a “fountain” above the surface comprised of very

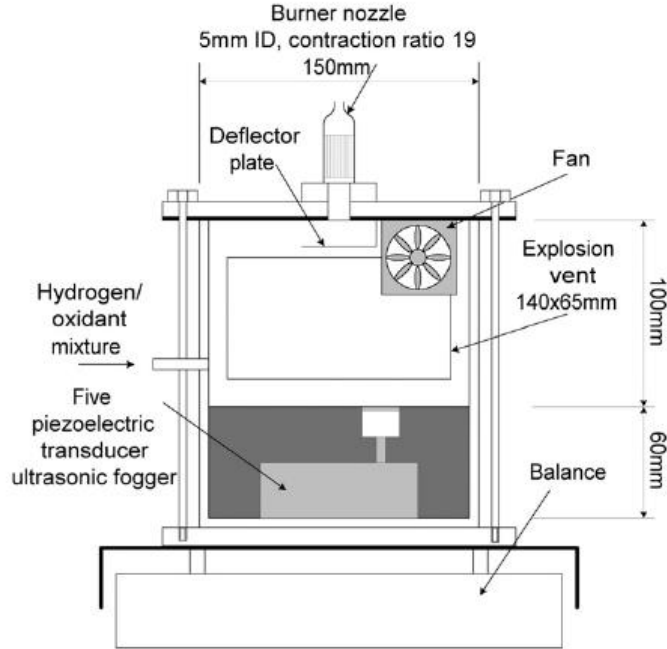


Figure 1.18: The burner and mist generation system. Scanned from [11].

fine water droplets, along with much larger droplets, which can be several millimeters in diameter (hence the need for a deflector plate). Gas mixtures (hydrogen-oxidant) were injected to the mist generation system by blending hydrogen with commercial oxidant mixtures supplied from different lines. Burning velocities were calculated according to the equation:

$$S_u = \frac{A_0}{A_f} \cdot V_0 \quad (1.49)$$

where A_0 is the area of burner mouth, V_0 is the average flow velocity in the burner mouth. Thus $A_0 \cdot V_0$ becomes the total flow rate and A_f is the curved surface area of the cone.

The main parameters considered during the experimental program are:

- the Sauter mean diameter, $D_{3,2} = 5 \mu\text{m}$;
- equivalence ratios between 0.6 and 3.0 (between 20% and 56% of H_2 in air)
- three Fuel-Free Oxygen fractions, $\Omega = 0.21$ (air), $\Omega = 0.16$, and $\Omega = 0.1$.
- water mist densities between 0.0 and 250 mg/l.

We mention that water mist density of 250 mg/l corresponds to a water volume fraction of 2.5×10^{-4} which is of the same order of magnitude as in a nuclear containment building during accidental scenarios.

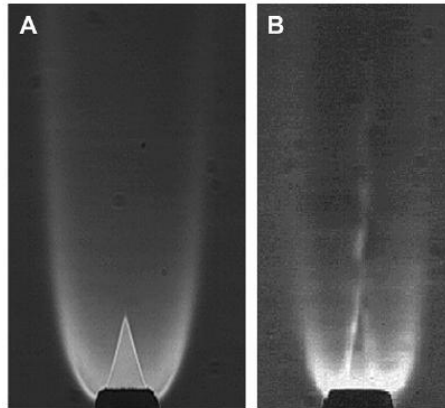


Figure 1.19: Schlieren images of hydrogen flame cones for (a) typical stable rich mixture and for (b) $\Phi = 0.6$ with 143 mg/l of water mist. Scanned from [11].

The major difficulty addressed by the authors lies in the accurate measurement of the flame front surface area. The Schlieren cones formed by rich mixtures have clear boundary and easy to measure. For lean mixtures, however, the quality of “cones” could be quite poor, particularly at higher mist concentrations as shown in Fig. 1.19.

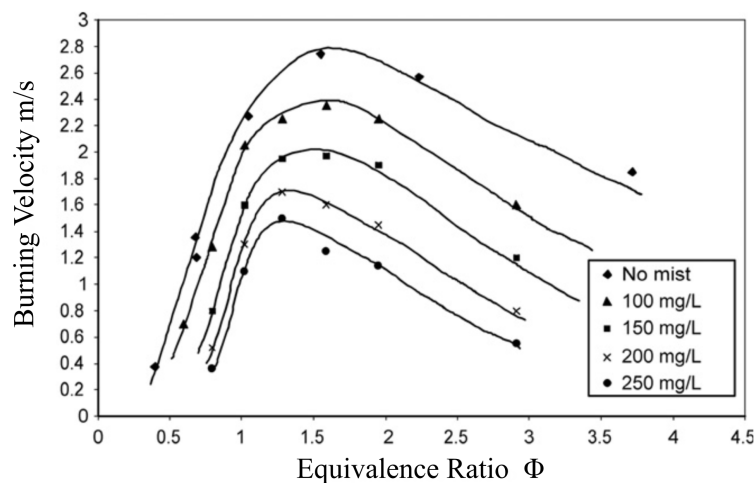


Figure 1.20: Variation of burning velocity with equivalence ratio, $\Omega = 0.21$. Scanned from [11].

The main conclusions of the experimental work can be drawn as following:

- Introduction of fine water mist greatly reduces the burning velocity of H_2 for all mixtures studied. The experimental measurement of the burning velocity variation with equivalence ratio for $\Omega = 0.21$ is



Figure 1.21: Comparison between the domes corresponding to ENACCEF (left) and ENACCEFII (right). Scanned from [12].

presented on Fig. 1.20. One can see that the small droplets of the water mists can have an efficient effect of the laminar flame velocity mitigation.

- Introduction of increasing amounts of water mist increases uncertainty and flame instability. Unfortunately, the burning velocities corresponding to poor mixtures, $X_{H_2} < 20\%$, were not measured as result of technical difficulties.
- Complete suppression of hydrogen-air flame with water mists will be very difficult to achieve. For the considered water mist loading and hydrogen molar fractions the flame quenching phenomenon was not observed.

Many other small-scale experiments exist in the literature and the details can be found in [60; 127].

1.8.2 Medium-scale experiments

Different experimental works have been performed using medium-scale configurations [12; 128; 63]. Here we give a short introduction to the works of Cheikhravat [12], which provide relative complete measurement information.

The experimental facility ENACCEF (ENceinte d'ACCElération de Flamme) is located at the Institut de Combustion Aérothermique Réactivité et Environnement (ICARE) of Orléans.

A view of ENACCEF facility together with the sketch of different parts is presented on Fig. 1.21. The facility is 5 m of height and is made of Z3CN18-10 stainless steel, which is divided into two parts:

- the acceleration tube (3.2 m long and 154 mm i.d.), in which repeated obstacles of various geometries can be inserted;

- the dome (1.7 m long, 738 mm i.d.).

The acceleration tube is equipped with two tungsten electrodes at 0.138 m from the bottom of the facility as a low-energy ignition device. Different obstacles of varying blockage ratio can be installed inside the tube. For the tests, nine annular obstacles of blockage ratio 0.63 have been installed in the acceleration tube; the first one being 0.638 m from the ignition point, and the distance between obstacles was fixed to 0.154 m.

ENACCEF facility is highly instrumented to follow the flame propagation: 16 UV-sensitive photomultiplier tubes (HAMAMATSU, 1P28) are mounted across silica windows (optical diameter: 8 mm, thickness: 3 mm) in order to detect the flame as it propagates (5 photomultiplier tubes are located along the dome and 11 along the acceleration tube). Table 1.7 gives the photomultiplier tube locations, as a distance from the ignition point.

Sensor	Distance from ign. point (m)	Sensor	Distance from ign. point (m)
PM1	4.3415	PM9	2.037
PM2	4.0915	PM10	1.772
PM3	3.8415	PM11	1.527
PM4	3.5915	PM12	1.277
PM5	3.3415	PM13	1.027
PM6	2.877	PM14	0.777
PM7	2.627	PM15	0.527
PM8	2.377	PM16	0.277

TABLE 1.7: Photomultiplier tubes positions along the facility.

Several high speed pressure transducers, (7 from CHIMIE METAL, 1 PCB and 1 KISTLER) are mounted flush with the inner surface of the tube in order to monitor the pressure variation in the tube as the flame propagates, and the pressure buildup is monitored via a Kistler pressure transducer mounted at the ceiling of the dome. Five gas samplings are located along the acceleration tube and one in the dome, which are used to measure the gas composition along the facility.

The dome of ENACCEFII has a volume of 685 L (as shown in Fig. 1.21) and is equipped with a spray device, which is an upgraded version of the dome of ENACCEF (658 L).

Two injectors are used in the experiments: 2.8W Fulljet nozzle and 14W Fulljet nozzle. The spray angle of both injectors is close to 120° , filled with water droplets as shown on the Fig. 1.23.

Measurements were made in order to characterize sprays using laser coliffraction, 25 cm from the nozzle. On Fig. 1.23 we present the test matrix together with results for maximal measured pressure (P_{max}), and the time for pressure increase (Δt_P). The following conclusions can be made from this work [12]:

- Generally, activation of spray leads to the lower maximal pressure.
- The choice of a nozzle does not influence the results.

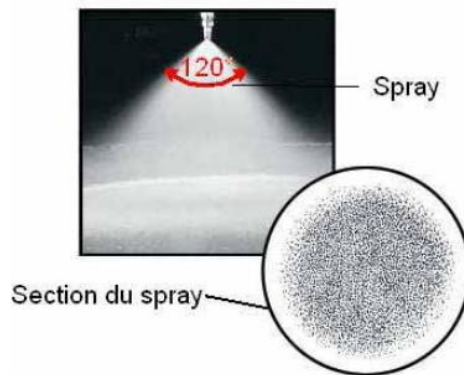


Figure 1.22: Spatial distribution of droplets generated by spray. Scanned from [12].

N° essai	XH ₂ [% Vol.]	Buse	P _{max} [bars]	Δt_P [ms]	P _{AICC} [bars]	% P _{AICC}
9g	10,62%	SEC	2,69	170	4,44	60,49
17g	10,71%	SEC	extinction	extinction	4,47	-
18g	10,66%	SEC	extinction	extinction	4,45	-
21g	10,52%	SEC	extinction	extinction	4,41	-
22g	10,50%	SEC	extinction	extinction	4,40	-
11g	11,72%	SEC	4,03	22,71	4,73	85,06
12g	11,49%	SEC	-	-	4,67	-
13g	11,51%	14	3,59	30,64	4,68	76,81
14g	11,55%	SEC	4,14	26,56	4,68	88,31
15g	11,50%	14	3,64	31,76	4,67	77,97
27g	11,72%	2.8W	3,68	31,91	4,73	77,81
28g	11,72%	2.8W	-	-	4,74	-
29g	11,77%	2.8W	3,63	29,83	4,75	76,50
7g	13,06%	SEC	5,11	29,32	5,09	100,32
8g	13,13%	14W	5,13	27,07	5,10	100,88
16g	13,12%	SEC	-	-	5,10	-
19g	13,00%	14W	3,15	23,60	5,07	62,12
20g	13,00%	SEC	3,84	24,73	5,05	75,96
23g	13,00%	2.8W	-	-	5,07	-
24g	13,22%	2.8W	3,45	25,00	5,12	67,36
25g	13,14%	2.8W	3,43	25,10	5,10	67,23
26g	13,13%	2.8W	3,28	25,95	5,10	64,29

Figure 1.23: Spatial distribution of droplets generated by spray. Scanned from [12].

1.8.3 Large-scale experiments

Here we give a brief introduction to the works of Gupta *et al.* [13] as an example of large-scale experiments. Some other researches can be found in [125; 126].

The tests HD-30 to HD-35 have been performed in the THAI containment test facility which is operated by Becker Technologies GmbH at Eschborn, Germany. The main component of the facility is a cylindrical stainless steel vessel of 9.2 m height and 3.2 m in diameter with a total volume of 60 m³ as given in Fig. 1.24. Vessel bottom and top are formed by dished heads (wall thickness 30 mm), both of which are penetrated in the vessel axis by cylinders with an ID of 1540 mm (wall thickness 40 mm) for the upper cylinder and an ID of 1368 mm for the bottom cylinder (wall thickness 30 mm). The upper cylinder carries a 120 mm thick top flange; the lower cylinder is closed by a 16 mm thick dished head.

The spray system installed in the THAI vessel consists of a single full cone whirl spray nozzle (BETE, model no. 3/4WL1230). Spray nozzles are positioned vertically downward at elevation $H = 7.4$ m in the geometric centre of the THAI vessel. A spray angle of 30° was selected to exclude any change in spray patterns due to interactions with the vessel walls. All tests were conducted with spray water flow rate of 1 kg/s. The spray droplet Sauter mean diameter, measured at 1 m distance from the nozzle, is 600 μm (970 μm for test HD-34). The waterline overpressure was 5 bar (2 bar for HD-34).

The Table 1.8 summarizes the specified and measured initial test conditions for tests HD-30 to HD-35.

TABLE 1.8: Initial test conditions specified and measured [15].

Test parameters	HD – 30	HD – 31	HD – 31SE	HD – 32.1	HD – 33	HD – 34	HD – 35
Gas temperature [°C]	25	90	90	90	90	90	90
Hydrogen content [vol %]	10	10	–	10	10	10	12
Spray temperature [°C]	20	20	20	90	90	20	90
Burning direction	↑	↑	↑	↑	↑	↑	↓
Time before ignition [s]	2	2	long	2	2	60	2

The main results can be drawn as follows:

- All HD-tests with spray and upward combustion exhibit lower peak pressures and temperatures compared to the reference tests without spray.
- All HD-tests with spray and upward combustion exhibit a higher flame speed immediately after ignition in the lower part of the vessel compared to the reference tests without spray, i. e. a turbulence enhancing effect of the spray was observed. For example, the initial flame velocity during the test HD-31 was approximately 8 m/s, while velocity corresponding to the case without spray is close to 2.5 m/s.

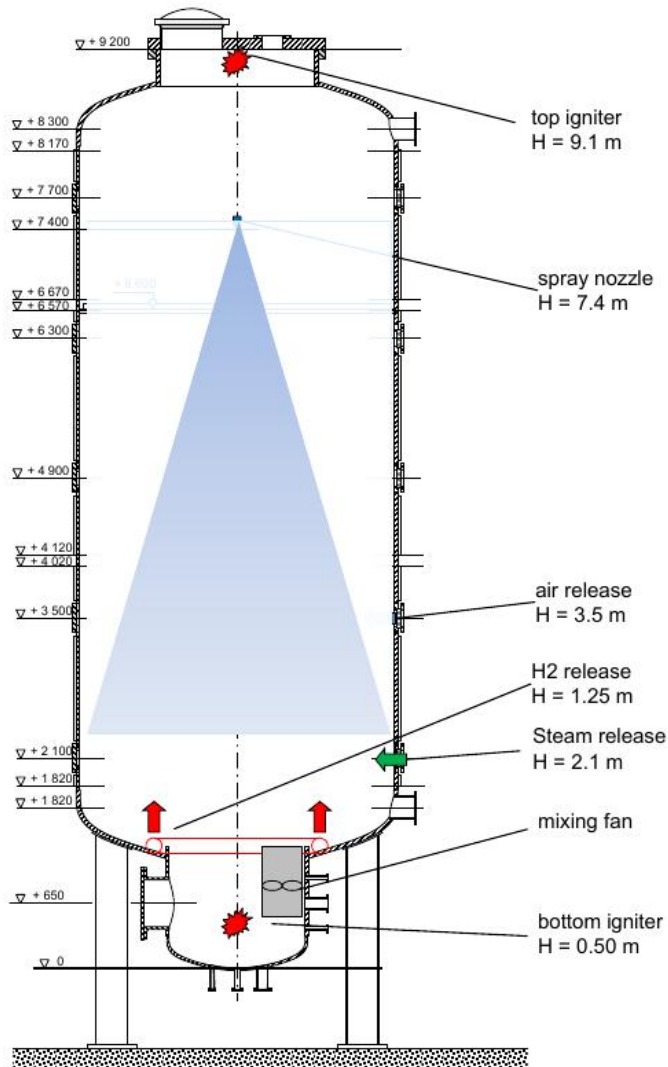


Figure 1.24: THAI test vessel configuration for HD-tests. Scanned from [13].

- For test HD-35 with downward combustion, flame speed in the upper part of the vessel is the same as for the reference test without spray. After having passed the spray nozzle, the flame accelerates extremely in the spray induced downward directed flow.
- For the tests with the vessel temperature of 90°C and a steam content of about 25 %, this steam content together with droplet vaporization is sufficient to suppress combustion completely for test HD-31, HD-32.1 and HD-33 in the spray cone zone down to approximately 1 m below the spray nozzle, a zone of high water concentration. Further below, the flame is decelerated but not totally suppressed. This effect was not observed for tests HD-30 (no steam) and HD-34 (larger droplets), which underlines the strong influence of steam and of the available total droplet surface on combustion suppression.
- Spray water temperature has no observable effect on combustion suppression.
- Test HD-35 with downward combustion was the only HD-test for which spray operation produced a 10 % higher peak pressure due to spray induced turbulent flow pattern and the related high flame speed compared to the reference test without spray.

In case of upward burn direction, the spray operation produces a flow pattern with a downward directed flow below the spray nozzle and within the spray cone. As a consequence, an upward directed flow close to the vessel walls occurs. This flow field is responsible for faster flame speeds close to the vessel walls for the tests with upward burn direction.

The experiments performed in large scale geometries have two common features. First, the explosive mixture ignition at the upper part of the facility (above the spray nozzle) in the presence of spray leads to *higher over-pressures* than the corresponding combustion with upper ignition without spray. This is explained by the influence of spray-created turbulence as well as the co-flow pattern of the spray. Second, the flame velocities and the gas velocities relative to spray droplets are not very high, of the order of 10 m/s. This means that the corresponding Weber numbers are small, generally of the order of $O(1)$, and the droplet breakup phenomenon, in our opinion, does not take place.

1.9 Scope of the current study

In this dissertation, we have concentrated our efforts on the investigations of several phenomena. The dominant phenomena considered in this manuscript are the spray-flame, spray-shock interactions and spray-induced turbulence, which are closely coupled in a real accidental scenario.

The existing droplet-resolved models for simulations of large-scale geometries such as nuclear confinement building are scarcely available, as a result of high computational costs, especially for high-Reynolds number flows. Thus, the developments of simple reduced-order modeling approaches are preferably considered in this manuscript. Evaluations of the existing empirical correlations and models are also taken into account.

The reduced-order and simple numerical models developed in this manuscript allow us to evaluate the mitigation or enhancement effects of each interaction without resolving physical phenomena of small time and

length scales. New physical observations such as droplet number density peak and turbulence enhancement induced by double industrial nozzles are presented in this study.

1.9.1 Outline of dissertation

This manuscript consists of three main parts. The first part presents the physical phenomena and scientific issues, followed by a lumped parameter study. The second part discusses the physical mechanism investigation and numerical modeling for spray/flame, flame/shock and spray/turbulence interactions. The third part provides conclusions and perspectives as well as the additional materials of the current study. Contents of each chapter are briefly described in the following paragraphs.

Chapter 1 – Introduction This chapter presents the main phenomena associated to the PWR containment spray system and accidental explosion phenomena. The important phenomena during the spray/flame interaction, spray/shock interaction and spray/turbulence interaction are discussed, such as droplets evaporation, breakup and spray dispersion etc. Governing equations and numerical modeling methods for droplet-laden flows and one-dimensional planar shock waves are presented. Different numerical codes used in this manuscript are briefly presented.

Chapter 2 – Lumped parameter study A lumped-parameter study is carried out to evaluate the effects of water droplets evaporation on the adiabatic isochoric complete combustion (AICC) of premixed hydrogen-air mixture. The asymptotic evolution of gas pressure and temperature are investigated for different initial gas compositions. The effects of the water spray volume fraction are assessed and the limit volume fraction for different equivalent ratios are reckoned. The asymptotic extenuation of the droplet cloud evaporation can provide guidelines for more sophisticated large-scale modelings.

Chapter 3 – Spray effects on the laminar flame velocities A methodology for pressure evolution modeling during combustion process in presence of water spray is proposed in this chapter. A simplified model based on empirical correlations allows the assessment of the main factors affecting the pressure evolution. Then, numerical simulations of laminar premixed hydrogen-air flames propagating freely into a spray of liquid droplets are carried out. A “Laminar Flame Velocity under Droplet Evaporation Model” (LVDEM) based on an over-all energy balance of the spray-flame system is developed. The effects on the hydrogen/air flame velocity of droplet size, liquid-water volume fraction, and mixture composition are numerically investigated.

Chapter 4 – Interaction between spray droplets and shock wave The effect of shock waves on the dispersion characteristics of a particle cloud is investigated both numerically and analytically. A one-dimensional analytical model is developed for the estimation of the cloud topology in the wake of a shock wave, as a function of time, space and characteristic response time τ_p of the cloud based on the one-way formalism. The effects of different parameters affecting the shock-spray interaction are elucidated and discussed. Then, a two-way analytical model is derived based on numerical observations and conservation

laws, in order to evaluate the post-shock gas properties and the spray dispersion topology. The presence of a particle number density peak is discussed and a necessary condition for its existence is proposed.

Chapter 5 – Spray induced turbulence In particle-laden flows, a turbulent field can be produced in the carrier phase by the movement of the particle/spray cloud. The intensity and the integral length scale of the particle-induced turbulence are investigated by means of a simple mechanistic model. The experimental results of DynAsp are investigated and simulated using a highly-resolved Navier-Stokes code named Neptune_CFD. An empirical correlation for the particle slip-velocity in the air is assessed using the numerical simulations.

We finish this manuscript by conclusions and giving perspectives that can be brought to the future work.

Chapter 2

Lumped parameter study

Several physical phenomena are involved in the spray interaction with a premixed hydrogen-air explosion, such as: droplet evaporation, shock-induced spray dispersion, spray-induced turbulence, etc. Among these phenomena, spray evaporation is noted to be the main reason for the flame deceleration and explosion attenuation [6; 29; 100]. The spray evaporation is sophisticated for highly-resolved simulations since it is closely related to and affected by various parameters and physical processes, such as droplet size, distribution, deformation, breakup, and coalescence, etc [72]. Ambient conditions can also much influence the droplet evaporation, for instance: temperature, pressure, gas compositions, gas velocity. Chemical dynamics of the combustion reaction can also contribute to the complexity of the problem since the exchange of mass and energy between the flame and droplets leads to the modification of the reaction mechanism [48].

In order to evaluate the effects of water spray evaporation on the equilibrium behavior of explosion pressure and temperature during accidental explosions, the lumped parameter models can be considered in order to focus on the thermodynamic aspects of the evaporation process. A lumped-parameter model, also called the lumped-element model, simplifies the description of the spatially distributed physical systems into a topology consisting of discrete entities that approximate the behavior of the system under certain conditions. Overall estimation of the pressure and the temperature evolutions are studied with a lumped-parameter model based on the conservation laws of mass and energy. The objectives of the lumped-parameter model development are two folds: 1) assessment of the spray thermodynamic effect on explosion mitigation and 2) providing equilibrium values for some variables in large-scale numerical simulations.

2.1 Fundamental assumptions

In the lumped-parameter modeling, a two-phase system is investigated as shown in Fig. 2.1. The system is closed and consists of two homogeneous phases: the fresh gas and the liquid phase. Two processes are involved: Adiabatic Isochoric Complete Combustion (AICC) and liquid evaporation. Several fundamental assumptions are proposed for the system evolutions. The gas mixtures are assumed to follow the ideal gas law.



Figure 2.1: Lumped-parameter study: equilibrium solution of the simplified system

Initial temperature and pressure are kept constant for different hydrogen-air compositions, which usually take the ambient value of $T_{ini} = 298 \text{ K}$ and $P_{ini} = 1.013 \text{ bar}$. Thus, the initial mass of the gas phase will change slightly for different gas compositions. Droplets are characterized by the volume fraction α defined by:

$$\alpha = \frac{V_{liquid}}{V_{liquid} + V_{gas}} \quad (2.1)$$

where V_{liquid} and V_{gas} denote the volume of the liquid and gas phase, respectively.

After AICC, the droplets are assumed to be totally evaporated and form a homogeneous phase of burnt gas, as illustrated in Fig. 2.1. No time or spatial evolution is resolved in this simple model. The interface between the two phases is not taken into account. The equilibrium pressure and temperature of the burnt gas are calculated and investigated.

The hydrogen-air combustion is assumed to be governed by a one-step irreversible, infinitely fast chemical reaction. Without loss of generality, one can consider a gas mixture containing H_2 , O_2 , H_2O and N_2 and the governing global combustion reaction is:



The molar x and mass fraction y variations during the chemical reaction are linked via

$$\frac{\Delta x_{H_2}}{1} = \frac{\Delta x_{O_2}}{1/2} = \frac{\Delta x_{H_2O}}{-1} \quad (2.3)$$

$$\frac{\Delta y_{H_2}}{M_{H_2}} = \frac{\Delta y_{O_2}}{0.5M_{O_2}} = -\frac{\Delta y_{H_2O}}{M_{H_2O}} \quad (2.4)$$

where M_i is the molar weight of the i^{th} species.

2.2 Model development and conservation laws

Two cases of the premixed hydrogen-air combustion are modeled: with and without water droplets evaporation. The system is assumed to be closed and adiabatic, there is no loss of mass or energy. One can get the governing equations for the two cases by considering conservation laws: mass and energy.

Suppose, that initially we have a volume V_{tot} filled up with gas mixture, under pressure P_{ini} and temperature T_{ini} , with molar fraction content X_i^{ini} , for $i \in \{H_2, O_2, N_2, H_2O^{vap}\}$

2.2.1 Conservation of mass

According to the conservation of mass, for any initial conditions, one can always have for the initial and final system mass:

$$\tilde{m}_0 = \tilde{m}_f. \quad (2.5)$$

The molar masses for all the species in our system of combustion are given (kg/mol):

$$M_{H_2} = 2 \times 1.00797 \times 10^{-3}, \quad (2.6)$$

$$M_{O_2} = 2 \times 15.9994 \times 10^{-3}, \quad (2.7)$$

$$M_{N_2} = 2 \times 14.0067 \times 10^{-3}, \quad (2.8)$$

$$M_{H_2O} = 18.01534 \times 10^{-3}, \quad (2.9)$$

Usually in the literature, the coefficient α is used to describe the volume fraction of liquid in a gas mixture i.e. $\alpha = \frac{V_{liq}}{V_{tot}}$. Then the mass of droplets could be obtained:

$$m_{H_2O}^{liq} = \alpha \rho_{H_2O} V_{tot}, \quad (2.10)$$

where V_{tot} is the total volume of the two phases. Then, considering the law of ideal gas, one can have the molar volume of gas phase:

$$\tilde{V} = \frac{V_{gas}^{ini}}{n_{gas}^{ini}} = \frac{RT^{ini}}{P^{ini}}, \quad (2.11)$$

then the material quantity of each species can be obtained:

$$n_i^{ini} = \frac{X_i^{ini}(1-\alpha)V_{tot}}{\tilde{V}}, \quad i \in \{H_2, O_2, N_2, H_2O^{vap}\}, \quad (2.12)$$

where X_i^{ini} is the initial molar composition of the gas mixture. The mass fraction Y_i^{ini} of the i^{th} species could be calculated knowing the molar fraction of the initial composition and the molar masses, as follows:

$$Y_i^{ini} = \frac{n_i^{ini} M_i}{\sum_{j=1}^4 n_j^{ini} M_j + m_{H_2O}^{liq}}, \quad i, j \in \{H_2, O_2, N_2, H_2O^{vap}\}, \quad (2.13)$$

and for liquid droplets:

$$Y_{H_2O}^{liq} = \frac{m_{H_2O}^{liq}}{\sum_{j=1}^4 n_j^{ini} M_j + m_{H_2O}^{liq}}, \quad (2.14)$$

Thus for the initial state, we can have for the total mass:

$$\tilde{m}_0 = \sum_{j=1}^4 n_j^{ini} M_j + m_{H_2O}^{liq}, \quad (2.15)$$

Concerning the complete combustion, one can have two types of gas mixture: the lean mixture ($\phi < 1$), and rich mixture ($\phi > 1$), with the definition of equivalence ratio:

$$\phi = \frac{\frac{m_{H_2}}{m_{O_2}}}{\left(\frac{m_{H_2}}{m_{O_2}}\right)_{stoich}}, \quad (2.16)$$

In this way, the equilibrium states of system depend on the relative quantity of the two species. For the first case one can have:

$$n_{H_2}^{fin} = n_{H_2}^{ini} - 2n_{O_2}^{ini}, \quad (2.17)$$

$$n_{O_2}^{fin} = 0, \quad (2.18)$$

$$n_{H_2O}^{fin} = n_{H_2O}^{ini} + 2n_{O_2}^{ini}, \quad (2.19)$$

$$n_{N_2}^{fin} = n_{N_2}^{ini}, \quad (2.20)$$

For the second case:

$$n_{H_2}^{fin} = 0, \quad (2.21)$$

$$n_{O_2}^{fin} = n_{O_2}^{ini} - 0.5n_{H_2}^{ini}, \quad (2.22)$$

$$n_{H_2O}^{fin} = n_{H_2O}^{ini} + n_{H_2}^{ini}, \quad (2.23)$$

$$n_{N_2}^{fin} = n_{N_2}^{ini}, \quad (2.24)$$

The initial steam and the steam evaporated from the liquid droplets are distinguished in order to make the calculation more consistent.

The final mass fraction Y_i^{fin} of the i^{th} species could be obtained:

$$Y_i^{fin} = \frac{n_i^{fin} M_i}{\sum_{j=1}^4 n_j^{fin} M_j + m_{H_2O}^{liq \rightarrow vap}}, \quad i, j \in \{H_2, O_2, N_2, H_2O^{vap}\}, \quad (2.25)$$

For the steam evaporated from the liquid droplets, we still have:

$$Y_{H_2O}^{liq \rightarrow vap} = \frac{m_{H_2O}^{liq \rightarrow vap}}{\sum_{j=1}^4 n_j^{fin} M_j + m_{H_2O}^{liq \rightarrow vap}}, \quad (2.26)$$

Thus, for the equilibrium states, the total mass can be expressed:

$$\tilde{m}_f = \sum_{j=1}^4 n_j^{fin} M_j + m_{H_2O}^{liq \rightarrow vap}, \quad (2.27)$$

2.2.2 Conservation of energy

The system total energy consists of two parts: the formation enthalpy and the internal energy, as expressed:

$$\tilde{e} = \sum_i Y_i h_i^0 + e = \sum_i Y_i h_i^0 + \int_0^T \left\{ \sum_i Y_i c_{v,i}(T') \right\} dT' \quad (2.28)$$

where Y_i is the mass fraction, T is the mixture temperature, $c_{v,i}(T)$ and h_i^0 are the constant volume specific heat and the formation enthalpy at 0 K, e denotes the sensible internal energy (J/kg), the subscript i represent the species i .

For the first term of Eq. (2.28), the formation enthalpies at 0 K (J/Kg) are used [129]:

$$h_{H_2}^0 = -4.195 \times 10^6, \quad (2.29)$$

$$h_{O_2}^0 = -2.634 \times 10^5, \quad (2.30)$$

$$h_{N_2}^0 = -2.953 \times 10^5, \quad (2.31)$$

$$h_{H_2O}^0 = -1.395 \times 10^7 \quad (2.32)$$

To calculate the internal energy, the heat capacity at constant volume can be expressed by the following polynomial functions (J/kg/K):

$$c_{v_{H_2}}(T) = 9834.91866 + 0.54273926T + 0.000862203836T^2 - 2.37281455 \times 10^{-07}T^3 + 1.84701105 \times 10^{-11}T^4 \quad (2.33)$$

$$c_{v_{H_2O}}(T) = 1155.95625 - 5.73129958 \times 10^{-05}T + 0.768331151T^2 - 1.82753232 \times 10^{-08}T^3 - 2.44485692 \times 10^{-12}T^4 \quad (2.34)$$

$$c_{v_{O_2}}(T) = 575.012333 + 0.350522002T - 0.000128294865T^2 + 2.33636971 \times 10^{-08}T^3 - 1.53304905 \times 10^{-12}T^4 \quad (2.35)$$

$$c_{v_{N_2}}(T) = 652.940766 + 0.288239099T - 7.80442298 \times 10^{-05}T^2 + 8.78233606 \times 10^{-09}T^3 - 3.05514485 \times 10^{-13}T^4 \quad (2.36)$$

In this case, one could get an explicit form of the second term of Eq. (2.28), and then the result of integration can be obtained:

$$\int_0^T \left\{ \sum_i Y_i c_{v,i}(T') \right\} dT' = \sum_i Y_i \sum_{j=0}^4 \frac{1}{j+1} A_{i,j} T^{j+1}, \quad i \in \{H_2, O_2, N_2, H_2O^{vap}\} \quad (2.37)$$

Combustion without water spray

The combustion without spray evaporation serves as a reference case for the lumped-parameter modeling, which can be used for the model assessment. Since there is no phase change, the conservation law is direct:

$$\tilde{e}_0 = \tilde{e}_f \quad (2.38)$$

According to Eq. (2.28), the total system energy of the initial state can be obtained:

$$\tilde{e}_0 = \sum_i Y_i^{ini} h_i^0 + e_0 = \sum_i Y_i^{ini} h_i^0 + \int_0^{T_0} \left\{ \sum_i Y_i^{ini} c_{v,i}(T') \right\} dT' \quad (2.39)$$

and the equilibrium state is:

$$\tilde{e}_f = \sum_i Y_i^{fin} h_i^0 + e_f = \sum_i Y_i^{fin} h_i^0 + \int_0^{T_f} \left\{ \sum_i Y_i^{fin} c_{v,i}(T') \right\} dT' \quad (2.40)$$

The conservation of energy reads:

$$\sum_i Y_i^{ini} h_i^0 + \int_0^{T_0} \left\{ \sum_i Y_i^{ini} c_{v,i}(T') \right\} dT' = \sum_i Y_i^{fin} h_i^0 + \int_0^{T_f} \left\{ \sum_i Y_i^{fin} c_{v,i}(T') \right\} dT' \quad (2.41)$$

rearranging the terms, one can have:

$$\underbrace{\sum_i (Y_i^{ini} - Y_i^{fin}) h_i^0}_{\text{chemical energy}} + \underbrace{\sum_i Y_i^{ini} \sum_{j=0}^4 \frac{1}{j+1} A_{i,j} T_0^{j+1}}_{\text{initial internal energy}} = \underbrace{\sum_i Y_i^{fin} \sum_{j=0}^4 \frac{1}{j+1} A_{i,j} T_f^{j+1}}_{\text{final internal energy}} \quad (2.42)$$

This formula could be coded directly in Cast3M to calculate the equilibrium temperature of AICC (Adiabatic Isochoric Complete Combustion).

Combustion with water spray

In this part, we assume that the liquid droplets are totally evaporated during the combustion, and that the combustion of the hydrogen/air mixture is complete. Compared to the case without droplets, a term of the internal energy for the liquid droplets should be added to the system energy. By using the database of Cast3M code, the internal energy for liquid water could be calculated using its specific enthalpy. Thus, for the initial state:

$$\tilde{e}_0 = \sum_i Y_i^{ini} h_i^0 + e_0 = \sum_i Y_i^{ini} h_i^0 + \int_0^{T_0} \left\{ \sum_i Y_i^{ini} c_{v,i}(T') \right\} dT' + Y_{H_2O}^{liq} \left(h_{H_2O}^{liq} - \frac{P_{tot}}{\rho_{H_2O}^{liq}} \right) \quad (2.43)$$

To ensure a coherent result, we calculate the internal energy of the steam formed from liquid droplets by its specific enthalpy. The equilibrium state can be:

$$\tilde{e}_f = \sum_i Y_i^{fin} h_i^0 + e_f = \sum_i Y_i^{fin} h_i^0 + \int_0^{T_f} \left\{ \sum_i Y_i^{fin} c_{v,i}(T') \right\} dT' + Y_{H_2O}^{liq} \left(h_{H_2O}^{vap} - \frac{P_{H_2O}^{vap}}{\rho_{H_2O}^{vap}} \right) \quad (2.44)$$

according to the ideal gas law, we could have:

$$\frac{P_{vap}}{\rho_{vap}} = \frac{RT}{M_{H_2O}} \quad (2.45)$$

with R the universal gas constant, M_{H_2O} the molar mass of water. Thus, the equilibrium states could be expressed:

$$\tilde{e}_f = \sum_i Y_i^{fin} h_i^0 + e_f = \sum_i Y_i^{fin} h_i^0 + \int_0^{T_f} \left\{ \sum_i Y_i^{fin} c_{v,i}(T') \right\} dT' + Y_{H_2O}^{liq} \left(h_{H_2O}^{vap} - \frac{RT_f}{M_{H_2O}} \right) \quad (2.46)$$

The governing equation can be finally obtained, which could be coded directly in Cast3M to calculate the equilibrium temperature and pressure:

$$\underbrace{\sum_i (Y_i^{ini} - Y_i^{fin}) h_i^0}_{\text{chemical energy}} + \underbrace{\sum_i Y_i^{ini} \sum_{j=0}^4 \frac{1}{j+1} A_{i,j} T_0^{j+1} + Y_{H_2O}^{liq} \left(h_{H_2O}^{liq} - \frac{P_{tot}}{\rho_{H_2O}} \right)}_{\text{initial internal energy}} \quad (2.47)$$

$$= \underbrace{\sum_i Y_i^{fin} \sum_{j=0}^4 \frac{1}{j+1} A_{i,j} T_f^{j+1} + Y_{H_2O}^{liq} \left(h_{H_2O}^{vap} - \frac{RT_f}{M_{H_2O}} \right)}_{\text{final internal energy}} \quad (2.48)$$

2.2.3 Modeling assessment

Cast3M is a software of calculation by the finite element method (FEM) for the structure mechanics and fluid mechanics. It is developed at the Department of System and Structures (DM2S) of the Nuclear Energy Direction (DEN) in the French Alternative Energies and Atomic Energy Commission (CEA) [130]. Cast3M includes not only solving process (solver) but also the model building functions (pre-processor) and exploitation of results (post-treatment). It is used in particular in the area of nuclear energy, as a simulation tool or as a development platform for specialized applications.

CHEMKIN is a proprietary software tool for solving complex chemical kinetics problems. It is used worldwide in the combustion, chemical processing, microelectronics and automotive industries, and also in atmospheric science. CHEMKIN solves thousands of reaction combinations to develop a comprehensive understanding of a particular process, which might involve multiple chemical species, concentration ranges, and gas temperatures [131]. The operator 'DETO' in Cast3M is developed for pure AICC combustion calculations of premixed fuel-air mixture. Chemical kinetics simulation software allows for a more time-efficient investigation of a potential new process compared to direct laboratory investigation. These two softwares are used in our study to assess the consistency of the lumped-parameter modeling.

2.3 Results and discussions

Several cases corresponding to different mixtures and different initial thermodynamic conditions are investigated with the lumped-parameter model as shown in Tab. 2.1.

The first is a reference case concerning a pure combustion process. To assess the development of the lumped-parameter model, the results of the pure combustion given by CHEMKIN and CASTEM are used for comparison. In Case II, we want to study the limit liquid volume fractions for different initial gas compositions which is crucial to keep the total evaporation assumption used in the modeling. Case III and IV present the effect of spray evaporation for combustion under normal ambient conditions and accidental scenario conditions, respectively. The accidental conditions are taken from the work of Kudriakov *et al.* [20]. The H_2 molar fractions are chosen in different cases according within the flammability limits.

TABLE 2.1: Initial conditions for different cases.

Case	P_{ini} (bar)	T_{ini}^{gas} (K)	T_{ini}^{liq} (K)	$X_{H_2}^{ini}$ (-)	$X_{H_2O}^{vap,ini}$ (-)	α (-)
I	1.0134	300.0	-	[0.04, 0.75]	0.0	0.0
II	1.0134	300.0	298.15	[0.04, 0.75]	0.0	$[0.0, 2.0 \times 10^{-3}]$
III	1.0134	293.15	293.15	[0.04, 0.75]	0.0	$(2.0, 3.0, 4.0) \times 10^{-4}$
IV	2.4	393.15	293.15	[0.09, 0.30]	0.45	$(2.0, 3.0, 4.0) \times 10^{-4}$

2.3.1 Case I

For Case I, the evolutions of the equilibrium pressure and temperature of a pure hydrogen-air AICC combustion are calculated for different compositions by using different methods. The initial conditions are presented in the Tab.2.1.

In Fig. 2.2a, we present equilibrium pressure evolutions as a function of hydrogen molar fraction. The results of the operator 'DETO' in Cast3M for AICC combustion is used for comparison with the lumped-parameter model. Moreover, the results of the CHEMKIN software are also presented.

One can notice that the differences in equilibrium pressure between Cast3M and the model are small. At a low molar fraction of hydrogen, the equilibrium pressure rises with the hydrogen concentration. After reaching a peak value (8.6 bar for Cast3M and 8.06 bar for CHEMKIN), the equilibrium pressure begins to decrease. As x_{H_2} increases, the quantity of oxygen becomes insufficient, leading to a slower release of chemical energy, therefore a lower equilibrium pressure.

The results of CHEMKIN code are lower than the two others, in particular in the proximity of the stoichiometric composition. In consideration of the detailed equilibriums among the elementary reactions, the hydrogen is not completely oxidized in air in CHEMKIN code. About 4.81% (molar fraction) of residual hydrogen can be noted in the combustion products for the stoichiometric mixture. Therefore, the results of the lumped-parameter model are more conservative than those of CHEMKIN code.

Fig. 2.2b shows the evolution of equilibrium temperature corresponding to AICC combustion, which has a similar tendency as the pressure. This can be explained that the gas is regarded as an ideal mixture. The maximum equilibrium temperature is reached when the molar fraction of hydrogen approaches the stoichiometric composition.

2.3.2 Case II

To keep the assumption of total evaporation, the chemical energy released during a combustion \mathcal{Q} should be larger than the latent heat of the water spray droplets \mathcal{L} for a given initial composition. Thus, there should be a maximum volume fraction of droplets α_{limit} , above which there would remain some liquid water. One

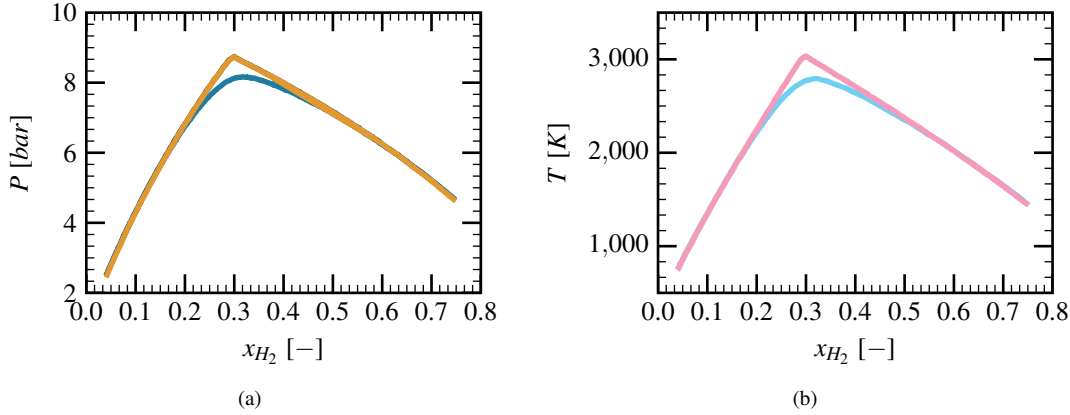


Figure 2.2: (a) Evolution of equilibrium pressure as a function of H_2 molar fraction, model results (—) are compared with Cast3M operator (—) and CHEMKIN code (—). (b) Evolution of equilibrium temperature as a function of H_2 molar fraction. Model results (—), Cast3M (—) and CHEMKIN (—); The model results are fully super-imposed with the results of Cast3M.

possible interpretation is that with a limit volume fraction of the water droplets, the total evaporation can absorb all the chemical energy released from the combustion, with α_{limit} satisfying:

$$\mathcal{L}\alpha_{limit} = \mathcal{L}\alpha_{limit}. \quad (2.49)$$

As shown in Fig. 2.3, the limit volume fractions of the droplets are calculated as a function of H_2 molar fraction using the lumped-parameter model. Hydrogen molar fractions are taken within the flammability limits. The curve has a similar shape as the evolution of equilibrium temperature in AICC combustion. One can see that the limit volume fraction of droplets reaches a peak value when the molar fraction of hydrogen comes close to 0.3. This maximum value can be reached when the energy released by the combustion reaction is totally used for the heat-up of the system and the evaporation of the liquid droplets. This similarity indicates that the fraction limit of droplets is well related to the equilibrium temperature, thus the chemical energy released from the combustion.

According to the calculation, even for the composition of maximum equilibrium temperature, the limit volume fraction is no more than 0.12%. The efficiency of the water droplets would be remarkable.

2.3.3 Case III

Case III is dedicated to study the influence of droplets on the combustion equilibrium state under normal initial conditions. According to the former work [20], the averaged liquid volume fraction inside a non-obstructed part of reactor building is between 2×10^{-4} and 4×10^{-4} . As for the hydrogen fraction, the upper and lower limit of flammability are calculated by using a subroutine in Cast3M.

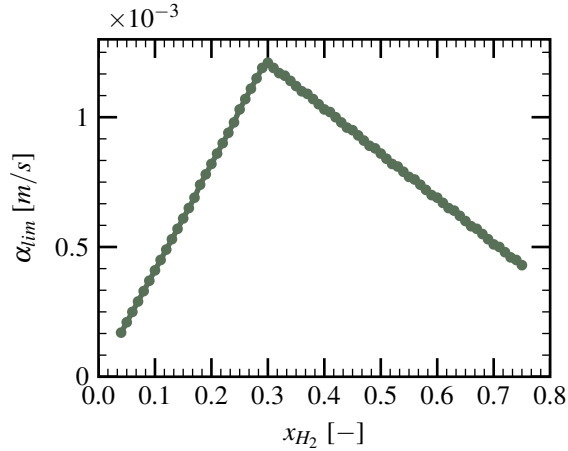


Figure 2.3: Limit volume fraction of liquid droplets as a function of H_2 molar fraction.

The evolution of equilibrium pressure for hydrogen-air combustion with spray evaporation is given in Fig. 2.4a. It is noticed that the shape of the pressure curve does not change as the liquid volume fraction varies. All curves reach the peak value at the same hydrogen-air composition, as a stoichiometric mixture.

According to AICC calculations, with stoichiometric conditions, the peak value for equilibrium pressure, in absence of water droplets, is 8.72 bar . For a liquid volume fraction of $\alpha = 2 \times 10^{-4}$, the highest equilibrium pressure is 7.68 bar , while for a liquid volume fraction of $\alpha = 4 \times 10^{-4}$, the highest pressure can be reduced to 6.9 bar . It is clear to see a depressurization effect as the increase of the volume fraction of droplets.

The evolution of equilibrium temperature as a function of H_2 molar fraction is presented in Fig. 2.4b. Similarly, the highest value of the equilibrium temperature is noted for the mixture of stoichiometric composition. From Fig. 2.2b, the stoichiometric equilibrium temperature can be 3022 K for AICC combustions. However, it can be decreased by 1000 K under the water volume fraction $\alpha = 2 \times 10^{-4}$, and can be reduced to 1460 K for $\alpha = 4 \times 10^{-4}$. The decrease of equilibrium temperature under the presence of droplets indicates the effectiveness of water evaporation for fire mitigation.

2.3.4 Case IV

In case IV, the behaviors of pressure and temperature under severe accident initial conditions are investigated. The averaged liquid volume fractions considered are still between $\alpha = 2 \times 10^{-4}$ and $\alpha = 4 \times 10^{-4}$.

As is shown in Fig. 2.5a, we have the evolution of equilibrium pressure as a function of H_2 molar fraction. A similar shape for the curves of equilibrium pressure as in Case III can be obtained.

Different from Case III, the peak value appears close to $x_{H_2} = 0.164$, instead of 0.3. This is due to the presence of steam in the initial gas mixture, which reduces the fraction of oxygen. The new stoichiometric composition for hydrogen molar fraction is close to $x_{H_2} = 0.164$. It could be noticed that the flammability limits for hydrogen ($0.08 - 0.296$) gets narrower in the presence of steam. The increase of pressure is fast,

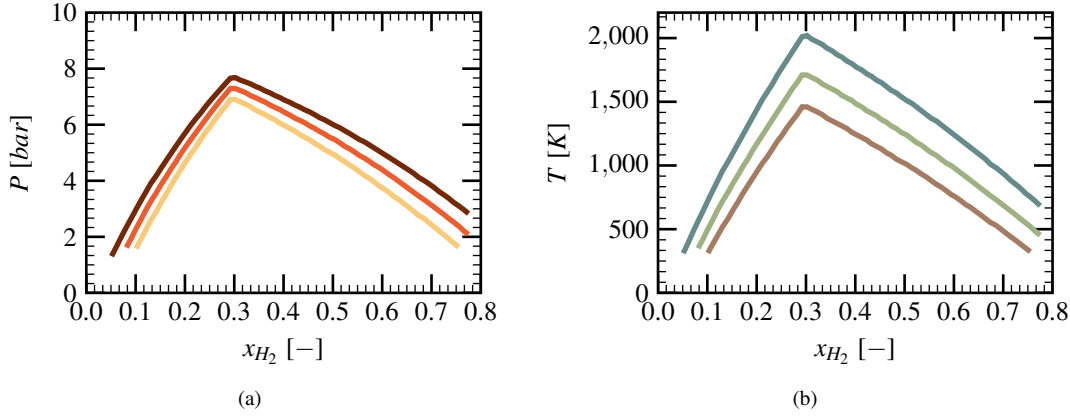


Figure 2.4: (a) Evolution of pressure as a function of H_2 molar fraction, results of $\alpha = 2 \times 10^{-4}$ (—) are compared with results of $\alpha = 3 \times 10^{-4}$ (—) and $\alpha = 4 \times 10^{-4}$ (—). (b) Evolution of equilibrium temperature as a function of H_2 molar fraction, $\alpha = 2 \times 10^{-4}$ (—), $\alpha = 3 \times 10^{-4}$ (—), $\alpha = 4 \times 10^{-4}$ (—).

which means that the equilibrium pressure after the combustion is very sensible to the original hydrogen fractions. The depressurization effect of the droplets is quite noticeable.

For the evolution of equilibrium temperature in Case IV, Fig. 2.5b shows that the evaporation of the droplets is effective. For the same initial composition, the equilibrium temperature can be reduced to 1396 K for the liquid volume fraction of $\alpha = 2 \times 10^{-4}$, compared to 3022 K for AICC combustions. One can notice that the presence of steam in the system can also largely reduce the equilibrium temperature after combustion, comparing the Figs. 2.4b and 2.5b. As indicated in Case I, we have more conservative results in the lumped-parameter model than the real combustion in accident scenarios. The real peak values for equilibrium pressure and temperature could be slightly lower.

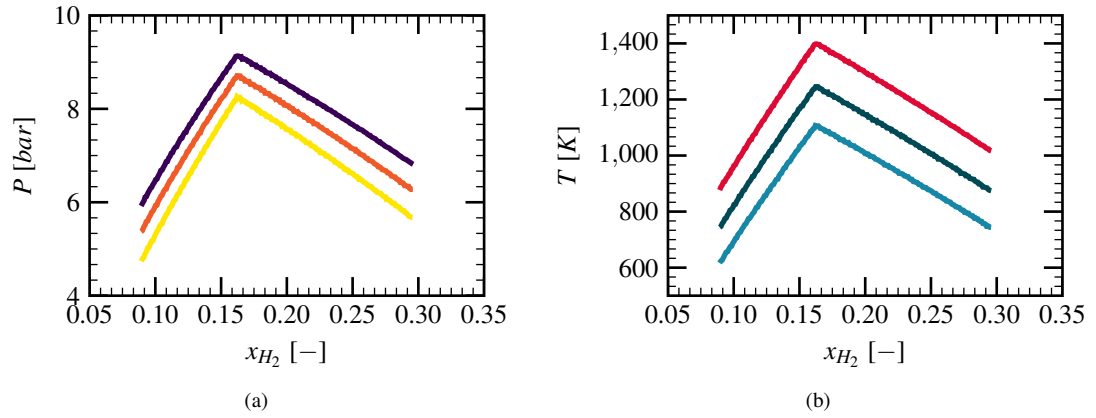


Figure 2.5: (a) Evolution of equilibrium pressure as a function of H_2 molar fraction, results of $\alpha = 2 \times 10^{-4}$ (—) are compared with results of $\alpha = 3 \times 10^{-4}$ (—) and $\alpha = 4 \times 10^{-4}$ (—). (b) Evolution of temperature as a function of H_2 molar fraction, $\alpha = 2 \times 10^{-4}$ (—), $\alpha = 3 \times 10^{-4}$ (—), $\alpha = 4 \times 10^{-4}$ (—).

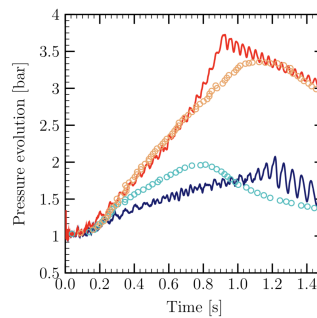
Chapter 3

Spray-flame Interaction

Section 1: Modeling pressure loads during a premixed hydrogen combustion in the presence of water spray

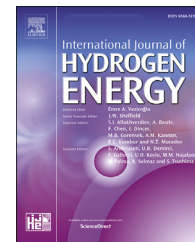
Highlights:

- A new methodology for investigating the pressure evolution during a hydrogen combustion process in presence of a water spray at medium scale is successfully assessed.
- A simplified algorithm for pressure evolution is developed.
- Empirical correlations are used to estimate the values of the main factors influencing the pressure evolution.
- A three-dimensional hydrodynamic, code based on CREBCOM combustion model, is used and assessed for large-scale hydrogen combustion.
- The employed methodology keeps the CFD code as simple as possible by using explicitly the available experimental data, thus gaining in efficiency and predictability.



Available online at www.sciencedirect.com

ScienceDirect

journal homepage: www.elsevier.com/locate/he

Modeling pressure loads during a premixed hydrogen combustion in the presence of water spray



Guodong Gai^a, Sergey Kudriakov^a, Abdellah Hadjadj^{b,*}, Etienne Studer^a, Olivier Thomine^a

^a DEN-DM2S-STMF, CEA, Université Paris-Saclay, France

^b Normandie University, INSA of Rouen, CNRS, CORIA, 76000 Rouen, France

ARTICLE INFO

Article history:

Received 2 July 2018

Received in revised form

17 December 2018

Accepted 19 December 2018

Available online 26 January 2019

Keywords:

Combustion

Water spray

CFD

Hydrogen safety

PWR

ABSTRACT

This paper proposes a method for pressure evolution modeling during combustion process in presence of water spray. A simplified model based on empirical correlations is developed, which allows the estimation of the main factors influencing the pressure evolution, such as the combustion rate, the convective heat loss and the droplet evaporation rate. The results are then used as a guideline to adjust the parameters of a three-dimensional hydrodynamic code based on CREBCOM combustion model developed and validated for large-scale hydrogen combustion. This methodology provides an approach to estimate the important parameters for the determination of the pressure loads. Simulation results for hydrogen-air combustion in presence of water spray using the present model compare favorably to the experimental data of Carlson et al. [1].

© 2019 Hydrogen Energy Publications LLC. Published by Elsevier Ltd. All rights reserved.

Introduction

In the hydrogen application industry, accidental hydrogen gas release can lead to a formation of the explosive air-gas mixture. In the case of ignition, the resulting explosion can present a potential danger due to its effects on people and property. In the nuclear industry, during severe accidents inside a Pressurized Water Reactor (PWR) containment building, hydrogen gas produced by a reactor core oxidation, can be released from the reactor coolant system and mix with containment atmosphere initially filled with air. A possible explosion can challenge the reactor containment and

potentially lead to a release of radioactive materials into the environment. The mitigation systems, such as sprays, are widely installed inside industrial buildings in order to prevent or reduce an unwanted scenario [3]. In a PWR containment building, the spray systems are used in order to limit the overpressure, enhance the gas mixing, avoid hydrogen accumulation, and wash out the fission products that may be released into the reactor building [2]. In the case when the ignition of air-hydrogen gas mixture occurred after the activation of the spray system, an estimation of the spray ability to mitigate the explosion is needed. In other words, one should be able to predict the overpressure evolution during the interaction process between a premixed flame and a spray

* Corresponding author.

E-mail address: hadjadj@coria.fr (A. Hadjadj).

<https://doi.org/10.1016/j.ijhydene.2018.12.162>

0360-3199/© 2019 Hydrogen Energy Publications LLC. Published by Elsevier Ltd. All rights reserved.

Nomenclature

$a_{0.5}$	averaged heat flux [W/cm ²]
c_{sp}	sound speed in the combustion products [m/s]
C_p	constant pressure specific heat [J/kg/K]
C_v	constant volume specific heat [J/kg/K]
D_p	diameter of the droplet [m]
e	specific energy [J/kg]
h	specific enthalpy [J/kg]
H	volumetric heat transfer coefficient [W/m ³ /K]
I	static pressure impulse [bar·s]
K_0	parameter related to flame velocity in CREBCOM model [m/s]
l	latent heat of evaporation [kJ/kg]
L	length of the experimental tube [m]
Le	Lewis number [–]
L_T	integral length scale [m]
N	ratio of the flame surface to the tube cross-section area [–]
p_{max}	maximum pressure [bar]
Q	surface heat transfer coefficient [kW/m ² /K]
Q_w	supply flow rate [l/s]
R	universal gas constant [J/K/mol]
S_L	laminar flame velocity [m/s]
S_t	turbulent flame velocity [m/s]
t_{max}	time needed for the flame to reach the maximum pressure [s]
v_t	visible turbulent flame velocity [m/s]
W	molar mass [kg/mol]
W_e	Weber number [–]
x_{H_2}	molar fraction of hydrogen [–]
α	liquid volumetric fraction [–]
$\dot{\alpha}$	volumetric evaporation rate [s ⁻¹]
γ	specific heat ratio [–]
δ	flame thickness [m]
Δx	average cell size [cm]
ϵ	parameter in the criterion function of the CREBCOM model [–]
ρ	mass density [kg/m ³]
σ	expansion ratio between density of unburnt and burnt gases [–]
σ_s	surface tension [N/m]
Σ	flame surface [m ²]
Ψ	criterion function for the ignition [–]
$\dot{\omega}$	chemical reaction rate [s ⁻¹]

at a scale of a typical industrial or reactor containment building.

A wealth of research material on flame-spray interaction phenomenon related to explosion mitigation in industrial environments is available in the open literature. Rather thorough analysis of main factors influencing flame evolution during spraying has been presented in Refs. [3,4]. Early small scale experiments [5] as well as recent small and medium scale experiments using hydrogen [6–9], have revealed that sprays containing small-size droplets, of the order of $\mathcal{O}(10 \mu\text{m})$ can be effective against premixed combustion.

Droplets generated by industrial water-spray systems are relatively large, having diameters of the order of $\mathcal{O}(100 - 1000 \mu\text{m})$, and these droplets will hardly evaporate in a flame propagating through a premixed gas mixture. Nevertheless, several studies have indicated that water sprays can lead to a significant reduction in explosion overpressure [10]. The primary mechanism that leads to mitigation is believed to be a reduction in mean droplet size as a result of aerodynamic interactions between the droplet and the explosion-induced flow field. The mitigation action of the spray is then attributed to the interaction of this finer spray with the combustion wave. Another results have shown that there are certain circumstances under which the presence of spray can cause a propagating flame to accelerate, as a result of the turbulence induced by spray, leading to a higher overpressure [10,11]. In certain situations, the gas velocity generated by the thermal expansion of combustion products is not sufficient for droplets break-up. Considering this case, which is the subject of this paper, the problem of explosion severity estimation is still a challenging subject.

The pressure evolution brought by turbulent combustion in the presence of sprays is a result of an interplay of several factors, such as a) turbulent combustion rate modified by the spray droplets, b) convective heat loss rate to internal solid structures and to water droplets, and c) heat loss rate due to droplet evaporation. A physical model should be able not only to incorporate these effects and reproduce a pressure signal, but also to do so at a large geometrical scale, typical of a reactor building.

The difficulties related to this task are twofold: i) combustion models integrated into the current *large-scale* numerical codes experience poor predictive capabilities [12], and ii) the experimental data devoted to turbulent combustion-spray interaction, due to inherent difficulties, often contain only pressure evolution and flame trajectory along some direction [1,13,14]. These data are not sufficient for code validation as they do not allow a correct estimation of order of magnitude for each of the above-mentioned factors.

In this paper, we describe a method for pressure evolution modeling during a combustion process in presence of a water spray. A simplified two-volume (burnt gas - fresh gas) model based on empirical correlations found in the open literature is developed. The model allows us to estimate the values for main factors influencing the pressure evolution, such as the combustion rate evolution, the convective heat loss rate to the structure and to the water droplets, and the heat loss rate due to droplet evaporation. The results of this model are used as a guideline for adjusting the parameters of a three-dimensional hydrodynamic code based on CREBCOM combustion model [15–17], developed and validated for large-scale hydrogen combustion.

Methodology

The following approach is adapted in order to determine the pressure loads during turbulent combustion in the presence of spray:

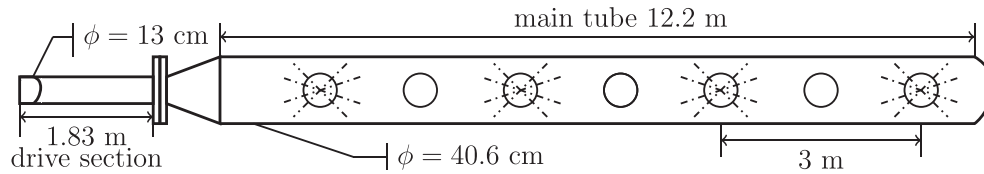


Fig. 1 – Sketch of the facility showing the location of spray nozzles used in Ref. [1].

- Based on a simplified numerical model for pressure evolution inside a closed volume, developed under LMN¹ hypothesis, we reveal the main mechanisms and lumped-parameter factors, such as turbulence combustion rate, volumetric heat-loss coefficient and volumetric water-evaporation rate, leading to a given pressure evolution.
- Using available experimental data and empirical correlations, we estimate the values of the main factors defined above and perform a sensitivity study based on DOE² approach.
- The outcomes of the two previous steps will serve as a guideline for adjusting the parameters of a full three-dimensional hydrodynamic code based on CREBCOM combustion model.

The present methodology will be demonstrated using a medium-scale experimental data of [1], briefly described here.

Experiments of Carlson et al. [1]

In this experiments, a shock tube was used as a main device. It consists of a long section carbon steel pipe of length $L_{tube} = 12.2\text{ m}$ and diameter $D_{tube} = 40.6\text{ cm}$, which is welded closed on one end. The other end of the tube is connected to a small-diameter driver tube ($L_{driver} = 1.83\text{ m}$, $D_{driver} = 13\text{ cm}$) through two standard bell reducers, as shown in Fig. 1. Dynamic (high-frequency response) pressure measurements using six Photocon (Model 525) pressure transducers were located on the sidewalls in both the driver and the shock tube. A Hewlett Packard (Model 3955) FM-type tape recorder was used to record the pressure measurements, which had a response limite of 20 kHz. The pressure signals were recorded on an oscillograph. The static pressure was measured by Taber transducers and recorded on Dynalog circular graphic inking recorders.

A sketch of the nozzle setup is shown in Fig. 1. Sufficient spray density was realized from the four sets of nozzles, as schematically depicted by dashed lines. The two nozzles spray in opposite directions along the shock tube as shown in Fig. 2. The test program kept the same spraying system as used in commercial reactor at comparable spacings and operating at equivalent pressure level ($D_p \approx 4.1\text{ bar}$). The authors indicate that the mean droplet diameter is $D_p \approx 500\text{ }\mu\text{m}$. The estimated liquid volumetric fraction is $\alpha = 5 \times 10^{-4}$, which is comparable to the containment spray system liquid volume fraction in a nuclear plant.

A total of 22 tests were conducted, with hydrogen concentration ranging from 5% to 16% (dry air concentrations) and initial pressure from 1 bar to 2 bar. Here, two tests are considered, and the corresponding initial conditions together with maximum pressure values measured during these experiments are presented in Table 1. The experimental results show that the water spray reduces the maximum pressure in the shock tube, as well as the time for the pressure elevation with regards to its initial value. The heat losses play an important role during the combustion process (see Fig. 3), as the maximum pressure is much lower than the adiabatic isochoric complete combustion (AICC) pressure. Note that in both tests, 7 and 8, $p_{AICC} = 5.9\text{ bar}$.

Simplified numerical model analysis

Here, a reduced-order model for pressure evolution inside a closed tube, developed under LMN assumption, is presented. The purpose is twofold: i) reveal the main mechanisms leading to a particular pressure evolution; ii) build a framework for sensitivity analysis that will be outlined later.

The model is based on sensible enthalpy conservation law [18]. Taking into account the fact that combustion takes place at LMN regime, by integration the ordinary differential equation for the pressure evolution inside the tube (see Appendix A for derivation details) is obtained:

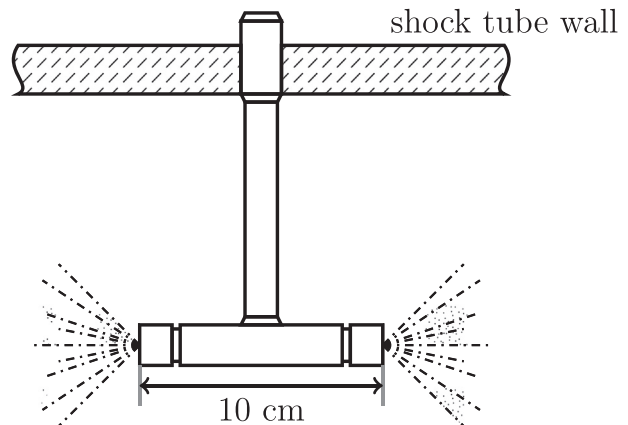


Fig. 2 – Water spray nozzle detail reproduced from Ref. [1].

Table 1 – Operating conditions for the flame test cases.

Test No.	x_{H_2} (dry)	Q_w [l/s]	p_0 [bar]	p_{max} [bar]
7	16.0	0.0	1.013	3.36
8	16.0	4.6	1.013	1.97

¹ Low Mach Number.

² Design Of Experiments.

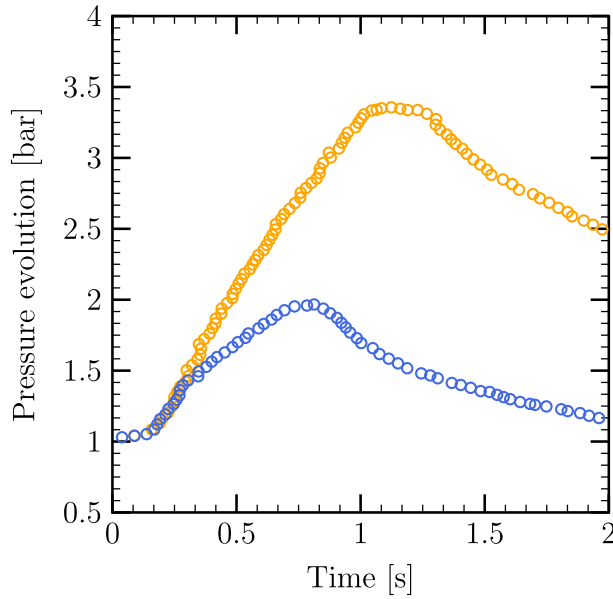


Fig. 3 – Pressure evolution as a function of time, results of Test 7 (○) and Test 8 (○). Scanned from Ref. [1].

$$\frac{d}{dt} \left[p \left(\frac{\gamma_b}{\gamma_b - 1} V_b + \frac{\gamma_f}{\gamma_f - 1} V_f - V_{tot} \right) \right] = \Sigma \cdot S_L \cdot \Delta H \cdot \rho_f \cdot Y_{H_2} - H \left(\frac{p}{\rho_b R_b} V_b + \frac{p}{\rho_f R_f} V_f - T_0 V_{tot} \right), \quad (1)$$

where p is the thermodynamic pressure, V_b and V_f are the volumes occupied by burnt and fresh gases, respectively (see Fig. 4). The closed volume is represented by V_{tot} , H is the volumetric heat loss coefficient, T_0 is the reference temperature, Σ is the flame surface, S_L is the laminar flame velocity, ΔH is the energy release per kg of burnt hydrogen gas, ρ_f is the fresh gas density, and Y_{H_2} is the mass fraction of hydrogen gas in the fresh mixture.

In case of spraying, another term has to be included in the right-hand side of Eq. (1). This term represents the energy losses related to the water evaporation, which can be expressed as:

$$-\rho_l \cdot \dot{\alpha} \cdot l \cdot V_b, \quad (2)$$

where ρ_l is the liquid density, l is the latent heat of evaporation, and $\dot{\alpha}$ is the volumetric evaporation rate. For simplicity, it is assumed that the evaporation takes place only inside the burnt volume.

Several variables in Eq. (1) have to be modeled: i) the volume of the burnt gas evolution (V_b), ii) the flame surface



Fig. 4 – Schematic representation of a flame propagation along a tube.

evolution (Σ), and iii) the evolution of the volumetric heat loss coefficient.

Evolution of the volume of the burnt gas is closely related to the visible flame velocity. The latter can be expressed as a sum of the gas velocity on the flame upstream side v_{gas} and the averaged burning velocity S_t , i.e.:

$$v_{flame} = v_{gas} + S_t. \quad (3)$$

For the burning velocity, S_t , the following expression is used:

$$S_t = S_L \frac{\Sigma}{A_{tube}} = S_L \cdot N, \quad (4)$$

where A_{tube} is the cross section area of the combustion tube. The burning velocity stays lower than the visible flame velocity. As a first approach, the constant values for H and N are adopted. The details on the solution algorithm of the simplified model is given in Appendix B.

Model application for test 8 (with spray)

Here, the above model is applied for Test 8. The spray was activated before the combustion, and the mixture properties are given in Table 2.

As an example, the averaged flame velocity is first fixed at a given value, $v_{flame}^{av} = 13$ m/s ($L_{tube} = 12.2$ m, the combustion takes around 0.93 s), and consider three cases with different parameters for energy loss coefficient and the volumetric evaporation rate (see Table 3). The purpose of this exercise is to show that very similar pressure evolutions can be obtained using different sets of model parameters. The values for the parameters might not be physical; their correct estimation is the subject of the next subsections.

The pressure evolutions computed using the proposed model display relatively similar character (see Fig. 5). Moreover, the maximum pressure values are almost the same and take place at close time instants: $p^{max} = 1.96$ bar at $t = 0.816$ s (for Case 1), $p^{max} = 1.953$ bar at $t = 0.802$ s (for Case 2) and $p^{max} = 1.986$ bar at $t = 0.814$ s (for Case 3). We compute the pressure evolution over time, known as the pressure impulse, as:

$$I_p(t) = \int_0^t p(t) dt. \quad (5)$$

Table 2 – Thermodynamic properties related to initial (subscript f) and final (subscript b) mixture properties.

x_{H_2}	S_L [m/s]	γ_f	γ_b	R_f [J/kg/K]	R_b [J/kg/K]
0.16	0.445	1.40	1.29	338.6	311.5

Table 3 – Test 8. Values used in the model. H_1 is the energy loss coefficient during combustion, H_2 is the energy loss coefficient after combustion.

Case	H_1 [kW/K/m ³]	H_2 [kW/K/m ³]	v_{flame}^{av} [m/s]	$\dot{\alpha}$ [s ⁻¹]	N [–]
1	6	3	13	2.2×10^{-4}	30
2	5	3	13	4.4×10^{-4}	30
3	3	3	13	8.7×10^{-4}	30

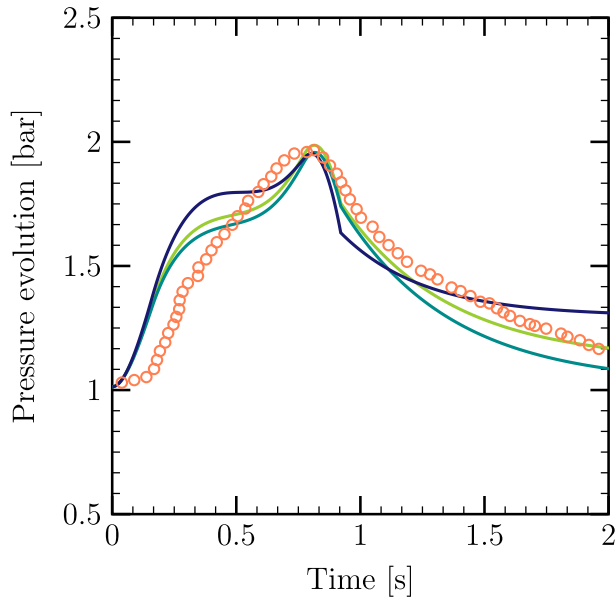


Fig. 5 – Test 8. Experimental pressure evolution (○) compared with computed pressure evolutions using $H_1 = 6000 \text{ W/K/m}^3$, $\dot{\alpha} = 2.2 \times 10^{-4} \text{ s}^{-1}$ (—); $H_1 = 3000 \text{ W/K/m}^3$, $\dot{\alpha} = 8.7 \times 10^{-4} \text{ s}^{-1}$ (—); and $H_1 = 5000 \text{ W/K/m}^3$, $\dot{\alpha} = 4.4 \times 10^{-4} \text{ s}^{-1}$ (—).

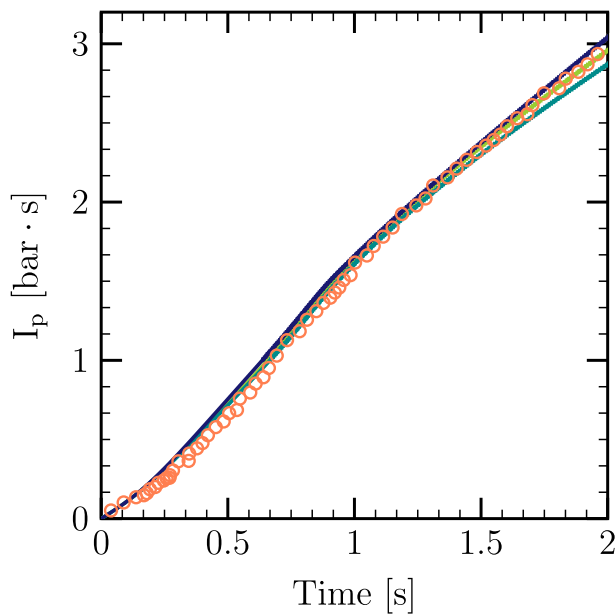


Fig. 6 – Test 8. Comparison between impulse evolutions corresponding to the experimental data (○) and to the computed data $H_1 = 6000 \text{ W/K/m}^3$, $\dot{\alpha} = 2.2 \times 10^{-4} \text{ s}^{-1}$ (—); $H_1 = 3000 \text{ W/K/m}^3$, $\dot{\alpha} = 8.7 \times 10^{-4} \text{ s}^{-1}$ (—); and $H_1 = 5000 \text{ W/K/m}^3$, $\dot{\alpha} = 4.4 \times 10^{-4} \text{ s}^{-1}$ (—).

The computed pressure impulse closely follows the experimental impulse evolution curve shown in Fig. 6. Note that the values of both maximum pressure p_{max} and impulse I_p are used for damage evaluation using P-I diagrams [19].

It can be observed that similar pressure evolution behavior can be obtained using different combinations of model parameters. More refined estimations or experimental data are needed for both parameters, H and $\dot{\alpha}$.

Estimation of the parameters

From the above subsection, one can note that there are several main mechanisms which can lead to a particular pressure evolution:

- Combustion rate evolution,
- Convective heat loss rate due to the structure,
- Heat loss rate due to droplet evaporation.

Hence, in order to correctly model the thermodynamic system in terms of pressure evolution, one needs to have an estimation (an order of magnitude) of different parameters related to these mechanisms. In the present section, some of these parameters are estimated using the experimental correlations.

Estimation of the averaged evaporation rate $\dot{\alpha}$

The results of [20] are used in order to estimate the mass evaporation rate of a single droplet subjected to a gas flow around it. An approximate model of moving droplet evaporation has been formulated. The two-films model has been adopted to describe both the gas and the liquid phases, which is described by an effective conductivity model.

By applying the theory developed in Ref. [20], one can compute the diameter evolution of a single droplet under high temperature, $T_{gas}^{AIBC} \approx 1547 \text{ K}$. This temperature corresponds to adiabatic isobaric complete combustion (AIBC). A comparison between the effective conductivity model and the other two

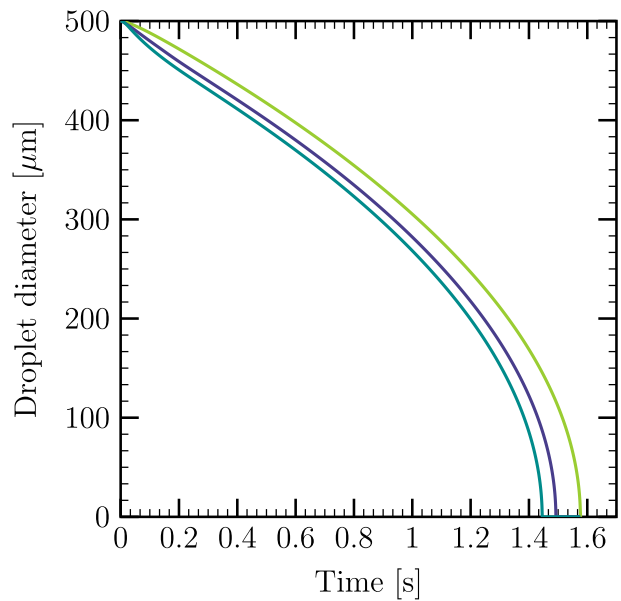


Fig. 7 – Diameter evolution of a single droplet, comparison between three models: conductivity limiting model (—), effective conductivity model (—) and conductivity infinity model (—).

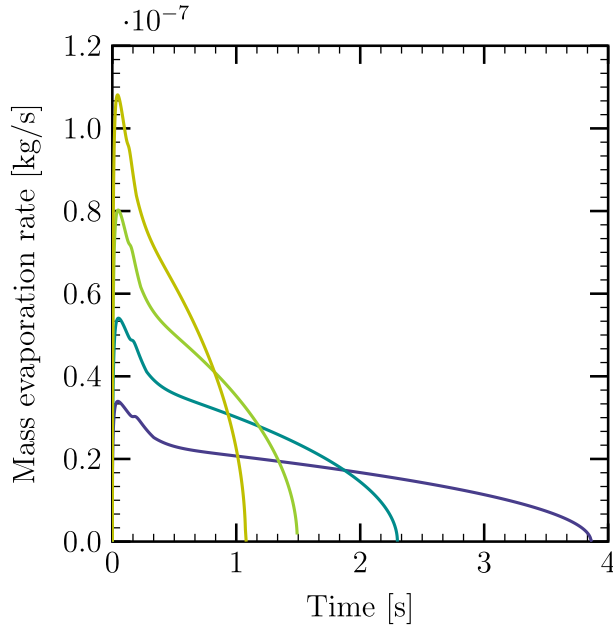


Fig. 8 – Influence of ambient temperature on the mass evaporation rate: 900 K (—), 1200 K (—), $T^{\text{AIBC}} = 1547$ K (—) and $T^{\text{AICC}} = 1885$ K (—).

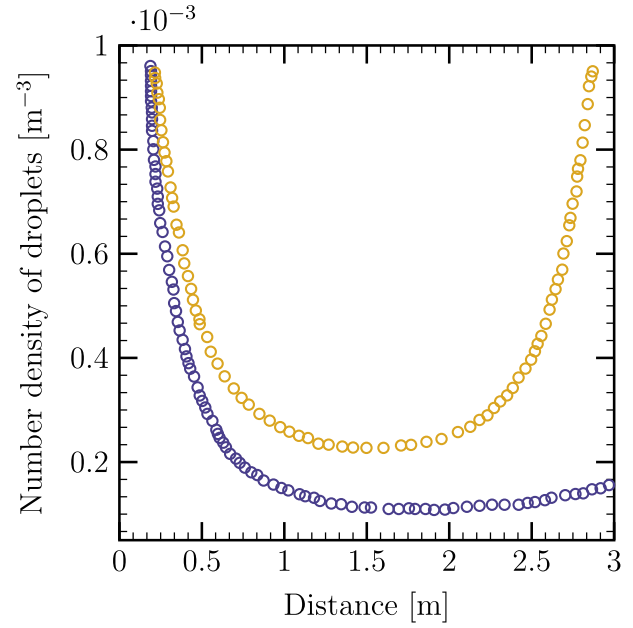


Fig. 9 – Droplet population density as a function of axial position between spray nozzles in the shock tube; single spray \circ , two sprays \circ [1].

models applied to a droplet of $D_p = 500 \mu\text{m}$ (corresponding to the droplet diameter of experiments [1]) and $T_{\text{ini}} = 373$ K, is given in the Fig. 7, from which one can see the variation of evaporation time in three different cases. The time taken for total evaporation varies for different models: infinite conductivity model (1.44 s), effective conductivity model (1.49 s) and conduction limit model (1.58 s). However, the estimated values are very close to each other.

Fig. 8 shows the variation of evaporation rate evolution for different ambient temperatures. Note that the temperatures corresponding to AIBC (1547 K) and AICC (1885 K) combustion are taken into consideration, as well as two other temperatures (900 K and 1200 K) for comparison. We can see that the evaporation rate strongly depends on the ambient temperature of the gas phase. One can also estimate that the mean evaporation rate of one single droplet during the combustion process is of magnitude of $\mathcal{O}(10^{-8})$ kg/s.

The volumetric spray evaporation rate can be estimated by the distribution of the water droplets in the computational space. In the experiment of [1], the number of droplets per unit volume for a single spray and the two opposing sprays in the shock tube are given in Fig. 9.

By integrating this curve in space, we can have the mean density of droplets between two nozzles:

$$n_{\text{droplets}} = 1.367 \times 10^6 \text{m}^{-3}, \quad (6)$$

as well as the volume fraction of the spray between two successive nozzles:

$$\alpha = \frac{V_{\text{liq}}}{V_{\text{tot}}} = 8.9 \times 10^{-5}. \quad (7)$$

It seems that this value for liquid volume fraction is different from the one given by the authors (5.0×10^{-4}) [1]. In

order to simplify the computation, the following assumptions are proposed:

- All droplets are suspended in the shock tube and will take part in the evaporation process
- The mass flow rate of the nozzle is constant during the combustion process
- All droplets have the same mean diameter, which is fixed at $D_p = 500 \mu\text{m}$,
- The number density of spray in terms of number of droplets per unit volume is kept constant.

By assuming that all droplets have the same mean diameter, we implicitly imply that the droplet break-up does not take place. The average flame velocity can be estimated by using the time instant when the pressure reaches its maximum value, i.e. the average flame velocity $v_{\text{flame}}^{\text{av}} \approx 13$ m/s, which would give the Weber number:

$$W_e = \frac{\rho v^2 D_p}{\sigma_s} = 1.2. \quad (8)$$

where ρ is the density of the droplet, v is its velocity, D_p is the diameter of the droplet and σ_s is the surface tension. One notes that this value is an order of magnitude smaller than the critical Weber number $W_e = 12$.

From these assumptions, the mean volume evaporation rate can be calculated to describe the mean evaporation rate of the liquid phase:

$$\dot{\alpha} = \frac{\dot{m}_0 \times n_{\text{droplets}}}{\rho_l}, \quad (9)$$

where \dot{m}_0 is the averaged mass evaporation rate of a single droplet, n_{droplets} the density of the spray in terms of number of

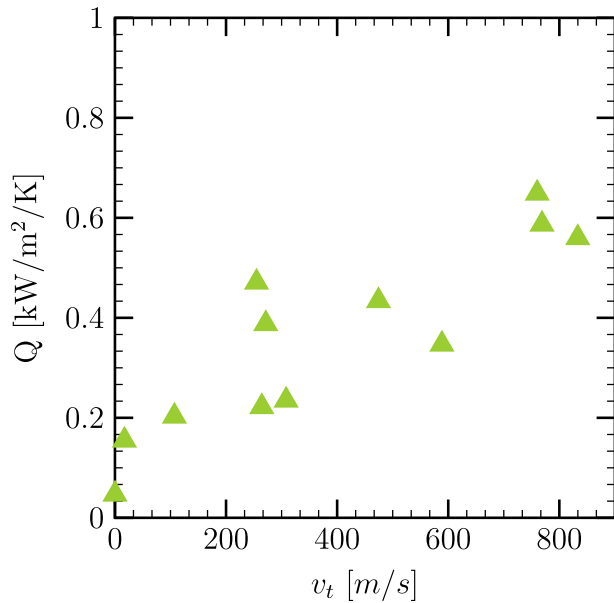


Fig. 10 – Evolution of surface heat transfer coefficient Q as a function of visible turbulent flame velocity v_t [21].

droplets per unit volume, ρ_l the density of water droplets. After calculation, we can obtain the estimated volume evaporation rate:

$$\dot{\alpha} = 6.01 \times 10^{-5} \text{ s}^{-1}. \quad (10)$$

Volumetric heat loss coefficient H [21]

It is shown in Ref. [21] that the main mechanism for heat loss from the combustion products of propagating turbulent flames in obstructed tubes is the convective heat transfer. The function of the estimated heat exchange coefficient on the flame speed is presented in Fig. 10. It is obtained by mounting the thermal gauges to the inner surface of the tube to measure the overall heat flux.

The surface heat transfer coefficient is defined as:

$$Q = \frac{a_{0.5}}{T_{AICC} - T_0}, \quad (11)$$

where T_{AICC} is the adiabatic isochoric combustion temperature of the mixture, T_0 is the ambient temperature, and $a_{0.5}$ is the averaged heat flux. Thus, the volumetric heat loss coefficient can be calculated by:

$$H = Q \frac{S_{tot}}{V_{tot}}, \quad (12)$$

where S_{tot} is the total surface of the tube, V_{tot} the volume of the system. For instance, a fraction of 16% hydrogen-air mixture will give a mean flame velocity close to 20 m/s in the tube, thus we can deduce the value for H :

$$Q = 0.14 \text{ kW/m}^2/\text{K} \rightarrow H = 4350 \text{ W/m}^3/\text{K}. \quad (13)$$

This estimation, as emphasized in Ref. [21], has a relative error of 50%.

Sensitivity analysis with respect to the flow parameters

Effects of the different flow parameters and their uncertainty on the pressure evolution can be quantified to complete the

assessment of the developed model. In our case, the DOE techniques [22] have been applied to optimise the number of calculations and perform the sensitivity analysis.

Four factors (namely the volume fraction evaporation rate $\dot{\alpha}$, the volumetric heat transfer coefficient H , the ratio of the flame surface to tube cross-section area N , the laminar flame velocity S_L) have been chosen to investigate their effects on the responses variables (p_{max} maximum pressure, t_{max} time to reach the maximum pressure, I_p impulse of pressure during the combustion computed up to 2 s). The variations chosen for all these parameters are summarized in Table 4. These variations come from estimated experimental uncertainty or engineering approximations.

A 2^{4-1}_{IV} fractional factorial design has been selected taking into account the main effects of single parameter and their 2-order interactions. Denote -1 the minimal estimated value for one parameter, and $+1$ the maximal value for this factor. The fractional factorial design can be expressed in Table 5 [23]:

One can describe the responses by a quadratic model:

$$\mathcal{Y} = \mathcal{Y}_0 \left(1 + \sum_{i=1}^4 \mathcal{E}_i x_i + \sum_{j=1}^2 \sum_{k>j}^3 \mathcal{E}_{jk} x_j x_k \right), \quad (14)$$

where \mathcal{Y} is the response, \mathcal{Y}_0 is the mean value for the response, x the studied parameter ($x = +1$ for maximal value, -1 for minimal value), \mathcal{E}_i , \mathcal{E}_{jk} are the main effect coefficient of parameter x_i and interaction effect of two parameters x_j and x_k , respectively.

The determination of these coefficients requires 8 calculations using the matrix shown in Table 5, where each column corresponds to a parameter and each row represents a calculation. For example, the main effect coefficient of the volume evaporation rate can be calculated by:

$$\mathcal{E}_{\dot{\alpha}} = \frac{1}{2\mathcal{Y}_0} \left(\frac{y_5 + y_6 + y_7 + y_8}{4} - \frac{y_1 + y_2 + y_3 + y_4}{4} \right), \quad (15)$$

where y_i are the responses of the i -th calculation, the factor $\frac{1}{2}$ comes from the superposition of the main effect $\dot{\alpha}$ and a higher order interaction of other parameters.

Table 4 – Selected parameters for the sensitivity study.

Parameter	Unit	Min	Mean	Max
$\dot{\alpha}$	s^{-1}	3.0×10^{-5}	6.0×10^{-5}	9.0×10^{-5}
H	$\text{Wm}^{-3}\text{K}^{-1}$	2200	4350	6500
N	–	20	30	40
S_L	m/s	0.32	0.45	0.58

Table 5 – DOE Matrix for main factor and 2-order interactions.

	$\dot{\alpha}$	H	N	S_L	$\dot{\alpha}H$	$\dot{\alpha}N$	HN
1	-1	-1	-1	-1	+1	+1	+1
2	-1	-1	+1	+1	+1	-1	-1
3	-1	+1	-1	+1	-1	+1	-1
4	-1	+1	+1	-1	-1	-1	+1
5	+1	-1	-1	+1	-1	-1	+1
6	+1	-1	+1	-1	-1	+1	-1
7	+1	+1	-1	-1	+1	-1	-1
8	+1	+1	+1	+1	+1	+1	+1

Table 6 – Results of the sensitivity analysis: influence of the parameters on the responses.

	t_{max} (s,%)	p_{max} (bar,%)	I (bar·s,%)
\mathcal{Y}_0	0.812	2.62	3.57
$\mathcal{E}_{\dot{\alpha}}$	-0.98	-0.22	-0.45
\mathcal{E}_H	-2.91	-23.67	-19.07
\mathcal{E}_N	-9.07	0.94	2.41
\mathcal{E}_{S_L}	-4.62	0.45	0.82
$\mathcal{E}_{\dot{\alpha}\cdot H}$	-2.58	1.40	-0.98
$\mathcal{E}_{\dot{\alpha}\cdot N}$	-1.21	-0.47	-1.39
$\mathcal{E}_{H\cdot N}$	-1.85	-1.02	-2.34

The sensitivity analysis has been applied for the proposed model and the results are listed in Table 6, where the coefficients are expressed in terms of fraction of response \mathcal{Y} mean values. For example, setting the heat transfer coefficient H to its maximal value (+1 in Table 5, $H = 6500 \text{ W/m}^2/\text{K}$) leads to a decrease (-sign in Table 6) of p_{max} by 23.67% from its mean value.

It can be deduced from Table 6 that the flame velocity, which is translated in time to reach the maximum pressure, t_{max} depends mainly on the flame surface, which is related to the turbulence level. The variation of the ratio between the flame surface and the cross-section area by 33% can change t_{max} by 9.07%.

The maximal pressure p_{max} is mainly affected by the heat transfer coefficient H as well as the flame surface area ratio N . If one increases the volumetric evaporation rate $\dot{\alpha}$ or the heat transfer coefficient H , the maximal pressure will be reduced, since the evaporation and the heat transfer can take out energy from the system. However, if the flame surface is increased, the peak pressure will be elevated. The faster the flame propagates the higher the maximal pressure p_{max} and its impulse I will be.

The heat transfer coefficient has a most important influence on the impulse I . This is firstly due to the experiment uncertainty of H . According to Ref. [21], the uncertainty of estimated H is 50%. It seems that the evaporation of the water droplets has less important influence than the variation of the heat transfer on the pressure evolution, in spite of the same degree of uncertainty.

Finally, it seems that the interaction between the parameters have less importance than the contributions of the main factors.

CFD simulation with CREBCOM model

In this section, the medium-scale experiments of Carlson et al. [1] have been investigated by the CREBCOM combustion model [15], to analyze the overpressure and the flame velocity.

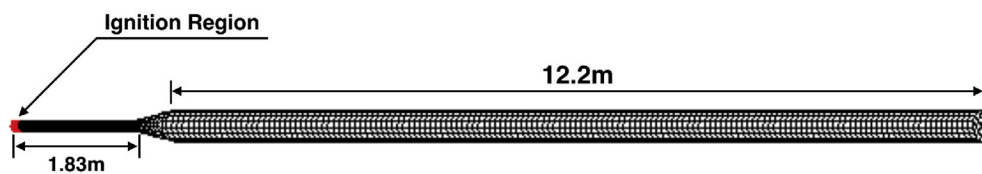


Fig. 11 – Geometry of a tube of two sections: $D_{driver} = 0.13 \text{ m}$ ($L_{driver} = 1.83 \text{ m}$) and $D_{tube} = 0.406 \text{ m}$ ($L_{tube} = 12.2 \text{ m}$); red color stands for the ignition region. (For interpretation of the references to colour in this figure legend, the reader is referred to the Web version of this article.)

A vaporization model has been used to reproduce some of the experimental data.

In order to fit with the experimental setup, we define a tube composed of three parts: the 1.83 m drive cylinder of diameter 0.13 m, the 12.2 m main tube with spray system of diameter 0.406 m and the middle section which relates the two cylinders of different sections, as described in Fig. 11.

In our model, a thin layer of cells at the left end of the driven tube is chosen to be the ignition region (Fig. 11). For the thermodynamic conditions assigned to the ignition zone, the final state of the same initial composition corresponds to the AICC combustion. For the first computations, the mesh of approximate cell size of $\Delta x = 10 \text{ cm}$ is used in the main tube. A series of equidistant transducers located are set in the main tube for tracking the flame arrival time.

Governing equations

The system of equations solved are: 1) the reactive Euler equations for a mixture of H_2 , O_2 , H_2O and N_2 , which express the conservation of total mass, the mass conservation for species k ($k = \{\text{H}_2, \text{O}_2, \text{H}_2\text{O}\}$), conservation of momentum and energy, and 2) the transport equations for K_0 , $Y_{\text{H}_2,i}$ and $Y_{\text{H}_2,f}$ the meaning of which will be explained below.

$$\frac{\partial \rho}{\partial t} + \nabla \cdot (\rho \vec{u}) = 0, \quad (16)$$

$$\frac{\partial \rho Y_k}{\partial t} + \nabla \cdot (\rho \vec{u} Y_k) = \rho \dot{\omega}_k, \quad (17)$$

$$\frac{\partial \rho \vec{u}}{\partial t} + \nabla \cdot (\rho \vec{u} \otimes \vec{u} + p\mathbf{I}) = \rho \vec{g}, \quad (18)$$

$$\frac{\partial \rho e_t}{\partial t} + \nabla \cdot (\rho \vec{u} h_t) = \rho \vec{g} \cdot \vec{u} - \rho \sum_j \Delta h_{f,j} \dot{\omega}_j + S_{cr}, \quad (19)$$

$$\frac{\partial \rho K_0}{\partial t} + \nabla \cdot (\rho \vec{u} K_0) = 0, \quad (20)$$

$$\frac{\partial \rho Y_{\text{H}_2,f}}{\partial t} + \nabla \cdot (\rho \vec{u} Y_{\text{H}_2,f}) = 0, \quad (21)$$

$$\frac{\partial \rho Y_{\text{H}_2,i}}{\partial t} + \nabla \cdot (\rho \vec{u} Y_{\text{H}_2,i}) = 0. \quad (22)$$

The mass fractions Y_k ($k = \text{H}_2, \text{O}_2, \text{H}_2\text{O}$), the species density ρ_k and the mixture density are related by:

$$Y_k = \frac{\rho_k}{\rho}. \quad (23)$$

Combustion modeling

In this section, the reaction rate $\dot{\omega}_k$ present as a source term in Eqs. (17) and (19) and the meaning of the transport Eqs. (20)–(22) are described. This has been presented in details in Ref. [24] and validated in Refs. [16,25] and the references therein, we shall briefly present it here for completeness. It is a general practice to use one-step chemical reaction for large-scale computations, i.e. where the mesh size is much larger than the flame thickness.

In each elementary control volume, the definition of the combustion progress variable ξ is:

$$\xi(\vec{r}, t) = \frac{Y_{H_2}(\vec{r}, t) - Y_{H_2f}(\vec{r}, t)}{Y_{H_2b}(\vec{r}, t) - Y_{H_2f}(\vec{r}, t)}, \quad (24)$$

where Y_{H_2} is the hydrogen mass fraction, and the indices f and b refer to the *unburned* and *burned* mixture (i.e. the mixture before and after combustion), respectively. The reaction rate for the progress variable ξ is:

$$\dot{\omega}_\xi = \frac{K_0}{\Delta x} \cdot \Psi, \quad (25)$$

where K_0 [m/s] is a parameter related to the flame velocity, Δx the mesh dimension (we consider here only uniform, or nearly uniform cartesian meshes). Ψ is a criterion function defined as:

$$\Psi = \begin{cases} 1 & \text{if } \varepsilon^2 = \varepsilon_{l,m,n}^2, \\ 0 & \text{if not} \end{cases}, \quad (26)$$

where

$$\varepsilon_{l,m,n}^2 = \varepsilon_{l+1,m,n}^2 + \varepsilon_{l-1,m,n}^2 + \varepsilon_{l,m+1,n}^2 + \varepsilon_{l,m-1,n}^2 + \varepsilon_{l,m,n+1}^2 + \varepsilon_{l,m,n-1}^2 - 3\varepsilon_{l,m,n}^2, \quad (27)$$

ε is a parameter in the criterion function of the CREBCOM model and l, m, n are the computational mesh index.

The reaction rates $\dot{\omega}_{H_2}$ and $\dot{\omega}_\xi$ are linked by:

$$\dot{\omega}_{H_2} = (Y_{H_2b} - Y_{H_2f})\dot{\omega}_\xi, \quad (28)$$

and the reaction rates for Y_{O_2} , Y_{H_2O} and Y_{N_2} can be deduced from:

$$\frac{\dot{\omega}_{H_2}}{W_{H_2}} = \frac{\dot{\omega}_{O_2}}{1/2W_{O_2}} = -\frac{\dot{\omega}_{H_2O}}{W_{H_2O}}. \quad (29)$$

From Eqs. (25), (28) and (29) one can compute the species reaction rates if K_0 , Y_{H_2b} and Y_{H_2f} are known. These functions depend on the lagrangian position, therefore we have to transport these quantities in lagrangian manner which leads to (20)–(22).

Note that for combustion modeling without spray effect and with initially uniform gas mixture, there is no need to resolve the set of equations (21)–(22), as initial and final hydrogen concentrations are constant both in time and space. When the spray effect is taken into account, these equations, on the contrary, have to be considered as the hydrogen concentration will change due to evaporation process.

The source term S_{cr} which expresses the transfer of energy from the system to its environment, of Eq. (19) is given by:

$$S_{cr} = -H(T - T_0), \quad (30)$$

where H and T_0 are taken constant.

Vaporization modeling study

Assuming an ideal gas mixture, the vaporization model focuses on the thermodynamic aspect of the vaporization of water droplets during the combustion.

In every cell, two successive phenomena are considered: the combustion of the premixed gas mixture, and the vaporization of the liquid phase. In our model, a criterion is introduced to start the vaporization process. When $\xi_i > \xi_{\text{threshold}}$, part of a liquid phase evaporates instantaneously in the i^{th} cell with evaporation rate $\dot{\alpha}$ and the *updated* variables by conservation laws can be obtained. The vaporization process takes place inside a closed adiabatic computational cell.

The conservation of mass for the post-evaporation gas phase gives:

$$\tilde{m}_i^{\text{ini}} = \tilde{m}_i^{\text{fin}} = \tilde{m}_{i,\text{gas}}^{\text{ini}} + \tilde{m}_{i,\text{liq}}^{\text{ini}}. \quad (31)$$

The total energy of the system in the i^{th} cell is defined as the sum of two parts: the formation enthalpy and the internal energy and we neglect the kinetic energy. For example, the initial state can be expressed as:

$$\begin{aligned} \tilde{e}_i^{\text{ini}} = & \sum_j Y_{ij}^{\text{ini}} h_j^0 + \int_0^{T_{\text{ini},i}} \left\{ \sum_j Y_{ij}^{\text{ini}} C_{v,j}(T') \right\} dT' \\ & + Y_{H_2O,i}^{\text{liq}} \left(h_{H_2O,i}^{\text{liq}} - \frac{p_{\text{tot},i}}{\rho_{H_2O,i}^{\text{liq}}} \right), \end{aligned} \quad (32)$$

where Y_j are the mass fractions for each specie j , T is the mixture temperature, $C_{v,j}(T)$ and h_j^0 are the constant volume specific heat and the formation enthalpy at 0 K of the species j , e is the sensible internal energy.

The first term of Eq. (32) denotes the formation enthalpy of the mixture at 0 K. Polynomial functions have been used [26] to calculate the heat capacity at constant volume. The internal energy for liquid water is calculated using its specific enthalpy.

Considering the ideal gas hypothesis, the energy at the final state is given by:

$$\begin{aligned} \tilde{e}_i^{\text{fin}} = & \sum_j Y_{ij}^{\text{fin}} h_j^0 + \int_0^{T_{\text{fin},i}} \left\{ \sum_j Y_{ij}^{\text{fin}} C_{v,j}(T') \right\} dT' \\ & + Y_{H_2O,i}^{\text{liq} \rightarrow \text{vap}} \left(h_{H_2O,i}^{\text{gas}} - \frac{RT_{\text{fin},i}}{M_{H_2O}} \right). \end{aligned} \quad (33)$$

The conservation of mass and energy in the i^{th} cell gives:

$$\tilde{e}_i^{\text{ini}} = \tilde{e}_i^{\text{fin}}. \quad (34)$$

The governing equations for the vaporization is thus obtained, which will be used to calculate the temperature and the pressure inside the computational cell, assuming ideal gas hypothesis.

Determination of the parameters in the CREBCOM model

In the CREBCOM model, the thermal conduction and species diffusion are not directly modeled. Their action is taken into account by introducing a correlation derived from experimental data that acts as a source term in Euler equations. The

model for the burning rate, parameter K_0 , is assumed to be constant throughout the combustion process, resulting in conservative estimations of pressure loads [15]. The parameter H related to heat losses can play an important role for slow flame developments. In this section, the strategy for choosing values for the aforementioned parameters is presented.

Determination of the parameter K_0

Determination of the visible flame speed, V_f , is important for the appropriate prediction of pressure load. However, it was not measured in the experiments of [1]. To solve this problem, one can determine the input parameter K_0 in the CREBCOM code, to obtain the expected value of V_f , by using the correlation proposed in Ref. [15]. The analysis for one-dimensional flame propagation shows that the following correlation between S_T , the so-called turbulent burning rate, and K_0 can be derived:

$$K_0 = \frac{S_T(\sigma + 1)}{4}, \quad (35)$$

where $\sigma = \frac{\rho_u}{\rho_b}$ is the expansion ratio, ρ_u and ρ_b are densities of the fresh and burnt gas. Following the estimation of Bradley [27], for a slow deflagration, the turbulent burning rate S_T can be modeled by:

$$\frac{S_T}{S_L} = 0.0008(\sigma - 1)^3 \left(\frac{L_T}{\delta}\right), \text{ for weak turbulence, } \frac{L_T}{\delta} < 500. \quad (36)$$

For Test 7, by using the parameters chosen in the experiments of [21] (see Table 7), one can calculate the constant K_0 for the hydrogen-air composition of $x_{H_2} = 16\%$, by referring to Eqs. (35)-(36):

$$K_0 \approx 5.73 \text{ m/s}. \quad (37)$$

It should be emphasized that the parameter K_0 is not the burning velocity even though it has the same dimension. By implementing transducers in the geometry, the evolution of visible flame velocity can be obtained as a function of flame propagation distance in the tube.

The works of [29,30] show that the maximal value for the visible flame velocity in Test 7 ($x_{H_2} = 16\%$) cannot reach the sound speed in the combustion product ($c_{sp} = 787 \text{ m/s}$). Another set of experiments [28] has given in detail the flame velocity evolutions as a function of X/D , where X denotes the distance of the flame propagation, for different gas mixtures and different blockage ratios. It was shown that a maximal flame velocity locates at the middle of the tube. One can deduce that the maximal visible flame velocity cannot exceed a maximal value of 70 m/s in Test 7 of [1].

According to the above arguments, $K_0 \approx 5.73 \text{ m/s}$ is taken which results in the visible flame velocity varying between 10 m/s and 40 m/s along the tube.

Determination of the parameter H

In section Methodology, it is shown that a) the value of the volumetric heat loss coefficient H can be chosen within the range of $H = 4000 \pm 50\% \text{ W/m}^3/\text{K}$ and b) this parameter has an important influence on the peak pressure.

The value of parameter H after completeness of combustion, past t_{max} , is noted to be different from that during the combustion. The difficulty lies in the fact that the experimentally obtained pressure signal after completeness of combustion is influenced by the high temperature, and cannot be reliable [31]. Nevertheless, for Test 7, an estimated value is proposed for this stage, $H_2 = 425 \text{ W/m}^3/\text{K}$, by matching numerical and experimental data.

The value $H_1 = 1700 \text{ W/m}^3/\text{K}$ chosen for the volumetric heat loss coefficient during combustion is lower than the range prescribed by Ref. [21]. Since the tube used in the experiments of [1] is smooth, and the results of [21] were obtained for the blockage ratio, $BR > 0$. One can argue that the heat loss due to convection is less important in the present case.

The Fig. 12 presents the results for pressure evolution corresponding to Test 7 (no spray) computed with CREBCOM model and the above estimated parameters.

Some conclusions can be drawn from the Fig. 12. First, it seems that the slopes of the computed pressure evolution are similar to the experimental data, which means that the parameters H_1 and H_2 are reasonably estimated for this test case. The peak value for pressure p_{max} appears at $t_{max} = 0.9 \text{ s}$, indicating that the $K_0 = 5.73 \text{ m/s}$ is well evaluated. The non-smooth pressure behavior at $t = t_{max}$ can be attributed to abrupt change of parameter H in our calculation.

It should be mentioned that a fully compressible numerical solver is used in the calculation, and the acoustic waves are

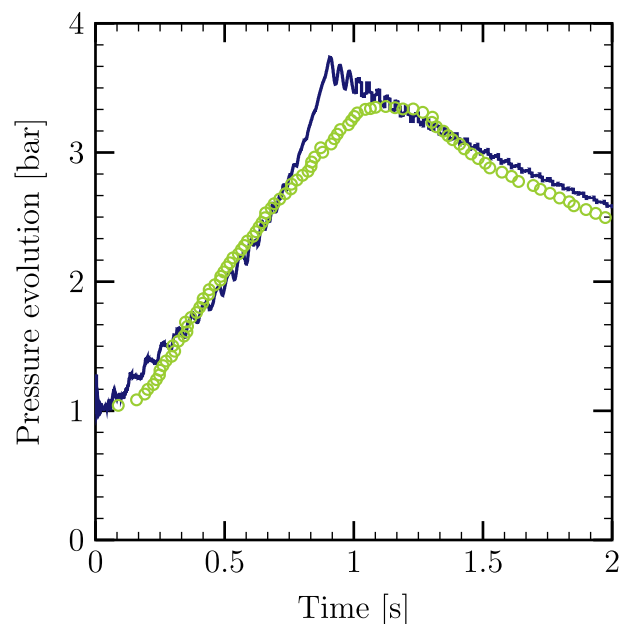


Fig. 12 – Test 7 (no spray). Pressure evolution as a function of time by setting $H_2 = 1700 \text{ W/m}^3/\text{K}$, $H_1 = 425 \text{ W/m}^3/\text{K}$. Comparison between experimental (○) and CFD results (—).

Table 7 – Mixture properties for $x_{H_2} = 16\%$ in database of [28] used in the model of [15].

x_{H_2} [-]	σ [-]	S_L [m/s]	Le	L_T/δ [-]	c_{sp} [m/s]
0.16	4.83	0.91	0.4	96	780

not filtered. Based on the investigation of adiabatic combustion in the tube, the pressure oscillations of the numerical solutions have frequency of $f_{osci}^{num} = 34$ Hz which corresponds well to the frequency of acoustic wave travelling back and forth through the burnt gas along the tube, i.e. $f_{accu} = 32$ Hz.

Water spray effect

After choosing K_0 and H for the combustion, the effect of water spray is investigated. Test 8 differs from Test 7 by the presence of a water spray of a supply flow rate $Q_w = 4.6$ l/s (see Table 1).

Modeling of test 8

The transient evolution of the static pressure during the combustion process in the CREBCOM model depends on K_0 , H and the evaporation rate of the water droplets. In this section, we present the results for Test 8 with $K_0 = 5.73$ m/s, which is the same as in Test 7, $H_1 = 3850$ W/m³/K and $H_2 = 800$ W/m³/K. The values for volumetric heat loss coefficient are higher than those in Test 7. Moreover the value for H_1 lies in range similar to Ref. [21]. This is justified by the fact that heat losses due to convection are higher due to the presence of relatively cold droplets.

The flow rate of the water spray system is: $Q_w = 4.6$ l/s, which can be considered to be a theoretical upper limit of the evaporation rate, that is:

$$\dot{\alpha}_{max} = \frac{Q_w}{V_{tube}} \approx 2.9 \times 10^{-3} \text{ s}^{-1}, \quad (38)$$

where V_{tube} is the volume of the main tube i.e. the region with water spray system.

The evaporation process is implemented at every time step, and is characterized by $\dot{\alpha}$ (s⁻¹). In each computational cell, this equality is related to the evaporated liquid mass during a time step Δt :

$$m_{cell}^{H_2O} = \dot{\alpha} \rho_{H_2O} V_{cell} \Delta t. \quad (39)$$

As the value estimated in the reduced-order model (see section Methodology), the value $\dot{\alpha} = 6.01 \times 10^{-5}$ s⁻¹ is used as the mean evaporation rate during the combustion process.

Fig. 13 shows the calculated pressure evolution compared to the experimental data of Test 8. It can be seen that by adjusting the parameters K_0 , H and $\dot{\alpha}$, it is possible to simulate the mitigation effect of the spray with a reasonable approximation. The peak pressure p_{max} is close to the experimental one, i.e. $p_{exp}^{max} = 1.9$ bar, $p_{cal}^{max} = 2.0$ bar. It is noticed that the slope corresponding to the computed pressure evolution differs from experimental counterpart. In fact, as shown in the literature [11], the spray flow from the nozzles can generate turbulence which might lead to the flame acceleration. In Test 7, the peak pressure p_{exp}^{max} takes place at $t_0 \approx 1$ s. However, in Test 8, the time needed to reach the p_{exp}^{max} is equal to 0.7 s, indicating that the flame velocity is higher in the later case. The peak pressure locates at $t \approx 1.2$ s in our simulation.

It is noted that the frequency of oscillation decreases under the effect of heat loss and spray evaporation. In Fig. 13, the pressure oscillations after completeness of combustion of the numerical

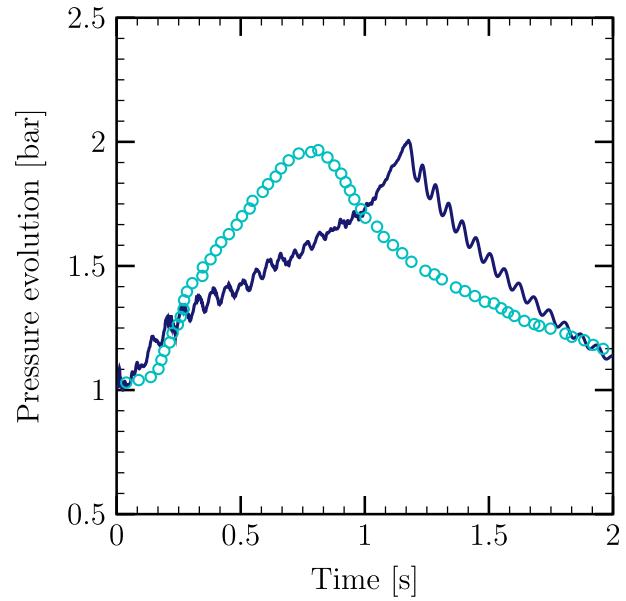


Fig. 13 – Test 8 (with spray). Pressure evolution for hydrogen-air mixture ($x_{H_2} = 0.16$), with $p_{ini} = 1.013$ bar, $H_1 = 3850$ W/m³/K, $H_2 = 800$ W/m³/K, $K_0 = 5.73$ m/s. Comparison between the experimental results (○) and CFD calculation results (—).

solution have frequency of $f_{osci}^{spray} \approx 18$ Hz. Since the pressure is mitigated, the velocity of the acoustic wave is also reduced.

The visible flame velocity is computed using the flame arrival data from numerical transducers. Fig. 14 shows the evolution of the visible flame speed under the influence of heat loss and the water spray. The calculations are performed by keeping the same value for K_0 . It can be noted that the heat loss and the spray effect reduce the flame velocity. Compared to the combustion without heat losses, the flame velocity can be decelerated by 5 m/s under the heat loss, and 10 m/s by the spray effect. In order to counterbalance these effects, the value of K_0 should be increased by a factor related to spray-generated turbulence, which however is unknown.

Energy balance analysis

By integrating the energy conservation equation on the computational domain, we can write symbolically:

$$\frac{d}{dt} \int_V \rho e_i dV = \int_V E_m dV + \int_V E_c dV + \int_V E_v dV.$$

where E_m , E_c and E_v denote combustion, convection and evaporation energy losses, respectively.

The first term on the right-hand side is the energy increase rate due to the combustion, while the other two terms are related to the energy loss due to the convective mechanism and the liquid water evaporation. These three terms are respectively characterized by three parameters K_0 (E_m), H (E_c) and $\dot{\alpha}$ (E_v).

Fig. 15 shows the energy change in the tube per unit volume and per second. The combustion process will increase the total energy, while the heat loss and the spray evaporation will consume the energy. The Fig. 15 shows that the

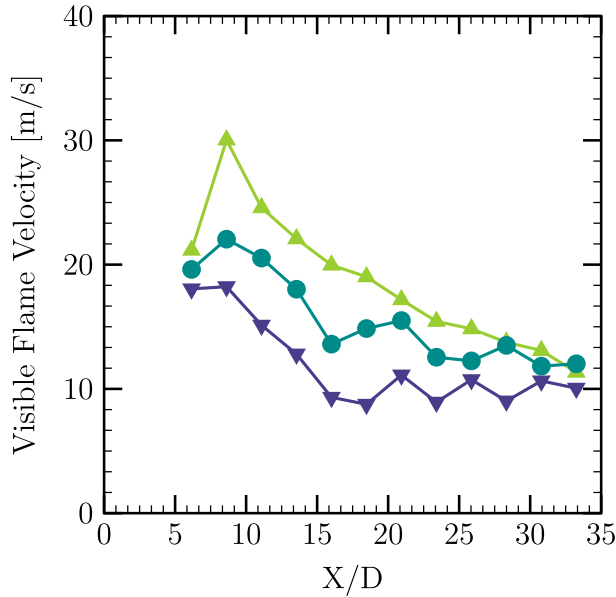


Fig. 14 – Visible flame velocity evolution for hydrogen-air mixture ($x_{H_2} = 0.16$) AICC combustion, with initial pressure $p_{ini} = 1.013$ bar (—▲—); effect of heat losses only (—●—), spray effect (—▼—).

contributions due to the combustion and the convective heat loss are of the same order of magnitude, $\sim 2 - 3$ MW/m³, while the contribution related to heat loss due to droplets evaporation is lower by one order of magnitude, ~ 0.1 MW/m³. Again, this confirms the importance of the convection heat losses (see Section [Methodology](#)). The relative increase in the contribution due to combustion, for $1 \text{ s} < t < 2 \text{ s}$ is related to the fact that at the end of the tube, the flame propagates through a pre-compressed mixture having higher energy per volume unit.

Cell size effect

In the CREBCOM model, the chemical reaction rate of combustion is related to the mesh cell size Δx . In the former studies, the water spray effects have been investigated by using the geometry having a mean cell size of $\Delta x = 10$ cm. In this section, a mesh sensitivity study is performed, i.e. by considering an averaged mesh size of $\Delta x = 5$ cm.

From [Fig. 16](#), one can notice that in our calculation once the mesh size changes from $\Delta x = 10$ cm to $\Delta x = 5$ cm, the parameter K_0 has to be adjusted in order to have similar behavior.

The computed results are given in the [Fig. 17](#), and compared to the experimental data of Tests 7 and 8. Note that by choosing $K_0 = 7.0$ m/s, a reasonable approximation between the calculation and the experimental data in Test 7 is found. The slope of the pressure is well estimated. The peak value for the pressure evolution p_{cal}^{max} is slightly higher compared to the experimental data. For Test 8, the same heat loss coefficient $H_1 = 3850$ W/m³/K and $\dot{\alpha} = 6.01 \times 10^{-5}$ s⁻¹ have

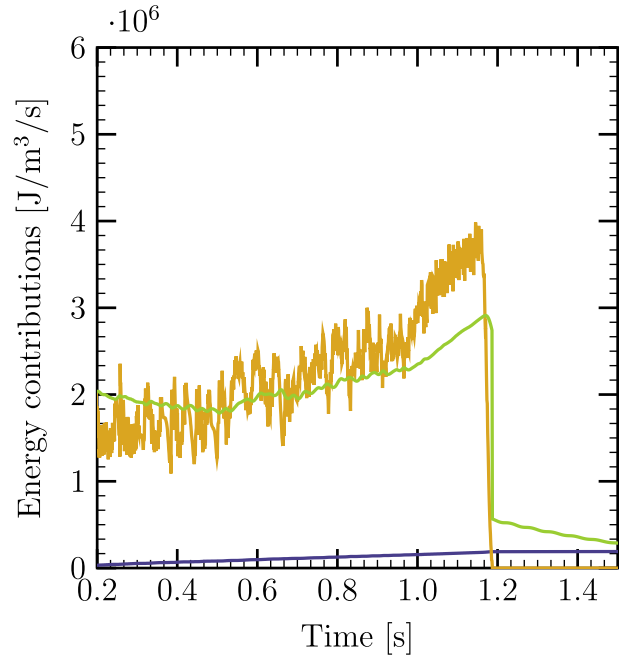


Fig. 15 – Test 8 (with spray). Evolution of three terms in Eq. (40): combustion heat (—), convective heat loss (—) and heat losses due to evaporation (—).

been used as for the test case with larger mesh size ($\Delta x = 10$ cm). Overall, the change in parameter K_0 is not significant ($< 20\%$) and it can be concluded that for the considered tests,

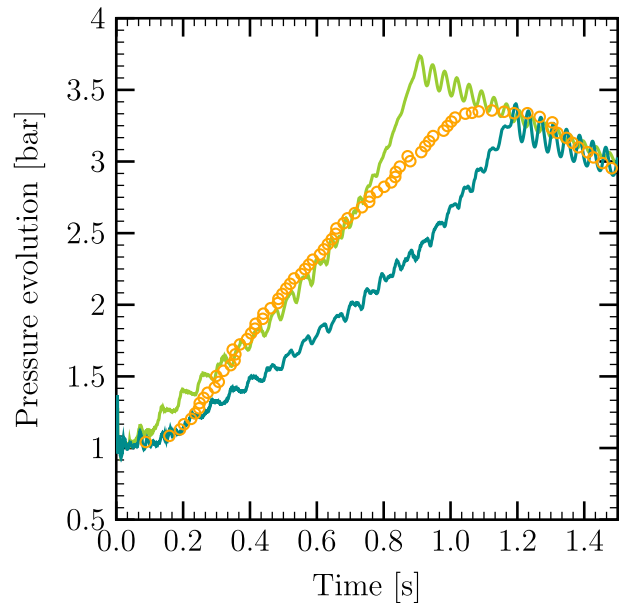


Fig. 16 – Test 7 (no spray). Pressure evolution for hydrogen-air mixture ($x_{H_2} = 0.16$), with $p_{ini} = 1.013$ bar, $H_1 = 1700$ W/m³/K, $H_2 = 425$ W/m³/K, $K_0 = 5.73$ m/s. The experimental results are given in (○). Comparison between the coarse mesh $\Delta x = 10$ cm (—) and the finer mesh $\Delta x = 5$ cm (—).

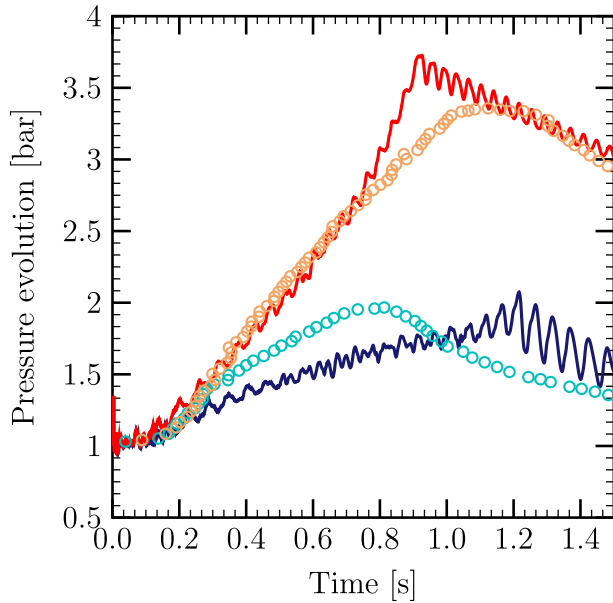


Fig. 17 – Tests 7 and 8. Pressure evolution for hydrogen-air mixture ($x_{H_2} = 0.16$), with $p_{ini} = 1.013$ bar; for Test 7, $H_1 = 1700$ W/m³/K, $H_2 = 425$ W/m³/K, $K_0 = 7.0$ m/s, for Test 8, $H_1 = 3850$ W/m³/K, $H_2 = 800$ W/m³/K, $K_0 = 7.0$ m/s, $\dot{\alpha} = 6.0 \times 10^{-5}$ s⁻¹, mesh size $\Delta x = 5$ cm. Comparison between the experimental results (no spray \circ , with spray \bullet), and CFD calculation results (no spray $—$, with spray $—$).

dividing by 2 the averaged mesh size, the same model parameters hold.

The higher amplitude of the oscillations corresponding to the numerical solution for pressure at the finer mesh can be attributed to the lower numerical viscosity, i.e. minor damping effect.

Conclusion

In this paper, a methodology is described to determine the pressure loads in a closed volume during turbulent combustion of hydrogen in the presence of the water spray.

Preliminary work has been performed using the simplified engineering model. One could observe that very similar pressure evolutions can be obtained by using different combinations of model parameters such as the combustion rate, volumetric heat-loss coefficient and evaporation rate. The DOE method has been employed to perform the sensitivity analysis with respect to these model parameters.

The outcomes of the simplified model serve as a guideline to estimate the CREBCOM CFD model parameters such as the flame velocity constant K_0 , the heat transfer coefficient H , and the volumetric evaporation rate $\dot{\alpha}$. Due to the lack of accurate data, the choices for these parameters can rely on the theoretical or other experimental results available in the literature.

The CREBCOM combustion model is used to determine the transient state of the combustion system, focusing on the evolution of pressure and the flame velocity, with and without water spray, using the previously estimated parameters. The experimental results corresponding to Tests 7 and 8 of [1] are

chosen for validation. It is shown that the pressure evolution is strongly affected by the following contributions: i) energy increase rate due to combustion, ii) convective energy loss rate and iii) the energy loss rate due to evaporation.

The calculations corroborate the experimental findings, that the water spray has an effective mitigation influence on the pressure evolution during the turbulent combustion. This methodology provides an approach to identify, estimate and evaluate the important parameters for the determination of the pressure loads due to combustion in the presence of sprays at large scale.

However, there is a room for improvement concerning a more sophisticated estimation of volumetric heat loss coefficient and of liquid evaporation rate, on the one hand, and for flame acceleration factor due to turbulence generated by a spray, on the other hand. This will be the subject of future research works.

Acknowledgement

This work has been performed with a financial support of the Electricité de France (EDF) in the framework of the Generation II&III reactor program, which is gratefully acknowledged. The authors would like to thank the CAST3M code development team.

Appendix A. Supplementary data

Supplementary data to this article can be found online at <https://doi.org/10.1016/j.ijhydene.2018.12.162>.

Appendix A. Simplified numerical model

A simple engineering model is presented for pressure evolution inside a closed volume, developed under LMN hypothesis.

Let us consider the sensible enthalpy conservation law [18]:

$$\rho \frac{Dh_s}{Dt} = \dot{\omega}_T + \frac{Dp}{Dt} + \nabla \cdot (\lambda \nabla T) - \nabla \cdot \left(\rho \sum_{k=1}^N h_{s,k} Y_k \mathbf{V}_k \right) + \tau_{ij} \frac{\partial u_i}{\partial x_j}, \quad (\text{A.1})$$

where specific sensible enthalpy h_s , species k diffusion velocity \mathbf{V}_k into the mixture, the viscous tensor τ_{ij} , and the energy release rate due to combustion $\dot{\omega}_T$ are defined as

$$h_s = \int_0^T C_p dT, \quad (\text{A.2})$$

$$\mathbf{V}_k \mathbf{x}_k = -D_k \nabla \mathbf{x}_k, \quad (\text{A.3})$$

$$\tau_{ij} = \mu \left(\frac{\partial u_i}{\partial x_j} + \frac{\partial u_j}{\partial x_i} \right) - \frac{2}{3} \mu \frac{\partial u_k}{\partial x_k} \delta_{ij}, \quad (\text{A.4})$$

$$\dot{\omega}_T = - \sum_{k=1}^N \Delta h_{f,k} \dot{\omega}_k. \quad (\text{A.5})$$

The Eq. (A.1) can be rewritten as

$$\rho \frac{Dh_s}{Dt} - \frac{Dp}{Dt} = \dot{\omega}_T + \mathcal{S}_{iff}, \quad (\text{A.6})$$

where \mathcal{S}_{iff} represents the diffusion term. For slow flames observed in some of the experiments, like in Tests 7 and 8, where fluid velocity is of the order of 10 m/s, the specific kinetic energy, $\rho |\mathbf{u}|^2/2$, is of the order of 100 kg/m/s², while the specific internal enthalpy is

$$\rho \int_0^T C_p dT = \rho \bar{C}_p T = \frac{\bar{\gamma}}{\bar{\gamma} - 1} p = \mathcal{O}(10^5 \text{ Pa}). \quad (\text{A.7})$$

Taking into account the fact that the combustion takes place at LMN regime (the speeds of sound in the fresh and burnt mixture are 376 m/s and 787 m/s, respectively), one can assume that the pressure is only function of time [32], i.e. the left-hand side of Eq. (A.6) can be written as

$$\frac{d}{dt} \left(\frac{\bar{\gamma}}{\bar{\gamma} - 1} p \right) - \frac{dp}{dt} \approx \dot{\omega}_T + \mathcal{S}_{iff}. \quad (\text{A.8})$$

We assume that the flame surface separates the gas into fresh and burnt mixture (combustion occurs at flamelet regime), each having constant properties (see Fig. 4).

Integrating the left hand side of Eq. (A.8) over the closed volume V_{tot} gives:

$$\frac{d}{dt} \left[p \left(\frac{\gamma_b}{\gamma_b - 1} V_b + \frac{\gamma_f}{\gamma_f - 1} V_f - V_{tot} \right) \right], \quad (\text{A.9})$$

where V_b and V_f are the volumes occupied by burnt and fresh gases, respectively. In the above formula we assume pressure equilibrium between burnt and fresh gases (Low Mach number hypothesis).

Integrating over the volume of the energy release rate gives:

$$\int_V \dot{\omega}_T = \Sigma \cdot S_L \cdot \Delta H \cdot \rho_f \cdot Y_{H_2}, \quad (\text{A.10})$$

with Σ being the flame surface, S_L the laminar flame velocity, Δh the energy release per unit mass of burnt hydrogen gas, ρ_f the fresh gas density, and Y_{H_2} the mass fraction of hydrogen gas in the fresh mixture.

The diffusion terms describing the rate of energy losses are often presented in a simplified form as:

$$\mathcal{S}_{iff} = H (T - T_0), \quad (\text{A.11})$$

where H is a volumetric heat loss coefficient, and T_0 is a reference temperature.

Finally, the ordinary differential equation for the pressure evolution inside the tube can be written as:

$$\frac{d}{dt} \left\{ p \left(\frac{\gamma_b}{\gamma_b - 1} V_b + \frac{\gamma_f}{\gamma_f - 1} V_f - V_{tot} \right) \right\} = \Sigma \cdot S_L \cdot \Delta H \cdot \rho_f \cdot Y_{H_2} - H \left\{ \frac{p}{\rho_b R_b} V_b + \frac{p}{\rho_f R_f} V_f - T_0 V_{tot} \right\}. \quad (\text{A.12})$$

In case of spraying, another term has to be included in the right-hand side of Eq. (A.12). This term represents the energy losses related to the water evaporation:

$$-\rho_L \cdot \dot{\alpha} \cdot l \cdot V_b, \quad (\text{A.13})$$

where ρ_L is the liquid density, l the latent heat of evaporation, and $\dot{\alpha}$ the liquid volume fraction rate of evaporation. For simplicity, it is assumed that the evaporation takes place inside the burnt volume.

Appendix B. Solution algorithm for the simplified model

Given the initial conditions for pressure p_0 , temperature T_0 , specific heats ratio related to burnt gas γ_b , to fresh gas γ_f , and laminar flame speed S_L . The algorithm contains the following steps:

- Choose values for:
 - (a) integral loss coefficient,
 - (b) evaporation rate for volume liquid fraction $\dot{\alpha}$,
 - (c) ratio of the flame surface to the tube cross-section area N ,
 - (d) averaged flame velocity v_{flame}^{av} (this value is needed for computing $t_{fin} = L_{tube}/v_{flame}^{av}$), and a profile for the v_{flame} (here the parabolic profile is used, for simplicity).
- Compute L_{flame} , which is the distance travelled by the flame at time t using the flame velocity evolution in time, and deduce the volume of the burnt gas $V_b = L_{flame} \cdot A_{tube}$.
- Calculate the increment of the mass of the burnt gas m_b and the mass of liquid evaporated m_{liq}^{ev} during the time interval Δt .
- Find the density of the burnt ρ_b and the fresh gases ρ_f .
- Compute the right-hand side of the Eq. (1) and deduce the new value of the pressure using classical differential schemes.

Set $S_L = 0$ when the flame reaches the end of the tube.

Appendix C. Evaporation model of a single droplet [20]

Appendix C.1. Gas phase

Here the practical step-by-step procedure of determination of the vaporization rate \dot{m} and the heat transferred into the droplet interior, Q_L is presented. For the justifications the reader can refer to the original article of [20]. Concerning the liquid phase analysis, it is assumed that the temperature within the droplet is uniform in space although the time is varying.

Assume that the droplet surface temperature T_s , velocity U , and the conditions of the free-stream flow are known: U_∞ , T_∞ , $Y_{F\infty}$. The solution algorithm is given below.

1. Calculate the molar and mass fluid vapor fractions at the droplet surface

$$x_{Fs} = p_{Fs}/p, Y_{Fs} = x_{Fs}M_F / \sum_i x_i M_i. \quad (C.1)$$

Here, p_{Fs} is the fluid vapor saturated pressure which is evaluated using the appropriate correlations

$$p_{Fs} = p_{Fs}(T_s), \quad (C.2)$$

2. Calculate the average physical properties

$$\bar{\rho}, \bar{C}_{pF}, \bar{C}_{pg}, \bar{\lambda}_g, \bar{\mu}_g, \bar{D}, \bar{Le} = \frac{\bar{\lambda}_g}{\bar{\rho}_g \bar{D} \bar{C}_{pg}}, \bar{Pr}, \bar{Sc}$$

in the gas film using the reference conditions given by:

$$\bar{T} = T_s + \frac{1}{3}(T_\infty - T_s), \quad (C.3)$$

$$\bar{Y}_F = Y_{Fs} + \frac{1}{3}(Y_{F\infty} - Y_{Fs}), \quad (C.4)$$

3. Calculate the Reynolds number, $Re = 2\rho_\infty|U - U_\infty|r_s/\mu_g$, as well as the Nusselt and the Sherwood numbers for a non-vaporizing droplet:

$$Nu_0 = 1 + (1 + Re \cdot Pr)^{1/3} f(Re), \quad (C.5)$$

$$Sh_0 = 1 + (1 + Re \cdot Sc)^{1/3} f(Re), \quad (C.6)$$

where $f(Re) = 1$ at $Re \leq 1$ and $f(Re) = Re^{0.077}$ at $Re \leq 400$,

4. Calculate the Spalding mass transfer number, B_M , diffusional film correction factor, F_M , modified Sherwood number, Sh^* , and the mass vaporization rate, \dot{m} :

$$B_M = \frac{Y_{Fs} - Y_{F\infty}}{1 - Y_{Fs}}, \quad (C.7)$$

$$F_M = (1 + B_M)^{0.7} \frac{\ln(1 + B_M)}{B_M}, \quad (C.8)$$

$$Sh^* = 2 + (Sh_0 - 2)/F_M, \quad (C.9)$$

$$\dot{m} = 2\pi\bar{\rho}_g \bar{D}_g r_s Sh^* \ln(1 + B_M), \quad (C.10)$$

5. Calculate the correction factor for the thermal film thickness, $F_T = F(B_T)$, using the value of the heat transfer number, B_T^{old} , from either the previous iteration or the previous time step,

6. Calculate the modified Nusselt number, Nu^* , the parameter ϕ and the corrected value of the heat transfer number, B_T :

$$Nu^* = 2 + (Nu_0 - 2)/F_T, \quad (C.11)$$

$$\phi = \left(\frac{\bar{C}_{pF}}{\bar{C}_{pg}} \right) \left(\frac{Sh^*}{Nu^*} \right) \frac{1}{Le}, \quad (C.12)$$

$$B_T = (1 + B_M)^\phi - 1, \quad (C.13)$$

7. Evaluate the heat penetrating into the liquid phase:

$$Q_L = \dot{m} \left(\frac{\bar{C}_{pF}(T_\infty - T_s)}{B_T} - l(T_s) \right). \quad (C.14)$$

Appendix C.2. Liquid phase

The transient liquid heating inside the droplet uses the effective conductivity model. Coupling the calculation of these two phases, the evaporation rate can be estimated.

The non-dimensional energy equation for the effective conductivity model is given as [20]:

$$\phi^2 \frac{\partial Z}{\partial \tau} = \beta \eta \frac{\partial Z}{\partial \eta} + \frac{1}{\eta^2} \frac{\partial}{\partial \eta} \left(\eta^2 \frac{\partial Z}{\partial \eta} \right), \quad (C.15)$$

where:

r_s is the current radius of the droplet;

$Z = (T - T_0)/T_0$ is the non-dimensional temperature of the droplet;

$\phi = r_s/r_0$ is the non-dimensional radius of the droplet;

$\eta = r/r_s$ is the non-dimensional coordinate;

$\tau = \alpha_L t/r_0^2$ is the non-dimensional time;

α_L is the liquid thermal diffusivity;

β is proportional to the regression rate of the droplet surfaces, which can be estimated by:

$$\beta = -\frac{1}{4\pi\alpha_L\rho_L r_s} \left[\dot{m} + \frac{1}{\rho_L C_{pL}} Q_L \right], \quad (C.16)$$

The following parameters have been used in the numerical solution [20,33];

$Pe_L = 2U_s r_0/\alpha_L$ is the liquid Peclet number, where U_s is the maximal surface velocity:

$$U_s = \frac{1}{32} (U_\infty - U) \left(\frac{\mu_g}{\mu_L} \right) Re_g C_F(Re_g), \quad (C.17)$$

$$C_F = \frac{12.69}{Re_g^{2/3} (1 + B_M)}, \quad (C.18)$$

$k_{eff} = \chi k_L$ is the effective thermal conductivity coefficient, where:

$$\chi = 1.86 + 0.86 \tanh[2.245 \log_{10}(Pe_L/30)]. \quad (\text{C.19})$$

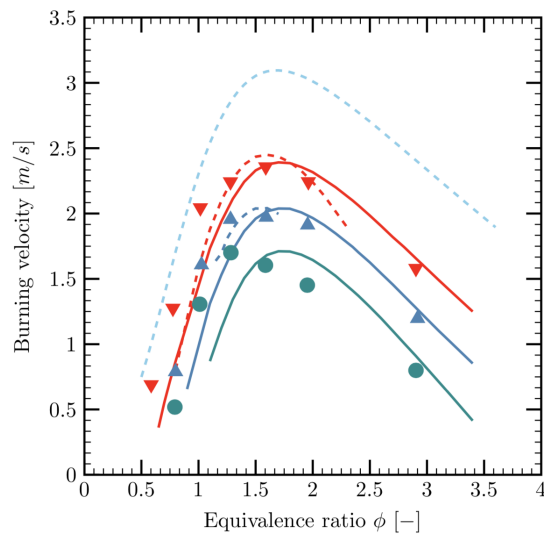
REFERENCES

- [1] Carlson LW, Knight RM, Henrie JO. Flame and detonation initiation and propagation in various hydrogen-air mixtures, with and without spray. *Atom Int Div Canoga Park Calif* 1973;6(6). AI-73-29.
- [2] Foissac A, Malet J, Vetrano MR, Buchlin JM, Mimouni S, Feuillebois F, et al. Droplet size and velocity measurements at the outlet of a hollow cone spray nozzle. *Atomization Sprays* 2011;21:893–905. <https://doi.org/10.1615/AtomizSpr.2012004171>.
- [3] Thomas GO, Brenton JR. An investigation of factors on relevance during explosion suppression by water sprays. *Health and safety executive-offshore technology report*; 1996.
- [4] Thomas GO. On the conditions required for explosion mitigation by water sprays. *Process Saf Environ Protect* 2000;78(5):339–54. <https://doi.org/10.1205/095758200530862>.
- [5] Zalosh RG, Bajpai SN. Water fog inerting of hydrogen-air mixtures. In: *Proc. 2nd Int Conf on the Impact of Hydrogen on Water Reactor Safety*. New Mexico, USA; 1982.
- [6] Boech LR, Kink A, Oezdin D, Hasslberger J, Sattelmayer T. Influence of water mist on flame acceleration, DDT and detonation in H₂-air mixtures. *Int J Hydrogen Energy* 2015;40(21):6995–7004. <https://doi.org/10.1016/j.ijhydene.2015.03.129>.
- [7] Ingram JM, Averill AF, Battersby PN, Holborn PG, Nolan PF. Suppression of hydrogen-oxygen-nitrogen explosions by fine water mist: part 1, burning velocity. *Int J Hydrogen Energy* 2012;37(24):19250–7. <https://doi.org/10.1016/j.ijhydene.2012.09.092>.
- [8] Holborn PG, Battersby P, Ingram JM, Averill AF, Nolan PF. Modelling the mitigation of lean hydrogen deflagrations in a vented cylindrical rig with water fog. *Int J Hydrogen Energy* 2012;37(20):15406–22. <https://doi.org/10.1016/j.ijhydene.2012.07.131>.
- [9] Holborn PG, Battersby P, Ingram JM, Averill AF, Nolan PF. Modelling the effect of water fog on the upper flammability limit of hydrogen-oxygen-nitrogen mixtures. *Int J Hydrogen Energy* 2013;38(16):6896–903. <https://doi.org/10.1016/j.ijhydene.2013.03.091>.
- [10] Wingerden KV, Wilkins B, Bakken J, Pedersen G. The influence of water sprays on gas explosions. Part 2: mitigation. *J Loss Prev Process Ind* 1995;8(2):61–70. [https://doi.org/10.1016/0950-4230\(95\)00007-N](https://doi.org/10.1016/0950-4230(95)00007-N).
- [11] Wingerden KV, Wilkins B. The influence of water sprays on gas explosions. Part 1: water-spray-generated turbulence. *J Loss Prev Process Ind* 1995;8(2):53–9. [https://doi.org/10.1016/0950-4230\(95\)00002-I](https://doi.org/10.1016/0950-4230(95)00002-I).
- [12] ISP-49 on Hydrogen Combustion. Nuclear Energy Agency; 2011. <https://www.oecd-nea.org/nsd/docs/2011/cnsi-r2011-9.pdf>.
- [13] Cheikhkravat H. Etude expérimentale de la combustion de l'hydrogène dans une atmosphère inflammable en présence de gouttes d'eau. PhD thesis. Université d'Orléans; 2009.
- [14] Gupta S, Schmidta E, Freitag M, Langrockb G, Funkeb F. Experimental investigations on containment spray performance under severe accident conditions. In: *The 8th European Review Meeting on Severe Accident Research -ERMSAR-2017*. Warsaw, Poland; 2017.
- [15] Efimenko AA, Dorofeev SB. CREBCOM code system for description of gaseous combustion. *J Loss Prev Process Ind* 2001;14(6):575–81. [https://doi.org/10.1016/S0950-4230\(01\)00049-3](https://doi.org/10.1016/S0950-4230(01)00049-3).
- [16] Kudriakov S, Beccantini A, Dabbene F, Paillere H, Studer E. Evaluation of different H₂-air combustion models for the simulation of large scale confined deflagrations. *J Energy Inst* 2006;79(4):200–6. <https://doi.org/10.1179/174602206X161392>.
- [17] Yang F, Kudriakov S, Studer E, Zou Z, Yu H. Numerical analysis of hydrogen risk related to severe accident scenario in chinese PWR. In: *24th international conference of nuclear engineering*; 2016. USA, <https://doi.org/10.1115/ICONE24-60671>.
- [18] Poinso T, Veynante D. *Theoretical and numerical combustion*. 3rd ed. RT Edwards Inc; 2005.
- [19] Baker WE, Cox PA, Westine PS, Kulesz JJ, Strehow RA. *Explosion hazards and evaluation*. 1st ed. Oxford, New York: Elsevier; 1983.
- [20] Abramzon B, Sirignano WA. Droplet vaporization model for spray combustion calculations. *Int J Heat Mass Tran* 1989;32(9):1605–18. [https://doi.org/10.1016/0017-9310\(89\)90043-4](https://doi.org/10.1016/0017-9310(89)90043-4).
- [21] Kuznetsov M, Matsukov I, Dorofeev S. Heat loss rates from hydrogen-air turbulent flames in tubes. *Combust Sci Technol* 2002;174(10):75–92. <https://doi.org/10.1080/00102200290021443>.
- [22] Cavazzuti M. *Optimization methods: from theory to design, scientific and technological aspects in mechanics*. Verlag Berlin Heidelberg: Springer; 2013.
- [23] Montgomery DC. *Design and analysis of experiments*. 5th ed. New York: John Wiley & Sons; 2000.
- [24] Beccantini A. Implementation of CREBCOM combustion model in TONUS code. *Technical Report CEA/DM2S*; 2001.
- [25] Kudriakov S, Dabbene F, Studer E, Beccantini A, Magnaud JP, Paillere H. The TONUS CFD code for hydrogen risk analysis: Physical models, numerical schemes and validation matrix. *Nucl Eng Des* 2008;238(3):551–65. <https://doi.org/10.1016/j.nucengdes.2007.02.048>.
- [26] NIST-JANAF thermochemical tables. *J Phys Chem Ref Data*.
- [27] Bradley D, Lau AKC, Lawes M, Smith FT. Flame stretch rate as a determinant of turbulent burning velocity. *Phil Trans Roy Soc Lond* 1992;338(1650):359–87. <https://doi.org/10.1098/rsta.1992.0012>.
- [28] Kuznetsov M, Alekseev V, Bezmelnitsyn A, Breitung W, Dorofeev S, Matsukov I, et al. Effect of obstacle geometry on behavior of turbulent flames. *Institut fur Kern-und Engergietechnik*; 1999.
- [29] Dorofeev SB. Hydrogen flames in tubes: critical run-up distances. *Int J Hydrogen Energy* 2009;34(14):5832–7. <https://doi.org/10.1016/j.ijhydene.2009.01.008>.
- [30] Silvestrini M, Genova B, Parisi G, Leon Trujillo FJ. Flame acceleration and DDT run-up distance for smooth and obstacles filled tubes. *J Loss Prevent Proc* 2008;21(5):555–62. <https://doi.org/10.1016/j.jlp.2008.05.002>.
- [31] Chaumeix N. Private communications.
- [32] Paolucci S. On the filtering of sound from the Navier–Stokes equations. 1982. NASA STI/Recon Technical Report N.
- [33] Abramzon B, Sazhin S. Droplet vaporization model in the presence of thermal radiation. *Int J Heat Mass Tran* 2005;48(9):1868–73. <https://doi.org/10.1016/j.ijheatmasstransfer.2004.11.017>.

Section 2: Numerical study on laminar flame velocity of hydrogen-air combustion under water spray effects

Highlights:

- Application of sprays for mitigation of Hydrogen explosion effects with deflagration waves.
- Development of a new predictive model for hydrogen/air laminar flame in presence of water droplets.
- Validation of the model using available experimental and numerical data.
- Physical analysis of the main factors influencing the laminar flame velocity in presence of water droplets.



Available online at www.sciencedirect.com

ScienceDirect

journal homepage: www.elsevier.com/locate/he

Numerical study on laminar flame velocity of hydrogen-air combustion under water spray effects

Guodong Gai^{a,*}, Sergey Kudriakov^a, Bernd Rogg^b, Abdellah Hadjadj^c, Etienne Studer^a, Olivier Thomine^a

^a DEN-DM2S-STMF, CEA, Université Paris-Saclay, France

^b Faculty of Mechanical Engineering, Ruhr-University, 44780 Bochum, Germany

^c Normandie University, INSA of Rouen, CNRS, CORIA, 76000 Rouen, France

ARTICLE INFO

Article history:

Received 19 December 2018

Received in revised form

27 March 2019

Accepted 22 April 2019

Available online 24 May 2019

Keywords:

Combustion

Laminar flame velocity

Water spray

Hydrogen safety

ABSTRACT

In the context of hydrogen safety and explosions in hydrogen-oxygen systems, numerical simulations of laminar, premixed, hydrogen/air flames propagating freely into a spray of liquid water are carried out. The effects on the flame velocity of hydrogen/air flames of droplet size, liquid-water volume fraction, and mixture composition are numerically investigated. In particular, an effective reduction of the flame velocity is shown to occur through the influence of water spray.

To complement and extend the numerical results and the only scarcely available experimental results, a “Laminar Flame Velocity under Droplet Evaporation Model” (LVDEM) based on an energy balance of the overall spray-flame system is developed and proposed. It is shown that the estimation of laminar flame velocities obtained using the LVDEM model generally agrees well with the experimental and numerical data.

© 2019 Hydrogen Energy Publications LLC. Published by Elsevier Ltd. All rights reserved.

Introduction

Spray systems are used as emergency devices for the mitigation of effects of explosions involving deflagration waves. Such systems are installed, for example, inside industrial buildings or on offshore facilities. Spray nozzles are also present inside some nuclear reactor buildings, and they are designed for preserving the containment integrity in case of a severe accident [1,2]. In case of an explosion, for a spray system to act successfully upon unwanted premixed-flame propagation, an understanding of, (i), the dynamics of the water spray exposed to the explosion-induced flow field, and, (ii), the ability of the spray to mitigate the explosion, is needed.

The droplets generated by industrial water-spray systems have a Sauter mean diameter of the order of 100 μm . For example, the spray systems usually installed on offshore platforms generate droplets of Sauter mean diameters in the range 200–700 μm [3] while those installed inside reactor buildings produce droplets of a Sauter mean diameter in the range 280–340 μm [1]. Numerous investigations have demonstrated [4–6] that, if certain conditions are met, large droplets might break up and cascade down into a large number of small droplets, i.e., droplets of a volume mean diameter of approximately 10 μm . These small droplets have the capability to evaporate fully, or almost fully, inside a laminar flame thus modifying the flame structure. Experimental results devoted to the interaction

* Corresponding author.

E-mail address: guodong.gai@cea.fr (G. Gai).

<https://doi.org/10.1016/j.ijhydene.2019.04.225>

0360-3199/© 2019 Hydrogen Energy Publications LLC. Published by Elsevier Ltd. All rights reserved.

Nomenclature

A_0	area of the burner mouth, m^2
A_f	area of the flame front, m^2
$C_{p,g}$	gas heat capacity at constant pressure, J/K
D	diameter of the droplet, μm
$D_{c,1}$	first critical droplet diameter, μm
$D_{c,2}$	second critical droplet diameter, μm
E_a	global activation energy, $kcal/mol$
l	latent heat of evaporation, kJ/kg
\dot{m}	evaporation rate of droplets, kg/s
n_{vol}	number of droplets per volume, m^{-3}
P_0	initial pressure, bar
r_0	initial radius of the droplet, μm
R	universal gas constant, J/K
S_L	laminar flame velocity, m/s
t_c	chemical reaction time, s
t_q	quenching time, s
T_0	initial temperature, K
v_0	average flow velocity in the burner, m/s
V_b	burnt gas velocity, m/s
V_f	fresh gas velocity, m/s
X_{H_2}	molar fraction of hydrogen, dimensionless
y	coordinates in the Cosilab code, mm
Y_{H_2}	mass fraction of hydrogen, dimensionless
α	liquid volumetric fraction, dimensionless
α_g	thermal diffusivity, m^2/s
δ	flame thickness, m
η	hydrogen-air mole ratio, dimensionless
λ	thermal conductivity, W/m
μ_g	dynamic viscosity of gas, $Pa \cdot s$
ρ	mass density, kg/m^3
ϕ	equivalence ratio, dimensionless
Nu	Nusselt number, dimensionless
Sc	Schmidt number, dimensionless
Pe	Peclet number, dimensionless
Pr	Prandtl number, dimensionless
Re	Reynolds number, dimensionless
Sh	Sherwood number, dimensionless
Le	Lewis number, dimensionless
B_M	Spalding mass transfer number, dimensionless
B_T	Spalding temperature transfer number, dimensionless
F	Correction factor in evaporation model, dimensionless
AIBC	Adiabatic IsoBaric complete Combustion
AICC	Adiabatic IsoChoric complete Combustion

of a laminar flame with small water droplets are scarce. Laboratory-scale tests reported in [7] showed that water droplets with diameters of the order of $10 \mu m$ have a similar influence on the structure of inert methane-air mixtures as water vapor. Early small scale experiments [8] as well as recent small and medium scale experiments using hydrogen [9,10] have revealed that sprays containing small-size droplets can be effective against premixed combustion. The experiments performed in [11] were devoted to hydrogen-air laminar flame velocity measurements in the presence of water mist.

In the context of spray-decelerated or spray-retarded deflagration waves that have originated from explosions, laminar-flame velocity – occasionally also termed “laminar flame speed” – is an important physical quantity. In particular, most of the combustion models used for simulation of large-scale, turbulent premixed combustion – see, e.g. [12–16], – contain the laminar-flame velocity as input parameter which has to be procured by some means such as suitable numerical simulation or suitable experiments. In the literature several correlations exist [17,18].

characterizing the flame speed of purely gaseous laminar hydrogen/air flames as a function of the mixture equivalence ratio. However, the small water droplets of a water spray modify the internal structure of the laminar flame and hence reduce its velocity. Thus a model is needed which takes into account the effect of water spray on flame structure and burning velocity.

In this paper, a “Laminar Flame Velocity under Droplet Evaporation Model” – abbreviated LVDEM – for hydrogen/air mixtures is proposed. This model has been constructed using the idea of Ballal and Lefebvre [19] who considered the energy balance inside the flame zone. The most crucial step is the model validation. For this purpose, the results obtained with the dedicated code Cosilab [20] and the experimental results of [11] are used. The results obtained using the LVDEM model generally agree well with the experimental and numerical data.

Phenomenology of computed flame structures

In this section, a description of the main phenomena related to the interaction of laminar hydrogen/air premixed, freely propagating flames with small droplets of a liquid water spray is given. The “small droplets” means droplets typically having a volume mean diameter of the order of $10 \mu m$ or smaller. For the numerical simulations, the Cosilab code [20] has been our main tool. This code can compute the internal structure of a laminar steady flame, with or without the presence of a liquid-water spray [21–23]. For completeness, the algorithm used in the code is shortly summarized in Appendix A. The main idea in using the code is to identify the mechanisms responsible for flame-droplets interactions, which will subsequently be used in our LVDEM model construction.

Specifically, two cases of hydrogen-air combustion are considered, i.e., cases without and cases with water spray. The purely gaseous cases, i.e., the cases without water spray serve as a reference for the two-phase cases with water spray.

In the numerical simulations with Cosilab, detailed chemistry, thermodynamics and molecular transport were taken into account. Specifically, the hydrogen/air system considered in the simulations comprised 10 chemical species which participate in 21 homogeneous reactions. For details of the reaction mechanism and the associated data [24], should be consulted.

The governing equations for a one-dimensional, flat, spray flame propagating at low Mach number can be found, e.g., in [25], Chaps. 1, 5 and 11. In particular, the dependent variables are discussed in [25] as well as the so-called *cold and hot boundaries* at either end of the computational domain together

with the suitable boundary conditions to be applied there. In addition, a detailed description of the so-called *burning rate-eigenvalue* can be found, in [25], Chap. 5, and how from that quantity in general the gaseous flow velocity throughout the flame is recovered and, especially, how the burning rate or flame speed is derived from it. Numerical solution methods for the problem are discussed, e.g., in [21,26]. Therefore, the governing equations and their solutions are not further discussed here.

At the cold flame boundary – which from the subsequent figures can be seen to be located at the left boundary of the computational domain – the gaseous composition of pure hydrogen and air is given in terms of the fuel-air equivalence ratio, ϕ , and the temperature, T_0 , is prescribed. Since the deflagration waves considered propagate in an open system at low Mach numbers, we adopt the low-Mach-number approximation [25] and take the pressure, P_0 , as spatially uniform and constant. For the cases with water spray, the spray is added at the cold boundary and is taken as mono-disperse with given droplet diameter D and given liquid volume-fraction α . At the cold boundary, zero slip-velocity between gas and liquid phase is assumed. Furthermore, liquid-load or volume fraction in this work are such that the case of a so-called *thin* spray is considered, that is effects of droplet break-up and agglomeration are neglected.

Interaction of the gaseous and the liquid flame principally occurs throughout the computational domain that, theoretically, extends from minus to plus infinity. Naturally, the computer-realized extension of the computational domain is finite, and its finite size has been chosen such that the boundary conditions are cleanly satisfied – for details see [25] – so that the flame speed or burning rate calculated is virtually independent of the size of the computational domain. As will be seen from the following figures, at the cold boundary the interaction of spray and gas consists essentially in spray evaporation. Some bit downstream, in the preheat zone where chemical reaction is negligible yet computed, the gas begins to accelerate due to the heat gained from the reaction zone by conduction against flow direction. In the reaction zone primarily the conduction and the reaction phenomena balance each other, while in the downstream recombination zone the dominating phenomena are the convection and the recombination reactions [25].

In this work, droplets are assumed to be totally evaporated when the ratio of local to initial droplet size has fallen below the computational roundoff-error – in the graphs below, the droplet diameter or radius is then virtually zero. For the flame structures to be presented in Figs. 1–5, the numerical values used for the conditions just described are summarized in Table 1.

The following comparison of the purely gaseous reference case, i.e., the case without water spray, and the two-phase case with water spray exposes details of the flame structures and also clearly shows the influence of the droplets on the overall flame structure. At this stage it is important to note that in Figs. 1–5 only a small portion of the actual computational domain is shown, namely that portion that is essential to visually capture the flame structures. In the

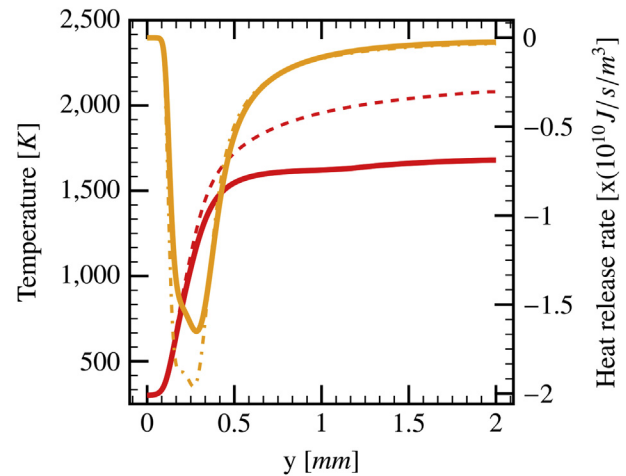


Fig. 1 – Profiles of temperature — and heat release rate —. Dashed lines: reference case without spray for temperature — and heat release rate —. Parameters are given in Table 1.

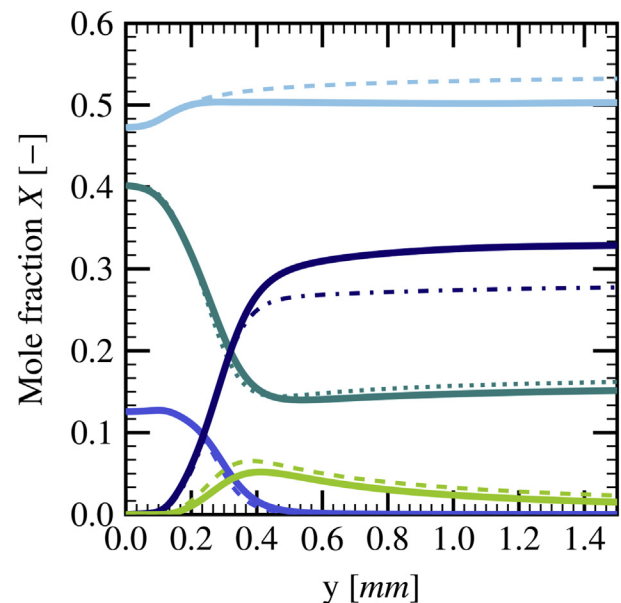


Fig. 2 – Profiles of the mole fractions of H_2 — O_2 —, H_2O —, H —, and N_2 —. Dashed lines: reference case without spray for H_2 —, O_2 —, H_2O —, H — and N_2 —. Parameters are given in Table 1.

computations the domain was substantially increased towards both the cold and the hot boundary to ensure that the boundary conditions were cleanly satisfied at either boundary to avoid the prediction of inaccurate flame structures and hence burning velocities, e.g., due to artificial heat losses to the cold boundary.

In the Figs. 1–5 subsequently presented and discussed, the results for the purely gaseous reference case without water spray are shown as dashed lines whereas the results

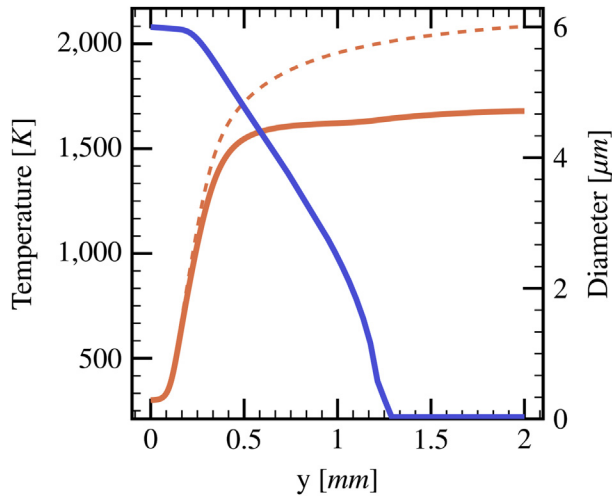


Fig. 3 – Spatial variation of droplet diameter — and gas-phase temperature —. Dashed lines: reference case without spray for the temperature ——. Parameters are given in Table 1.

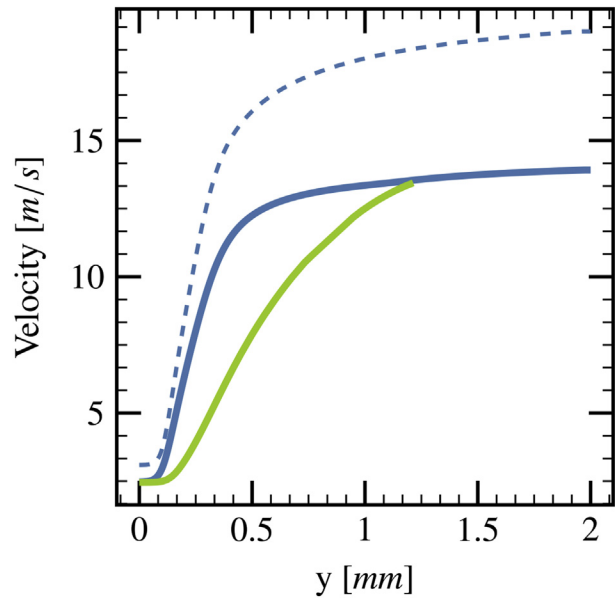


Fig. 5 – Spatial variation of gas-phase velocity — and liquid-phase velocity —. Dashed lines: reference case without spray for the gas velocity ——. Parameters are given in Table 1.

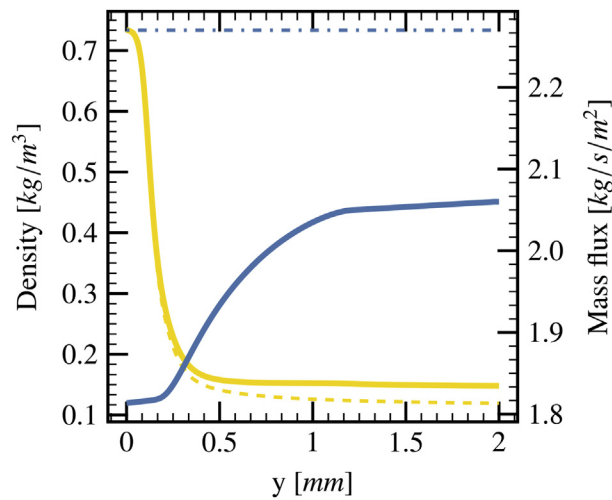


Fig. 4 – Spatial variation of gas density — and gas mass flux —. Dashed lines: reference case without spray for the gas density — and mass flux ——. Parameters are given in Table 1.

for the two-phase case with water spray are represented by solid lines.

Gasphase temperature

Shown in Fig. 1 are the profiles of temperature and volumetric heat release. A series of computations with differently sized domains of total length of up to 6 mm was carried out in order to satisfy cleanly both the upstream and downstream boundary conditions. The results shown here were obtained on a non-uniform, self-adaptive computational mesh with a

Table 1 – Parameters used with Cosilab to obtain the results shown in Figs. 1–5.					
case	ϕ	T_0 [K]	P_0 [bar]	D [μm]	α
gaseous	1.6	300	1.013	–	–
gas/spray	1.6	300	1.013	6	10^{-4}

mean cell size of $\Delta y = 12 \mu\text{m}$. The mesh is substantially denser ($\Delta y_{\min} = 1.1841 \mu\text{m}$) within the thin reaction zone and expands towards the cold and the hot boundary ($\Delta y_{\max} = 41.84 \mu\text{m}$), respectively.

From Fig. 1 it is seen that the temperature in the reaction zone and further downstream is drastically reduced as a consequence of the droplets evaporating in the flame – e.g., at $y = 2 \text{ mm}$ the temperature is reduced from approximately 2100 K to approximately 1700 K. Accordingly, the rate of temperature increase is reduced inside the flame as can be inferred from the difference of the heat-release-rate profiles. The cooling effect due to the presence of droplets is particularly important in both the preheat zone and the reaction zone – this is where evaporation is strongest as will also be seen below when considering the variation of droplet diameter through the flame.

At this stage is appropriate to define the “flame thickness” δ . Throughout this section, the flame thickness will be taken as the width of the preheat zone (in Fig. 1 for the spray flame ranging approximately from 0.1 mm to 0.4 mm, thus $\delta \approx 0.3 \text{ mm}$). Formally this definition of flame thickness can be expressed as the width of that spatial zone cut out by the intersection of the tangent to the temperature profile at that location in the flame where the temperature gradient is steepest with, (i), the spatially constant profile at cold

boundary temperature, (ii), the straight line with constant slope approximating the slightly rising temperature profile in the post-flame region. It is noted that this definition of flame thickness is popular but, of course, not unique.

In summary, one notes that in the presence of liquid water droplets the cooling effect through convective heat losses of the gasphase to the droplets and through evaporation reduce the maximal rate of heat release, thus leading to a lower gas temperature and hence burning velocity.

Species concentrations

Shown in Fig. 2 are profiles of selected species mole fractions through the flame.

The variation of the mole fraction of molecular nitrogen, N_2 , indicates that the total number of gas moles decreases during combustion accompanied by spray evaporation. Also, in the two-phase case, the increase of water steam through the flame is not only due to homogeneous chemical reaction but also to evaporation of liquid drops. The mole fraction of the hydrogen radical, H, increases, reaches its maximum at $y = 0.4 \text{ mm}$, and then decreases further downstream.

It can be noted that the evaporation rate increases when the reaction rates and hence gasphase temperature reach high levels. Beyond that, further downstream, the increase of the mole fraction of gaseous water, or water steam, is relatively slow.

Droplet diameter

Fig. 3 shows the variation of the droplet diameter through the flame together with the gasphase temperature profile. From the figure it can be seen that the droplets are not evaporating completely inside the preheat zone. Downstream of the preheat zone evaporation of the droplets continues, i.e., in the reaction zone and even in the post-flame region evaporation of droplets still has a certain influence on the flame propagation and hence burning velocity. Thus, when constructing the LVDEM model below, it will be necessary to estimate the amount of water evaporating inside the preheat zone (whose thickness corresponds to the flame thickness), which has a direct effect on the flame velocity.

One notices that the droplets rapid evaporation in the zone $0.2 \text{ mm} < y < 0.5 \text{ mm}$ is accompanied by considerable temperature reduction, compared to the reference case without spray. The droplet diameter decreases to approximately $3 \mu\text{m}$ at $y = 0.8 \text{ mm}$, but are considered totally evaporated only at $y = 1.3 \text{ mm}$.

Gasphase mass density and mass flux

Shown in Fig. 4 are the mass density and mass flux variation of the gas mixture during the combustion. For both the purely gaseous reference case and the two-phase case with water spray the gas gasphase mass density profiles are as expected on physical grounds: they simply express the gas expansion due to the heat released in the homogeneous chemical reactions. The gas mass flux profile of the reference case is

uniformly constant as enforced by overall mass conservation. On the other hand, the gasphase mass-flux profile of the two-phase case increases in flow direction due to the continuously gained water steam stemming from liquid-drop evaporation. It can be noted that, of course, the overall mass of liquid and gas is conserved throughout the flame. The mass flux in the two-phase case is lower than the pure gas combustion case, since the laminar flame velocity is reduced by the evaporation of the droplets.

Gasphase and droplet velocity

Finally, Fig. 5 shows the profiles of the velocities of gas and liquid through the flame. For the purely gaseous reference case the velocity profile is as expected, namely proportional to the reciprocal of mass density and roughly proportional to temperature. Also the two velocity profiles of the two-phase case show the expected behavior. In accordance with the model of a freely propagating one-dimensional flame, there is no slip between the phases at the cold boundary. Downstream of the cold boundary, the gasphase velocity then quickly increases due to the expansion of the gas. The droplets are dragged by the accelerating gas and hence are also accelerated, but due to their inertia they lag behind the gaseous fluid. This leads to the observed slip between the phases. Further downstream, when the droplets have become very small or have even vanished – see Fig. 3 –, the slip decreases, and at approximately $y = 1.2 \text{ mm}$ the liquid velocity catches up with the gasphase velocity. The droplets become easier to accelerate due to the evaporation. After $y = 1.25 \text{ mm}$, the droplets are totally evaporated. In the spray case, overall the gasphase velocity remains substantially lower than in the purely gaseous reference case because of the energy losses due to the droplets evaporation and the addition of steam.

The comparison of the two cases shows that the spray droplets effectively damp, or mitigate, the flame velocity. Specifically, in the cases of Fig. 5, the velocity of the burnt gas is reduced from approximately 18 m/s to approximately 14 m/s .

Burning velocity

Flame structures and hence laminar burning velocities for both the purely gaseous reference case and the two-phase case with water spray were computed for a wide range of conditions. The respective results will be presented and discussed below in the context of the LVDEM model.

Conclusions from the numerical results

First, from the numerical results presented so far, it can be concluded that droplets of small diameter greatly affect the internal flame structure in terms of temperature, species distribution and gas velocity profiles. Second, the following observation has been made relating to the importance of the amount of water evaporating inside the flame zone: in the present case ($D = 6 \mu\text{m}$), the droplets do not evaporate

completely inside the flame preheat zone which has a thickness of the order of the flame thickness; hence it would be a mistake to assume in a model complete droplet evaporation in that zone. Rather, evaporation takes place in a zone somewhat longer than the preheat zone, i.e., it extends over a region that is wider than the flame thickness.

LVDEM model for S_L under droplets evaporation

In this section, the LVDEM numerical model of laminar flame velocity based on the energy balance is described. The comparison between the LVDEM model and the results of the Cosilab code is presented. Experimental results are used to validate the two methods.

Laminar flame velocity under droplet evaporation model

The aim is to construct a model in which several phenomena can affect the laminar flame propagation: 1) the evaporation of the droplets will absorb energy released from the chemical reaction; 2) the steam evaporated from the droplets will mix with the remaining gas and change its thermal properties. Ballal [19] has proposed a method to estimate the laminar flame velocity for the evaporation and combustion of fuel droplets using the energy balance inside the flame. The similar idea can be used for the estimation of the laminar flame velocity in this study. The main assumption of the model is that the quench time of the reaction zone is equal to the chemical reaction time, i.e.

$$t_q = t_c \quad (1)$$

The quench time can be obtained as the ratio of the excess enthalpy of the reaction zone to the rate of heat loss by conduction to the fresh mixture.

$$t_q = \frac{c_{p,g}\rho_g\Delta T_{ad}\delta A - l\dot{m}t_c n_{vol}\delta A}{\lambda_g(\Delta T_{red}/\delta)A} \quad (2)$$

Where the $\Delta T_{ad} = T_{AIBC} - T_0$, ΔT_{red} is the temperature reduction due to the evaporation of droplets; δ is the thickness of the flame and A is the area of a considered surface; t_c is chemical reaction time, n_{vol} is the number density of the droplets in the mixture; l is the latent heat of the evaporation; $c_{p,g}$ is the gas heat capacity under constant pressure, λ_g is the gas heat conductivity.

Hence

$$t_q = \frac{(c_{p,g}\rho_g\Delta T_{ad} - l\dot{m}t_c n_{vol})\delta^2}{\lambda_g\Delta T_{red}} \quad (3)$$

Here the flame thickness can be estimated with the laminar flame velocity without spray effects $S_{L,0}$:

$$\delta_L = \frac{\alpha_g}{S_{L,0}} \quad (4)$$

with α_g being the thermal diffusivity of burnt gas mixture, the chemical reaction time of a premixed mixture is given by:

$$t_c = \frac{\delta_L}{S_{L,0}} = \frac{\alpha_g}{S_{L,0}^2} \quad (5)$$

The simulation results of the Cosilab code [20] can be used

for the estimation of $S_{L,0}$. The correlation given by Konnov [18] has also been consulted for the variation of $S_{L,0}$ [m/s] as a function of X_{H_2} [vol.%]:

$$S_{L,0} = -1.55236 \times 10^{-9} X_{H_2}^6 + 3.49519 \times 10^{-7} X_{H_2}^5 - 2.82975 \times 10^{-5} X_{H_2}^4 + 9.35480 \times 10^{-4} X_{H_2}^3 - 9.97510 \times 10^{-3} X_{H_2}^2 + 5.00120 \times 10^{-2} X_{H_2} - 8.32830 \times 10^{-2}. \quad (6)$$

The comparison between these two models is given in Fig. 6, where the correlation of Dahoe [17] is also given for comparison.

Since mixtures diluted by steam have lower burnt gas temperatures than undiluted ones, Koroll has proposed a correlation that takes into account the change of thermal diffusivity due to dilution [27]:

$$S_{L,w} = S_{L,0} \cdot \sqrt{\frac{\alpha_{dil}}{\alpha_{pure}}} \left(1 - \frac{X_{dil}}{X_{dil,flame}}\right) \quad (7)$$

Where α_{dil} is the thermal diffusivity of the diluted mixture, α_{pure} is the thermal diffusivity of undiluted mixture, X_{dil} stands for the molar fraction of the water steam, and $X_{dil,flame}$ is the maximal molar fraction of steam under which the flame can propagate. This limit water loads can be approximated by the correlation:

$$X_{dil,flame}(\eta) = 0.507 - 0.2443 \cdot \ln(\eta) - 0.185 \cdot [\ln(\eta)]^2 \quad (8)$$

for $0.1 \leq \eta \leq 3$,

Where $\eta = X_{H_2}/X_{air}$ is the hydrogen-air mole ratio. The validation of this correlation can be referred to [27]. The effect of presence of water steam on the hydrogen air combustion has also been discussed in a more recent work of [28], which presents another correlation for $S_{L,w}$.

Substituting the equations (3) and (5) into the equation (1) gives:

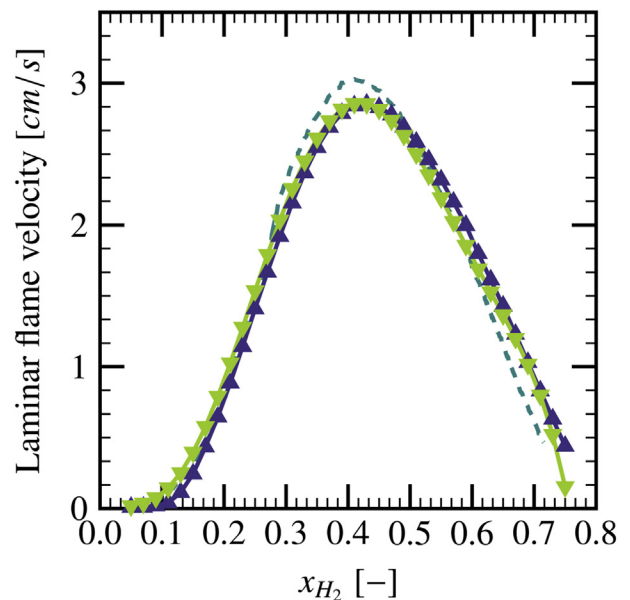


Fig. 6 – Laminar flame velocity evolution for different hydrogen composition, comparison between three models: Dahoe ---, the Cosilab code —▲ and Konnov —▲.

$$\delta = \left[\frac{\lambda_g \Delta T_{red}}{c_{p,g} \rho_g \Delta T_{ad} - \dot{m} n_{vol} \left(\frac{\alpha_g}{S_{L,0}^2} \right) \frac{\alpha_g}{S_{L,0}^2}} \right]^{0.5} \quad (9)$$

and by applying equation (4), one can have:

$$S_L = \alpha_g \left[\frac{\lambda_g \Delta T_{red}}{c_{p,g} \rho_g \Delta T_{ad} - \dot{m} n_{vol} \left(\frac{\alpha_g}{S_{L,0}^2} \right) \frac{\alpha_g}{S_{L,0}^2}} \right]^{-0.5} \quad (10)$$

The equation (10) is deduced from the energy balance, by taking into consideration of the evaporation process. Combining the equations (7) and (10), the laminar flame velocity can be approximated by:

$$S_L = \alpha_g \sqrt{\frac{\alpha_{dil}}{\alpha_{pure}} \left(1 - \frac{X_{dil}}{X_{dil,flame}} \right)} \left[\frac{\lambda_g \Delta T_{red}}{c_{p,g} \rho_g \Delta T_{ad} - \dot{m} n_{vol} \left(\frac{\alpha_g}{S_{L,0}^2} \right) \frac{\alpha_g}{S_{L,0}^2}} \right]^{-0.5} \quad (11)$$

The mass evaporation rate for a droplet \dot{m} can be computed by using the works of [29,30] as discussed in the above section.

Since the model of [29] gives the mass evaporation rate of one droplet as a function of time at a given temperature, one has to estimate the evaporated mass of water droplets during the combustion within the flame thickness. As discussed before, the evaporation rate depends on the droplet diameter and the ambient temperature. Thus, its value changes all along the droplet evolution inside the hot gas mixture. The way to estimate the average mass evaporation rate is presented in the next subsection (point 5).

Solution algorithm

Consider now the step-by-step procedure to determine the laminar flame velocity S_L under the influence of water droplets. Assume that the initial temperature T_{ini} and pressure P_{ini} are known. The free propagating flame assumption is kept in this section.

1. Calculate the initial molar fraction X_{0,H_2} , X_{0,O_2} , X_{0,N_2} and X_{0,H_2O} ;
2. Calculate the temperature corresponding to AIBC¹ combustion T_{ad} without water spray effects;
3. Calculate the laminar flame velocity without water spray effects $S_{L,0}$ using the equation (6) as a reference flame velocity. This flame velocity can be replaced by the reference value given by the Cosilab code;
4. Calculate the average physical properties $\bar{c}_{p,g}$, $\bar{\lambda}_g$ in the gas-liquid interaction film, using the “1/3 rule” [29]:

$$\bar{T} = T_s + \frac{1}{3}(T_\infty - T_s) \quad (12)$$

$$\bar{Y} = Y_s + \frac{1}{3}(Y_\infty - Y_s) \quad (13)$$

Where the subscript s denotes the surface properties of the

droplet and ∞ stands for the properties of the gasphase (for example, the AIBC temperature);

5. Calculate the mean evaporation rate \dot{m} , as well as the latent heat l . According to the model of [29], the evaporation rate is calculated by assuming a constant ambient temperature. This is not the case inside the flame thickness. By definition, the gas temperature varies from the unburnt gas to the burnt gas. Moreover, the evaporation can affect the temperature variation within the flame thickness. Thus, one can calculate the evaporation rate under two AICC² temperatures, T_{AICC} and $\frac{1}{2}T_{AICC}$, and then take the average of $\dot{m}_{T_{AICC}}$ and $\dot{m}_{\frac{1}{2}T_{AICC}}$.
6. Calculate the thermal diffusivity within the flame thickness:

$$\alpha_g = \frac{\lambda_u}{c_{p,u} \rho_u} \frac{\rho_u}{\rho_b} = \frac{\lambda_u}{c_{p,u} \rho_b} \quad (14)$$

This step is crucial in the algorithm, and these temperature values have been chosen by trial and error, in order to minimize the difference between the present results and the experimental results. Fig. 7 shows the variation of evaporation rate evolution for different ambient temperatures. Note that the temperatures corresponding to AIBC (1547 K) and AICC (1885 K) combustion are taken into consideration, as well as two temperatures (900 K and 1200 K) for comparison. It can be seen that the evaporation rate strongly depends on the ambient temperature of the gasphase. One can also estimate that the mean evaporation rate of one single droplet during the combustion process is of the order of magnitude of $\mathcal{O}(10^{-8})$ kg/s for droplet diameter $D = 350 \mu m$ as presented in Fig. 7. The evaporation rate of the spray is calculated by multiplying the single droplet evaporation rate with the number density of droplets n_{vol} . The effect of the spray evaporation is considered to be a superposition of all the single droplets. Where λ_u , ρ_u and $c_{p,u}$ are respectively the thermal conductivity, density and heat capacity of the fresh gas inside the flame thickness, ρ_b is the density of the burnt gas. Inspired by [31], the correction factor ρ_u / ρ_b is introduced in order to better estimate α_g .

7. Estimate the flame thickness and the chemical reaction time

$$\delta_L = \frac{\alpha_g}{S_{L,0}}, \quad t_c = \frac{\alpha_g}{S_{L,0}^2} \quad (15)$$

which is used to quantify the mass of water evaporated inside the flame thickness:

$$\alpha_w = \frac{t_c \cdot \dot{m} n_{vol}}{\rho_w} \quad (16)$$

Where ρ_w is the density of water droplets, n_{vol} is the number of droplets in unit volume under liquid volume fraction α and droplet diameter D :

$$n_{vol} = \frac{6\alpha}{\pi D^3} \quad (17)$$

¹ Adiabatic IsoBaric complete Combustion.

² Adiabatic IsoChoric complete Combustion.

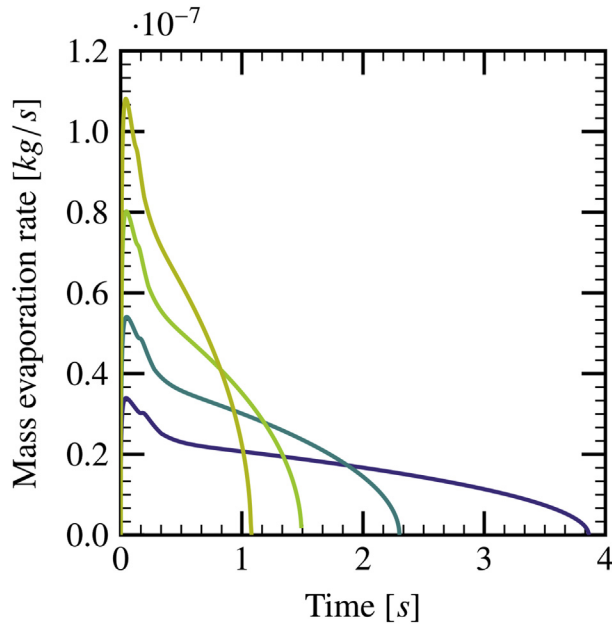


Fig. 7 – Influence of ambient temperature on the mass evaporation rate: 900 K —, 1200 K —, $T^{AIBC} = 1547$ K — and $T^{AICC} = 1885$ K —, droplet diameter $D = 350$ μm .

Here, an estimation for the flame thickness is taken and thus the real mass evaporated within the flame thickness, can be characterized by α_w ;

8. Calculate the reduced gas temperature T_{red} after combustion in the presence of the water droplets of volumetric fraction α_w evaporated using a lumped-parameter subroutine;
9. Calculate the thermal diffusivity of the pure gas mixture under initial temperature T_{ini} , α_{pure} (X_{O,H_2} , X_{O,O_2} , X_{O,N_2} , X_{O,H_2O}), as well the thermal diffusivity after dilution α_{dil} (X_{a,H_2} , X_{a,O_2} , X_{a,N_2} , X_{a,H_2O}); calculate the limit molar fraction of steam for the propagation of flame $X_{dil,flame}$;
10. Calculate temperature differences

$$\Delta T_{ad} = T_{ad} - T_{ini} \quad (18)$$

$$\Delta T_{red} = T_{red} - T_{ini} \quad (19)$$

11. Calculate the laminar flame velocity S_L taking into account the dilution effect of the water steam generated via droplet evaporation [27]:

$$S_L = \alpha_g \sqrt{\frac{\alpha_{dil}}{\alpha_{pure}}} \left(1 - \frac{X_{dil}}{X_{dil,flame}} \right) \left[\frac{\lambda_u \Delta T_{red}}{c_{p,u} \rho_b \Delta T_{ad} - \ln n_{vol} \left(\alpha_g / S_{L,0}^2 \right) \frac{\alpha_g}{S_{L,0}^2}} \right]^{-0.5} \quad (20)$$

Model validation

The LVDEM model is validated using a) the results of the Cosilab code (see Appendix A) and b) the experimental results of [11]. Here, a briefly description of the experimental facility and related results of [11] is given for completeness.

Experimental Results [11].

A work program has been undertaken to investigate the effects of fine water mists on the laminar flame velocity of the hydrogen-air explosion. The objective is to provide more specific experimental results on the mitigation effects of small water droplets on hydrogen-air explosions.

The experimental apparatus which is shown in the Fig. 8 contains a converging nozzle burner and a mist generation system. With a flow-straightener, the authors pay special attention to the flow rates of the gas and fog mixture in order to have a straight-side cone of flame at the burner nozzle. A large vent has been used to mitigate the effects of the blow-backs and a small mixing fan was used to homogenize the distribution of the water mists. To minimize the flame stretch, the authors have set conditions so that flame heights were between one and three times the nozzle diameter. The laminar flame velocity is calculated from the schlieren image by using the formula [32]:

$$S_L = \frac{A_0}{A_f} \cdot v_0 \quad (21)$$

Where A_0 is the area of burner mouth, A_f is the area of the flame front and v_0 is average flow velocity in the burner mouth. The commercial ultrasonic units are used to produce the water mist, which are positioned beneath a column of water, below the surface. The high frequency vibration of the piezoelectric discs generates at the water surface a “fountain” comprised of water droplets of various sizes.

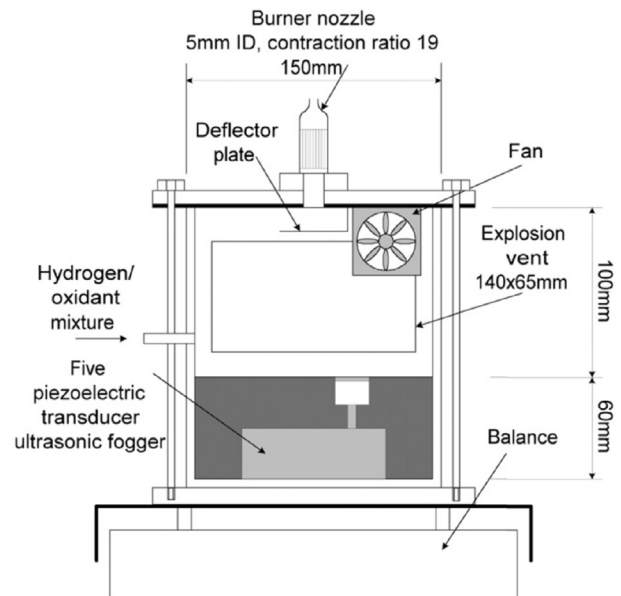


Fig. 8 – The burner and mist generation system scanned from [11].

The authors have performed a series of experiments for different equivalence ratios, taken between 0.6 and 3, with water mist volume fraction varying from 0 to 2.50×10^{-4} . The droplets of water mists considered in these experiments are of volume mean diameter $6 \mu\text{m}$.

From the Fig. 9(b), it can be seen that the presence of fine water mists can greatly reduce the burning velocity over a wide range of equivalence ratio for the hydrogen-air mixtures. The schlieren image shows that the flame cone becomes thicker as the droplets number density increases which indicates an increasing flame instability. These experimental results are used in this study for the validation of the LVDEM models for laminar flame velocity.

It has to be mentioned that the authors noticed a poor quality of the flame “cone”, particularly at higher mist concentrations and for lean mixtures ($0.6 < \phi < 0.9$), as shown in the Fig. 9(a). This makes it difficult to estimate the flame surface A_f , meaning that there is an uncertainty corresponding to lean mixture ($\phi < 1$). This uncertainty, unfortunately, has not been estimated during the experiments [33].

Effect of the mass density of water droplets

The evaporation of the water droplets within the flame thickness has a mitigation effect on the flame propagation, especially for small droplets. By neglecting the turbulence generated by the big droplets, the mitigation effect increases with the density of water droplets. The results of the model can be compared to the calculation of the Cosilab code [20]. To reduce errors, the reference values of $S_{L,0}$ in the Cosilab code has been used in the LVDEM model. The comparison between the results of the LVDEM model with the results given by the Cosilab code is given for different liquid volume fractions from $\alpha = 1 \times 10^{-5}$ to $\alpha = 1 \times 10^{-4}$.

The Fig. 10 shows the laminar velocities calculated by the LVDEM model for volume fraction from $\alpha = 1 \times 10^{-5}$ to $\alpha = 8 \times 10^{-5}$. The results for the same combustion using the Cosilab code are given. It can be seen that both methods show a reduction of the laminar flame velocity under spray effects with respect to the pure combustion case. The flame velocity

calculated by the model compares well with the results of the Cosilab code for a wide range of equivalence ratios. For $\alpha = 1 \times 10^{-5}$, the maximal relative error is 1.0%.

However, one can notice a rising difference between the two methods with the increase of droplets number density. Especially for the rich compositions, the LVDEM model gives higher burning velocities than the Cosilab code, especially for $\phi > 2$.

To explain the difference between the two methods, one uses the experimental results of [11] for the validation of the LVDEM model. The authors have investigated the effect of different volume fractions of the liquid phase (1.0×10^{-4} , 1.5×10^{-4} and 2.0×10^{-4} etc.) with mean droplets diameter $D = 6 \mu\text{m}$ on the hydrogen-air combustion. The reference values for the laminar flame velocity without spray effect are presented as well. A comparison between the simulation of the Cosilab code and the LVDEM model is given in Fig. 11.

It can be noted that the water spray has an important mitigation effect on the laminar flame velocity as the quantity of spray increases. Under spray density of 2.0×10^{-4} , the laminar flame velocity can be decreased from 3.0 m/s to 1.7 m/s for the equivalence ratio $\phi = 1.7$.

Both the results of the Cosilab code and those of the LVDEM model can not perfectly fit the experimental results. For the lean mixture ($\phi < 1$), the LVDEM model as well as the Cosilab code provides lower values for the laminar flame velocity. In [11] the authors emphasize high uncertainty for this part of the measurement.

Comparing the results given by the LVDEM model and that of the Cosilab code, similar behaviors for the equivalence ratios $\phi < 1.5$ can be noticed. For higher equivalence ratios, no sufficient number of data corresponding to the Cosilab code are available due to numerical instabilities of the calculations. Nevertheless, the burning velocity evolution tendency shows that the Cosilab code has underestimated the burning velocity for ($\phi > 2.0$). In contrast, all the estimations for the laminar flame velocity of the LVDEM model are in the vicinity of the experimental results. The most possible reason for this difference comes from the modeling of the evaporation rate. It can be noted that the flammability limits

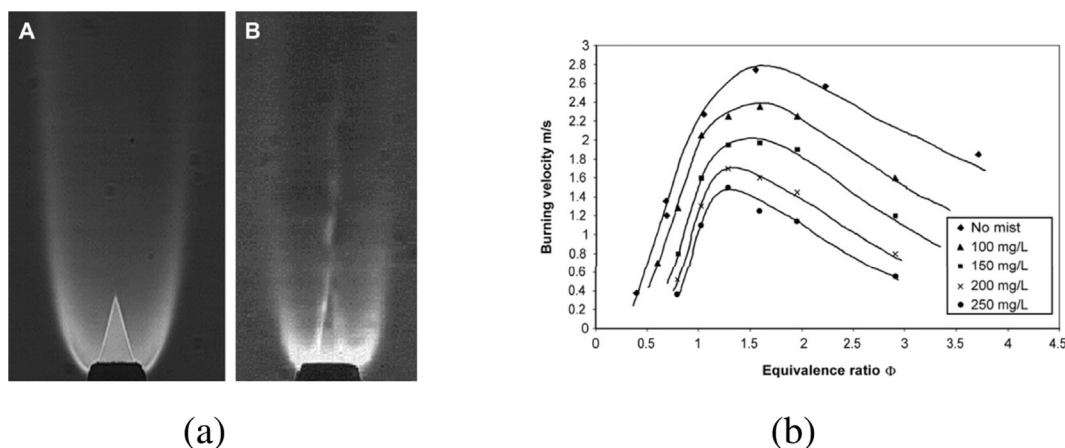


Fig. 9 – (a) images of hydrogen flame “cones” (A) for typical stable rich mixture and (B) for $\phi = 0.6$, with 1.43×10^{-4} of water mist; (b) Variation of burning velocity with equivalence ratio, hydrogen-air mixture [11].

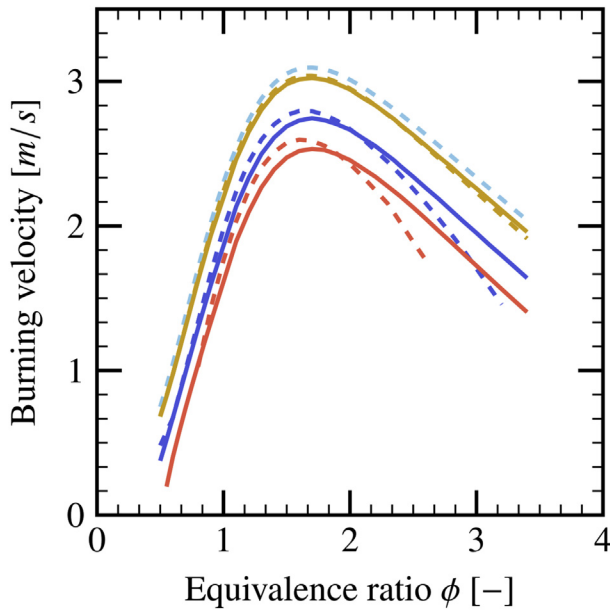


Fig. 10 – Laminar flame velocity for liquid volume fraction $\alpha = 1 \times 10^{-5}$ as a function of equivalence ratio. The no spray reference case in the Cosilab code ---, the calculation results of the Cosilab code with spray for volumic fraction $\alpha = 1 \times 10^{-5}$ ---, $\alpha = 5 \times 10^{-5}$ ---, $\alpha = 8 \times 10^{-5}$ --- and the results of LVDEM model for respectively $\alpha = 1 \times 10^{-5}$ —, $\alpha = 5 \times 10^{-5}$ —, $\alpha = 8 \times 10^{-5}$ —; $D = 6 \mu\text{m}$.

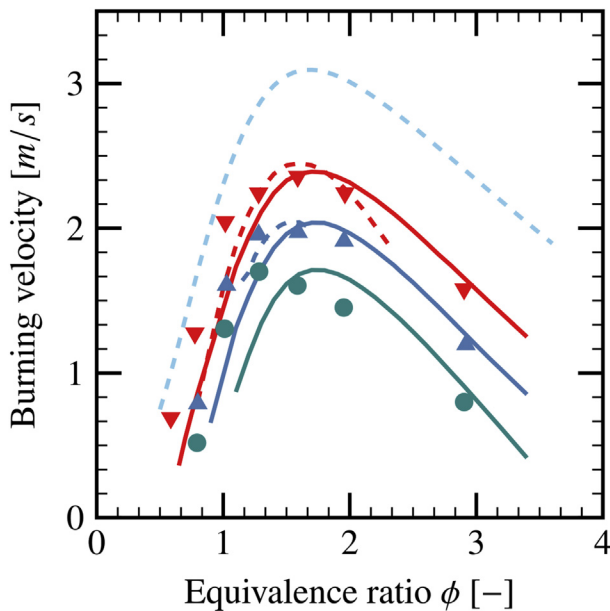


Fig. 11 – Laminar flame velocity as a function of equivalence ratio. The no spray reference case in the Cosilab code ---, the calculation results of the Cosilab code with spray of 1.0×10^{-4} ---, 1.5×10^{-4} ---; the results of laminar velocity model of spray 1.0×10^{-4} —, 1.5×10^{-4} — and 2.0×10^{-4} —; the experimental results are given in points: spray density 1.0×10^{-4} ▽, 1.5×10^{-4} ▲ and 2.0×10^{-4} ●.

are larger in the LVDEM model. In the Cosilab code for water volume fraction 1.0×10^{-4} , the calculation can not converge for the initial gas mixture of equivalence ratio $\phi > 2$. With the LVDEM model, one can calculate the laminar velocity for equivalence ratio up to $\phi = 3.4$.

The combustion limits are important parameters in study of ignition and quenching of the premixed flames. The problem of flammability limits of a combustible gaseous mixture is discussed thoroughly by [34]. The simplified theory [25] states that the flame propagation will not be sustained, or the mixture is not flammable, if:

$$T_f < T_{ad} \left(\frac{RT_{ad}}{E_a} + 1 \right)^{-1} \quad (22)$$

Where T_f is the burnt gas temperature in the presence of heat loss, T_{ad} is the adiabatic burnt gas temperature, R is the universal gas constant and E_a is the global activation energy of the reaction. The Fig. 12 shows the combustion limit temperatures, see Equation (22), for two different global activation energies. The temperature evolution inside the flame thickness for hydrogen-air mixtures in the presence of the water mists is given in solid lines (water volume fractions 1.0×10^{-4} , 1.5×10^{-4} and 2.0×10^{-4}). According to the equation (22), the mixture is flammable if the temperature is higher than the dashed line.

The global activation energy E_a varies for different H_2 -air compositions [35,36]. The values of E_a suggested by a recent work of [37] have been used in Equation (22). One can see that the combustion limits obtained using the LVDEM model are close to the theoretical combustion limits. Moreover, the experiments of [38] provide combustion limits for hydrogen/air/steam mixtures with $X_{H_2O} = 12\%$ and $0.1 < X_{H_2} < 0.65$. The flammable range estimated by LVDEM is narrower since, in our case, not only the presence of steam but also the evaporation process plays an important role on the flame propagation.

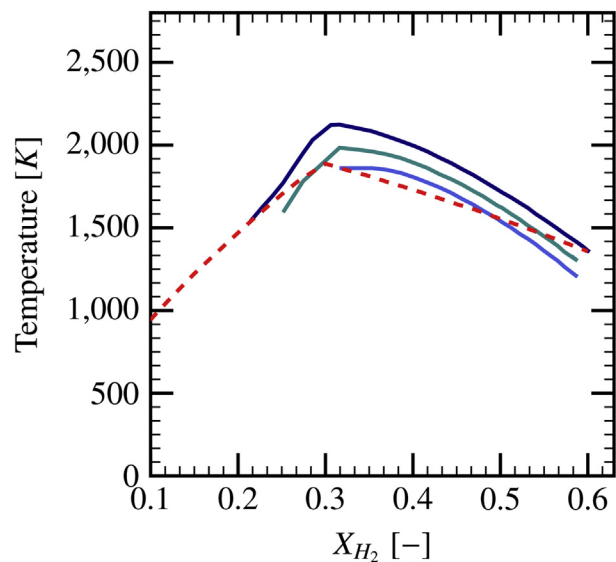


Fig. 12 – Combustion limits for different H_2 -air compositions ---; the temperature evolutions given by the laminar flame model are given for spray volume fractions: 1.0×10^{-4} —, 1.5×10^{-4} — and 2.0×10^{-4} —.

Flame thickness

Flame thickness is related to the combustion intensity and the flame propagation velocity. According to [31], the most accurate measurement of the flame thickness can be obtained by using the temperature profile. Unfortunately, one can not estimate the flame thickness before knowing the temperature profile of the flame propagation for the hydrogen-air mixtures in the presence of water droplets.

From the Fig. 13 and Fig. 14, it can be seen that the flame thickness obtained by the LVDEM model behaves like a parabolic function with respect to the equivalence ratio. The minimum of the flame thickness corresponds to the maximal value of the flame velocity. It can be noted that the flame thickness increases with the density of the water spray. Moreover, the Fig. 14 shows that the large water density has bigger influence on the lean and rich hydrogen-air mixture. This is due to the fact that the larger thickness of these compositions leads to a more evaporation time and thus a more important influence on the combustion process. The comparison between the LVDEM model and the results of the Cosilab code, obtained for $D = 6 \mu\text{m}$ using temperature profiles, shows that the flame thickness estimation has the same order of magnitude. The low combustion limits given by LVDEM model increases with higher droplets volume fraction α . This is due to the increase evaporation rate of the droplets of high volume fraction, which takes in the energy necessary to maintain the combustion for lean mixtures.

The effects of variation of droplets diameter on the flame thickness are given in Fig. 15. It can be seen that the increase of the droplets diameter while keeping α constant leads to the decrease of the flame thickness. In the other words, it can be deduced that the smaller droplets have more important effects on the flame behavior as the droplets surface area increases. The evolution of flame thickness does not vary for droplets of diameter bigger than $20 \mu\text{m}$; the two curves corresponding to $20 \mu\text{m}$ and $40 \mu\text{m}$ are very similar.

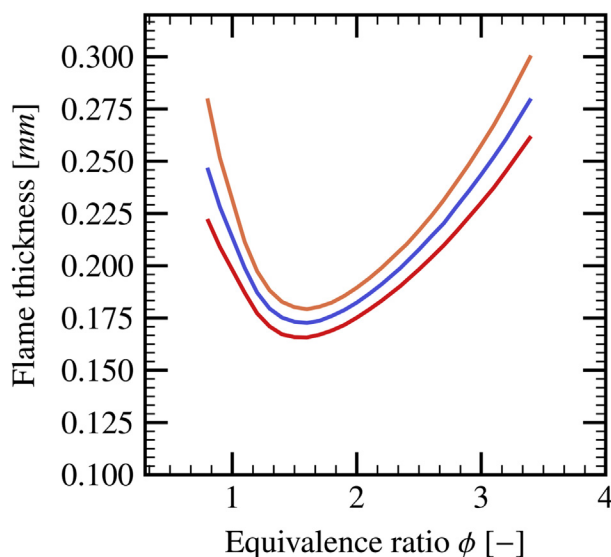


Fig. 13 – Flame thickness evolution as a function of equivalence ratio for different water fraction volumetric: $\alpha = 1 \times 10^{-5}$ —, $\alpha = 5 \times 10^{-5}$ — and $\alpha = 8 \times 10^{-5}$ —.

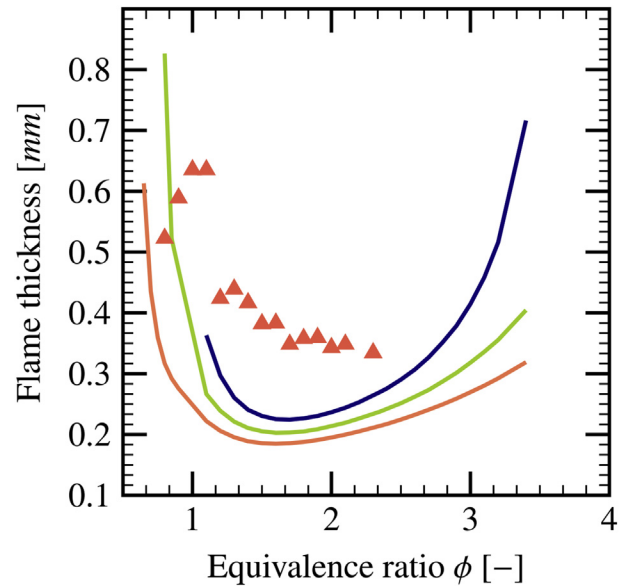


Fig. 14 – Flame thickness evolution as a function of equivalence ratio for different water density on fraction volumetric: $\alpha = 1 \times 10^{-4}$ —, $\alpha = 1.5 \times 10^{-4}$ — and $\alpha = 2 \times 10^{-4}$ —; the results of Cosilab \blacktriangle for $\alpha = 1 \times 10^{-4}$ is given for comparison.

Evaporation rate

During the flame propagation, the presence of droplets can affect the flame thickness and thus flame velocity mainly due to the evaporation within the flame thickness. The evaporation can absorb energy released from the chemical reaction thus leading to a lower burnt gas temperature. However, the evaporation rate depends on the temperature inside the flame thickness. As a consequence, these two phenomena are

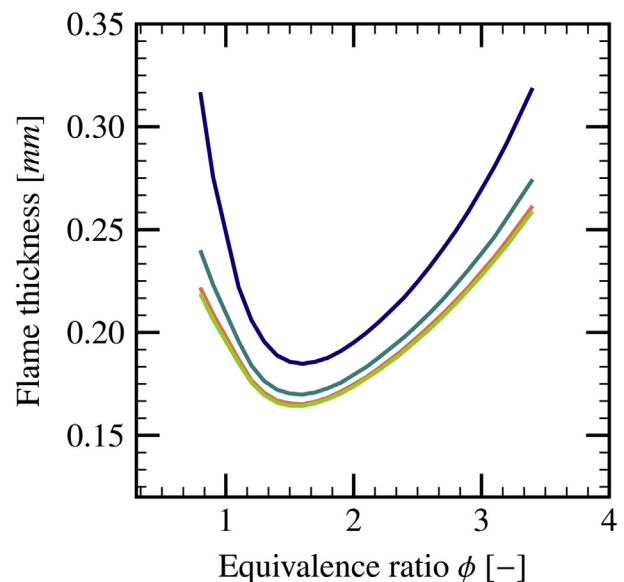


Fig. 15 – Flame thickness evolution as a function of equivalence ratio for different droplet diameters: $6 \mu\text{m}$ —, $10 \mu\text{m}$ —, $20 \mu\text{m}$ —, $40 \mu\text{m}$ —, $\alpha = 1 \times 10^{-4}$.

coupled. Determination of the evaporation rate is very important for the estimation of the laminar flame velocity.

First, the evaporation during the combustion of one single droplet is investigated using the LVDEM model. The Fig. 16 shows the mass evaporation rate of a single droplet as a function of equivalence ratio. In the LVDEM model, a maximal evaporation rate corresponding to the stoichiometric mixture, $\phi = 1$. Away from the stoichiometry, the evaporation rate decreases as a result of the decrease of combustion temperature. It can be noted that the evaporation rate increases with the droplet diameter for a fixed volume fraction α , since a bigger droplet has a larger surface for mass and energy exchange with the gasphase.

The Fig. 17 shows the overall evaporation rate of a droplet cloud during the combustion process. In order to highlight the effect of diameter variation, the volume fraction of the liquid phase is fixed as $\alpha = 1 \times 10^{-4}$ for these calculations. It can be noted that the effect of diameter variation on the overall evaporation rate is inverse compared to the single droplet evaporation rate. More precisely, the overall evaporation rate decreases with the increase of the droplet diameter for the same liquid volume fraction. This is due to the fact that, for a fixed volume fraction the liquid-gas interface diminishes with increasing droplet diameter. Thus, it can also be noted from the Fig. 18 that the flame velocity increases with bigger droplet diameters.

Effect of droplet diameter

During the combustion process, droplet diameter is one of the most important parameters affecting the evaporation rate. It has been noted that small droplets are easier to evaporate

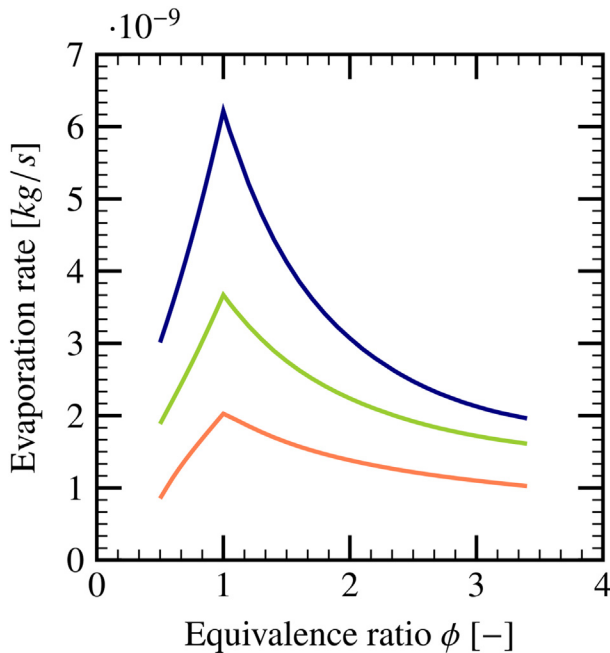


Fig. 16 – Evaporation rate of a single droplet as a function of equivalence ratio for different droplet diameters: 10 μm —, 20 μm —, 40 μm —, $\alpha = 1 \times 10^{-4}$.

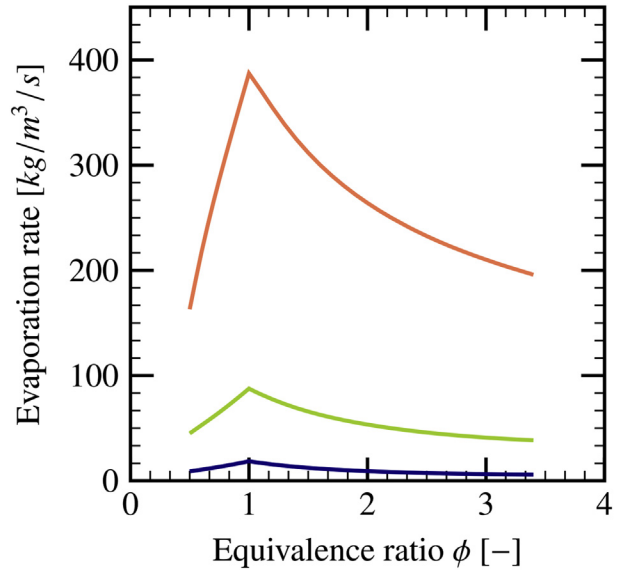


Fig. 17 – Evaporation rate of all droplets as a function of equivalence ratio for different droplet diameters: 10 μm —, 20 μm —, 40 μm —, $\alpha = 1 \times 10^{-4}$.

under high temperature, while for the large droplets, it takes more time to evaporate the whole liquid phase, thus leading to a lower evaporation rate.

Under the same volumetric fraction of the liquid phase, the droplet diameter has an important influence on the flame velocity. From the Fig. 16, one can see that the bigger droplet

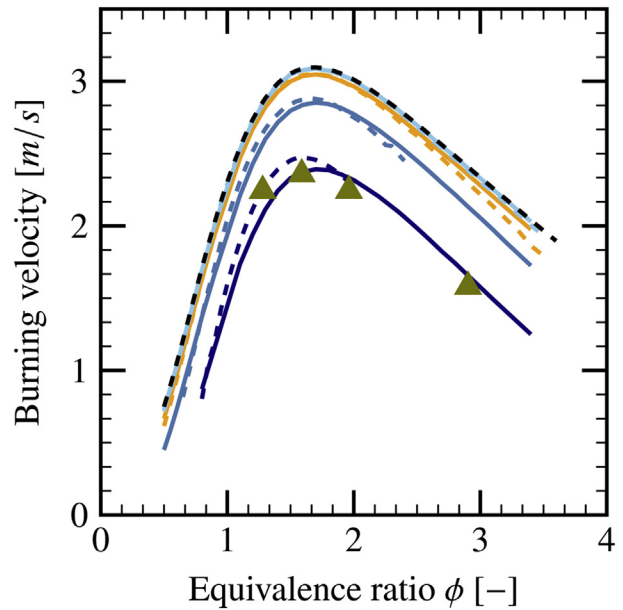


Fig. 18 – Evolution of laminar flame velocity as a function of equivalence ratio for different droplet diameters; comparison between the Cosilab code 6 μm ---, 10 μm ---, 20 μm ---, 40 μm --- and the LVDEM model 6 μm —, 10 μm —, 20 μm —, 40 μm —; the experimental results for 6 μm are given in \blacktriangle , the reference without spray ---, $\alpha = 1 \times 10^{-4}$.

has a higher mass evaporation rate. However, the overall evaporation rate is higher for smaller droplets under a fixed volumetric fraction of spray. This can also be seen from the Fig. 18, where the droplets of volume mean diameter $20\ \mu\text{m}$ and $40\ \mu\text{m}$ does not diminish significantly the flame velocity compared to the case without spray. A critical droplet diameter can be chosen, above which the droplets do not affect the flame velocity. For example, one can take $D_{c,1} = 35\ \mu\text{m}$ as the critical diameter, since the flame velocity is reduced only by less than 1.2% for all considered equivalence ratios. For smaller droplets, the flame velocity decreases with the decrease of droplet diameters. In Fig. 18, the volumetric fraction of spray is $\alpha = 1 \times 10^{-4}$.

The comparison between the LVDEM model and the Cosilab code is presented as well in the Fig. 18. Results of the model compare well with those of the Cosilab code, especially for the large droplets. This difference can be explained by the uncertainties of the evaporation model and the estimation of evaporation rate within the flame thickness. Moreover, the experimental results of [11] are well matched by the LVDEM model.

It is noticed in the results of the LVDEM model, for most values of equivalence ratio ϕ , the droplets of diameter $6\ \mu\text{m}$ can not totally evaporate within the flame thickness. Thus, the droplets can penetrate the flame and continue to evaporate in the burnt gas. This is not the case for the very lean or very rich compositions. Another critical diameter can be chosen $D_{c,2} = 3.9\ \mu\text{m}$, below which, the droplets can be totally evaporated for all the equivalence ratio values.

Conclusions

In this paper, a “Laminar Flame Velocity under Droplet Evaporation Model” (LVDEM) for hydrogen/air mixtures has been developed and validated using the results of the Cosilab code [20] and the experimental results of [11]. Initially, the hydrogen-air mixture is supposed to be at normal ambient conditions and the water droplet diameter of the order of $\mathcal{O}(10)\ \mu\text{m}$.

A key ingredient of the LVDEM-model is the droplet evaporation model of [29]. Application of the latter model is necessary in order to determine the amount of liquid water evaporating in the flame zone. Two critical droplet diameters have been considered: (i), $D_{c,1} = 35\ \mu\text{m}$ above which the droplets do not affect the laminar flame velocity for the specific droplet volume fraction $\alpha = 10^{-4}$ and, (ii), $D_{c,2} = 3.9\ \mu\text{m}$, below which the droplets totally evaporate for all equivalence ratios and for droplet volume fractions in the range $0 \leq \alpha \leq 2 \times 10^{-4}$.

In general, for all considered droplet diameters, the laminar-flame velocity diminishes with increasing water-volume fraction. The laminar flame thickness obtained by the LVDEM-model has the same order of magnitude as that computed with the Cosilab code. In the basis of the presented model, further developments can be envisaged which would take into account the non-ambient initial mixture conditions in terms of pressure, temperature and gas compositions.

Acknowledgement

This work has been performed with a financial support of the Electricité de France (EDF) in the framework of the Generation II&III reactor program, which is gratefully acknowledged.

Appendix A. The Cosilab Code Algorithm

In the Cosilab code [20], the coupling mechanism of the gaseous and liquid phase is similar to the one presented in [29,30]. One-dimensional governing equations are solved to obtain a steady solution of a freely propagating, premixed spray flame. Specifically, the gasphase equations are the Eulerian conservation equations of overall mass, species mass, momentum, and energy. The liquid-phase is computed by tracking a stream of droplets in a Lagrangian manner monitoring droplet mass in terms of droplet size, droplet momentum or velocity, respectively, and droplet temperature. To relate droplet number density and droplet velocity, the analytical solution of a suitable conservation equation is used [29]. The gasphase and liquid-phase governing equations include phase-exchange terms for liquid and gaseous mass, momentum and energy. In the present computations, ideal gas and ideal liquid behavior has been assumed. Due to the assumption of low-Mach-number flow, the pressure could be taken as thermochemically constant and hence the gasphase momentum equation could be dropped. The exchange of droplets with the surrounding gas is based on the so-called “stagnant-film theory”, which incorporates the effect of Stefan flow on the thickness of the droplet-surrounding gaseous boundary layer or film. To describe the heat transfer from the gasphase to a liquid drop moving relative to it, radial symmetry is assumed for the drop but, in the Lagrangian sense, an instationary, non-uniform temperature profile inside the drop is considered. The liquid phase is taken as a thin, mono-disperse, single-component spray.

The overall numerical two-phase solution to a spray flame is obtained by coupling the numerical evolution of the two phases. Specifically, the gasphase and liquid-phase governing equations are solved iteratively “in tandem” until the numerical solution in either phase has converged.

At a certain iteration step of the overall two-phase tandem solution procedure, based on a solution of the Eulerian gas-phase governing equations, the subsequent solution of the Lagrangian liquid-phase governing equations is obtained as follows. The vector of primary unknowns is $(D(t), v_{liq}(t), T_s(t))$, where t is the time, and D , v_{liq} , and T_s denote the instantaneous diameter, velocity and surface temperature, respectively, of the tracked drop.

In the following, the methodology to obtain the droplet surface temperature $T_s(t)$ is summarized. The remaining details of the Lagrangian equations and their solution for $D(t)$ and $v_{liq}(t)$, respectively, are straightforward and hence for them the reader is referred to Abramzon and Sirignano [29].

To obtain T_s at a particular instant of time.

- (1) the molar and mass fluid vapor fractions in the surface film of the tracked drop,

$$X_{Fs} = P_{Fs}/P, \quad Y_{Fs} = X_{Fs}M_F / \sum_i X_i M_i \quad (\text{A.1})$$

are calculated. Here P_{Fs} denotes the fluid vapor saturated pressure which is evaluated using appropriate correlations

$$P_{Fs} = P_{Fs}(T_s) \quad (\text{A.2})$$

(2) the instantaneous average gas-phase properties

$$\bar{\rho}, \bar{C}_{pF}, \bar{C}_{pg}, \bar{\lambda}_g, \bar{\mu}_g, \bar{D}, \bar{Le} = \frac{\bar{\lambda}_g}{\bar{\rho}_g \bar{D} \bar{C}_{pg}}, \bar{Pr}, \bar{Sc}$$

in the gas film are calculated – for a definition see the table of contents – using the reference conditions given by the so-called one-third rule, viz.,

$$\bar{T} = T_s + \frac{1}{3}(T_\infty - T_s) \quad (\text{A.3})$$

$$\bar{Y}_F = Y_{Fs} + \frac{1}{3}(Y_{F\infty} - Y_{Fs}) \quad (\text{A.4})$$

(3) the instantaneous Reynolds number, $Re = 2\rho_\infty|U - U_\infty|r_s/\mu_g$, and the instantaneous Nusselt and Sherwood numbers for a non-vaporizing droplet are calculated, viz.,

$$Nu_0 = 1 + (1 + Re \cdot Pr)^{1/3} f(Re) \quad (\text{A.5})$$

$$Sh_0 = 1 + (1 + Re \cdot Sc)^{1/3} f(Re) \quad (\text{A.6})$$

Where $f(Re) = 1$ at $Re \leq 1$ and $f(Re) = Re^{0.077}$ at $Re \leq 400$.

(4) the instantaneous Spalding mass transfer number, B_M , the corresponding diffusional film correction factor, F_M , the modified Sherwood number, Sh^* , and the mass vaporization rate, \dot{m} , are calculated, viz.,

$$B_M = \frac{Y_{Fs} - Y_{F\infty}}{1 - Y_{Fs}} \quad (\text{A.7})$$

$$F_M = (1 + B_M)^{0.7} \frac{\ln(1 + B_M)}{B_M} \quad (\text{A.8})$$

$$Sh^* = 2 + (Sh_0 - 2)/F_M \quad (\text{A.9})$$

$$\dot{m} = 2\pi\bar{\rho}_g \bar{D}_g r_s Sh^* \ln(1 + B_M) \quad (\text{A.10})$$

(5) the correction factor for the thermal film thickness, $F_T = F(B_T)$, is calculated using the value of the heat transfer number, B_T^{old} , from the previous iteration or time step.

(6) the modified Nusselt number, Nu^* , the parameter ζ and the corrected value of the heat transfer number, B_T , are calculated, viz.,

$$Nu^* = 2 + (Nu_0 - 2)/F_T \quad (\text{A.11})$$

$$\zeta = \left(\frac{\bar{C}_{pF}}{\bar{C}_{pg}} \right) \left(\frac{Sh^*}{Nu^*} \right) \frac{1}{Le} \quad (\text{A.12})$$

$$B_T = (1 + B_M)^\phi - 1 \quad (\text{A.13})$$

(7) the heat transferred from the gaseous to the liquid phase,

$$Q_L = \dot{m} \left\{ \frac{\bar{C}_{pF}(T_{gas} - T_s)}{B_T} - l(T_s) \right\} \quad (\text{A.14})$$

is calculated. Here T_{gas} denotes the gasphase temperature at the position at which the tracked drop is instantaneously located.

At any discrete time, or time-step, in the Lagrangian solution procedure of the liquid-phase governing equations, the non-dimensional energy equation for the “effective thermal conductivity model” is solved [29], viz.,

$$(\psi)^2 \frac{\partial Z}{\partial \tau} = \beta \eta \frac{\partial Z}{\partial \eta} + \frac{1}{\eta^2} \frac{\partial}{\partial \eta} \left(\eta^2 \frac{\partial Z}{\partial \eta} \right) \quad (\text{A.15})$$

Where $Z(\eta, \tau) = (T_d(r, t) - T_0)/T_0$ is the non-dimensional drop temperature, $\psi(\tau) = r_s(t)/r_0$ the instantaneous non-dimensional drop radius, $\tau = \alpha_L t/r_0^2$ the non-dimensional time, $\eta = r/r_s(t)$ the non-dimensional radial coordinate, α_L the liquid thermal diffusivity, and β is proportional to the regression rate of the droplet surfaces, which can be estimated by

$$\beta = - \frac{1}{4\pi\alpha_L \rho_L T_s} \left[\dot{m} + \frac{1}{\rho_L C_{pL}} Q_L \right]. \quad (\text{A.16})$$

It is important to note that Eq. (A.15) is solved simultaneously with the ordinary differential equations that describe the evolution of the liquid phase in terms of the primary liquid-phase dependent variables $D(t)$, $v_{liq}(t)$ and $T_s(t)$ discussed above. In particular, at any time t one has $T_s(t) = T_0(1 + Z(1, \alpha_L t/r_0^2))$ where $r_0 = D(0)/2$.

Further details of the Lagrangian equations governing $D(t)$, $v_{liq}(t)$ and $T_s(t)$ are straightforward and can be found in Abramzon and Sirignano [29].

REFERENCES

- [1] Foissac A, Malet J, Vetrano MR, Buchlin JM, Mimouni S, Feuillebois F, et al. Droplet size and velocity measurements at the outlet of a hollow cone spray nozzle. *Atomization*

- Sprays 2011;21:893–905. <https://doi.org/10.1615/AtomizSpr.2012004171>.
- [2] Joseph-Augustea C, Cheikhravat H, Chaumeix N, Deria E. On the use of spray systems: an example of R&D work in hydrogen safety for nuclear applications. *Int J Hydrogen Energy* 2009;34(14):5970–5. <https://doi.org/10.1016/j.ijhydene.2009.01.018>.
- [3] Wingerden KV, Wilkins B, Bakken J, Pedersen G. The influence of water sprays on gas explosions. Part 2: mitigation. *J Loss Prev Process Ind* 1995;8(2):61–70. [https://doi.org/10.1016/0950-4230\(95\)00007-N](https://doi.org/10.1016/0950-4230(95)00007-N).
- [4] Pilch M, Erdman CA. Use of breakup time data and velocity history data to predict the maximum size of stable fragments for acceleration-induced breakup of a liquid drop. *Int J Multiphase Flow* 1987;13(6):741–57. [https://doi.org/10.1016/0301-9322\(87\)90063-2](https://doi.org/10.1016/0301-9322(87)90063-2).
- [5] Chou W-H, Hsiang L-P, Faeth GM. Temporal properties of drop breakup in the shear breakup regime. *Int J Multiphase Flow* 1997;23(4):651–69. [https://doi.org/10.1016/S0301-9322\(97\)00006-2](https://doi.org/10.1016/S0301-9322(97)00006-2).
- [6] Meng JC, Colonius T. Numerical simulation of the aerobreakup of a water droplet. *J Fluid Mech* 2018;835:1108–35. <https://doi.org/10.1017/jfm.2017.804>.
- [7] Sapko MJ, Furno AL, Kuchta JM. Quenching methane-air ignitions with water sprays. Bureau of Mines Report of Investigations.; 1977. RI 8214.
- [8] Zalosh RG, Bajpai SN. Water fog inerting of hydrogen-air mixtures. 1982. Proc. 2nd int conf on the impact of hydrogen on water reactor safety. New Mexico, USA.
- [9] Boech LR, Kink A, Oezdin D, Hasslberger J, Sattelmayer T. Influence of water mist on flame acceleration, DDT and detonation in H₂-air mixtures. *Int J Hydrogen Energy* 2015;40(21):6995–7004. <https://doi.org/10.1016/j.ijhydene.2015.03.129>.
- [10] Holborn PG, Battersby P, Ingram JM, Averill AF, Nolan PF. Modelling the effect of water fog on the upper flammability limit of hydrogen-oxygen-nitrogen mixtures. *Int J Hydrogen Energy* 2013;38(16):6896–903. <https://doi.org/10.1016/j.ijhydene.2013.03.091>.
- [11] Ingram JM, Averill AF, Battersby PN, Holborn PG, Nolan PF. Suppression of hydrogen-oxygen-nitrogen explosions by fine water mist: part 1, burning velocity. *Int J Hydrogen Energy* 2012;37(24):19250–7. <https://doi.org/10.1016/j.ijhydene.2012.09.092>.
- [12] Gai G, Kudriakov S, Hadjadj A, Studer E, Thomine O. Modeling of pressure loads during a premixed hydrogen combustion in the presence of water spray. *Int J Hydrogen Energy* 2019;44(10):4592–607. <https://doi.org/10.1016/j.ijhydene.2018.12.162>.
- [13] FLACS. V 10.2. User's Manual. GexCon AS; 2014.
- [14] Keenan JJ, Makarov DV, Molkov VV. Rayleigh-Taylor instability: modelling and effect on coherent deflagrations. *Int J Hydrogen Energy* 2014;39(35):20467–73. <https://doi.org/10.1016/j.ijhydene.2014.03.230>.
- [15] Bauwens CR, Chaffee J, Dorofeev SB. Vented explosion overpressures from combustion of hydrogen and hydrocarbon mixtures. *Int J Hydrogen Energy* 2011;36(3):2329–36. <https://doi.org/10.1016/j.ijhydene.2010.04.005>.
- [16] Velikorodny A, Studer E, Kudriakov S, Beccantini A. Combustion modeling in large scale volumes using EUROPLEXUS code. *J Loss Prev Process Ind* 2015;35:104–16. <https://doi.org/10.1016/j.jlp.2015.03.014>.
- [17] Dahoe AE. Laminar burning velocities of hydrogen-air mixtures from closed vessel gas explosions. *J Loss Prevent Proc* 2015;18(3):152–66. <https://doi.org/10.1016/j.jlp.2005.03.007>.
- [18] Konnov AA. Remaining uncertainties in the kinetic mechanism of hydrogen combustion. *Combust Flame* 2008;152(4):507–28. <https://doi.org/10.1016/j.combustflame.2007.10.024>.
- [19] Ballal DR, Lefebvre AH. Flame propagation in heterogeneous mixtures on fuel droplets, Fuel vapor and air. 18th Symposium (International) on Combustion. The Combustion Institute; 1981. [https://doi.org/10.1016/S0082-0784\(81\)80037-9](https://doi.org/10.1016/S0082-0784(81)80037-9).
- [20] Cosilab (V 4.1) Software. User manual two-phase flames. 2018. www.rotexo.com.
- [21] Neophytou A, Mastorakos E. Simulations of laminar flame propagation in droplet mists. *Combust Flame* 2009;156(8):1627–40. <https://doi.org/10.1016/j.combustflame.2009.02.014>.
- [22] Grosseuvres R, Comandini A, Bentaib A, Chaumeix N. Combustion properties of H₂/N₂/O₂/steam mixtures. *Proc Combust Inst* 2019;37(2):1537–46. <https://doi.org/10.1016/j.proci.2018.06.082>.
- [23] Satija A, Huang X, Panda PP, Lucht PR. Vibrational CARS thermometry and one-dimensional simulations in laminar H₂/air counter-flow diffusion flames. *Int J Hydrogen Energy* 2015;40(33):10662–72. <https://doi.org/10.1016/j.ijhydene.2015.06.150>.
- [24] Connaire MO, Curran HJ, Simmie JM, Pitz WJ, Westbrook CK. A comprehensive modeling study of hydrogen oxidation. *Int J Chem Kinet* 2004;36(11):603–22. <https://doi.org/10.1002/kin.20036>.
- [25] Williams FA. Combustion theory. 2nd ed. CRC Press; 1994.
- [26] Kee RJ, Coltrin ME, Glarborg P, Zhu H. Chemically reacting flow: theory, modeling, and simulation. 2nd ed. Wiley; 2017.
- [27] Koroll GW, Kumar RK, Bowles EM. Burning velocities of hydrogen-air mixtures. *Combust Flame* 1993;94(3):330–40. [https://doi.org/10.1016/0010-2180\(93\)90078-H](https://doi.org/10.1016/0010-2180(93)90078-H).
- [28] Szabó T, Yañez J, Kotchourko A, Kuznetsov M, Jordan T. Parameterization of laminar burning velocity dependence on pressure and temperature in hydrogen/air/steam mixtures. *Combust Sci Technol* 2012;184:1427–44. <https://doi.org/10.1080/00102202.2012.690253>.
- [29] Abramzon B, Sirignano WA. Droplet vaporization model for spray combustion calculations. *Int J Heat Mass Transf* 1988;32(9):1605–18. [https://doi.org/10.1016/0017-9310\(89\)90043-4](https://doi.org/10.1016/0017-9310(89)90043-4).
- [30] Sirignano WA. Fluid dynamics and transport of droplets and sprays. 2nd ed. Cambridge University Press; 2010.
- [31] Poinot T, Veynante D. Theoretical and numerical combustion. Philadelphia: Edwards; 2001.
- [32] Gaydon AG, Wolfhard HG. Flames: their structure, radiation and temperature. 4th ed. London: Chapman and Hall; 1979.
- [33] Ingram JM. Private communication.
- [34] Luangdilok W, Bennett RB. Fog inerting effects on hydrogen combustion in a PWR ice condenser containment. *J Heat Transf* 1995;117(2):502–7. <https://doi.org/10.1115/1.2822550>.
- [35] Travis JR. A heat, mass, and momentum transport model for hydrogen diffusion flames in nuclear reactor containments. *Nucl Eng Des* 1987;101:149–66.
- [36] Gavrikov AI, Bezmelnitsyn AV, Leliakin AL, Dorofeev SB. Extraction of basic flame properties from laminar flame speed calculations. 23th International colloquium on the dynamics of explosions and reactive systems. 2001.
- [37] Yanez J, Kuznetsov M. An analysis of flame instabilities for hydrogen-air mixtures based on Sivashinsky equation. *Phys Lett* 2016;380(33):2549–60. <https://doi.org/10.1016/j.physleta.2016.05.048>.
- [38] Cheikhravat H. Etude expérimentale de la combustion de l'hydrogène dans une atmosphère inflammable en présence de gouttes d'eau. PhD. Thesis. Université d'Orléans; 2009.

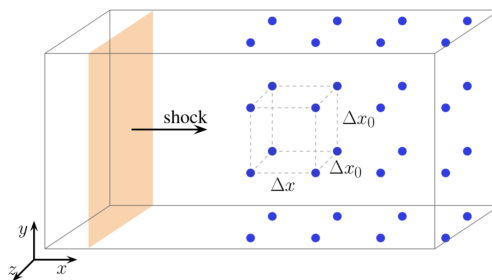
Chapter 4

Spray-shock Interaction

Section 1: Modeling of particle cloud dispersion in compressible gas flows with shock waves

Highlights:

- Development of a one-dimensional analytical model for the estimation of the cloud topology in the wake of a shock wave based on the one-way formalism.
- Validation of the analytical model using direct numerical simulations.
- Analysis of the effects of different parameters affecting the shock-spray interaction.
- An extension of the one-way formalism to the two-way by considering the post-shock gas deceleration due to the presence of particles.
- The two-way formalism can better describe the effects of the particles on the propagation of the shock wave.



Modeling of particle cloud dispersion in compressible gas flows with shock waves

Cite as: Phys. Fluids **32**, 023301 (2020); <https://doi.org/10.1063/1.5135774>

Submitted: 08 November 2019 . Accepted: 14 January 2020 . Published Online: 03 February 2020

Guodong Gai , Olivier Thomine, Abdellah Hadjadj, and Sergey Kudriakov



View Online



Export Citation



CrossMark

ARTICLES YOU MAY BE INTERESTED IN

[Stability of a vertical Couette flow in the presence of settling particles](#)

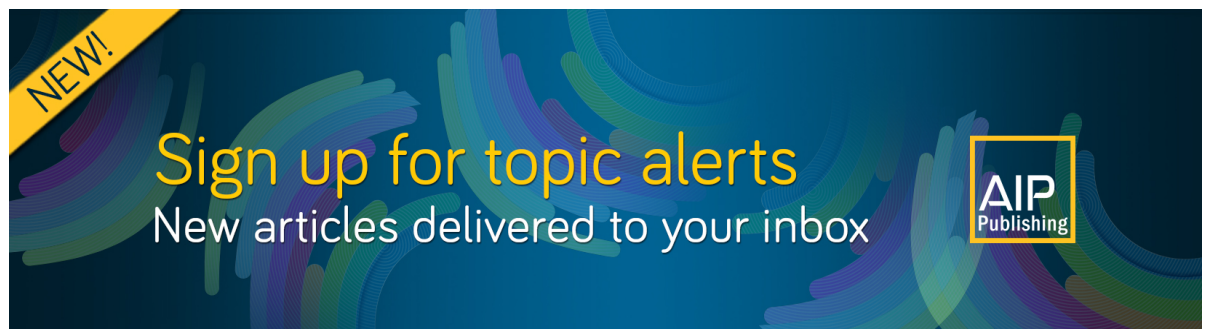
Physics of Fluids **32**, 024104 (2020); <https://doi.org/10.1063/1.5140422>

[Linear and weakly nonlinear stability analysis on a rotating anisotropic ferrofluid layer](#)

Physics of Fluids **32**, 024101 (2020); <https://doi.org/10.1063/1.5133102>

[Numerical study on shock-accelerated gas rings](#)

Physics of Fluids **32**, 026102 (2020); <https://doi.org/10.1063/1.5135762>



NEW!

Sign up for topic alerts

New articles delivered to your inbox

AIP Publishing

Modeling of particle cloud dispersion in compressible gas flows with shock waves

Cite as: Phys. Fluids 32, 023301 (2020); doi: 10.1063/1.5135774

Submitted: 8 November 2019 • Accepted: 14 January 2020 •

Published Online: 3 February 2020



View Online



Export Citation



CrossMark

Guodong Gai,^{1,2,a)}  Olivier Thomine,¹ Abdellah Hadjadj,² and Sergey Kudriakov¹

AFFILIATIONS

¹DEN-DM2S-STMF, Commissariat à l'Énergie Atomique et aux Énergies Alternatives, Université Paris-Saclay, 91191 Gif-sur-Yvette, France

²University of Normandy, INSA, CORIA UMR - 6614 CNRS, 76000 Rouen, France

^{a)}Author to whom correspondence should be addressed: guodong.gai@cea.fr

ABSTRACT

The effect of shock waves on the dispersion characteristics of a particle cloud is investigated both numerically and analytically. A one-dimensional analytical model is developed for the estimation of the cloud topology in the wake of a shock wave, as a function of time, space, and characteristic response time τ_p of the cloud based on the one-way formalism. The model is compared with the results obtained with numerical simulations over a wide range of incident Mach numbers M_s and particle volume fraction $\tau_{v,0}$. An extension of the one-way formalism to the two-way is proposed by taking into account the post-shock gas deceleration due to the presence of particles. A significant increase in the cloud density is noticed. The effects of different parameters affecting the shock-spray interaction are elucidated and discussed. The two-way formalism is seen to better describe the effects of the particles on the propagation of the shock wave.

Published under license by AIP Publishing. <https://doi.org/10.1063/1.5135774>

I. INTRODUCTION

The interaction between shock waves and particles has been an active research field for decades.^{1–5} Many theoretical and experimental studies are conducted in order to understand the interaction mechanisms of shock waves with droplets or solid particles,^{6–10} since it is present and of major importance in various industrial applications. For instance, the compression waves can coalesce and generate shock waves in internal engines.¹¹ The shocked fuel spray has different dispersion topologies, thus changing the combustion properties. Other applications concern explosion in the confinement building, where the shock waves can be initiated accidentally. In order to mitigate their effects, an aqueous foam^{12–15} or a water spray system¹⁶ can be used. In this case, the shock-spray interaction can change dramatically the dispersion of droplets, leading to the change in the mitigation capacity of the spray system.^{17–19} On the contrary, the particle cloud can also affect the propagation of the shock wave.²⁰

Basically, as a result of the high velocity of the shocked gas, the shock-droplet interaction can generate complex coupled phenomena such as droplet deformation, atomization, collision, coalescence, and evaporation.^{11,21,22} Moreover, the polydispersion of the droplets

adds further difficulties to the investigations. To simplify the problem, various studies focus on the interaction between a shock wave and a single or an array of particles,^{23–25} where the effects of particles on gas flow are weak. Dense particle or particle curtains are also investigated,^{3,26} in which the collision between the particles is important.

Given the complexity of the droplet behavior during the interaction, rigid particles of uniform diameters are commonly used to simplify the shock-particle interaction. Even though the qualitative phenomena are well known,^{1,3} the interaction mechanisms between shock and particles are yet to be elucidated quantitatively in both well-conducted experiments and in numerical simulations and modelings.²⁷ Particularly, the particle clouds of the volume fraction $\mathcal{O}(10^{-4}–10^{-3})$ are of great interest in nuclear industrial applications.

The integral properties of the particle cloud movements such as volume fraction distribution and velocity distribution are also important for the large-scale simulations.²⁸ However, to the best knowledge of the authors, the existing particle-resolved models for simulations of large-scale geometries such as nuclear confinement building are scarce, as a result of high computational expenses, especially for high Reynolds number flows. Thus, simple reduced-order

modeling approaches and empirical correlations are considered to be the alternative solutions.

In this study, a new analytical model is developed to quantify the shocked gaseous flow impact on the dispersed phase using a one-way formalism. An extended two-way theoretical model is proposed, which takes into consideration the deceleration effect of the particles on the gas phase. The objectives of this study are threefold: (i) provide a simplified analytical formulation of particle cloud dispersion after the interaction with a shock wave, (ii) elucidate the importance of the two-way formalism on the description of the shock–cloud interaction, and (iii) identify the main parameters and their effects on the shock–cloud interaction. The theoretical model is validated with high-resolved numerical simulations.

This paper is organized as follows: Section II discusses the characteristics of the particle cloud. Section III presents an analytical formulation of particle dispersion with a shock wave. Section IV discusses the assessment of the analytical model, and the comparisons between the analytical results and the numerical simulations are presented in Sec. V. Finally, the main conclusions together with recommendations for future work are given in Sec. VI.

II. CHARACTERISTICS OF THE CLOUD PARTICLES

In this study, assumptions are made so that the gas is considered as inviscid and follows the perfect-gas law, the particles are supposed to be rigid and spherical, with small volume fractions, the collisions between them are neglected,²⁹ only viscous drag forces act on the particles, and the heat transfer between gas and particles is neglected.

Initially at rest, the particles are assumed to be uniformly distributed throughout the computational domain. After the passage of the shock, the particles are accelerated by the gas flow. In order to determine the evolution of the particles, we compute the force applied by the flow of velocity $\mathbf{u}(\mathbf{x}, t)$ on a spherical particle of coordinate \mathbf{x} , with a velocity $\mathbf{V}(t)$ and a diameter d_p . The general equation of motion reads

$$m_p \frac{d\mathbf{V}(t)}{dt} = \sum \mathbf{F}, \tag{1}$$

where $m_p = \pi \rho_p d_p^3 / 6$ is the particle mass and ρ_p is the particle density. Here, we neglect the gravity, the Magnus' force, and the Basset force as a result of the high ratio between the densities of the liquid and gas phases. The viscous drag force gives

$$\mathbf{F} = \frac{\pi}{8} \rho_p d_p^2 C_D |\mathbf{u}(\mathbf{x}, t) - \mathbf{V}(t)| (\mathbf{u}(\mathbf{x}, t) - \mathbf{V}(t)), \tag{2}$$

where C_D is the drag coefficient of the particles defined as

$$C_D = \frac{24}{Re_p}, \quad \text{with } Re_p = \frac{\rho_g |\mathbf{u}(\mathbf{x}, t) - \mathbf{V}(t)| d_p}{\mu_g}, \tag{3}$$

where Re_p is the particular Reynolds number related to the flow around the particle and μ_g is the dynamic viscosity of the gas. The diameters of the particles considered in this study vary from 10 nm to 50 μm . Due to the small size of particles, the drag coefficient is given by the Stokes coefficient for laminar flow. The equation of motion for each particle can be obtained as

$$\frac{d\mathbf{V}(t)}{dt} = \frac{1}{\tau_p} (\mathbf{u}(\mathbf{x}, t) - \mathbf{V}(t)), \quad \text{with } \tau_p = \frac{\rho_p d_p^2}{18\mu_g}. \tag{4}$$

In the case of a two-way interaction, and in order to estimate the effect of the particles on the gas, the momentum conservation is taken into consideration. For a gas volume \mathcal{V} containing one particle with a velocity variation $\frac{d\mathbf{V}}{dt}$, the particle can decelerate the gas with respect to the following equality:

$$\frac{d\mathbf{u}}{dt} = - \frac{m_p}{\rho_g \mathcal{V}} \frac{d\mathbf{V}(t)}{dt}. \tag{5}$$

III. ANALYTICAL DETERMINATION OF PARTICLE DISPERSION WITH SHOCK WAVE

A. Eulerian cloud velocity

In the one-way formalism, the evolution of the particles allows us to determine analytically their velocities and coordinates as a function of time, when a constant velocity gas is applied. Let M_s denote the Mach number of the shock wave. The pre- and the post-shock gas properties can be found in Appendix A. Consider any point in the particle-laden domain at a time t , with the position x , denoted as (x, t) . The time origin corresponds to the beginning of the cloud interaction, with the shock initially at $x = 0$. For each point in the (x, t) diagram (see Fig. 1), two configurations are possible, depending on whether the shock wave has already passed the interface ($x \geq M_s c t$) or not (c being the sound speed in the gas at rest).

It is possible to calculate the initial position and time of each particle. Let x' be the distance covered by the particle after the interaction with the shock, and t' the duration of the interaction. The distance covered by the particle during t' is $x' = x(t') = x - x_0$, and the distance covered by the shock wave is $M_s c t' = M_s c t - x_0$. Knowing the shock velocity, $V_s = M_s c$, and the gas velocity behind the shock u_g , one can deduce from Eq. (4) the velocity as well as the distance covered by a particle x' as a function of time t' during which it is exposed to the gas of a velocity u_g ,

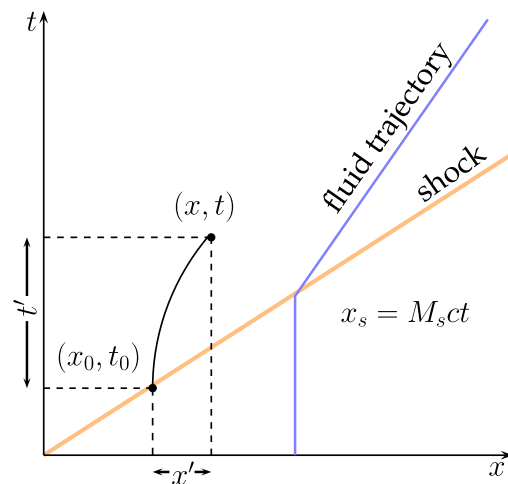


FIG. 1. Space–time diagram (x, t) of the considered system with x_s the shock position, x' the distance covered by a particle located initially at x_0 , and t' the duration of the interaction of the particle with the shock.

$$\begin{cases} V(t', \tau_p, u_g) = u_g(1 - e^{-t'/\tau_p}) \\ x(t', \tau_p, u_g) = \int_0^{t'} V(t, \tau_p, u_g) dt = u_g(t' - \tau_p(1 - e^{-t'/\tau_p})). \end{cases} \quad (6)$$

The two unknown variables x' and t' satisfy the following relations:

$$\begin{cases} x' = x(t', \tau_p, u_g) = x - x_0 \\ M_s ct' = M_s ct - x_0. \end{cases} \quad (7)$$

By excluding x_0 from Eq. (7) and substituting the expression for x' from Eq. (6), one can deduce that

$$u_g \tau_p (e^{-t'/\tau_p} - 1) + M_s ct - x = (M_s c - u_g)t'. \quad (8)$$

Solving this equation (cf. Appendix B) gives the following expression:

$$t'(x, t, u_g) = \tau_p \mathcal{W} \left(\frac{u_g e^\eta}{M_s c - u_g} \right) + \frac{M_s ct - u_g \tau_p - x}{M_s c - u_g}, \quad (9)$$

where

$$\eta = \frac{u_g \tau_p - M_s ct + x}{\tau_p (M_s c - u_g)}. \quad (10)$$

The Lambert function \mathcal{W}^{30} is defined implicitly as the solution of the equation $\alpha \exp(\alpha) = \beta$ (see Appendix B). It is also possible to obtain the Eulerian velocity of the cloud u as

$$u(x, t, \tau_p, u_g) = V(t'(x, t, u_g), \tau_p, u_g) = u_g(1 - \exp(-t'(x, t)/\tau_p)). \quad (11)$$

B. Mean cloud density

Using the conservation of mass, it is possible to determine the global spray characteristics in the post-shock area. If one considers that the time t of the interaction of the shock with the cloud is very large with respect to the response time τ_p , the first particle distance covered can be approximated with $x(t, \tau_p/t \rightarrow 0) = u_g t$. It allows us to determine the cloud length in the post-shock area as

$$L(t, \tau_p/t \rightarrow 0, u_g) = M_s ct - x(t, \tau_p/t \rightarrow 0, u_g) = (M_s c - u_g)t. \quad (12)$$

Considering that the particles are solid and undeformable, the initial cloud length is $M_s ct$ and becomes $(M_s c - u_g)t$, we deduce that the post-shock density of the particles $\bar{\tau}_v$ can be linked to the pre-shock density $\tau_{v,0}$ by

$$\bar{\tau}_v(t, \tau_p, u_g) = \tau_{v,0} \frac{M_s c}{M_s c - u_g}. \quad (13)$$

The initial and the post-shock cloud lengths are represented in Fig. 2(b). Using Eq. (A1), one can obtain

$$\frac{\bar{\tau}_v}{\tau_{v,0}} = \frac{1}{\frac{\gamma - 1}{\gamma + 1} + \frac{2}{\gamma + 1} \frac{1}{M_s^2}}. \quad (14)$$

The evolution of the ratio $\bar{\tau}_v/\tau_{v,0}$ as a function of M_s is given in Fig. 2(a). One can see that when $M_s \rightarrow \infty$, $\bar{\tau}_v/\tau_{v,0}$ approaches $(\gamma + 1)/(\gamma - 1) = 6.0$ for air, a value that $\bar{\tau}_v/\tau_{v,0}$ can never exceed.

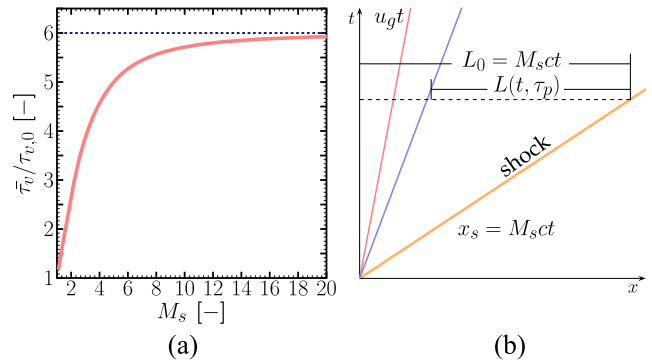


FIG. 2. Cloud density as a function of the Mach number and the length of cloud in the post-shock area. (a) Evolution of $\bar{\tau}_v/\tau_{v,0}$ as a function of M_s ; the dashed blue line represents the asymptotic limit given by $(\gamma + 1)/(\gamma - 1)$ with $\gamma = 1.4$. (b) Space-time diagram showing the cloud length pre- and post-shock.

When the inertia of the particles cannot be neglected, one can obtain a mean load rate after the shock passage using Eqs. (6) and (12),

$$\bar{\tau}_v(t, \tau_p, u_g) = \tau_{v,0} \frac{M_s c}{M_s c - u_g + u_g \frac{\tau_p}{t} (1 - \exp(-t/\tau_p))}. \quad (15)$$

Equations (13) and (15) show accumulation of particles after the shock at the contact surface. The evolutions of the particle load rate for different τ_p and for a fixed $M_s = 1.1$ are given in Fig. 3. We can see that the time necessary to reach the asymptotic value for the particle load rate increases with particle response time as expected.

C. Eulerian cloud density evolution

One more hypothesis is necessary to estimate the Eulerian cloud density evolution. Let us assume that the particles are initially regularly disposed with a mean distance of Δx_0 between them. The

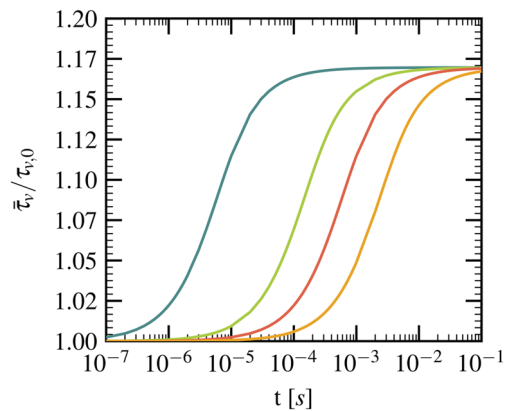


FIG. 3. Mean load rate evolutions for particles of different τ_p in air: $\tau_p = 3 \times 10^{-6}$ s (blue solid line), $\tau_p = 7.5 \times 10^{-5}$ s (green solid line), $\tau_p = 3 \times 10^{-4}$ s (red solid line), $\tau_p = 1.2 \times 10^{-3}$ s (orange solid line), $\rho_p = 10^3$ kg/m³, $M_s = 1.1$, and $u_g = 55.19$ m/s.

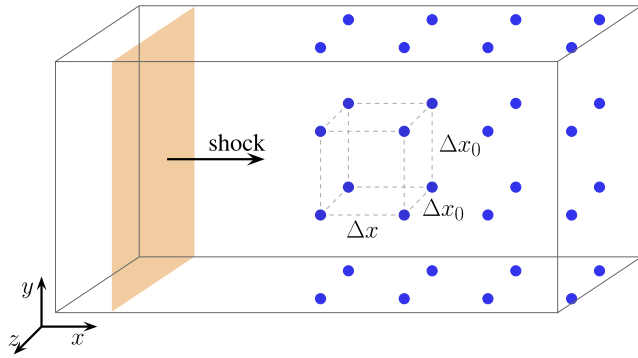


FIG. 4. Initial configuration of the shock/particle interaction.

cloud is also initially structured according to a cubic particle shape. The load rate $\tau_{v,0}$ of this cloud is also the ratio between the volume taken by the particles and the volume of the gas. The initial organization of the particles and the initial load rate are shown in Fig. 4. With such a cubic arrangement, the load rate is

$$\tau_{v,0} = \frac{\pi d_p^3}{6 \Delta x_0^3}. \tag{16}$$

Knowing that the shock propagates along the x -direction, the load rate of the shocked particle-laden region can be

$$\frac{\tau_v(t', \tau_p, u_g)}{\tau_{v,0}} = \left[\left(1 - \frac{u_g}{M_s c} \right) + \underbrace{\sqrt{\frac{\rho_p}{18 \mu \tau_p}}^3 \sqrt{\frac{6 \tau_{v,0}}{\pi}} u_g \tau_p \exp(-t'/\tau_p) \left(\exp\left(\sqrt{\frac{18 \mu_g \tau_p}{\rho_p}} \sqrt{\frac{\pi}{6 \tau_{v,0} M_s c \tau_p}} \right) - 1 \right)}_{\mathcal{A}} \right]^{-1}. \tag{20}$$

Two evident conclusions can be deduced. The term \mathcal{A} is always positive and

$$\tau_v(t', \tau_p, u_g) < \tau_{v,0} \frac{M_s c}{M_s c - u_g} = \tau_{v,max}, \tag{21}$$

which is the maximal value of the post-shock density estimated by Eq. (15). In the one-way formalism, we can conclude that for any physical parameters, the maximal density of the cloud can never exceed the mean density that a null-inertia cloud could have. The second point is that, for a very low τ_p , one can have $\mathcal{A} \rightarrow 0$. In this case, the cloud density increases to a constant value $\tau_{v,max}$. This model is applicable for various particle cloud density ratios ρ_p/ρ_g , provided that the gravity of the particles is negligible compared to the drag force.

D. Extension to two-way formalism

With the existence of the particle-gas interaction, the gas velocity decreases due to the conservation of momentum. We can assume that this velocity is reduced by a value $\varepsilon(u_g)$. The next particle will

$$\tau_v(t, \tau_p, u_g) = \frac{\pi d_p^3}{6 \Delta x_0^2 \Delta x(t, \tau_p, u_g)}. \tag{17}$$

Let us consider two neighbor particles on the x -axis at initial positions x_2^0 and x_1^0 such as $x_2^0 - x_1^0 = \Delta x_0$. With previous results, it is possible to estimate the time t' during which the particles are in the post-shock area. Let us denote $\Delta t = \Delta x_0/M_s c$, the interval time taken by the shock to cover the inter-particle distance. The distance between these two particles as a function of t' is

$$\begin{aligned} \Delta x(t', \tau_p, u_g) &= x_2(t' - \Delta t, \tau_p, u_g) - x_1(t', \tau_p, u_g) \\ &= (x_2^0 + x(t' - \Delta t, \tau_p, u_g)) - (x_1^0 + x(t', \tau_p, u_g)) \\ &= \Delta x_0 + x(t' - \Delta t, \tau_p, u_g) - x(t', \tau_p, u_g). \end{aligned} \tag{18}$$

Substituting Eqs. (6) and (16) into (18) and according to the definition of Δt and τ_p , one can deduce

$$\begin{aligned} \Delta x &= \Delta x_0 \left(1 - \frac{u_g}{M_s c} \right) + u_g \tau_p \exp(-t'/\tau_p) \\ &\times \left[\exp\left(\sqrt{\frac{18 \mu_g \tau_p}{\rho_p}} \sqrt{\frac{\pi}{6 \tau_{v,0} M_s c \tau_p}} \right) - 1 \right]. \end{aligned} \tag{19}$$

Dividing Eq. (19) by x_0 , one can obtain according to Eqs. (16), (17), and the definition of τ_p ,

relax to a velocity of $u_g - \varepsilon(u_g)$. Figure 5 shows the acceleration of two successive particles by the shock wave in the two-way model. In this case, the load rate will severely increase at the cloud extremity. In addition, the presence of particles can slow down the post-shock gas velocity. It is at the cloud extremity that the particles slipping velocity is the highest. It is also at this location that the gas is most impacted by the presence of particles, and that ε has the

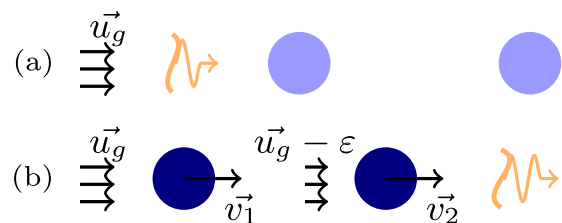


FIG. 5. Sketch of two successive particle motion (a) before and (b) after the shock passage.

highest values. Knowing that the density and the local velocity of the cloud have no analytical solutions, one can only determine the mean characteristics of the cloud after the shock.

First, it is assumed that the Mach number of the transmitted shock takes a constant value equal to $M_s = 1.1$ in the two-way modeling. According to numerical simulations, this assumption is justified for small particle volume fractions $\tau_{v,0} < 10^{-3}$. Our attempt is to obtain the mean post-shock gas velocity \tilde{u}_g . Let us consider a volume element \mathcal{V} inside, which is the particle volume $\tau_{v,0}\mathcal{V}$. This analysis is considered in the case where the particles have completely relaxed to the post-shock gas velocity \tilde{u}_g . With respect to the kinetic energy conservation, one can directly deduce

$$\rho_g u_g^2 \mathcal{V} = \rho'_g \tilde{u}_g^2 \mathcal{V}' + \tau_{v,0} \mathcal{V}' \rho_p \tilde{u}_g^2, \text{ where } \mathcal{V}' \simeq \mathcal{V} \left(1 - \frac{u_g}{M_s c}\right) \quad (22)$$

and

$$\frac{\rho'_g}{\rho_g} = \frac{(\gamma + 1) M_s^2}{2 + (\gamma - 1) M_s^2}, \quad (23)$$

where ρ_p is the density of the particles. So, we obtain

$$\tilde{u}_g = \frac{u_g}{\sqrt{1 - \frac{u_g}{M_s c} \sqrt{\frac{(\gamma+1)M_s^2}{2+(\gamma-1)M_s^2} + \tau_{v,0} \frac{\rho_p}{\rho_g}}}}. \quad (24)$$

Taking the mean load rate given by Eq. (15), we have

$$\tilde{\tau}_v = \tau_{v,0} \frac{M_s c}{M_s c - \tilde{u}_g}. \quad (25)$$

IV. ASSESSMENT OF THE ANALYTICAL MODEL

Here, we consider the numerical simulation of the interaction between a shock wave and a gas-particle in the two-phase mixture as illustrated in Fig. 6. This is a basic configuration commonly used to study shock wave attenuation particle-laden regions.³¹ A piston moving at a speed u_g can generate a shock traveling at a velocity V_s (see Appendix A).

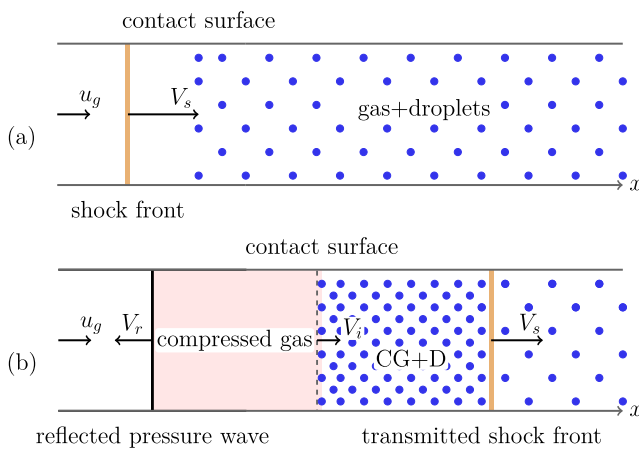


FIG. 6. Sketch of the shock and contact surface before (a) and after the interaction (b); CG: compressed gas, D: droplets.

TABLE I. Post- and pre-shock gas flow characteristics, $M_s = 1.1$, $\rho_p/\rho_g = 553.7$.

Gas flow parameters	Post-shock	Pre-shock
u_g (m/s)	58.21	0
ρ_g (kg/m ³)	1.21	1.04
p_g (bar)	1.25	1.01
T_g (K)	396	370

The simulations are conducted using an *in-home* compressible Navier–Stokes code named *Asphodele*, developed in CORIA laboratory Rouen France.³² The Eulerian–Lagrangian approach is used with an Unresolved Discrete Particle Model (UDPM). The space discretization uses a fifth-order WENO (weighted essentially non-oscillatory) scheme with global Lax–Friedrichs splitting.³³ A third-order Runge–Kutta method is adopted for time marching. The minimal storage time-advancement scheme³⁴ is used to reconstruct the Runge–Kutta method for the temporal resolution. The one-dimensional computational domain $L_0 = 1$ m consists of 1000 points, with 1000 particles initially defined in each elementary cell.

The analytical model and the numerical results are compared together in this section. The difference between theoretical and numerical cloud velocities in the one-way formalism is first studied. As illustrated in Fig. 6, the shock wave and the contact surface are initially located at $x_0 = 0$. These characteristics of the gas in the pre- and the post-shock domain are given in Table I.

The cloud velocity and the gas velocity are studied for particles with five distinct diameters ranging from nano to micro meters. The particles have a mass density of $\rho_p = 664.4$ kg/m³ at atmospheric temperature and pressure corresponding to a given gas (here, we consider cycloheptene C_7H_{16} , as an example). Table II gives the particle diameters and the related equivalent characteristic response time τ_p . In what follows, we choose the initial pre-shock properties as characteristic scales such as $u_{g,0}$, $\tau_{v,0}$, and P_0 . The length of the calculation domain L_0 is chosen as the characteristic scale of the coordinates.

For very small particles ($d_p = 10$ nm and $d_p = 1$ μ m), one can assume that their velocity increases rapidly toward the gas velocity and coincides with it. As a consequence, two areas are noted in Figs. 7(a) and 7(b): the pre-shock area, where both particles and gas are at rest, and the post-shock area, where the gas and the particles velocity are equal to u_g .

In the case where the particles inertia cannot be neglected, they progressively accelerate to relax toward the gas velocity.

TABLE II. Diameter of particles and corresponding equivalent characteristic response time τ_p .

Droplet diameter d_p (μ m)	Response time τ_p (μ s)
0.01	$1.575 \cdot 10^{-4}$
1	1.575
10	157.5
20	630
50	3937

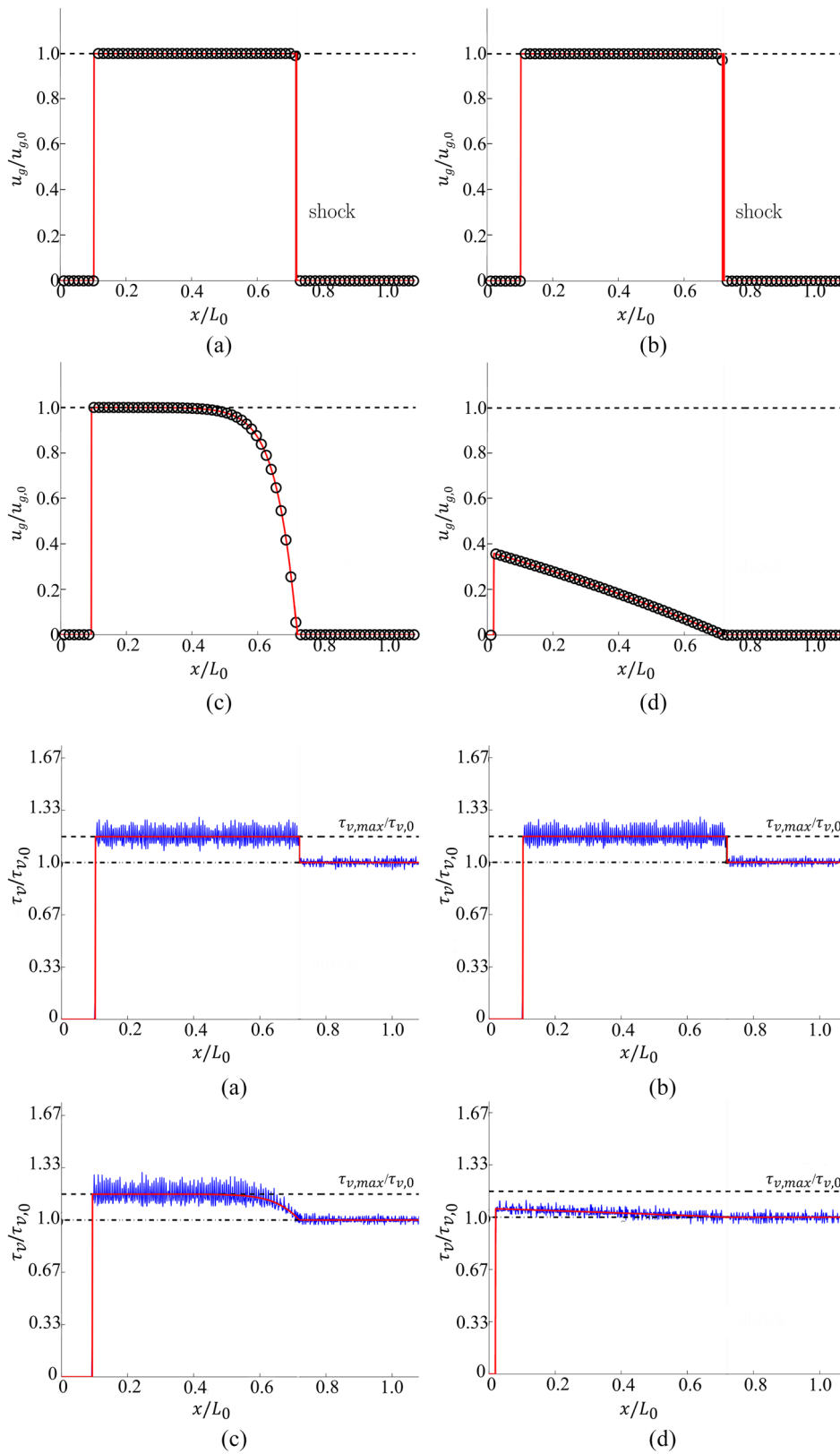


FIG. 7. Eulerian cloud velocity within the one-way formalism. Numerical results (black circle), theoretical model (red solid line), and their maximal value (u_g) for different diameters at $t = 1.756$ ms and $M_s = 1.1$, $u_{g,0} = 58.21$ m/s, $\rho_p = 664.4$ kg/m³; (a) $d_p = 10$ nm, (b) $d_p = 1$ μ m, (c) $d_p = 10$ μ m, and (d) $d_p = 50$ μ m.

FIG. 8. Droplet volume fraction in the one-way formalism. Numerical results (blue solid line), theoretical model (red solid line), and maximum ($\tau_{v,max}/\tau_{v,0}$) for different diameters at $t = 1.756$ ms, $M_s = 1.1$, and $\rho_p = 664.4$ kg/m³; (a) $d_p = 10$ nm, (b) $d_p = 1$ μ m, (c) $d_p = 10$ μ m, and (d) $d_p = 50$ μ m.

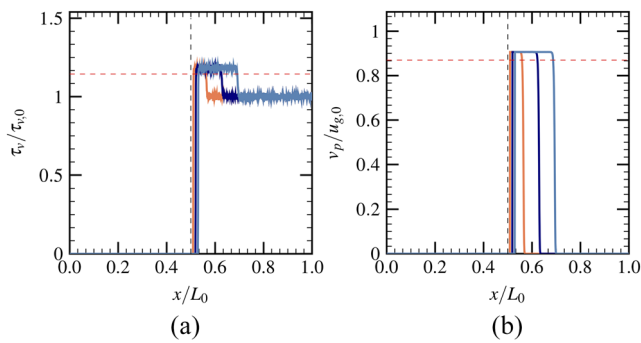


FIG. 9. Comparison between the theoretical model and numerical simulations at 0.2 ms (orange solid line), 0.4 ms (dark blue solid line), 0.6 ms (blue solid line), theoretical results (red dashed line); $\tau_{v,0} = 5.2 \times 10^{-4}$, $d_p = 1 \mu\text{m}$, $\rho_p = 664.4 \text{ kg/m}^3$, original contact surface (black dashed line); (a) droplet volume fraction and (b) droplet velocity evolution.

The time necessary for this relaxation process is τ_p [see Figs. 7(c) and 7(d)], which increases with their diameters. A comparison between analytical and numerical results shows a good agreement in terms of gas and particle velocities (see Fig. 7).

Figure 8 shows comparisons of the temporal evolutions of the cloud density τ_v between the numerical simulations and the analytical model given by Eq. (21) for particle cloud of different diameters. Different from the continuous solution given by the analytical model, the numerical results show some oscillatory behavior as a result of the random repartition of particles in the Lagrangian formalism used in the Navier–Stokes code. The mean cloud density is seen to be close to the analytical prediction, which is limited by the maximal cloud density obtained by Eq. (21).

The small particles respond immediately to the gas flow [see Figs. 8(a) and 8(b)], while the larger ones accelerate progressively [see Figs. 8(c) and 8(d)]. It can be concluded that the relationship established before in a one-way formalism is validated by the numerical simulations.

The extended two-way theoretical model is studied by comparison with the numerical simulations using two-way formalism as given in Fig. 9. The volume fraction evolution of the particles is shown in Fig. 9(a) for particles of diameter $1 \mu\text{m}$. The maximal value for the volume fraction increases from 5.2×10^{-4} to 6.08×10^{-4} . Similarly, Fig. 9(b) shows the comparison of particle velocities, which increases sharply toward a maximal value that is lower than the initial post-shock gas velocity. The theoretical particle velocity is slightly smaller than the calculation, which results in a lower estimation of the volume fraction as shown in Fig. 9(a). In fact, Eq. (24) can only give a global estimation of the real particle velocity. The relative error of the volume fraction is 2% in the case of $1 \mu\text{m}$.

V. NUMERICAL RESULTS

A. One-way vs two-way simulations

In this section, the comparison of numerical results using one-way and two-way formalisms is given. Figure 10(a) shows the evolution of volume fraction of particles in the computational domain

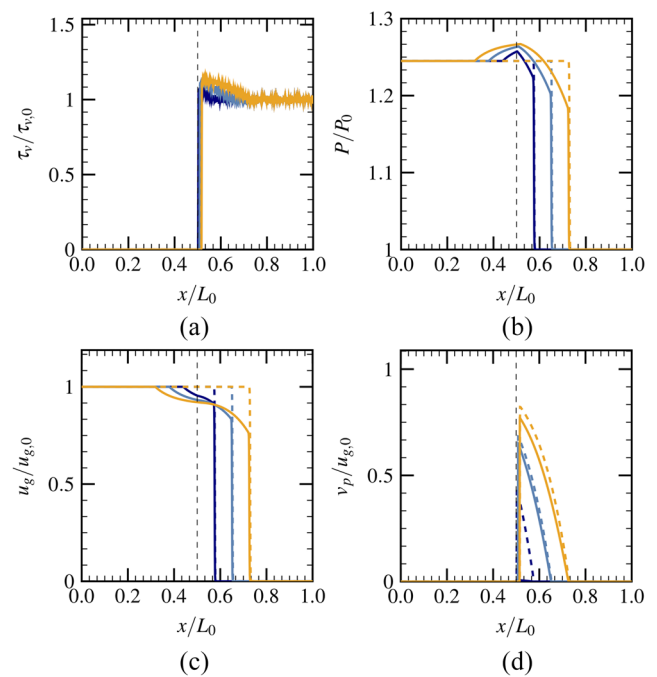


FIG. 10. Comparison one-way/two-way for different time instants. One-way on 0.2 ms (dark blue dashed line), 0.4 ms (blue dashed line), and 0.6 ms (orange dashed line) and two-way on 0.2 ms (dark blue solid line), on 0.4 ms (blue solid line), 0.6 ms (orange solid line); $\tau_{v,0} = 5.2 \times 10^{-4}$, $d_p = 10 \mu\text{m}$, $\rho_p = 10^3 \text{ kg/m}^3$, original contact surface (black dashed line); (a) droplet volume fraction, (b) gas pressure, (c) gas velocity, and (d) droplet velocity.

for $t = 200\text{--}600 \mu\text{s}$. It can be seen that the volume fraction of the particles increases after the passage of the shock. The amplification of the high volume fraction is around 1.1 times the original volume fraction. The interface of the pure gas and the particle-laden domain is pushed downstream of the gas flow. The mass density of particles takes the value of $\rho_p = 10^3 \text{ kg/m}^3$ in the following simulations.

Figure 10(b) shows the pressure evolution in the computational domain. Results of the two-way simulations are highlighted by solid lines, while the corresponding one-way simulations are depicted by dashed lines. First, as a result of the attenuation effects of particles, one can notice that the pressure of the post-shock gas is lower than the one-way coupling. This shows that the strength of the shock is decreased due to the presence of particles. Second, the reflection pressure waves are seen only in the two-way simulation. The maximal value for the post-shock pressure is 1.27 bar located at the interface of the two domains. Moreover, the reflection pressure wave propagates at a velocity lower than the original shock wave.

Figure 10(c) shows the evolution of the gas velocity. The one-way simulation indicates that there is no change in the post-shock gas velocity, while this quantity is much reduced in the two-way method, with a maximal velocity of gas smaller than 55 m/s. An effective change of particle velocity can be seen in Fig. 10(d) for the two-way simulation. After the passage of the shock, the particle velocities are smaller in the two-way simulation compared to the one-way case.

The comparison indicates that the two-way formalism should be taken into account to better describe the interaction process between the shock wave and the particle cloud.

B. Effects of particle response time

It is noted that several characteristics of the cloud such as the characteristic response time τ_p and the volume fraction of particle $\tau_{v,0}$ can have important effects on the interaction mechanism. These effects are studied numerically in this part.

Figure 11(a) shows the gas velocity evolution after the passage of the shock wave through the cloud. Different particle sizes are simulated to elucidate the effect of the response time. The interaction between the particles and the shock can effectively decelerate the post-shock gas velocity. For example, the velocity is reduced from 55 m/s to 50 m/s for particles having a diameter of 1 μm and a volume fraction of $\tau_{v,0} = 5.2 \times 10^{-4}$. The small particles respond rapidly to the shock wave, and give a piece-wise structure of the gas properties during the shock-particle interaction. The larger particles are more difficult to accelerate; thus, they reduce gradually the gas velocity.

The evolution of the particle volume fraction after the passage of the shock is given in Fig. 11(b). One can see that the small particles can give an upper bound of cloud density for the larger ones, which confirms the statement deduced from Eq. (21) through an analytical model.

C. Effect of particle volume fraction

The last section concerns the study of the effect of the particle volume fraction. Figure 12(a) shows the gas velocity evolution for different particle volume fractions. The reduction of the gas velocity is much reinforced by the increase in the particle volume fraction. However, the reflected and the transmitted wave velocities seem to be independent of the volume fraction. For a very dense cloud, where $\tau_{v,0} = 5 \times 10^{-3}$, the post-shock gas velocity reduces to zero at 600 μs , which means that there is no more transmitted pressure wave.

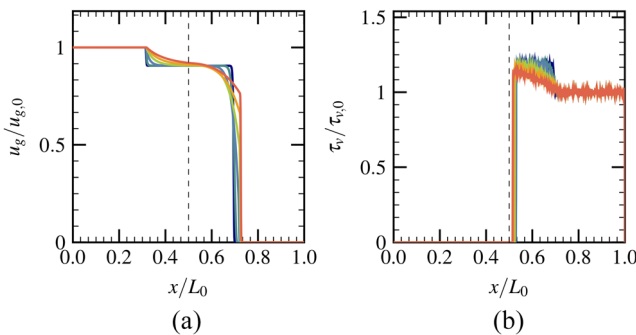


FIG. 11. Evolutions of flow parameters for different particle diameters: $d_p = 1 \mu\text{m}$ (dark blue solid line), $d_p = 2 \mu\text{m}$ (dark green solid line), $d_p = 4 \mu\text{m}$ (blue solid line), $d_p = 6 \mu\text{m}$ (green solid line), $d_p = 8 \mu\text{m}$ (orange solid line), $d_p = 10 \mu\text{m}$ (red solid line); $t = 600 \mu\text{s}$, $\tau_{v,0} = 5.2 \times 10^{-4}$, $M_s = 1.1$, $\rho_p = 10^3 \text{ kg/m}^3$, original contact surface (black dashed line); (a) gas velocity evolution, (b) droplet velocity evolution.

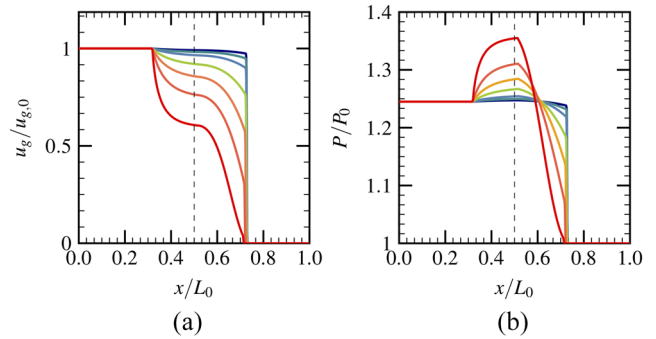


FIG. 12. Evolutions of flow parameters for different particle volume fractions: $\tau_{v,0} = 5 \times 10^{-5}$ (dark blue solid line), $\tau_{v,0} = 1 \times 10^{-4}$ (dark green solid line), $\tau_{v,0} = 2 \times 10^{-4}$ (blue solid line), $\tau_{v,0} = 5 \times 10^{-4}$ (green solid line), $\tau_{v,0} = 1 \times 10^{-3}$ (orange solid line), $\tau_{v,0} = 2 \times 10^{-3}$ (dark orange solid line), $\tau_{v,0} = 5 \times 10^{-3}$ (red solid line); $t = 600 \mu\text{s}$, $d_p = 10 \mu\text{m}$, $M_s = 1.1$, $\rho_p = 10^3 \text{ kg/m}^3$, original contact surface (black solid line); (a) gas velocity and (b) gas pressure.

Figure 12(b) gives the pressure evolution after the interaction between a shock and the cloud of diameter $d_p = 10 \mu\text{m}$. One can notice that the particles of volume fraction $\tau_{v,0} = 5 \times 10^{-5}$ have less influence on the pressure evolution. A higher volume fraction $\tau_{v,0} = 5 \times 10^{-3}$ shows an evident pressure increase at the interface between the pure gas and the particle-laden region. It seems that the transmitted pressure is completely attenuated at around $x = 0.75 \text{ m}$ in this case. The reflection pressure wave can be noted for all particle volume fractions, and the velocity of the reflected wave seems to be very close.

The comparison shows that the particle volume fraction can enhance the reflection pressure value and play an important role in the attenuation of the transmitted shock.

VI. CONCLUSIONS

An analytical model is developed to study the cloud topology after the passage of a shock wave in the framework of a one-way interaction formalism. Special attention is made to the momentum exchange between the shock and particles in order to elucidate the dynamic aspects of the shock-cloud interaction mechanisms. The assessment of the model is conducted through a comparison with numerical simulations performed using a high accuracy Navier-Stokes solver.

The extension of the one-way analytical model to the two-way formulation is proposed and compared to the numerical two-way simulations. The two-way theoretical model shows less accuracy than the one-way modeling, but still remains predictable in the scope of this study.

The necessity of using the two-way formalism in the numerical simulation of the shock-cloud interaction is discussed. Various mechanisms such as shock reflection and attenuation can be observed in the two-way simulations, which are neglected in the one-way formalism.

Small particles of diameter $\mathcal{O}(1) \mu\text{m}$ are more sensitive to the drag of the post-shock gas and the present piece-wise structures of

the shock–cloud interaction. An important shock attenuation effect is noticed for the particle cloud of high volume fractions $\mathcal{O}(10^{-3})$.

More studies can be performed considering the two- or three-dimensional shock–spray interactions to study the role of the transverse waves on the spray dispersion. The polydispersion of the cloud particles as well as the secondary breakup of the water spray can also be included in the simulations to improve the spray dispersion modeling.

ACKNOWLEDGMENTS

The authors gratefully acknowledge the financial support from Electricité de France (EDF) within the framework of the Generation II and III reactor research program.

APPENDIX A: CHARACTERISTICS OF THE PLANAR SHOCK

A planar shock wave can be generated by a piston as shown in Fig. 13. The piston starts moving at $t = 0$ with a velocity V_p , generating a shock wave with a velocity V_s . Two areas are divided by the shock wave: the post- (1) and the pre-shock area (2). Given the sound speed in the pre-shock area, c_2 , one can obtain the piston velocity, V_p , by the following relation:

$$\frac{2}{\gamma + 1} \frac{M_s^2 - 1}{M_s} = \frac{V_p}{c_2}; \quad V_s = M_s c_2. \tag{A1}$$

The post-shock gaseous flow is assumed to have the same velocity as that of the piston. Analytical solutions are available for the relationship of the pre- and post-shock thermodynamic quantities,³⁵

$$\frac{p_1}{p_0} = \Gamma_1(M_s, \gamma), \quad \frac{T_1}{T_0} = \frac{\Gamma_1(M_s, \gamma)\Gamma_2(M_s, \gamma)}{M_s^2}, \quad \frac{\rho_1}{\rho_0} = \frac{p_1 T_0}{p_0 T_1}, \tag{A2}$$

where

$$\Gamma_1(M_s, \gamma) = \frac{2}{\gamma + 1} \left(\gamma M_s^2 - \frac{\gamma - 1}{2} \right), \quad \Gamma_2(M_s, \gamma) = \frac{2}{\gamma + 1} \left(1 + \frac{\gamma - 1}{2} M_s^2 \right). \tag{A3}$$

APPENDIX B: RESOLUTION OF EQ. (8)

Equation (8) has the form

$$t'(M_s c - u_g) = u_g \tau_p \left(\exp\left(-\frac{t'}{\tau_p}\right) - 1 \right) + M_s c t - x, \tag{B1}$$

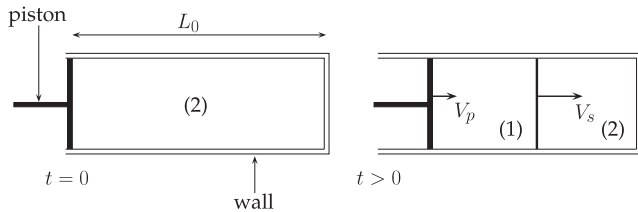


FIG. 13. Shock wave generation in a piston tube.

which can be written, by the arrangement of terms, as

$$\underbrace{\left[\frac{t' - \frac{M_s c t - x - u_g \tau_p}{\tau_p}}{\tau_p} \right]}_{\alpha} \exp\left(\frac{t' - \frac{M_s c t - x - u_g \tau_p}{\tau_p}}{\tau_p} \right) = \underbrace{\frac{u_g}{M_s c - u_g} \exp\left(-\frac{M_s c t - x - u_g \tau_p}{\tau_p} \right)}_{\beta}. \tag{B2}$$

The previous equation can also be written as $\alpha \exp(\alpha) = \beta$. We obtain, thanks to the \mathcal{W} Lambert function,³⁰ $\alpha = \mathcal{W}(\beta)$. As a consequence, one can obtain

$$t' = \tau_p \mathcal{W} \left[\frac{u_g}{M_s c - u_g} \exp\left(-\frac{M_s c t - x - u_g \tau_p}{\tau_p} \right) \right] + \frac{M_s c t - x - u_g \tau_p}{M_s c - u_g}. \tag{B3}$$

REFERENCES

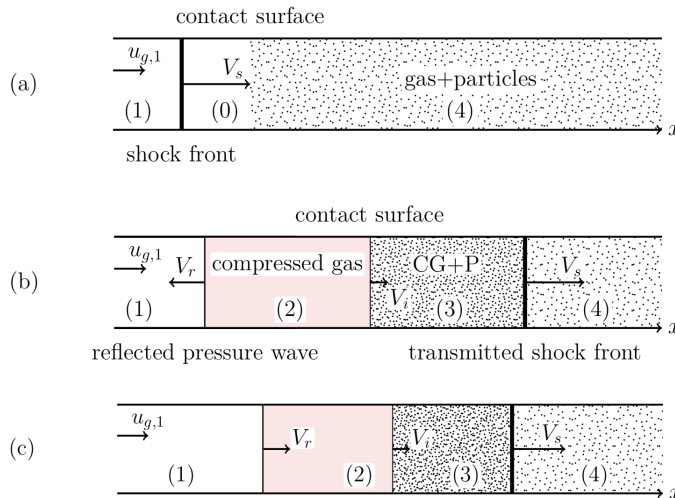
- 1 G. Carrier, “Shock waves in a dusty gas,” *J. Fluid Mech.* **4**, 376–382 (1958).
- 2 G. Jourdan, L. Biamino, C. Mariani, C. Blanchot, E. Daniel, J. Massoni, L. Houas, R. Tosello, and D. Praguine, “Attenuation of a shock wave passing through a cloud of water droplets,” *Shock Waves* **20**, 285–296 (2010).
- 3 T. Theofanous, V. Mitkin, and C.-H. Chang, “The dynamics of dense particle clouds subjected to shock waves. Part 1. Experiments and scaling laws,” *J. Fluid Mech.* **792**, 658–681 (2016).
- 4 J. Kersey, E. Loth, and D. Lankford, “Effect of evaporating droplets on shock waves,” *AIAA J.* **48**, 1975–1986 (2010).
- 5 O. Williams, T. Nguyen, A.-M. Schreyer, and A. Smits, “Particle response analysis for particle image velocimetry in supersonic flows,” *Phys. Fluids* **27**, 076101 (2015).
- 6 G. Rudinger, “Some properties of shock relaxation in gas flows carrying small particles,” *Phys. Fluids* **7**, 658–663 (1964).
- 7 M. Olim, G. Ben-Dor, M. Mond, and O. Igra, “A general attenuation law of moderate planar shock waves propagating into dusty gases with relatively high loading ratios of solid particles,” *Fluid Dyn. Res.* **6**, 185–199 (1990).
- 8 J. Geng, A. V. de Ven, Q. Yu, F. Zhang, and H. Grönig, “Interaction of a shock wave with a two-phase interface,” *Shock Waves* **3**, 193–199 (1994).
- 9 Y. Ling, L. Wagner, S. Beresh, S. Kearney, and S. Balachandar, “Interaction of a planar shock wave with a dense particle curtain: Modeling and experiments,” *Phys. Fluids* **24**, 113301 (2012).
- 10 J. McFarland, W. Black, J. Dahal, and B. Morgan, “Computational study of the shock driven instability of a multiphase particle-gas system,” *Phys. Fluids* **28**, 024105 (2016).
- 11 B. Gelfand, “Droplet break-up phenomena in flows with velocity lag,” *Prog. Energy Combust. Sci.* **22**, 201–265 (1996).
- 12 A. Hadjadj and O. Sadot, “Shock and blast waves mitigation,” *Shock Waves* **23**, 1–4 (2013).
- 13 A. Britan, H. Shapiro, M. Liverts, G. Ben-Dor, A. Chinnayya, and A. Hadjadj, “Macro-mechanical modelling of blast wave mitigation in foams. Part I: Review of available experiments and models,” *Shock Waves* **23**, 5–23 (2013).
- 14 E. D. Prete, A. Chinnayya, L. Domergue, A. Hadjadj, and J.-F. Haas, “Blast wave mitigation by dry aqueous foams,” *Shock Waves* **23**, 39–53 (2013).
- 15 G. Jourdan, C. Mariani, L. Houas, A. Chinnayya, A. Hadjadj, E. D. Prete, J.-F. Haas, N. Rambert, D. Counilh, and S. Faure, “Analysis of shock-wave propagation in aqueous foams using shock tube experiments,” *Phys. Fluids* **27**, 056101 (2015).
- 16 A. Foissac, J. Malet, M. Vetrano, J. Buchlin, S. Mimouni, F. Feuillebois *et al.*, “Droplet size and velocity measurements at the outlet of a hollow cone spray nozzle,” *Atomization Sprays* **21**, 893–905 (2011).

- ¹⁷G. Thomas, "On the conditions required for explosion mitigation by water sprays," *Process Saf. Environ.* **78**, 339–354 (2000).
- ¹⁸G. Gai, S. Kudriakov, A. Hadjadj, E. Studer, and O. Thomine, "Modeling pressure loads during a premixed hydrogen combustion in the presence of water spray," *Int. J. Hydrogen Energy* **44**, 4592–4607 (2019).
- ¹⁹T. Hanson, D. Davidson, and R. Hanson, "Shock-induced behavior in micron-sized water aerosols," *Phys. Fluids* **19**, 056104 (2007).
- ²⁰A. Chauvin, G. Jourdan, E. Daniel, L. Houas, and R. Tosello, "Experimental investigation of the propagation of a planar shock wave through a two-phase gas-liquid medium," *Phys. Fluids* **23**, 113301 (2011).
- ²¹M. Pilch and C. Erdman, "Use of breakup time data and velocity history data to predict the maximum size of stable fragments for acceleration-induced breakup of a liquid drop," *Int. J. Multiphase Flow* **13**, 741–757 (1987).
- ²²D. Guildenbecher, C. Lopez-Rivera, and P. Sojka, "Secondary atomization," *Exp. Fluids* **46**, 371–402 (2009).
- ²³Y. Ling, A. Haselbacher, and S. Balachandar, "Importance of unsteady contributions to force and heating for particles in compressible flows. Part 2: Application to particle dispersal by blast waves," *Int. J. Multiphase Flow* **37**, 1013–1025 (2011).
- ²⁴Y. Mehta, T. Jackson, J. Zhang, and S. Balachandar, "Numerical investigation of shock interaction with one-dimensional transverse array of particles in air," *J. Appl. Phys.* **119**, 104901 (2016).
- ²⁵J. Dahal and J. McFarland, "A numerical method for shock driven multiphase flow with evaporating particles," *J. Comput. Phys.* **344**, 210–233 (2017).
- ²⁶J. Wagner, S. Beresh, S. Kearney, W. Trott, J. Castaneda, B. Pruett, and M. Baer, "A multiphase shock tube for shock wave interactions with dense particle fields," *Exp. Fluids* **52**, 1507–1517 (2012).
- ²⁷Y. Sugiyama, H. Ando, K. Shimura, and A. Matsuo, "Numerical investigation of the interaction between a shock wave and a particle cloud curtain using a CFD-DEM model," *Shock Waves* **29**, 499–510 (2018).
- ²⁸K. Wingerden and B. Wilkins, "The influence of water sprays on gas explosions. Part 2: Mitigation," *J. Loss Prev. Process Ind.* **8**, 61–70 (1995).
- ²⁹S. Elghobashi, "An updated classification map of particle-laden turbulent flows," in *IUTAM Symposium on Computational Approaches to Multiphase Flow* (Springer, 2006), Vol. 81, pp. 3–10.
- ³⁰R. Corless, G. Gonnet, D. Hare, D. Jeffrey, and D. Knuth, "On the Lambert W function," *Adv. Comput. Math.* **5**, 329–359 (1996).
- ³¹E. Chang and K. Kailasanath, "Shock wave interactions with particles and liquid fuel droplets," *Shock Waves* **12**, 333–341 (2003).
- ³²O. Thomine, "Development of multi-scale methods for the numerical simulation of biphasic reactive flows," Ph.D. thesis, University of Rouen, France, 2011.
- ³³G.-S. Jiang and C.-W. Shu, "Efficient implementation of weighted ENO schemes," *J. Comput. Phys.* **126**, 202–228 (1996).
- ³⁴A. Wray, "Minimal storage time-advancement schemes for spectral methods," Technical Report No. MS 202, NASA Ames Research Center, 1991.
- ³⁵F. White, *Fluid Mechanics*, McGraw-Hill Series in Mechanical Engineering (McGraw-Hill, 2011).

Section 2: A new formulation of spray dispersion model for particle/droplet-laden flows subjected to shock waves (**submitted**)

Highlights:

- A novel reduced-order modeling (ROM) strategy is proposed for the prediction of the post-shock gas properties and the spray dispersion topology.
- Validation of the ROM methodology using available high-fidelity numerical simulations.
- A necessary condition is found to explain the presence of a spray droplets number density peak.
- Two regimes of shock-waves reflection are identified and analyzed.
- The ROM strategy is used for large-scale applications as to guide the physical modeling and to validate the fully numerical strategies.



A new formulation of a spray dispersion model for particle/droplet-laden flows subjected to shock waves

G. Gai^{1,2}, O. Thomine¹, S. Kudriakov¹ and A. Hadjadj²†

¹DES-DM2S-STMF, CEA, Université Paris-Saclay, Paris, France

²CORIA, UMR-6614, CNRS, INSA, University of Normandy, 76000 Rouen, France

(Received 10 October 2019; revised 14 August 2020; accepted 25 August 2020)

A new analytical model is derived based on physical concepts and conservation laws, in order to evaluate the post-shock gas velocity, the gas density and the spray dispersion topology during the interaction of a shock wave and a water spray in a one-dimensional configuration. The model is validated against numerical simulations over a wide range of incident Mach numbers M_s and particle volume fractions $\tau_{v,0}$. Two regimes of shock reflection have been identified depending on M_s , where the reflected pressure expansion propagates either opposite to the incident shock-wave direction for weak incident Mach numbers or along with it for strong Mach numbers. The numerical simulations reveal the presence of a particle number-density peak for $M_s > 2$ and with particle diameters of the order of $O(10)$ μm . The formation of the number-density peak is discussed and a necessary condition for its existence is proposed for the first time.

Key words: gas dynamics, shock waves, particle/fluid flow

1. Introduction

High-pressure blast waves are present and important in many natural and industrial processes, such as rocket propulsion systems, aerial boosters and explosions. Particularly important for current industrial safety issues, the accidental initiation of shock waves, such as hydrogen explosions in a confinement building, can lead to a potential hazard due to devastating effects on human lives and subsequent damage to the integrity of buildings. For safer engineering applications, several shock- and blast-wave mitigation techniques are proposed. A water spray system is one of the possible techniques used inside industrial buildings or on offshore facilities to preserve the containment integrity in case of severe accidents (Foissac *et al.* 2011). The mitigation effects of a spray system are directly dependent on the spray dispersion topology, which can be much affected by the shock-wave propagation. The interaction between spray and shock wave is also important in reacting flows, such as in internal combustion engine systems, where the combustion properties are much affected by the liquid fuels. As reported by Gelfand (1996), compression waves can, under some circumstances, coalesce and generate shock waves in two-phase reactive flows.

† Email address for correspondence: abdellah.hadjadj@insa-rouen.fr

In the past, there have been many theoretical and experimental studies investigating the physics of the interaction of droplets or solid particles/obstacles with shock waves (Carrier 1958; Rudinger 1964; Olim *et al.* 1990; Geng *et al.* 1994; Chaudhuri *et al.* 2012, 2013; Balakrishnan & Bellan 2017; Mouronval *et al.* 2019; Gai *et al.* 2020). Commonly, the particles are assumed to be at rest before they meet the shock at a given velocity. In terms of flow dynamics and after the passage of the shock, the shocked gas induces high-velocity flow, which accelerates the particles. On the other hand, the particles decelerate the post-shock gas and thus attenuate the shock intensity (Jourdan *et al.* 2010, 2015; Britan *et al.* 2013; Del Prete *et al.* 2013). In the case of a water spray and for high gas velocity, a secondary liquid droplet atomization may be encountered under certain flow conditions (e.g. Weber number $We > 12$), which leads to the formation of a fine droplet spray that enhances shock energy dissipation (Pilch & Erdman 1987; Gelfand 1996; Guildenbecher, Lopez-Rivera & Sojka 2009). The role of atomization processes is thus to increase the transfer surface (Yeom & Chang 2012) and to intensify the heat (evaporation) as well as the mass transfer. These transfer processes largely affect the thermal equilibrium conditions of the post-shock gas (Kersey, Loth & Lankford 2010) and may change the topology of the cloud dispersion, leading to shock-wave mitigation and/or a flame extinction in the case of reacting flows (Thomas 2000; Gai *et al.* 2019).

The physical mechanism of shock–droplets interaction is yet to be elucidated both quantitatively and qualitatively by means of well-conducted experiments and/or numerical modelling for low- and high-Mach-number regimes (Sugiyama *et al.* 2019). Considering the complexity of droplet deformation, evaporation and the breakup mechanisms, rigid particles are easier to handle from the experimental viewpoint and simpler to model from the numerical side. The basic concept of the interactions between a shock wave and a single particle or an array of particles has been much discussed in the recent literature (Ling, Haselbacher & Balachandar 2011; Mehta *et al.* 2016; Dahal & McFarland 2017), where the effects of particles on the gas flow are weak. Dense particles or droplet curtains have also been investigated (Wagner *et al.* 2012; Theofanous, Mitkin & Chang 2016) in which the collision between the particles becomes important.

In this study, we focus on the problem of shock waves interacting with particles having a volume fraction of the order of $O(10^{-4}–10^{-3})$, which are typical values for the sprays found in industry. According to Elghobashi (2006), a two-way formalism, which accounts for the mutual interaction between the gas flow and the droplets, can be used in such a case to describe the shock–spray interaction, meaning that the deceleration effects of the particles on the gas flow have to be taken into account, while the collisions between particles can be neglected.

From a practical point of view, concerning the modelling of an industrial building, the current existing numerical simulations cannot be applied directly as a result of high computational expense, especially for the simulation of high-Reynolds-number flows. By the necessity to develop a simple model, this paper presents a new methodology for modelling a shock wave propagating into spray droplets. The objective is twofold: (i) developing a reduced-order model of spray dispersion in the presence of shock waves taking into account the two-way interaction; and (ii) better understanding the different regimes of reflected pressure waves for both weak- and strong-Mach-number cases. From the highly resolved numerical simulation results, several fundamental hypotheses can be deduced for the shock–spray interaction. The reduced-order model is established by conservation laws, then validated through numerical simulations. The formation of the compressed gas zone is particularly discussed and a number-density peak of cloud particles is predicted, which is also seen in the highly resolved numerical simulations.

2. Modelling assumptions

In general, the following assumptions and simplifications are made in the numerical simulations: (i) The gas is considered as inviscid and obeys the perfect-gas law, and the fluid viscosity and conductivity are neglected except in the interaction with the particles. (ii) The particles are considered as inert, spherical, rigid and of uniform diameter, with constant heat capacity and a uniform temperature distribution. (iii) The volume fraction of the particles is taken to be small so that collisions between particles can be neglected, while the two-way shock–particles interaction is considered (Elghobashi 2006). (iv) Only the viscous drag forces are supposed to act on the particles. The particle-to-gas density ratio is assumed to be of the order of $O(10^3)$, the Basset force can be neglected (Thomine 2011) and we assume that the particles do not spin (the Magnus force is neglected). Gravity is at least one order of magnitude smaller than the drag force for the range of parameters in this study, and therefore it is neglected. (v) Heat transfer between gas and particles is not considered at present for the dilute, homogeneous cloud of particles (Theofanous, Mitkin & Chang 2018). (vi) Finally, the turbulent fluctuations of the solid particles are neglected in the one-dimensional configuration.

3. Governing equations

The structure of the shock–spray interaction is elucidated through direct numerical simulations carried out with a Navier–Stokes solver, named Asphodele, developed in CORIA Rouen to simulate two-phase dispersed fluid flows (Thomine 2011). The Eulerian–Lagrangian approach is used with an unresolved discrete particle model (UDPM), which relies on a larger computation cell with regard to the particle sizes and uses a drag force model to describe the gas–particle interactions. The space discretization uses a fifth-order weighted essentially non-oscillatory (WENO) scheme of Jiang & Shu (1996) with a global Lax–Friedrichs splitting, and the time resolution employs a third-order Runge–Kutta method, with a minimal storage time-advancement scheme of Wray (1991).

In the Eulerian–Lagrangian frame, the mass, momentum and energy equations for the carrier gas phase can be written as:

$$\frac{\partial \rho_g}{\partial t} + \frac{\partial}{\partial x}(\rho_g u_g) = 0, \quad (3.1)$$

$$\frac{\partial}{\partial t}(\rho_g u_g) + \frac{\partial}{\partial x}(\rho_g u_g^2 + p) = -f_D, \quad (3.2)$$

$$\frac{\partial}{\partial t}(\rho_g E_g) + \frac{\partial}{\partial x}(\rho_g H_g u_g) = -u_g f_D, \quad (3.3)$$

with

$$f_D = \frac{3}{4D} C_D \tau_v \rho_g |u_g - v_p| (u_g - v_p), \quad (3.4)$$

where the subscripts g and p represent the gas and particle phases, τ_v denotes the particle volume fraction, H_g is the specific total enthalpy of air, u and v represent the air and particle velocities, C_D is the drag coefficient defined as

$$C_D = \frac{24}{Re_p} (1 + 0.15 Re_p^{0.687}) \quad \text{with } Re_p = \frac{\rho_g |u_g - v_p| D}{\mu_g}, \quad (3.5)$$

Re_p is the particle Reynolds number, μ_g is the dynamic viscosity of the gas and D is the diameter of the particles.

For a solid particle, the general motion equation gives

$$m_p \frac{dV(t)}{dt} = F_D = \frac{\pi D^3}{6\tau_v} f_D, \quad (3.6)$$

where $m_p = \pi \rho_p D^3 / 6$ is the particle mass, ρ_p is the particle density and F_D is the drag force on the particle.

Conventionally, the unsteady terms of the gas–particle interaction, such as the added-mass effect and unsteady viscous force, are neglected for the conditions addressed, as a result of the high particle–gas density ratio $\rho_p / \rho_f = O(10^3)$ and the low particle volume fraction $\tau_{v,0} = O(10^{-4})$ in the highly dilute homogeneous gas–cloud system (Ling, Parmar & Balachandar 2013; Theofanous & Chang 2017). In this study, we mainly focus on the dynamic aspect of the shock–particle interaction. The heat transfer between the particle cloud and the gas flow may indirectly influence the gas and particle motion. However, this effect is considered to be of secondary importance for the development of the one-dimensional analytical model (Ling *et al.* 2012). The drag law is reported to yield good agreements with the dispersive behaviour found in experiments of one-dimensional shock–particle cloud interactions (Theofanous *et al.* 2018). The turbulent dispersion of the particle cloud is not considered during the shock passage.

4. Interaction mechanism

In this study, we consider the problem of the interaction between a planar shock wave and a gas–particle two-phase mixture, as illustrated in [figure 1\(a\)](#). This test problem represents one of the basic configurations commonly used to study shock-wave attenuation in multiphase flows (Chang & Kailasanath 2003). A wave travelling at velocity V_s in a shock tube of constant cross-sectional area is generated by a piston moving at a speed $u_{g,1}$. After the passage of the wave, four states can be distinguished: (1) the pure gas, (2) the compressed gas, (3) the post-shock gas–particle mixture and (4) the pre-shock gas–particle mixture. Let $M_s = V_s / c_0$ (with c_0 being the speed of sound in the unshocked gas region) denote the incident shock Mach number. For a low-velocity impact, i.e. weak Mach number ($M_s < 2$), the incident shock generates a transmitted wave and a reflected left-running pressure wave with respect to the incident shock (see [figure 1\(b\)](#)). The gas–particle contact surface moves with the transmitted shock at velocity V_i . For stronger incident Mach number, the reflected pressure expansion is seen to propagate along the original shock-propagation direction as shown in [figure 1\(c\)](#).

Space–time diagrams are plotted for the two different regimes of shock reflection, as seen in [figures 2\(a\)](#) and [2\(b\)](#). The propagation direction of the pressure expansion is closely related to the properties of the compressed gas region. For simplicity, the properties are denoted with the indices of the corresponding area as presented in [figure 1](#). The spherical particles are assumed to have a volume fraction of $\tau_{v,0} = \mathcal{V}_p / (\mathcal{V}_p + \mathcal{V}_g) = 5.2 \times 10^{-4}$, where \mathcal{V}_p and \mathcal{V}_g are the volume of particles and the volume of gas, respectively.

Particles with a mean diameter of 1 μm are used in the numerical simulations to investigate the shock–spray interaction mechanism, since they have a small characteristic response time τ_p . [Figure 3](#) gives a space distribution of gas density ρ_g ([figure 3a](#)) and velocity u_g ([figure 3b](#)) at a given time. One can identify the different zones of the interaction as well as the two regimes of shock reflection for weak- and

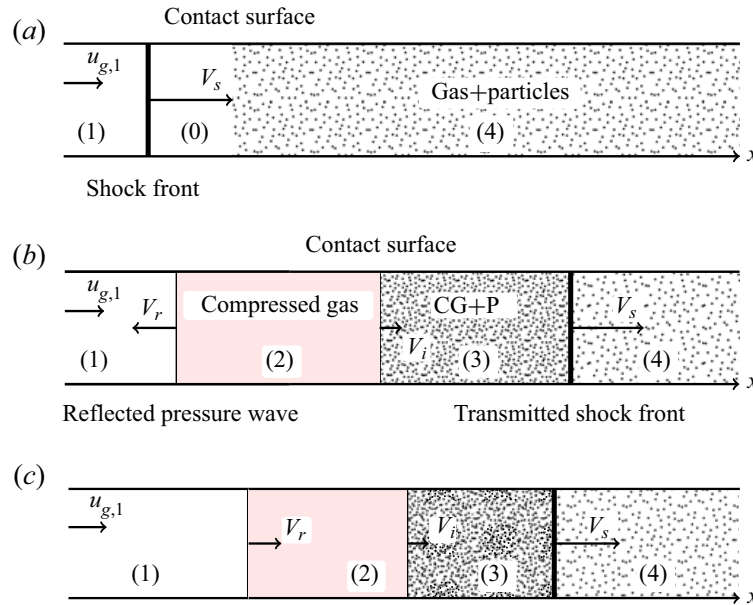


FIGURE 1. Sketch of the two regimes of shock–particle cloud interaction: (a) initial configuration; (b) weak Mach number $M_s < 2$; and (c) strong Mach number $M_s > 2$. Here CG = compressed gas, and P = particles.

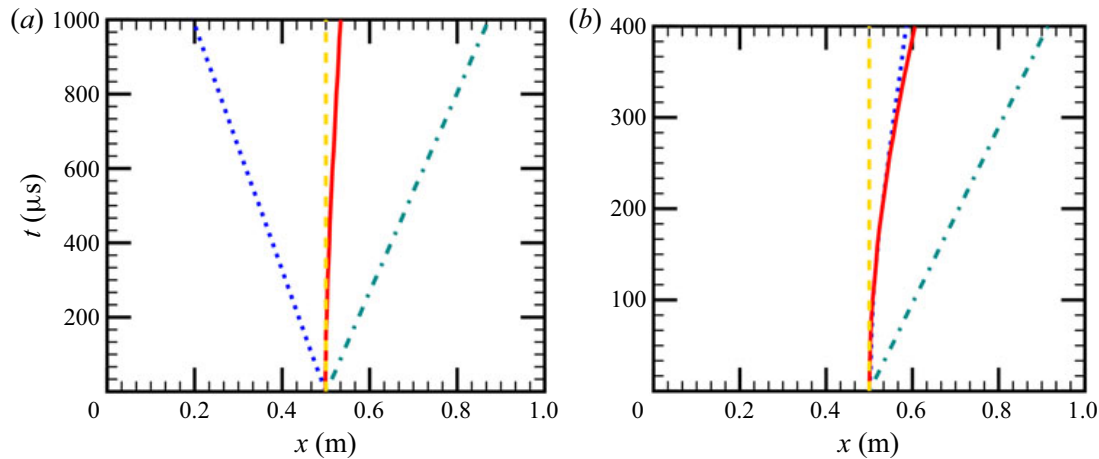


FIGURE 2. Space–time diagrams of shock–particles interaction for numerical simulations at two different Mach numbers: (a) $M_s = 1.1$ and (b) $M_s = 4.0$. Curves: transmitted wave (blue–green dot–dashed); reflected wave (blue dotted); particle interface (red solid); and initial particle interface (orange dashed).

strong-Mach-number cases as described in figure 1. In what follows we will derive the relationships between pressure, gas density and velocity. These observations will contribute to the development of the reduced-order modelling approach.

4.1. Pressure and density relationships in the compressed gas

To better represent the quantities in different zones, the gas density and velocity evolutions in figures 3(a) and 3(b) are sketched in figure 4. The evolutions of the particle volume fraction and the particle mean density are shown in figures 3(c) and 3(d). As illustrated in

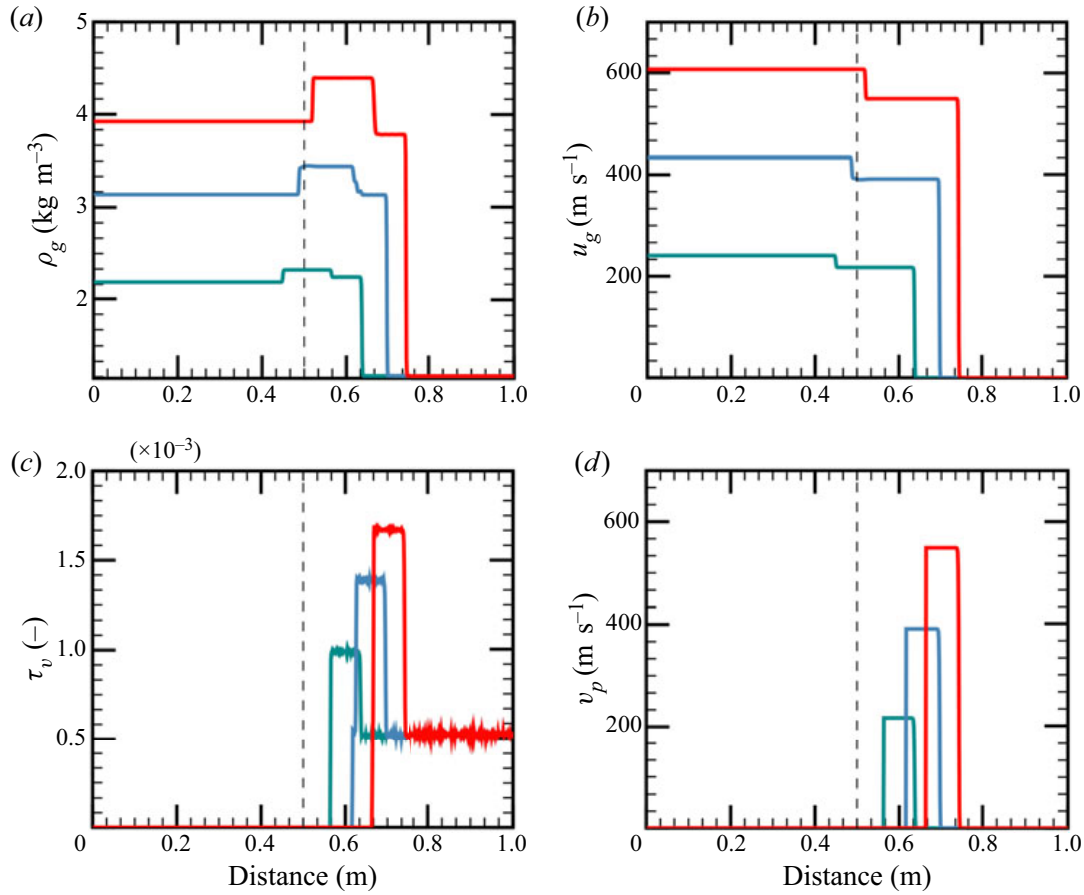


FIGURE 3. Evolution of (a) gas mass density ρ_g , (b) gas velocity u_g , (c) particle volume fraction τ_v and (d) particle mean velocity v_p for numerical simulations, at $t = 300 \mu\text{s}$, $D = 1 \mu\text{m}$ and $\tau_{v,0} = 5.2 \times 10^{-4}$, for different Mach numbers. Curves: $M_s = 1.5$ (blue-green); $M_s = 2.0$ (blue); $M_s = 2.5$ (red); and original gas–particle contact surface (black dashed).

figure 1(b) and (c), after the interaction of the shock with the gas–particle contact surface, a compressed gas zone (2) is generated. From a modelling point of view, it is important to derive relationships between the pure gas zone (1) and the compressed gas zone (2), as follows:

$$p_{g,1} < p_{g,2}, \quad \rho_{g,1} < \rho_{g,2}, \quad u_{g,1} > u_{g,2}. \quad (4.1a-c)$$

Similarly, between the compressed gas zone (2) and the post-shock gas–particle mixture (3), one has the following:

$$p_{g,2} = p_{g,3}, \quad \rho_{g,2} > \rho_{g,3}, \quad u_{g,2} = u_{g,3}. \quad (4.2a-c)$$

With regard to the gas density distribution, and as depicted in figure 4(a), the gas density inside the post-shock gas–particle mixture $\rho_{g,3}$ might be higher than, lower than or equal to the density of the pure gas zone $\rho_{g,1}$. One can use $\rho_{g,3l}$, $\rho_{g,3c}$ and $\rho_{g,3r}$ to denote the three different cases. The numerical results show that, when one has $\rho_{g,1} < \rho_{g,3l}$ (for weak M_s), the reflected pressure expansion tends to propagate towards the x^- direction, while if $\rho_{g,1} > \rho_{g,3r}$ (for strong M_s), the pressure expansion propagates inversely for most numerical simulations.

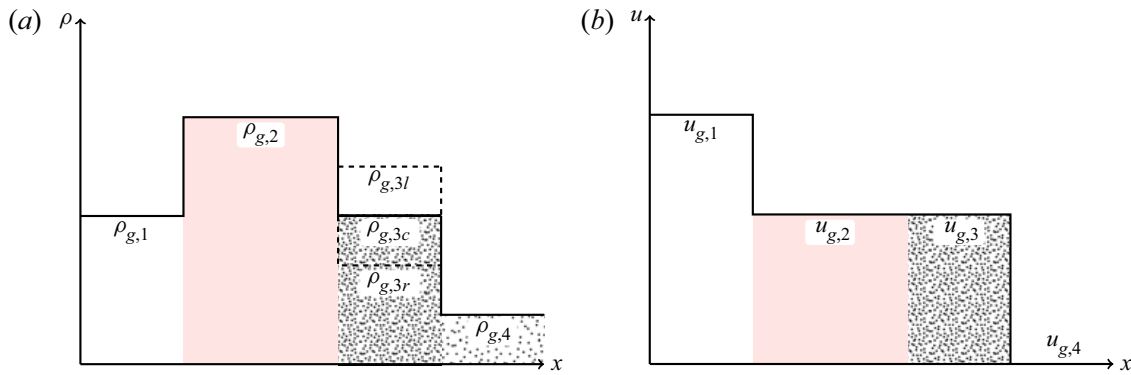


FIGURE 4. Sketch of gas properties after the shock–particle cloud interaction: (a) density and (b) gas velocity evolutions.

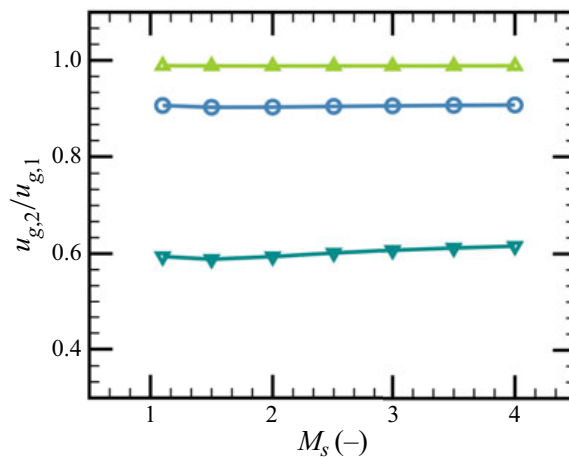


FIGURE 5. Velocity ratio $u_{g,2}/u_{g,1}$ over a wide range of incident shock Mach numbers, for $D = 1 \mu\text{m}$ and: $\tau_{v,0} = 5.2 \times 10^{-5}$ (green), $\tau_{v,0} = 5.2 \times 10^{-4}$ (blue) and $\tau_{v,0} = 5.2 \times 10^{-3}$ (blue-green).

The gas velocity evolution, described in figure 4(b), indicates that, during the interaction, one always has $u_{g,1} > u_{g,2}$, $u_{g,2} = u_{g,3}$ and $u_{g,3} > u_{g,4} = 0$. It is interesting to note that, for a wide range of particle volume fractions ($\tau_{v,0} \approx O(10^{-5}–10^{-3})$), the velocity ratio in the pure and in the compressed gas regions is almost constant over a wide range of Mach numbers ($1 < M_s < 4$) (see figure 5). We assume therefore that

$$\frac{u_{g,2}}{u_{g,1}} \approx f(\tau_{v,0}), \quad (4.3)$$

where $\tau_{v,0}$ is the initial particle volume fraction, which is considered to be the main factor influencing the variation of $u_{g,2}/u_{g,1}$. Equations (4.1a–c) to (4.3) are considered as the fundamental hypothesis of the reduced-order modelling.

5. Reduced-order modelling

For practical applications, the development of a reduced-order model that takes into consideration the two-way shock–spray interaction is given in this section. The rationality

of the above-mentioned hypotheses is discussed and the validation of the model is carried out with the Navier–Stokes (NS) code.

Mass conservation through the interface between the pure gas (1) and the compressed gas (2) gives

$$\int_{x_1}^{x_2} \left(\frac{\partial \rho_g}{\partial t} \right) dx = \rho_{g,1} u_{g,1} - \rho_{g,2} u_{g,2}, \quad (5.1)$$

where the integral expression on the left-hand side provides the direction of the pressure expansion. The pressure wave propagates towards the x^+ direction if the integral is negative and *vice versa*. Thus the quantity $(\rho_{g,1} u_{g,1} - \rho_{g,2} u_{g,2})$ can be used as a criterion for the identification of the reflection regime of the pressure wave. This criterion is valid for cases corresponding to the initial configuration given in [figure 1\(a\)](#).

The properties of the pure gas zone (1) can be obtained analytically (White 2011):

$$\frac{2}{\gamma + 1} \frac{M_s^2 - 1}{M_s} = \frac{u_{g,1}}{c_0}, \quad (5.2)$$

$$\frac{p_1}{p_0} = \mathcal{F}_1(M_s, \gamma), \quad \frac{T_1}{T_0} = \frac{\mathcal{F}_1(M_s, \gamma) \mathcal{F}_2(M_s, \gamma)}{M_s^2}, \quad \frac{\rho_1}{\rho_0} = \frac{p_1 T_0}{p_0 T_1}, \quad (5.3a-c)$$

where

$$\mathcal{F}_1(M_s, \gamma) = \frac{2}{\gamma + 1} \left(\gamma M_s^2 - \frac{\gamma - 1}{2} \right), \quad \mathcal{F}_2(M_s, \gamma) = \frac{2}{\gamma + 1} \left(1 + \frac{\gamma - 1}{2} M_s^2 \right). \quad (5.4a,b)$$

Note that the gas properties in the gas–particle mixture (4) are identical to those of the pre-shock pure gas area (0). Meanwhile, the gas properties in zones (2) and (3) need to be estimated properly.

5.1. Velocity of the compressed gas

It is noted from various numerical simulations that, for weak initial Mach numbers, the reflected pressure expansion has the velocity of the sound speed in zone (1). Here we consider the particular case where $\rho_{g,1} = \rho_{g,3c}$, as illustrated in [figure 4\(a\)](#). In this case, the interface between zone (1) and zone (2) remains stationary in the laboratory frame, which can be characterized by $u_{g,1} = c_1 = \sqrt{\gamma p_1 / \rho_{g,1}}$, with c_1 being the sound speed in zone (1). Using the gas properties across the shock wave (White 2011), one can deduce that

$$c_0 \frac{2}{\gamma + 1} \frac{M_s^2 - 1}{M_s} = \sqrt{\frac{\gamma p_1}{\rho_{g,1}}}, \quad (5.5)$$

which can be simplified to

$$(M_s^2 - 1)^2 = \left(\frac{\gamma + 1}{2} \right)^2 \mathcal{F}_1(M_s, \gamma) \mathcal{F}_2(M_s, \gamma). \quad (5.6)$$

The Mach number that satisfies (5.6) is known as the critical Mach number, and is $M_{s,cr} = 2.0$ for a monatomic ideal gas ($\gamma = 7/5$). The results of [figure 3\(a\)](#) show that

$\rho_{g,3} = \rho_{g,1}$ and $u_{g,3} = u_{g,2}$ when $M_s = M_{s,cr}$. The conservation of kinetic energy before and after the passage of the shock gives

$$\rho_{g,1}u_{g,1}^2 = \tau_{v,0}\rho_p u_{g,3}^2 + (1 - \tau_{v,0})\rho_{g,3}u_{g,3}^2, \tag{5.7}$$

where $u_{g,3}$ is the velocity of the shocked gas in the gas–particle mixture and ρ_p is the mass density of the particles. By combining (4.3) and (5.7), the estimate of $u_{g,2}$ can be obtained for a given $\tau_{v,0}$ as

$$\frac{u_{g,2}}{u_{g,1}} \approx \left(\frac{u_{g,2}}{u_{g,1}} \right)_{cr} = \sqrt{\frac{1}{1 - \tau_{v,0} + \tau_{v,0} \frac{\rho_p}{\rho_{g,1}}}}. \tag{5.8}$$

5.2. Density of the compressed gas

To estimate the density of the compressed gas $\rho_{g,2}$, one can assume that the pressure wave reflection process obeys an isentropic expansion. The isentropic hypothesis is discussed in appendix A. The conservation of momentum leads to

$$\rho_{g,2}u_{g,2}^2 + p_1 \left(\frac{\rho_{g,2}}{\rho_{g,1}} \right)^\gamma = \rho_{g,1}u_{g,1}^2 + p_1. \tag{5.9}$$

For a given estimated $u_{g,2}$, the solution of (5.9) can provide an estimate of $\rho_{g,2}$. A Newton–Raphson method is used to solve (5.9).

The estimate of $\rho_{g,2}$ can also contribute to the evaluation of the intensity of the pressure expansion. Moreover, knowing the two properties of the flow, $u_{g,2}$ and $\rho_{g,2}$, one can easily predict the propagation direction of the pressure expansion after the interaction of the shock with the spray by using the criterion given by (5.1).

5.3. Spray dispersion

Equation (5.7) can also be applied to estimate the particle dispersion in the post-shock gas–particle mixture (3). Figure 6 shows the configuration in the proximity of the transmitted shock inside the gas–particle zone in the shock-attached frame, where the properties across the transmitted shock wave are depicted in figure 6. One knows that

$$p_3 = p_2, \quad u_{g,3} = u_{g,2}, \quad u_{g,4} = 0, \tag{5.10a–c}$$

where $u_{g,3}$ and $u_{g,2}$ are estimated quantities. Thus, the conservation of mass across the shock wave gives

$$\rho_{g,3}(V_s - u_{g,2}) = \rho_{g,4}V_s. \tag{5.11}$$

Taking into account the initial volume fraction $\tau_{v,0}$ of particles, the conservation of momentum gives

$$p_2 + \rho_{g,3}(1 - \tau_v)(V_s - u_{g,2})^2 + \rho_p \tau_v (V_s - u_{g,2})^2 = p_4 + \rho_{g,4}(1 - \tau_{v,0})V_s^2 + \rho_p \tau_{v,0}V_s^2, \tag{5.12}$$

where τ_v is the volume fraction of the particles in the post-shock region (3). Before the shock passage, the initial cloud length is $V_s t$ and becomes $(V_s - u_{g,2})t$ afterwards.

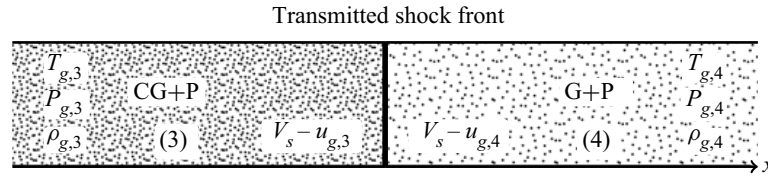


FIGURE 6. Sketch of the shock front transmitted into the gas–particle zone in the shock-attached frame. Here CG = compressed gas, P = particles, and G = unshocked gas.

Therefore, the post-shock volume fraction of the particles τ_v can be linked to the pre-shock volume fraction $\tau_{v,0}$ through

$$\tau_v = \tau_{v,0} \frac{V_s}{V_s - u_{g,2}}. \quad (5.13)$$

By combining (5.11)–(5.13), one can deduce an analytical expression for the velocity of the transmitted shock wave V_s :

$$V_s = \frac{p_2 - p_4}{(\rho_{g,4} + \rho_p \tau_{v,0}) u_{g,2}}. \quad (5.14)$$

Knowing V_s , the volume fraction of the particles in region (3) can be calculated by (5.13).

5.4. Assessment of the reduced-order model

From the above discussion, the modelling is achieved for $u_{g,2}$, $\rho_{g,2}$, p_2 and τ_v , for a given initial volume fraction $\tau_{v,0}$ and incident Mach number M_s . The estimates of $\rho_{g,2}$ and τ_v rely especially on the accuracy of $u_{g,2}$. However, the post-shock maximal particle volume fraction has similar values for particles of different diameters. The maximal volume fractions of small particles can provide guideline values for the larger ones. The assessment of the proposed model, especially for the estimation of $u_{g,2}$, $\rho_{g,2}$ and τ_v , is achieved through a direct comparison with the results from the NS solver.

Taking an example of the initial particle volume fraction $\tau_{v,0} = 5.2 \times 10^{-4}$, in critical conditions, in which $\rho_{g,3c} = \rho_{g,1}$, the velocity ratio calculated by the NS code is $u_{g,2}/u_{g,1} = 0.9$, and (5.7) gives a ratio of 0.93. If the gas velocity $u_{g,2}$ in the compressed zone is correctly estimated, the model evaluations for $\rho_{g,2}$ and p_2 are in good agreement with the numerical simulations, as shown in figure 7(a–d). For $\tau_{v,0} = 5.2 \times 10^{-4}$ and $M_s = 2.0$, the density estimated by (5.9) is $\rho_{g,2} = 3.4 \text{ kg m}^{-3}$, and the value calculated by the NS code is $\rho_{g,2} = 3.44 \text{ kg m}^{-3}$.

For the ratio of the particle volume fraction $\tau_v/\tau_{v,0}$, using (5.13), one can have higher relative differences compared to the numerical simulation, since the estimation of this ratio is based on the modelling of both $u_{g,2}$ and $\rho_{g,2}$. In the case where these two parameters have a relative difference of 5%, one may have a relative difference of 28% for $\tau_v/\tau_{v,0}$ as a result of the difference accumulation, as shown in figure 7(d).

The analytical model is assessed in this study by the NS solver for the interaction between supersonic flows of Mach number $M_s = 1.1$ –4 and a particle cloud of volume fraction $\tau_{v,0} = 10^{-5}$ – 10^{-3} and of particle diameters $D = 1$ – $10 \text{ }\mu\text{m}$. For shock waves of Mach number higher than $M_s = 5$, the heat transfer induced by the hypersonic shock should be considered. The present model can be applied to solid particles or liquid droplets having relatively high surface tension values. For higher volume fraction $\tau_{v,0} > 10^{-3}$ of particle clouds, the interactions among the particles become important, such as particle

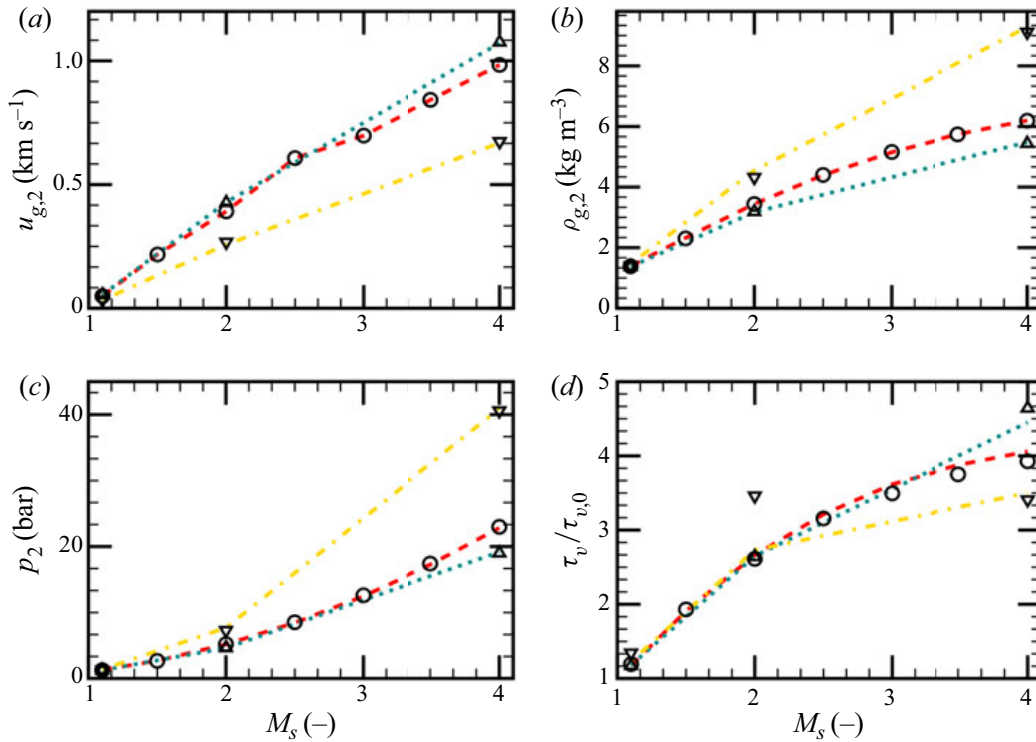


FIGURE 7. Evolution of different flow properties as a function of M_s : (a) gas velocity, (b) gas density, (c) gas pressure and (d) particle volume fraction. Simulation using NS code: $\tau_{v,0} = 5.2 \times 10^{-3}$ (yellow dot-dashed); $\tau_{v,0} = 5.2 \times 10^{-4}$ (red dashed); and $\tau_{v,0} = 5.2 \times 10^{-5}$ (blue-green dotted). Current model: $\tau_{v,0} = 5.2 \times 10^{-3}$ (inverted triangles); $\tau_{v,0} = 5.2 \times 10^{-4}$ (circles); and $\tau_{v,0} = 5.2 \times 10^{-5}$ (triangles).

collision and coalescence of droplets, as noted by Elghobashi (1994). For water droplets of diameter larger than $D > 10 \mu\text{m}$, the breakup of the droplets in high-velocity gas flow becomes important. Particles of diameter $O(10 \mu\text{m})$ can be regarded as stable fragments of larger droplets according to Pilch & Erdman (1987).

5.5. Influence of the particle response time τ_p

The particle response time scale τ_p is defined to describe the response ability of the particles to the carrier flow movement, which can have a simple expression:

$$\tau_p = \frac{\rho_p D^2}{18\mu_g} \frac{1}{\Phi(Re_p)}, \quad \Phi(Re_p) = 1.0 + 0.15Re_p^{0.687}. \quad (5.15a,b)$$

Here ρ_p is the mass density of the particles, D is the diameter of the particles, μ_g is the dynamic viscosity of air, and Re_p is the particle Reynolds number.

Let us consider a shock wave of $M_s = 1.1$ interacting with a cloud of particles. The influence of the particle response time on resulting flow evolution is shown in figure 8 at $t = 600 \mu\text{s}$ after the start of the interaction.

Figure 8(a) shows the evolution of the particle volume fractions for different particle diameters varying from $1 \mu\text{m}$ to $10 \mu\text{m}$, with particle response time varying from 2.3×10^{-6} s to 1.1×10^{-4} s. For a given particle diameter, the particle volume fraction increases

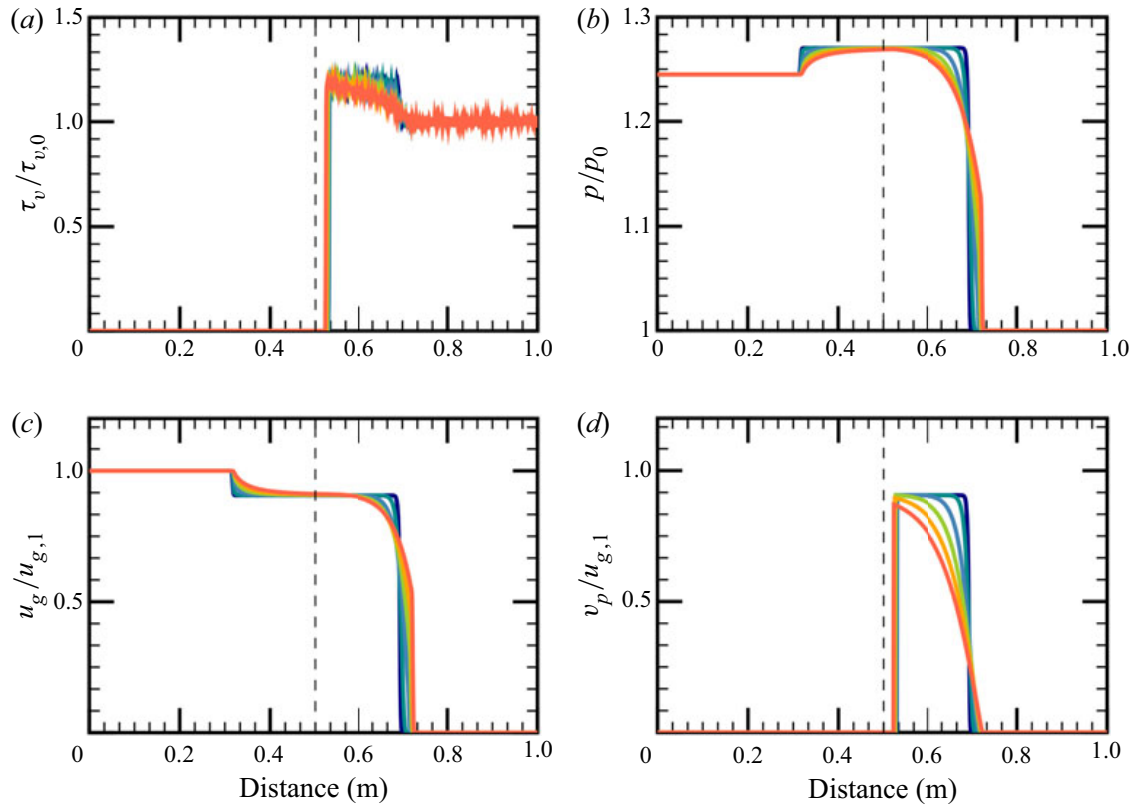


FIGURE 8. Evolution with distance of normalized (a) particle volume fraction, (b) gas pressure, (c) gas velocity and (d) particle velocity, at $t = 600 \mu\text{s}$, $M_s = 1.1$, $\tau_{v,0} = 5.2 \times 10^{-4}$, $p_0 = 1.013 \text{ bar}$ and $u_{g,0} = 55.19 \text{ m s}^{-1}$, for different particle diameters. Curves: $D = 1 \mu\text{m}$, $\tau_p = 2.3 \mu\text{s}$ (dark blue); $D = 2 \mu\text{m}$, $\tau_p = 7.7 \mu\text{s}$ (blue-green); $D = 4 \mu\text{m}$, $\tau_p = 25 \mu\text{s}$ (blue); $D = 6 \mu\text{m}$, $\tau_p = 49 \mu\text{s}$ (green); $D = 8 \mu\text{m}$, $\tau_p = 78 \mu\text{s}$ (orange); $D = 10 \mu\text{m}$, $\tau_p = 0.1 \text{ ms}$ (red); and original gas–particle contact surface (black dashed).

after the passage of the shock. The smaller particles respond faster than the larger ones. Thus, the gas–particle contact surface moves faster for the smaller particles.

Figure 8(b) shows the pressure evolution for different particle diameters. When the shock reaches the gas–particle contact surface, the pressure increases, generating two pressure waves in opposite directions: transmitted and reflected waves. The reflected wave is slower than the transmitted one. The attenuation effect of the small particles on the shock velocity is more evident. The velocity of the reflected pressure wave does not depend on the particle diameter.

The gas velocity evolution for the passage of a shock wave through a cloud of particles is depicted in figure 8(c). The small particles respond rapidly to the shock wave and the gas velocity is reduced immediately after the shock passage. The larger particles are more difficult to accelerate as a result of high inertia, as one can see in figure 8(d), showing the evolution of the particles after the passage of a shock wave.

From figure 8, the general conclusion that can be drawn is that the particles of larger diameter have a stronger attenuation effect on the transmitted shock wave as well as on the reflected pressure wave profiles. The opposite is true for the transmitted shock-wave velocity, i.e. the smaller the particles are, the slower the corresponding shock wave is. The interesting fact is that the velocity of the reflected pressure wave does not depend on the particle diameter. Moreover, analyses of the computed results show that the entropy

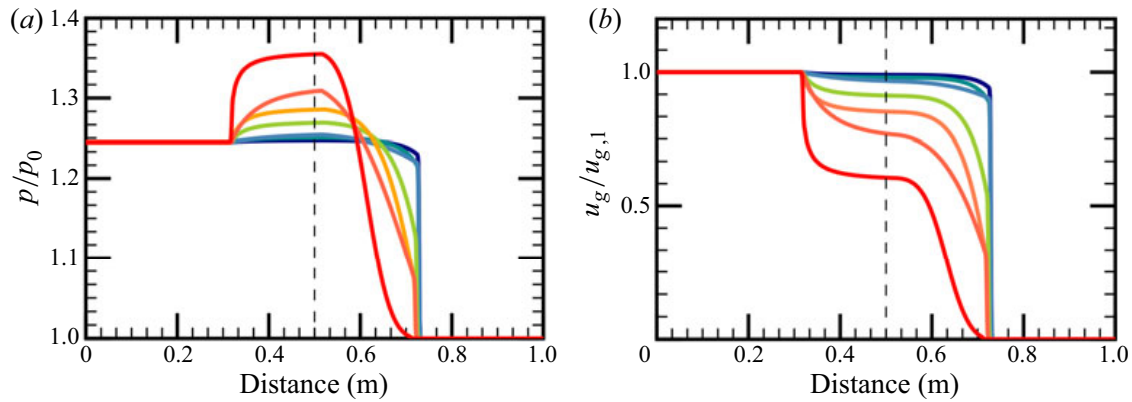


FIGURE 9. Evolution with distance of normalized (a) pressure p and (b) gas velocity u_g , at $t = 600 \mu\text{s}$, $M_s = 1.1$, $D = 10 \mu\text{m}$, $p_0 = 1.013 \text{ bar}$ and $u_{g,0} = 55.19 \text{ m s}^{-1}$, for different particle volume fractions. Curves: $\tau_{v,0} = 5 \times 10^{-5}$ (dark blue); $\tau_{v,0} = 1 \times 10^{-4}$ (blue-green); $\tau_{v,0} = 2 \times 10^{-4}$ (blue); $\tau_{v,0} = 5 \times 10^{-4}$ (green); $\tau_{v,0} = 1 \times 10^{-3}$ (orange); $\tau_{v,0} = 2 \times 10^{-3}$ (orange-red); $\tau_{v,0} = 5 \times 10^{-3}$ (red); and original gas–particle contact surface (black dashed).

measure, i.e. P/ρ^γ , is nearly constant across the reflected wave. This property is used in the reduced-order modelling.

5.6. Effects of the particle volume fraction

In this section, the effects of the initial particle volume fraction $\tau_{v,0}$ are investigated. Particles of diameter $10 \mu\text{m}$ are used with volume fractions varying from 5×10^{-5} to 5×10^{-3} .

Figure 9(a) gives the pressure evolutions after the shock passage. The particles of volume fraction $\tau_{v,0} = 5 \times 10^{-5}$ have a very small influence on the pressure evolution. A high volume fraction $\tau_{v,0} = 5 \times 10^{-3}$ seems to totally attenuate the transmitted shock at around $x = 0.7 \text{ m}$. The reflected pressure wave can be noted for all particle volume fractions. The comparison shows that a high particle volume fraction can increase the reflected pressure magnitude and attenuate the transmitted shock wave. Moreover, the reflected shock waves have similar velocities for different volume fractions. The gas velocity evolutions for different particle volume fractions are presented in figure 9(b). The reduction of the gas velocity is much reinforced by the increase of the particle volume fraction.

6. Particle number-density peak

In this section, we discuss the formation mechanism of the compressed gas zone (2), which leads to a particle number-density peak, when some necessary conditions are met. This number-density peak can dramatically change the spray dispersion topology.

6.1. Formation of the compressed gas zone

As illustrated in figure 1(a), initially the gas–particle contact surface separates the pure gas (1) from the gas–particle zone (4). After the passage of the shock, the pure gas zone (1) interacts directly with the post-shock gas–particle zone (3), before the formation of the compressed gas zone (2), where no reflected pressure expansion exists (see figure 10a).

In order to simplify the analysis, one can locate the origin of the coordinates at the gas–particle contact surface as illustrated in figure 10(b). Denoting the velocity of the

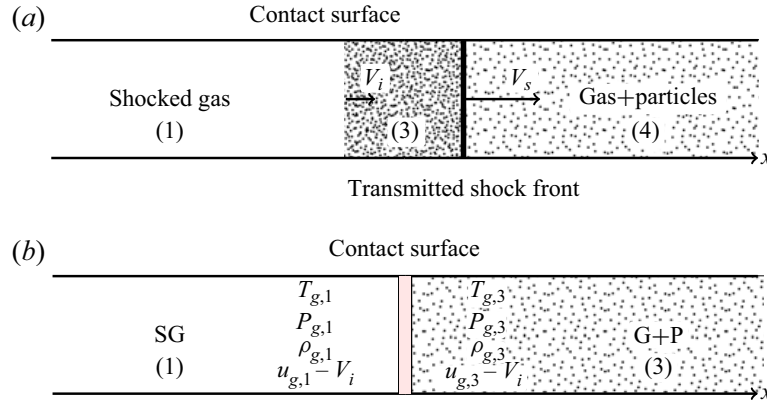


FIGURE 10. Sketch of the shock and gas–particle contact surface during the particle acceleration period. (a) Global acceleration configuration. (b) Local acceleration configuration in the proximity of the contact surface in the interface-attached frame. The red zone denotes the creation of the compressed gas. Here SG = shocked gas, G = gas, and P = particles.

contact surface as V_i , the gas velocity of the upstream flow is $(u_{g,1} - V_i)$. Similarly, the post-shock gas velocity in zone (3) can be expressed as $(u_{g,3} - V_i)$. Mass conservation across the contact surface gives

$$\rho_{g,1}(u_{g,1} - V_i) = \rho_{g,3}(u_{g,3} - V_i). \tag{6.1}$$

Assuming that the gas velocity before the first particle u_g is constant, we have the interface velocity $V_i(t) = u_{g,1}[1 - \exp(-t/\tau_p)]$, where τ_p is the particle response time.

The gas velocity in zone (3) can be estimated from the momentum conservation equation at point x_0 :

$$\frac{du(x_0, t)}{dt} = -\frac{m_p}{\rho_g \mathcal{V}_g} \frac{dV_i}{dt} = -\tau_{v,0} \frac{\rho_p}{\rho_g} \frac{dV_i}{dt}. \tag{6.2}$$

For the simplicity of the analysis, we assume that the particle response time with nonlinear correction term defined in (5.15a,b) remains constant during the particle acceleration process. Thus, one has

$$\frac{dV_i}{dt} = \frac{1}{\tau_p}(u(x_0, t) - V_i(x_0, t)). \tag{6.3}$$

The gas velocity before the first particle is assumed to be constant, $u(x_0, t) = u_{g,1}$. Considering that the gas properties around the contact particles are similar to those in the upstream flow $\rho_g = \rho_{g,1}$, one has

$$\frac{du}{dt} = -\frac{\tau_{v,0}}{\tau_p} \frac{\rho_p}{\rho_{g,1}} u_{g,1} \exp\left(-\frac{t}{\tau_p}\right). \tag{6.4}$$

Knowing that $u = u_{g,1}$ at $t = 0$, the gas velocity of zone (3) can be obtained:

$$u_{g,3}(t) = u_{g,1} + \frac{\tau_{v,0}\rho_p}{\rho_{g,1}} u_{g,1} \left[\exp\left(-\frac{t}{\tau_p}\right) - 1 \right]. \tag{6.5}$$

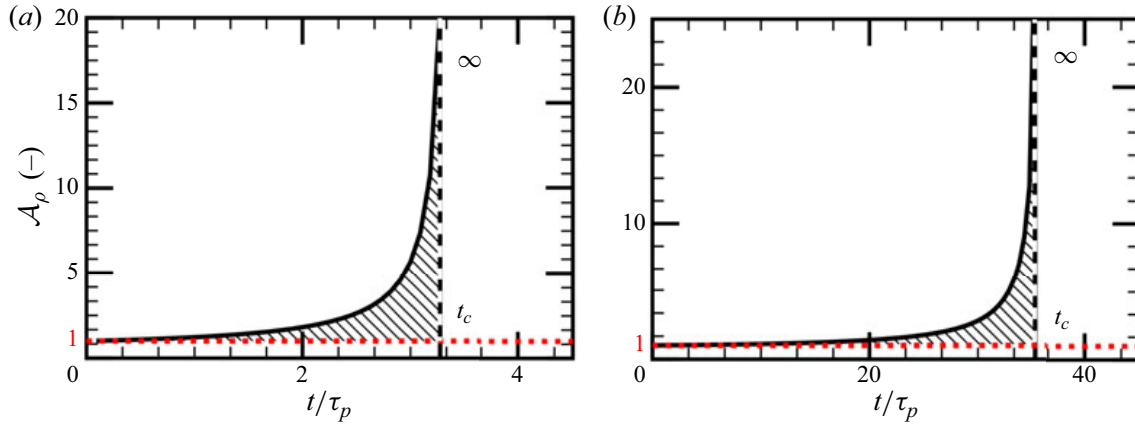


FIGURE 11. Amplification factor \mathcal{A}_ρ for two different incident Mach numbers: (a) $M_s = 1.1$, $\tau_p = 0.1$ ms with $D = 10$ μm and $\tau_{v,0} = 5.2 \times 10^{-4}$; and (b) $M_s = 4.0$, $\tau_p = 21$ μs with $D = 10$ μm and $\tau_{v,0} = 5.2 \times 10^{-4}$.

By combining (6.5) and (6.1), one has

$$\frac{\rho_{g,3}(t)}{\rho_{g,1}} = \mathcal{A}_\rho = \frac{1}{1 + \frac{\tau_{v,0}\rho_p}{\rho_{g,1}} - \frac{\tau_{v,0}\rho_p}{\rho_{g,1}} \exp\left(\frac{t}{\tau_p}\right)}. \quad (6.6)$$

The right-hand side of (6.6) can be seen as an amplification factor \mathcal{A}_ρ of the gas density due to the deceleration of the gas flow in the presence of particles. This factor is plotted as a function of the normalized time in figure 11.

With the assumption that the upstream gas density $\rho_{g,1}$ and velocity $u_{g,1}$ are constant during the acceleration process and to ensure the conservation of mass across the gas–particle contact surface, the density of the gas might diverge to a very high value, as well as the gas pressure inside the gas–particle zone (3) (see figure 11). This is the reason why a compressed gas in zone (2) is created aside from the gas–particle contact surface in the pure gas region (1).

6.2. Necessary condition for the density peak

Before the formation of the compressed gas zone, the post-shock gas density can increase up to a very high value at t_c when

$$1 + \frac{\tau_{v,0}\rho_p}{\rho_{g,1}} - \frac{\tau_{v,0}\rho_p}{\rho_{g,1}} \exp\left(\frac{t_c}{\tau_p}\right) = 0. \quad (6.7)$$

One can see that the gas velocity in the gas–particle zone (3) decreases from $u_{g,1}$ to a lower value during the time interval $[0, t_c]$. A negative gas velocity gradient leads to a negative particle velocity gradient, which forms the number-density peak of particles inside the gas–particle zone (3), if this negative gradient exists for a long enough time in the gas–particle mixture.

However, if one has $t_c \approx O(\tau_p)$, the compressed gas zone is created immediately when the shock reaches the gas–particle contact surface. In this case, the particle number-density peak cannot be obtained. For example, when $D = 10$ μm , $M_s = 1.1$, no number-density

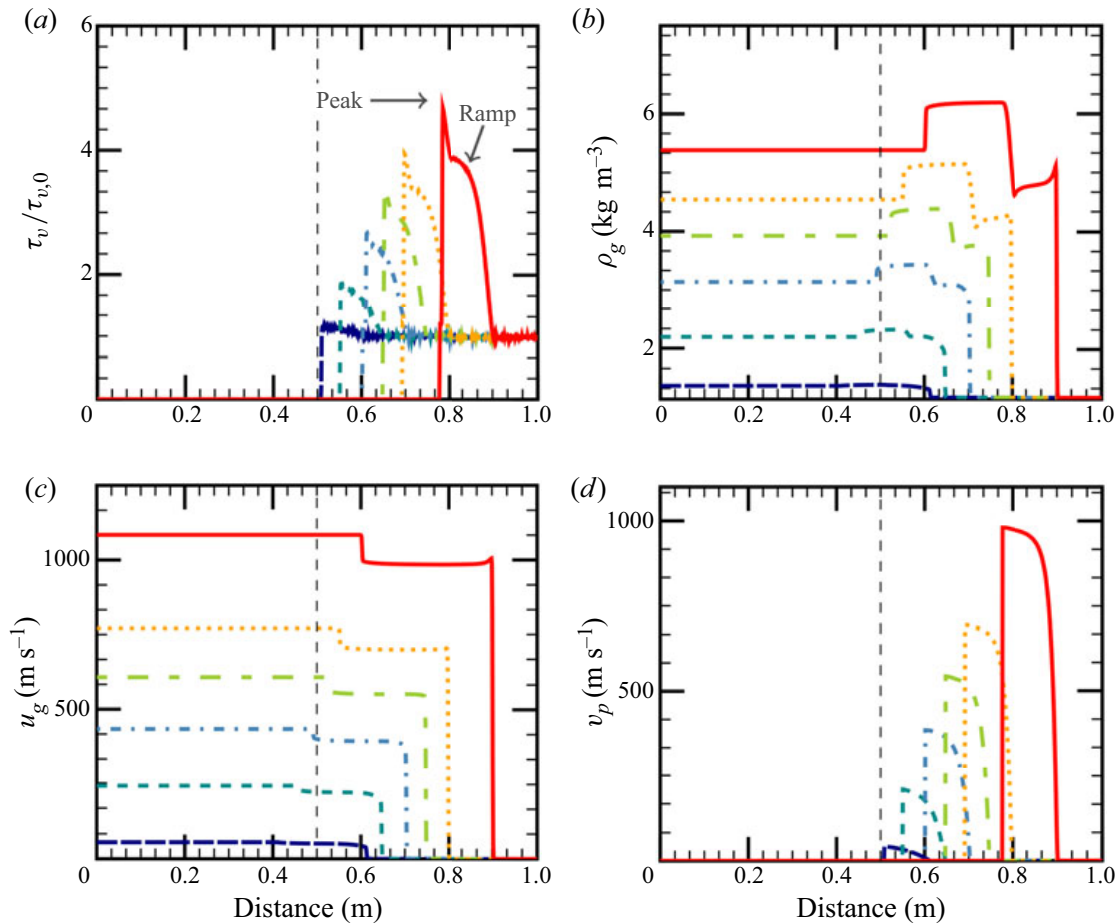


FIGURE 12. Evolution of (a) particle volume fraction τ_v , (b) gas mass density ρ_g , (c) gas velocity u_g and (d) particle mean velocity v_p , at $t = 300 \mu\text{s}$, $D = 10 \mu\text{m}$ and $\tau_{v,0} = 5.2 \times 10^{-4}$, for different Mach numbers. Curves: $M_s = 1.1$ (dark blue long dashed); $M_s = 1.5$ (blue-green dashed); $M_s = 2.0$ (blue dot-dashed); $M_s = 2.5$ (green long/short dashed); $M_s = 3.0$ (yellow dotted); $M_s = 4.0$ (red solid); and original gas–particle contact surface (black dashed).

peak can be seen in [figure 11\(a\)](#). The condition $t_c \gg \tau_p$ seems to be necessary for the appearance of the number-density peak, since only in this case can the negative velocity gradient be obtained for a long enough period inside the gas–particle zone (3).

The amplitude of the number-density peak is related to two factors: the residence time of the negative gas velocity gradient t_c , and the amplitude of the density change, which can be determined by both the particle cloud and the shock-wave intensity. In other words, this phenomenon is associated with the deceleration capacity of the particles characterized by τ_p and $\tau_{v,0}$ as well as the incident Mach number M_s .

The prediction of the number-density peak is confirmed by the numerical simulations and presented in [figure 12\(a\)](#). For a given volume fraction $\tau_{v,0} = 5.2 \times 10^{-4}$, particles of diameter $D = 10 \mu\text{m}$ give a number-density peak after the passage of a shock wave of Mach number $M_s = 4.0$ ($t_c \gg \tau_p$). It is seen that the density peak increases with the initial Mach number M_s . The particle number-density peak is depicted in [figure 12\(a\)](#); it differs from the volume fraction ramp presented in Saito, Marumoto & Takayama (2003). The number density is located inside the ramp and has a higher value for particle volume fraction.

The evolution of the gas density is shown in [figure 12\(b\)](#). One can note that the gas density increases abruptly at the location of the particle number-density peak. The decrease of the gas density downstream of the transmitted shock is due to the two-way coupling. The evolutions of the gas and particle mean velocity are given in [figure 12\(c\)](#) and [\(d\)](#), respectively.

7. Summary

In this paper, the problem of shock-wave propagation into a dispersed spray area is investigated both numerically and analytically in a one-dimensional shock tube configuration. Numerical results reveal the existence of two regimes of shock reflections, depending on the initial shock Mach number, in which the reflected pressure expansion can propagate either along or opposite to the incident-shock direction. The formation of a compressed gas layer at the gas–spray interface is seen to be a trigger of the two shock reflection regimes. The change of the post-shock spray dispersion is discussed, and it is found that the evaluation of the spray dispersion, characterized by the volume fraction of the particles, mainly depends on the correct estimation of post-shock gas properties.

Accordingly, a new analytical model is derived to evaluate the post-shock gas velocity as well as the gas density in the compressed zone. A two-way approach is adopted in this model to account for the mutual interaction between the shock and the spray. The presence of a particle number-density peak is predicted for strong Mach numbers ($M_s > 2$) and moderate particle diameter ($D = 10 \mu\text{m}$). A necessary condition for the formation of a particle density peak is found, and the peak density amplitude is seen to increase with increasing M_s . The predictions of the model show quite good agreement with the numerical data, thereby demonstrating the predictive capabilities of the proposed model. Further analysis can be achieved using the present approach with a possible extension to large-scale applications to guide physical modelling and to validate the three-dimensional numerical approach. Also, the presence of the particle number-density peak, which has been explained for the first time, is of interest, especially when dealing with practical problems such as explosion mitigation in safety engineering or two-phase reacting flows in propulsive systems.

The interaction between the spray particles and oblique shock waves is an interesting topic and will be a subject of our future work. The current one-dimensional analytical model cannot be applied in a straightforward manner to the case of oblique reflection of shock waves, as the underlying structure is more complex than the one-dimensional interaction.

Acknowledgements

The authors gratefully acknowledge the financial support from Electricité de France (EDF) within the framework of the Generation II & III Reactor Research and Development programme.

Declaration of interests

The authors report no conflict of interest.

Appendix A. Isentropic hypothesis of the reflected wave

It can be noticed that the reflected pressure waves experience a rather steep gradient and, indeed, may look like shock waves, especially for particles of small diameter or large

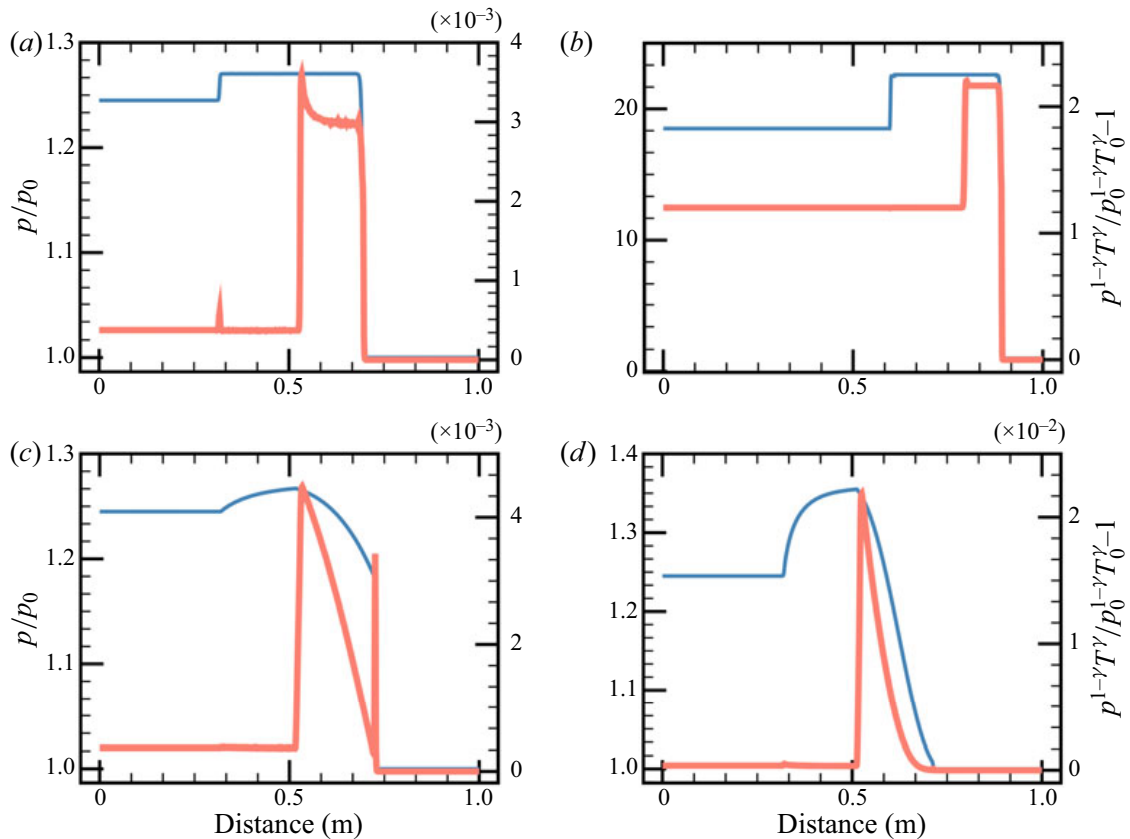


FIGURE 13. Illustration of the isentropic hypothesis for the reflected pressure wave. Evolution with distance of the gas pressure p/p_0 (blue; left axis) and $p^{1-\gamma}T^\gamma/p_0^{1-\gamma}T_0^\gamma - 1$ (red; right axis): (a) $M_s = 1.1$, $D = 1 \mu\text{m}$, $\tau_{v,0} = 5.2 \times 10^{-4}$; (b) $M_s = 4.0$, $D = 1 \mu\text{m}$, $\tau_{v,0} = 5.2 \times 10^{-4}$; (c) $M_s = 1.1$, $D = 10 \mu\text{m}$, $\tau_{v,0} = 5.2 \times 10^{-4}$; and (d) $M_s = 1.1$, $D = 10 \mu\text{m}$, $\tau_{v,0} = 5.2 \times 10^{-3}$.

volume fraction, as shown in figures 8 and 9. In order to verify the isentropic hypothesis for the reflected pressure wave, we proceed with the assessment in the following steps.

First, using the numerical simulation results, one can calculate $p^{1-\gamma}T^\gamma$, which is a measure of entropy ($S = C_v \ln(p^{1-\gamma}T^\gamma)$), across the reflected waves. The results for different combinations of particle diameter D , incident shock Mach number M_s and initial particle volume fraction $\tau_{v,0}$ are depicted in figure 13. One can see that the quantity $p^{1-\gamma}T^\gamma$ is constant across reflected waves for all considered parameters. The small spike of $p^{1-\gamma}T^\gamma$ across the reflected wave, shown in figure 13(a) and (c), can be attributed to a numerically generated artefact.

Secondly, one can calculate the velocity of the reflected wave in order to see if it is sonic or nearly sonic (compression wave or weak shock wave). For the incident shock of $M_s = 1.1$, as illustrated in figure 13(a), the velocity of the reflected wave is $V_r = 355.19 \text{ m s}^{-1}$, which is approximately equal to the sound velocity $c = 357 \text{ m s}^{-1}$. For the incident shock of $M_s = 4.0$, as in figure 13(b), the velocity increases to $V_r = 784.19 \text{ m s}^{-1}$, which is 13% higher than the sound velocity $c = 695 \text{ m s}^{-1}$. This could indicate that the reflected wave is a weak shock wave, since the isentropic hypothesis still holds according to numerical results (figure 13b).

Thirdly, one can estimate directly the entropy jump across the reflection wave, using the expression for a weak shock wave in Landau & Lifshits (1959),

$$S_2 - S_1 = \frac{1}{12T_1} \left(\frac{\partial^2 V}{\partial p_1^2} \right)_s (p_2 - p_1)^3, \quad (\text{A } 1)$$

where the subscripts 1 and 2 denote the pre- and post-wave properties of the reflection wave, and $V = 1/\rho$. Simplifying the above equation, one can obtain

$$S_2 - S_1 = \frac{1}{12T_1} \left(\frac{\gamma + 1}{\gamma^2} \right) \frac{(p_2 - p_1)^3}{\rho_1 p_1^2}. \quad (\text{A } 2)$$

For the bounding case, i.e. when the incident $M_s = 4.0$, the above expression gives as relative difference: $(S_2 - S_1)/S_1 = 0.0034 \%$. This small value can explain the constant numerically computed entropy across the reflected waves even for relatively high incident Mach numbers, and justify the usage of an isentropic condition in (5.9).

REFERENCES

- BALAKRISHNAN, K. & BELLAN, J. 2017 High-fidelity modeling and numerical simulation of cratering induced by the interaction of a supersonic jet with a granular bed of solid particles. *Intl J. Multiphase Flow* **99**, 1–29.
- BRITAN, A., SHAPIRO, H., LIVERTS, M., BEN-DOR, G., CHINNAYYA, A. & HADJADJ, A. 2013 Macro-mechanical modeling of blast-wave mitigation in foams. Part I: review of available experiments and models. *Shock Waves* **23** (1), 5–23.
- CARRIER, G. F. 1958 Shock waves in a dusty gas. *J. Fluid Mech.* **4** (4), 376–382.
- CHANG, E. J. & KAILASANATH, K. 2003 Shock wave interactions with particles and liquid fuel droplets. *Shock Waves* **12** (4), 333–341.
- CHAUDHURI, A., HADJADJ, A., SADOT, O. & BEN-DOR, G. 2013 Numerical study of shock-wave mitigation through matrices of solid obstacles. *Shock Waves* **23**, 91–101.
- CHAUDHURI, A., HADJADJ, A., SADOT, O. & GLAZER, E. 2012 Computational study of shock-wave interaction with solid obstacles using immersed boundary methods. *Intl J. Numer. Meth. Engng* **89** (8), 975–990.
- DAHAL, J. & MCFARLAND, J. A. 2017 A numerical method for shock driven multiphase flow with evaporating particles. *J. Comput. Phys.* **344**, 210–233.
- DEL PRETE, E., CHINNAYYA, A., DOMERGUE, L., HADJADJ, A. & HAAS, J.-F. 2013 Blast wave mitigation by dry aqueous foams. *Shock Waves* **23** (1), 39–53.
- ELGHOBASHI, S. 1994 On predicting particle-laden turbulent flows. *Appl. Sci. Res.* **52** (4), 309–329.
- ELGHOBASHI, S. 2006 An updated classification map of particle-laden turbulent flows. In *IUTAM Symposium on Computational Approaches to Multiphase Flow*, vol. 81, pp. 3–10. Springer.
- FOISSAC, A., MALET, J., VETRANO, M. R., BUCHLIN, J. M., MIMOUNI, S., FEUILLEBOIS, F. & SIMONIN, O. 2011 Droplet size and velocity measurements at the outlet of a hollow cone spray nozzle. *Atomiz. Sprays* **21**, 893–905.
- GAI, G., KUDRIAKOV, S., HADJADJ, A., STUDER, E. & THOMINE, O. 2019 Modeling pressure loads during a premixed hydrogen combustion in the presence of water spray. *Intl J. Hydrogen Energ.* **44** (10), 4592–4607.
- GAI, G., THOMINE, O., HADJADJ, A. & KUDRIAKOV, S. 2020 Modeling of particle cloud dispersion in compressible gas flows with shock waves. *Phys. Fluids* **32** (2), 023301.
- GELFAND, B. E. 1996 Droplet break-up phenomena in flows with velocity lag. *Prog. Energy Combust. Sci.* **22** (3), 201–265.
- GENG, J. H., VAN DE VEN, A., YU, Q., ZHANG, F. & GRÖNIG, H. 1994 Interaction of a shock wave with a two-phase interface. *Shock Waves* **3** (3), 193–199.
- GUILDENBECHER, D. R., LOPEZ-RIVERA, C. & SOJKA, P. E. 2009 Secondary atomization. *Exp. Fluids* **46**, 371–402.

- JIANG, G.-S. & SHU, C.-W. 1996 Efficient implementation of weighted ENO schemes. *J. Comput. Phys.* **126** (1), 202–228.
- JOURDAN, G., BIAMINO, L., MARIANI, C., BLANCHOT, C., DANIEL, E., MASSONI, J., HOUAS, L., TOSELLO, R. & PRAGUINE, D. 2010 Attenuation of a shock wave passing through a cloud of water droplets. *Shock Waves* **20** (4), 285–296.
- JOURDAN, G., MARIANI, C., HOUAS, L., CHINNAYYA, A., HADJADJ, A., DEL PRETE, E., HAAS, J.-F., RAMBERT, N., COUNILH, D. & FAURE, S. 2015 Analysis of shock-wave propagation in aqueous foams using shock tube experiments. *Phys. Fluids* **27** (5), 056101.
- KERSEY, J., LOTH, E. & LANKFORD, D. 2010 Effect of evaporating droplets on shock waves. *AIAA J.* **48** (9), 1975–1986.
- LANDAU, L. D. & LIFSHITS, E. M. 1959 *Fluid Mechanics*. Pergamon Press.
- LING, Y., HASELBACHER, A. & BALACHANDAR, S. 2011 Importance of unsteady contributions to force and heating for particles in compressible flows. Part 2: application to particle dispersal by blast waves. *Intl J. Multiphase Flow* **37** (9), 1013–1025.
- LING, Y., PARMAR, M. & BALACHANDAR, S. 2013 A scaling analysis of added-mass and history forces and their coupling in dispersed multiphase flows. *Intl J. Multiphase Flow* **57**, 102–114.
- LING, Y., WAGNER, L., BERESH, S. J., KEARNEY, S. P. & BALACHANDAR, S. 2012 Interaction of a planar shock wave with a dense particle curtain: modeling and experiments. *Phys. Fluids* **24** (11), 113301.
- MEHTA, Y., JACKSON, T. L., ZHANG, J. & BALACHANDAR, S. 2016 Numerical investigation of shock interaction with one-dimensional transverse array of particles in air. *J. Appl. Phys.* **119** (10), 104901.
- MOURONVAL, A.-S., TIE, B., HADJADJ, A. & MOEBS, G. 2019 Investigation of shock/elastic obstacles interactions by means of a coupling technique. *J. Fluid Struct.* **84**, 345–367.
- OLIM, M., BEN-DOR, G., MOND, M. & IGRA, O. 1990 A general attenuation law of moderate planar shock waves propagating into dusty gases with relatively high loading ratios of solid particles. *Fluid Dyn. Res.* **6** (3), 185–199.
- PILCH, M. & ERDMAN, C. A. 1987 Use of breakup time data and velocity history data to predict the maximum size of stable fragments for acceleration-induced breakup of a liquid drop. *Intl J. Multiphase Flow* **13** (6), 741–757.
- RUDINGER, G. 1964 Some properties of shock relaxation in gas flows carrying small particles. *Phys. Fluids* **7** (5), 658–663.
- SAITO, T., MARUMOTO, M. & TAKAYAMA, K. 2003 Numerical investigations of shock waves in gas–particle mixtures. *Shock Waves* **13**, 299–322.
- SUGIYAMA, Y., ANDO, H., SHIMURA, K. & MATSUO, A. 2019 Numerical investigation of the interaction between a shock wave and a particle cloud curtain using a CFD–DEM model. *Shock Waves* **29** (4), 499–510.
- THEOFANOUS, T. G. & CHANG, C.-H. 2017 The dynamics of dense particle clouds subjected to shock waves. Part 2. Modeling/numerical issues and the way forward. *Intl J. Multiphase Flow* **89**, 177–206.
- THEOFANOUS, T. G., MITKIN, V. & CHANG, C.-H. 2016 The dynamics of dense particle clouds subjected to shock waves. Part 1. Experiments and scaling laws. *J. Fluid Mech.* **792**, 658–681.
- THEOFANOUS, T. G., MITKIN, V. & CHANG, C.-H. 2018 Shock dispersal of dilute particle clouds. *J. Fluid Mech.* **841**, 732–745.
- THOMAS, G. O. 2000 On the conditions required for explosion mitigation by water sprays. *Process Saf. Environ.* **78** (5), 339–354.
- THOMINE, O. 2011 Development of multi-scale methods for the numerical simulation of diphasic reactive flows. PhD thesis, University of Rouen, France.
- WAGNER, J., BERESH, S., KEARNEY, S., TROTT, W., CASTANEDA, J., PRUETT, B. & BAER, M. 2012 A multiphase shock tube for shock wave interactions with dense particle fields. *Exp. Fluids* **52** (6), 1507–1517.
- WHITE, F. M. 2011 *Fluid Mechanics*. McGraw Hill.
- WRAY, A. A. 1991 Minimal storage time-advancement schemes for spectral methods. *Tech. Rep.* MS202. NASA Ames Research Center.
- YEOM, G.-S. & CHANG, K.-S. 2012 Dissipation of shock wave in a gas-droplet mixture by droplet fragmentation. *Intl J. Heat Mass Transfer* **55** (4), 941–957.

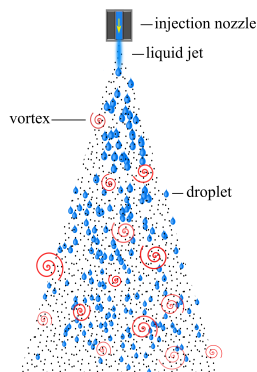
Chapter 5

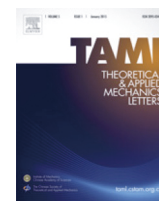
Spray-induced Turbulence

Section 1: Modeling of particle cloud dispersion in compressible gas flows with shock waves (**submitted**)

Highlights:

- Application of sprays for mitigation of Hydrogen explosion effects involving deflagration waves.
- Development of a new predictive model for hydrogen/air laminar flame in presence of water droplets.
- Physical analysis of the main factors influencing laminar flame velocity interacting with water droplets.
- Validation of the model using available experimental and numerical data.





Letter

Particles-induced turbulence: A critical review of physical concepts, numerical modelings and experimental investigations

Guodong Gai^{a,b}, Abdellah Hadjadj^{b,*}, Sergey Kudriakov^a, Olivier Thomine^a

^a DEN-DM2S-STMF, CEA, Université Paris-Saclay, France

^b University of Normandy, INSA, CORIA UMR - 6614 CNRS, 76000 Rouen, France



HIGHLIGHTS

- Experimental and numerical studies on spray-induced turbulence is briefly reviewed
- Main physical concepts of turbulence modulation are summarized and discussed
- Different modelling approaches are presented with a numerical validation

ARTICLE INFO

Article history:

Received 13 January 2020

Received in revised form 6 March 2020

Accepted 10 March 2020

This article belongs to the Fluid Mechanics.

Keywords:

Particle-induced turbulence

Turbulence modulation

Physical and numerical modeling

ABSTRACT

The presence of solid particles or water droplets in continuous fluid flow can either induce turbulence attenuation or amplification. The modification of the state of the turbulence depends on the characteristics of the particles, such as volume fraction, mean diameter, mass density, or carrier phase flow properties. In this brief review, the main physical concepts related to the most important physical aspects of turbulence modulation are summarized. Different criteria used to distinguish the enhancement or the attenuation effects of the particles on the carrier phase flows are recalled. For the interest of large-scale industrial applications, several theoretical, experimental and empirical approaches are discussed, which provides an interesting framework for the study of the effect of particles on turbulence behavior modification.

©2020 The Authors. Published by Elsevier Ltd on behalf of The Chinese Society of Theoretical and Applied Mechanics. This is an open access article under the CC BY-NC-ND license (<http://creativecommons.org/licenses/by-nc-nd/4.0/>).

In particle-laden flows, the presence of particle cloud can have two opposite effects on the turbulence state of the carrier flow: either attenuation or enhancement. The modulation of turbulence in the presence of particles can be regarded as a phenomenon induced by several factors such as the distortion of the carrier phase velocity gradient, the streamline curvatures, the vortex shedding of the particles or the damping of turbulence motion by particles-induced drag forces [1]. Experimental investigations on dispersed two-phase media mainly focused on the measurements of the mean flow velocity and the Reynolds stresses of the carrier-phase flow. Higher-order statistics such as Lagrangian particle-velocity correlations, carrier-phase turbulent dissipation and phase-phase velocity correlations are also

studied [2].

In terms of experimental measurements, the hot-wire anemometry technique was widely used in gas-droplet jets [3] to measure the flow velocity in the particle-laden flow. An example of a water spray and a spray-induced turbulence vortex under an injection nozzle is given in Fig. 1. Later on, a Laser Doppler Velocimetry (LDV) technique was used to better characterize the topology of turbulent flows in the presence of particles. This technique relies on the use of small-particle seeds as tracers to measure the motion of the carrier flow. It was shown that larger dispersed particles produce a stronger signal, that can be discriminated from the carrier phase. For the gaseous carrier phase, the tracers typically have diameters of $\mathcal{O}(1)$ μm , while the dispersed particles have larger diameters of $\mathcal{O}(10 - 1000)$ μm [2].

Kulick et al. [4] studied experimentally the effects of particles on the fully developed turbulent pipe flows for different particles

* Corresponding author.

E-mail address: abdellah.hadjadj@insa-rouen.fr (A. Hadjadj).

with sizes smaller than the Kolmogorov length-scale η . The particles were found to attenuate the turbulence when increasing the Stokes number S_i and the mass loading. Reduction in turbulence intensity was found to be larger in the cross-flow direction compared to the stream-wise direction. The experiments were modeled by Yamamoto et al. [5], with particular emphasis on particle-particle and particle-wall interactions. It was shown that these two interactions played a key role in the turbulence attenuation. Other experiments were also conducted by Paris [6] in a vertical fully-developed channel flow with particles smaller than η . It was found that the mass-loading ratio increases the effect of turbulence attenuation at low particle Reynolds numbers Re_p whose definition is given in Eq. (1). The latter was revealed to be an important parameter for turbulence attenuation. It was concluded that modifications of the carrier-phase turbulence structure by particles are significantly important in turbulence attenuation of particle-laden channel flows.

Measurements of air and particle velocities of the two-phase flow in a vertical pipe were also performed by LDV [7]. It was seen that large particles increased the air turbulence throughout the pipe section, while small particles reduced it [8]. The turbulence was amplified around the pipe center and damped near the wall, which was also reported in Refs. [9] and [10]. Kussin and Sommerfeld [11] came to the same conclusion for particles with a diameter larger than η in horizontal pipe flows.

From experimental point of view, five key factors appear to contribute to the turbulence modulation induced by particles [1]: *i*) Surface effects: particle size normalized by a length scale d_p/l_t ; *ii*) Inertial effects: flow Reynolds number Re and particle Reynolds number Re_p ; *iii*) Response effects: particle response time τ_p , or Stokes number S_i ; *iv*) Loading effects: particle volume fraction α_p ; *v*) Interaction effects: particle-particle, particle-wall.

In the following, we will discuss different parameters used for the classification of turbulence modulation.

Gore and Crowe [8] summarized the experimental investigations of turbulence modulation, including jets, pipes, gas-particle and gas-liquid flows. A general trend indicates that small particles ($d_p < 200 \mu\text{m}$) contribute to turbulence attenuation, while large particles ($d_p > 200 \mu\text{m}$) tend to enhance turbulence. The criterion proposed by Gore and Crowe [8] is based on the ratio of particle diameter to turbulence length scale, d_p/l_t .

The summarized data is shown in Fig. 2. For various types of particle-laden flows, a fairly distinct value $d_p/l_t \approx 0.1$ was noted below which the particles enhance turbulence dissipation and above which the turbulence is amplified. The behavior of particles in turbulent flows is thought to be similar to grid-screen turbulence. This rough criterion is widely approved in the literature [12]. Many researchers report that the attenuation of turbulence occurs for $d_p/l_t < 0.1$ [1]. A wide range of experimental observations is made in Ref. [8] including jet and pipe flows with various orientations, at flow Reynolds number ranging from 8000 to 10^5 , density ratio between 0.0012 and 2500 and volume fraction between 10^{-6} and 0.2.

Elghobashi and Truesdell [13] proposed a length-scale ratio of d_p/η , which was also used as a classification parameter in Refs. [2] and [14]. It is widely agreed that the particle size plays an important role in the turbulence modulation [15] and the particles of $d_p/\eta \ll 1$ have little influence on the turbulence modulation of the particle-laden flows. Sato et al. [16] claimed that the interparticle spacing can also be considered as a critical

parameter for turbulence modulation.

The particle Reynolds number, Re_p , which is the ratio of inertial to viscous forces is much used when dealing with particle turbulence modulation. Clift et al. [17] argued that, in a particle-laden flow, the wake instability occurs at $Re_p \approx 130$ and the vortex shedding starts at $Re_p \approx 270$. Hetsroni [10] used the experimental data of Ref. [8] and proposed another criterion based on the particle Reynolds number, defined as

$$Re_p = \frac{(\rho_p - \rho_f) |u_f - u_p| d_p}{\mu_f}, \quad (1)$$

where μ is the dynamic viscosity, ρ is the mass density, u is the velocity, d_p is the diameter. The subscripts p and f denote particle and fluid properties, respectively. Hetsroni [10] suggested that flows with high particle Reynolds numbers, $Re_p > 400$, would induce vortex shedding instability that enhances the

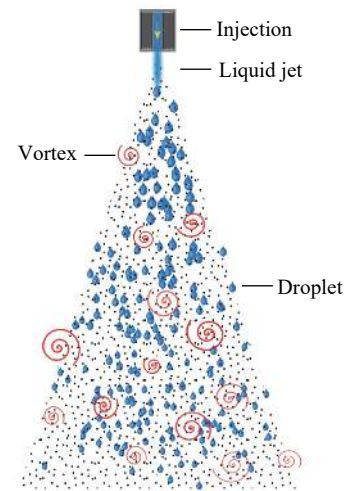


Fig. 1. Schematic representation of a liquid jet spray issuing from an injector nozzle and inducing spray-turbulence generation with vortex formation.

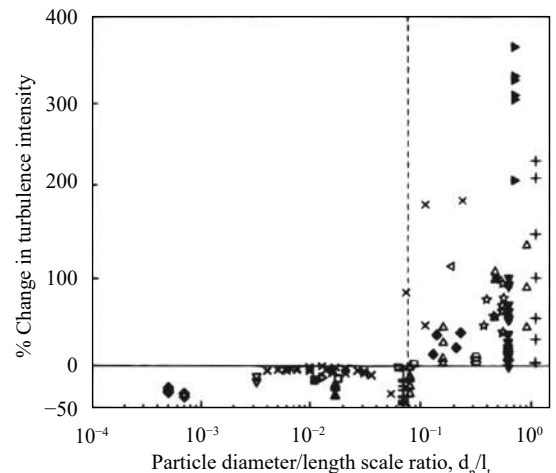


Fig. 2. The percentage change in the turbulence intensity as a function of the ratio of particle size to turbulence length scale, d_p/l_t , from a wide range of experiments. Adopted from Gore and Crowe [8].

turbulence intensity. The energy from the average velocity is transferred to higher frequencies. However, it was reported by Geiss et al. [18], that evident turbulence production can also be observed at Re_p less than 400. A lower critical value of vortex shedding $Re_p \approx 270$ was proposed as the value which distinguishes the two opposite effects. Despite this difference in critical values of Re_p , the study of Ref. [18] confirms the order of magnitude estimated in Ref. [10]. It was argued that the vortex shedding cannot be the only explanation for the enhancement of turbulent intensity [12].

The Stokes number characterizes the behavior of particles evolving within a carrier flow. It is defined as

$$S_t = \frac{\tau_p}{\tau_k}, \quad (2)$$

where τ_p is the particle response time and τ_k is the Kolmogorov time scale defined as $\tau_k = (\nu/\varepsilon)^{1/2}$, ν being the kinematic viscosity and ε the mean rate of dissipation per unit mass of fluid. The smaller particles just follow the streamline and behave like tracers of the carrier phase, while the larger particles separate from the carrier flow. Ferrante and Elghobashi [19] used the Stokes number to characterize the turbulence modulation. It was shown that for particles with $S_t \ll 1$, the viscous dissipation rate is larger than those in particle-free turbulence. In this case, the particles denoted ghost particles $S_t \approx 0.25$ are considered to bring neither amplification nor attenuation of the turbulent kinetic energy (TKE). For larger Stokes number $S_t > 1$, both turbulent length and time scales grow faster. For particles with $d_p/\eta \approx 1$, the observations yield an increase in the rate of TKE dissipation and a corresponding reduction of turbulence [20].

It was argued that the Stokes number is not the main-driver parameter of turbulence modulation [21, 22], since the turbulent intensity can be attenuated even for $S_t < 60$.

The volume fraction of particles, α_p , is a parameter widely used to describe the number of particles in a given volume, closely related to the interparticle distance and the particle mass loading. An illustrative classification in terms of volume fraction is given by Elghobashi [23] and shown in Fig. 3.

Three regimes of turbulence modulation are proposed [23]. For $\alpha_p < 10^{-6}$, there is a large distance between the particles to have a significant effect on the carrier phase and the interaction is governed by a one-way coupling. The individual effects of the particles are considered. For particle volume fractions in the range of 10^{-6} to 10^{-3} , the amount of particles starts to influence turbulent modulation or modification of the carrier phase. This is referred to the two-way coupling regime. For clouds with $\alpha_p > 10^{-3}$, the interactions among particles such as collisions or droplets coalescences become an important factor in the turbulence modulation. This is known as four-way coupling regime.

Other researches [24–26] argued that even with a very small volume fraction, the dispersed phase can still influence the turbulence in the carrier phase. However, the volume fraction solely cannot clearly discern the attenuation or the enhancement of turbulence.

Tanaka and Eaton [21] mapped out 30 experimental databases, from the open literature with different values of Re and S_t (see Fig. 4). The particle momentum number, Pa_{S_t} , was proposed in Ref. [21], by solving dimensionless particle-laden Navier-Stokes equation [27, 28]

$$Pa_{S_t} = S_t Re^2 \left(\frac{\eta}{l_t} \right)^3 = \frac{1}{54} \frac{R_e^2}{\sqrt{2S_t}} \left(\frac{\rho_p}{\rho_f} \right)^{3/2} \left(\frac{d_p}{l_t} \right)^3. \quad (3)$$

The collapsed turbulence modulation data for various particle-laden flows show that turbulence attenuation occurs for $10^3 < Pa_{S_t} < 10^5$, whereas turbulence augmentation was lower for $Pa_{S_t} < 10^3$ and higher for $Pa_{S_t} > 10^5$. A weakness in the experimental databases is noted, since there are no turbulence modulation experiments at higher Reynolds number than 3×10^4 . Moreover, it can be mentioned that only the Stokes drag force is considered for the turbulence modulation, which is not able to describe the effects of the vortex shedding [29]. Using the relation between the turbulent length scale and the Kolmogorov length scale $l_t/\eta \approx Re^{3/4}$, Losche [30] suggested that the particle momentum number can be written as

$$Pa_{S_t} \approx \frac{S_t}{Re^{1/4}}. \quad (4)$$

Another rescaling of the particle momentum number is proposed by Luo et al. [29]. The ratio of S_t over Pa_{S_t} is used as a crit-

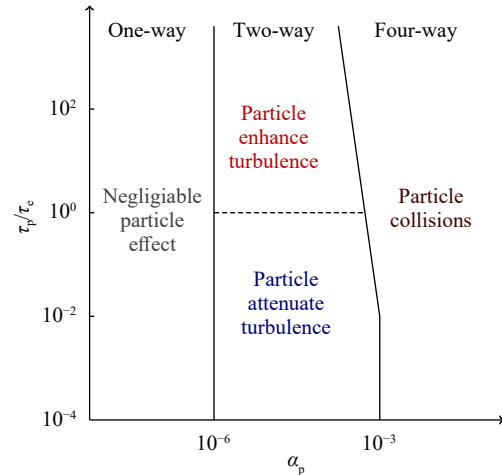


Fig. 3. Map of different regimes of interaction between particles and turbulence [23]. τ_p is the response time of particles, τ_e is the turnover time of large eddies defined as $\tau_e = l_t/u_{rms}$ where l_t is the integral length scale, $u_{rms} = \sqrt{u'u'}$ is the root-mean-square velocity.

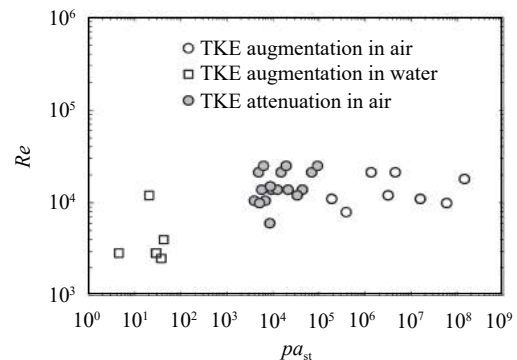


Fig. 4. Mapping of the turbulence modulation experiments based on Pa_{S_t} and Re [21].

ical parameter to distinguish the attenuation and the enhancement of turbulence

$$Cr_{S_r} = \frac{S_r}{Pa_{S_r}} = 54\sqrt{2} \left(\frac{\rho_p}{\rho_f} \right)^{-\frac{1}{2}} \left(\frac{l_t}{d_p} \right)^3 Re^{-2} S_r^{\frac{3}{2}}. \quad (5)$$

In general, as discussed by Tanaka and Eaton [21], more data is required before a decisive conclusion can be made. At the moment, there exists no broad consensus in the literature regarding a unique dimensionless number that can perfectly describe the influence of particles in turbulence modulation [20].

Several numerical approaches have been developed to study turbulence modulation associated with dilute particle-laden flows. However, there is still a lack of suitable models that can account for most important physical factors [31]. The mechanisms of turbulence modulation are not well understood [1] as a result of the complex process of fluid-particle interactions. According to Crowe et al. [1], the actual research trend has focused mainly on the development of either two-equation, or full Reynolds stress models. For large scale industrial applications, the RANS models are still applicable. However, the use of more sophisticated modeling approaches such as LES or DNS is prohibitive given the excessive amount of required computational resources. Therefore, reduced-order modeling strategies taking into consideration the main effects of turbulence modulation are of great interest for large-scale engineering applications.

Yuan and Michaelides [32] developed a rather simple mechanistic model for the prediction of turbulence modification in particle-laden flows based on the interaction of a single particle with turbulent eddies. Two predominant mechanisms of turbulence modulation are identified: (a) the dissipation of energy from a turbulent eddy that damps the turbulence; (b) the flow velocity redistribution disturbance due to vortex shedding is important for the enhancement of the turbulence. The derived model is based on the particle size, the relative velocity, the Reynolds number and the density differences between the two phases. The mean rate of turbulent dissipation of the carrier phase flow by the acceleration of the particles is given by

$$\bar{\varepsilon} = \frac{\pi}{12} d_p^3 \rho_p (\bar{u} - \bar{v}_0)^2 \left[1 - \exp\left(-\frac{2c_1\tau}{\tau_p}\right) \right], \quad (6)$$

with \bar{u} being the mean velocity of the flow, \bar{v}_0 the mean velocity of the particle interacting with the turbulent eddies, τ_p the response time of the particle, $c_1 = (1 + 0.15Re_p^{0.687})$ and τ the interaction time between the particle and the eddy

$$\tau = \min\left(\frac{l_t}{|\bar{u} - \bar{v}|}, \frac{l_t^2}{\nu}\right), \quad (7)$$

where l_t is the eddy size, estimated experimentally [33].

The mean turbulent energy production rate is given by

$$\bar{P} = \frac{\pi}{12} d_p^2 \rho_f (\bar{u}^2 - \bar{v}_0^2) \mathcal{G}(L_w), \quad (8)$$

where $\mathcal{G}(L_w)$ is a length-scale function linked to the region behind the particle, and L_w is the effective length of the wake [17]. It was reported by Crowe et al. [1] that the production term in Eq. (9) is related to the direction and the magnitude of the relative velocity between the two phases. However, the particle

concentration effects are not described. The source term acting on the turbulence modulation, $S = \bar{P} - \bar{\varepsilon}$, is given by

$$S = \frac{\pi}{12} d_p^2 \rho_f (\bar{u}^2 - \bar{v}_0^2) \mathcal{G}(L_w) - \frac{\pi}{12} d_p^3 \rho_p (\bar{u} - \bar{v}_0)^2 \left[1 - \exp\left(-\frac{2c_1\tau}{\tau_p}\right) \right], \quad (9)$$

which describes the turbulence energy variation due to the presence of particles. This source term can be used to characterize the modification of the carrier phase turbulence intensity in large-scale simulations. The resulting model was reported to show good agreements with the experimental data of Tsuji et al. [7] as depicted in Fig. 5a.

Yarin and Hetsroni [34] proposed a simplified theory to study the effects of particle size on the turbulence modulation in dilute particle-laden flows. Two sources of turbulence are considered: a) the carrier fluid velocity gradients and b) the turbulent wake behind coarse particles. The modified mixing-length theory and the turbulent kinetic-energy balance were combined together to derive a simplified model to quantitatively describe the process of turbulence dissipation and generation in particle-laden flows

$$\frac{\sqrt{u'u'}}{u_R} = C_e \left(\frac{\gamma}{\rho_{pf}} C_D^{3/2} \right)^{4/9}, \quad (10)$$

where u' is the fluid fluctuating velocity, $u_R = |\bar{u} - \bar{v}|$ is the particle relative velocity, γ is the mass content of the particles in the fluid element, $\rho_{pf} = \rho_p/\rho_f$ is the particle to carrier phase density ratio, C_e is an empirical constant and C_D is the drag coefficient expressed as $C_D = \frac{24}{Re} (1 + 0.15Re^{0.687})$. The Eq. (10) can give an estimation of the modification of the carrier-phase turbulence in presence of particles. The effects of particle size are given by the relation [34]

$$\left(\frac{L_w}{d_p} \right)^{1/3} = \Omega \left(\frac{\rho_{pf}}{\gamma} \right)^{1/9}, \quad (11)$$

where $\Omega \approx 1$ is an empirical constant. Equation (10), referred as the "4/9-power" law by Yarin and Hetsroni [34], indicates that particles with larger diameters can enhance the turbulence intensity of the carrier phase. This relation holds only for dilute particle-laden flows, with a small volume fraction of particles. Figure 5b shows the dependence of the carrier fluid velocity fluctuations on $\gamma C_D^{3/2}/\rho_{pf}$. The prediction given by Eq. (10) shows a good agreement with the experimental data of particle-water flow [35] and particle-air flow [36].

For fully developed dilute particle-laden flows in a vertical pipe, Crowe [37] simplified the volume averaged turbulent kinetic-energy equation by taking into account the turbulence generation of velocity gradients (VG), generation by particle drag (PD) and the viscous dissipation (VD), and obtained

$$\underbrace{-\alpha_f \rho_f \langle \delta u_i \delta u_j \rangle \frac{\partial \langle u_i \rangle}{\partial x_j}}_{VG} + \underbrace{\alpha_p \rho_p \frac{\mathcal{F}}{\tau_p} |\langle u_i \rangle - \langle v_i \rangle|^2}_{PG} - \underbrace{\alpha_f \langle \varepsilon \rangle}_{VD} = 0, \quad (12)$$

where α is the volume fraction and ρ is the fluid density. As mentioned above, f and p denote the properties of the carrier phase and the particles, respectively. i and j are tensor notations.

$\langle u_i \rangle$ is the volume averaged velocity and $\langle \delta u_i \rangle$ is the deviation from the volume averaged velocity, \mathcal{F} is the ratio of the particle drag to the Stokes drag and $\langle \varepsilon \rangle$ is the mean viscous dissipation rate of the turbulent energy. For high Reynolds number flows, the drag factor \mathcal{F} can be approximated as [37]

$$\mathcal{F} = (1 + 0.15Re^{0.687}) \approx \left(0.058 \frac{gT_p d_p \rho_f}{\mu_f} \right)^{2/5}, \quad (13)$$

where τ_p is the response time of the particles and g is the gravity acceleration.

By assuming that the volume fraction of the particle is very small, $\alpha_p \ll 1$ ($\alpha_f \rightarrow 1$), the ratio of the inherent length scale L_i and the hybrid length scale L_h gives [37]

$$\frac{L_i}{L_h} = \frac{1}{2} + \frac{L_i}{2\lambda} = \frac{1}{2} + \frac{L_i}{2d_p \left[\left(\frac{\pi}{6\alpha_p} \right)^{1/3} - 1 \right]} \approx \frac{1}{2} + \frac{1}{2} \left(\frac{6\alpha_p}{\pi} \right)^{1/3} \frac{L_i}{d_p}, \quad (14)$$

with the hybrid length scale defined as [38]

$$L_h = \frac{2L_i\lambda}{L_i + \lambda}, \quad (15)$$

and λ being the mean inter-particle distance of the dispersed particles.

Combing Eqs. (12)–(14), the author obtained the turbulence energy modulation given by

$$\mathcal{M} = \frac{\sigma - \sigma_0}{\sigma_0} = \left[2 \times \frac{1 + \alpha_p \left(\frac{gL_i}{\langle u \rangle^2} \right)^2 \frac{\rho_f \langle u \rangle L_i}{\mu_f} \frac{1.5^{-3/2} (d_p)^2}{18\mathcal{F}\sigma_0 (L_i)}}{1 + \left(\frac{6\alpha_p}{\pi} \right)^{1/3} \frac{L_i}{d_p}} \right]^{1/3} - 1, \quad (16)$$

where $\langle u \rangle$ is the velocity of the carrier phase, $\sigma = u' / \langle u \rangle$ is the turbulence intensity of the particle-free flow and σ_0 represents

the intrinsic turbulence intensity without spray. Positive and negative values of the turbulence modulation factor \mathcal{M} correspond to the enhancement and the attenuation of the carrier phase turbulence, respectively. It should be emphasized that, using the hybrid length scale definition Eq. (15), the Eq. (16) has a difference of factor 2 with the one proposed by Ref. [37].

It can be noted from Eq. (16) that the ratio of particle size to turbulence length scale, d_p/L_i , plays an important role in the turbulence modulation, in accordance with the observations made by Gore and Crowe [8]. Moreover, the gravity of particles has also an important effect on the turbulence modulation through the Froude number, $Fr = gL_i/u^2$. One can also see the effects of volume fraction, α_p , in Eq. (16). Figure 6 compares the model performance with the experimental data. It is seen that the model can predict the general trend of the turbulence modulation, supported by different experimental data [37].

Equation (16) is used to compare the model prediction with experimental results in Ref. [12]. The parameter \mathcal{M} in Eq. (16) seems to provide a poor fit to the experimental data for small values of d_p/L_i . An exponential decay term is added to \mathcal{M} , such as

$$\mathcal{M}_m = \mathcal{M} e^{C/\alpha_p}, \quad (17)$$

where $C = -7 \times 10^{-6}$. It is seen that the modified parameter \mathcal{M}_m provides a better fit with some of the experimental data of Mando [12].

Mando [12] have investigated the effects of large spherical particles ($900 \mu\text{m} < d_p < 2000 \mu\text{m}$) on the turbulence modulation of the gaseous carrier phase. An empirical correlation based on the compilation of a large amount of experimental data is proposed for the estimation of the modulation strength due to the presence of solid particles in gaseous flow. This correlation is expressed in terms of \mathcal{M} as

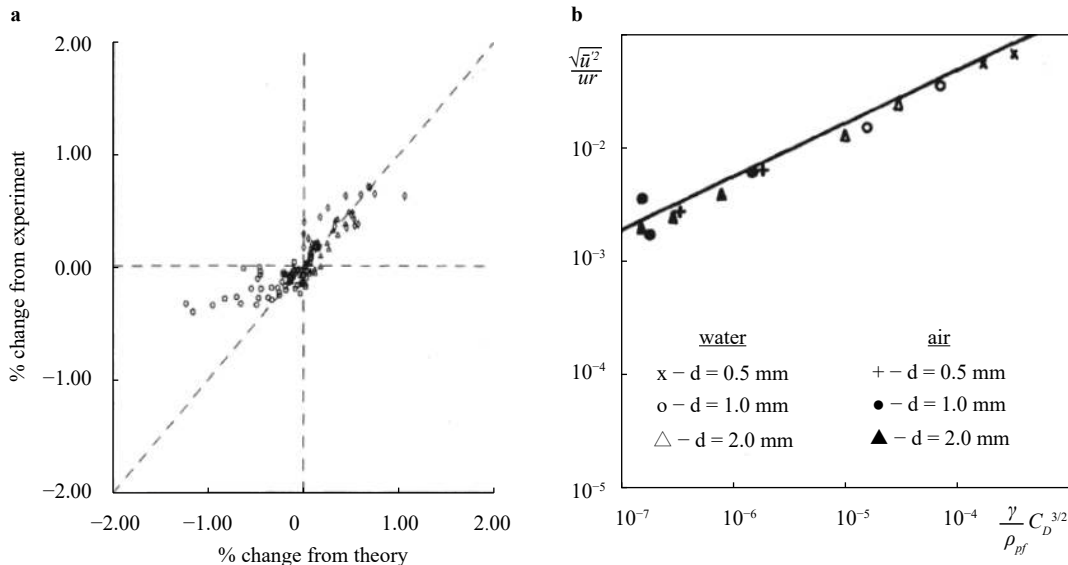


Fig. 5. **a** Comparison of Yuan model and experimental values for a pipe flow [32]; **b** Carrier phase fluctuations of homogeneous turbulence prediction by Yarin theory [34].

$$\mathcal{M} = \frac{\dot{m}_p}{\mu d_p} \left(0.34 \frac{d_p}{l_t} - 0.05 \right), \quad (18)$$

where \dot{m}_p is the particle mass flux defined as $\dot{m}_p = \alpha_p \rho_p u_p A_s$ with A_s being the cross-sectional area of the particle stream. This correlation is claimed to be valid for volume fraction between $2 \times 10^{-5} \leq \alpha_p \leq 1 \times 10^{-3}$, mass loading between 0.5 to 1.7; particle diameter between 0.9 mm and 1.8 mm and d_p/l_t ratios between 0.1 and 0.5.

Luo et al. [29] have made efforts to obtain quantitative description of the turbulence modulation through the multivariable linear regression formulation of selected experimental data [4, 7, 11, 39]. An empirical formula is obtained for the estimation of the magnitude of the turbulence modulation

$$|\mathcal{M}| = 0.0757 \left(\frac{\rho_p}{\rho_f} \right)^{0.1457} \left(\frac{l_t}{d_p} \right)^{-0.5091} (Re)^{0.2564} (Re_p)^{0.05}. \quad (19)$$

This correlation is reported to match the experimental data with a relative error lower than 25 %. Both attenuation and enhancement effects due to the presence of particles can be distinguished by either the particle momentum number Pa_{S_p} or Cr_{S_p} . However, the direct comparison between empirical formulations and experimental data was not provided.

Kenning and Crowe [38, 40] proposed another simple mechanistic model to account for the turbulence modulation through the turbulent kinetic energy balance. As shown in Fig. 7, four sources of turbulent energy of the carrier phase are considered: the inherent turbulence of the carrier phase \bar{P}_i , the turbulence generated by the dispersed particle motion \bar{P}_p , the inherent viscous dissipation of the carrier phase $\bar{\epsilon}_i$ and the dissipation due to the drag of dispersed particles $\bar{\epsilon}_p$. The transport equation of the turbulent kinetic energy rate (TKE) is [38]

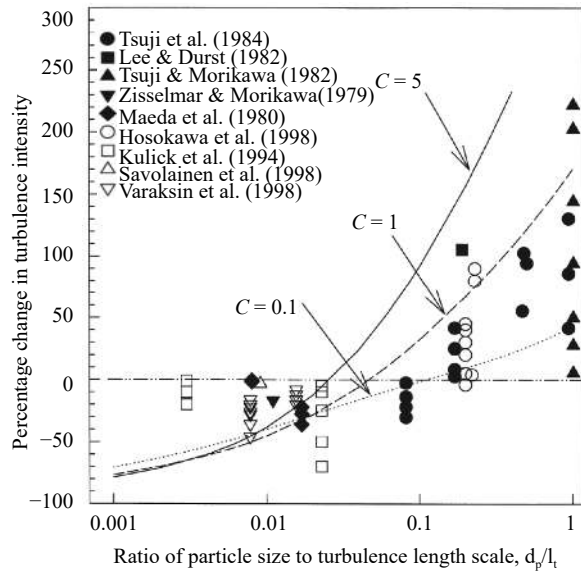


Fig. 6. Comparison of model predictions and experimental data for turbulence modulations for particle-laden flow in a vertical pipe [37], $C = \alpha_p \frac{\rho_f}{\rho_p}$ is the mass ratio of dispersed particles to the carrier fluid.

$$\frac{dk}{dt} = \frac{\alpha_p}{1 - \alpha_p} \left(\frac{\rho_p}{\rho_f} \right) (\bar{P}_p - \bar{\epsilon}_p) + (\bar{P}_i - \bar{\epsilon}_i), \quad (20)$$

where k is the turbulent kinetic energy. The expressions for production and dissipation terms can be found in Ref. [38].

Considering that the particles cannot only generate turbulence but also change the dissipation of the carrier flow, Kenning [38] proposed a formalism of turbulent energy dissipation by particles such as

$$\bar{\epsilon}_p = \frac{k^{3/2}}{L_h}. \quad (21)$$

Using \mathcal{M} as a dimensionless parameter, one can note that the turbulence is attenuated if $\mathcal{M} < 0$ and strengthened if $\mathcal{M} > 0$. \mathcal{M} can be deduced from

$$\mathcal{M} = \left[\frac{L_h}{L_i} + \frac{L_h}{k^{3/2}} \frac{f(\bar{u} - \bar{v})^2 \rho_p}{\tau_p \rho_f} \right]^{1/3} - 1. \quad (22)$$

The Kenning's model predicts that the turbulence can be attenuated with small value of L_h . A comparison of the turbulence intensity ratio M and the experimental data of Refs. [7, 39, 41] shows good agreements. However, an extension of the model is needed for comparison with more recent experimental data [37].

In this study, two examples of calculations are performed to investigate the effects of these parameters. The results are shown in Figs. 8a-8b, where the evolution of the turbulence density is plotted as a function of the mean diameter of particles using Kenning's model [38].

It is found that small particles with higher slip velocities can have more important mitigation on the carrier flow (see Fig. 8a).

Figure 8b shows the influence of the volume fraction of particles present in the two-phase flow. The range of water spray density varies between $10^{-5} \leq \alpha_p \leq 10^{-3}$, which is commonly used in the nuclear power plant spray systems for different accident scenarios. It is interesting to notice that the evolution of the turbulence modulation parameter is more sensitive to smaller volume fraction of particles. The attenuation and enhancement effects become more evident in this case.

The particle momentum number, Pa_{S_p} , is calculated and compared with Kenning model. The transition from attenuation to enhancement with the increase of particle diameter d_p is shown with a red dashed line in Fig. 8b.

Finally, the Kenning's model is seen to be no longer applicable for quite small values of d_p/l_t ratios.

This brief report provides an overview of the most important physical concepts and experimental data of particle-induced turbulence. One can conclude that the turbulence modulation cannot be fully characterized by a single parameter. The existing

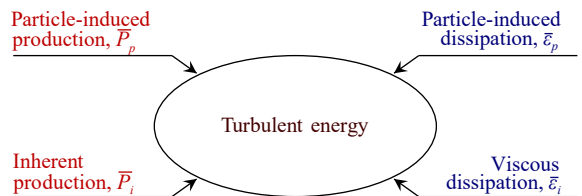


Fig. 7. Schematic model for turbulence modulation [40].

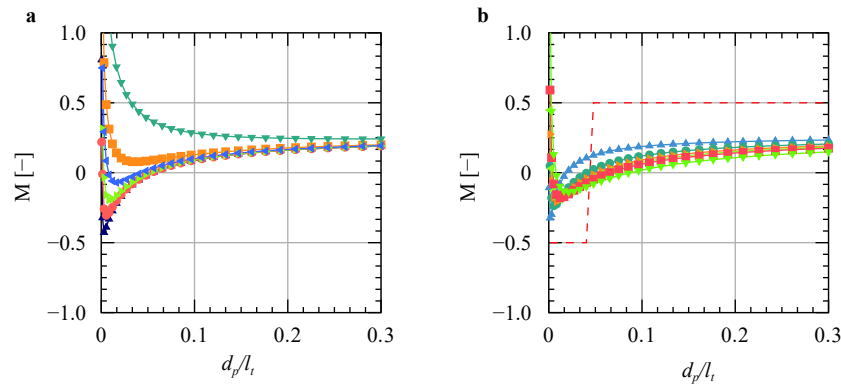


Fig. 8. Results from current numerical simulations of turbulent modulation as a function of mean particle diameters for a different: (a) relative velocities $\bar{v}_p - \bar{u} = 0.1$ m/s (\circ), $\bar{v}_p - \bar{u}_g = 0.5$ m/s (\square), $\bar{v}_p - \bar{u}_g = 0.9$ m/s (\triangle), $\bar{v}_p - \bar{u}_g = 1.5$ m/s (\diamond), $\bar{v}_p - \bar{u}_g = 2.5$ m/s (\star), $\bar{v}_p - \bar{u}_g = 5.0$ m/s (\times); (b) volume fractions of particles $\alpha_p = 1 \times 10^{-5}$ (\circ), $\alpha_p = 2 \times 10^{-5}$ (\square), $\alpha_p = 3 \times 10^{-5}$ (\triangle), $\alpha_p = 4 \times 10^{-5}$ (\diamond), $\alpha_p = 1 \times 10^{-4}$ (\star) and $\alpha_p = 1 \times 10^{-3}$ (\times); Tomohiko Model (\circ).

criteria such as the length-scale ratio, d_p/l_p and the particle momentum number, Pa_{sp} , need further experimental/numerical data for full validation and assessment. Several existing physical and theoretical models have been applied to predict turbulence modulation. Among them, the mechanistic model of Kenning is the easiest to implement and provides reasonable results. We believe that this simple model can be reasonably used for the turbulence modulation prediction in large-scale applications of spray systems and that further numerical simulations are required to assess the model.

Acknowledgement

The authors gratefully acknowledge the financial support from Electricité de France (EDF) within the framework of the Generation II & III nuclear reactor research program.

References

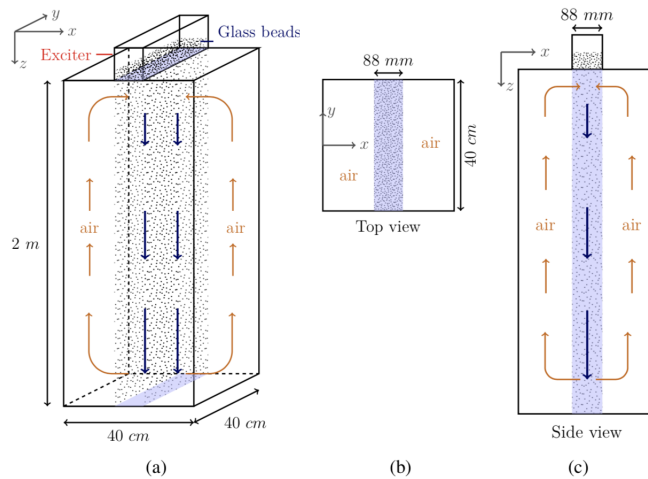
- [1] C.T. Crowe, J.D. Schwarzkopf, M. Sommerfeld, et al., *Multiphase Flows with Droplets and Particles*, CRC, Taylor and Francis (2012). ISBN:9781439840504.
- [2] S. Balachandar, J.K. Eaton, Turbulent dispersed multiphase flow, *Ann. Rev. Fluid Mech.* 42 (2010) 111–133.
- [3] G. Hetsroni, M. Sokolov, Distribution of mass velocity and intensity of turbulence in a two-phase turbulent jet, *ASME J. Appl. Mech.* 38 (1971) 315–327.
- [4] J.D. Kulick, J.R. Fessler, J.K. Eaton, Particle response and turbulence modification in fully developed channel flow, *J. Fluid Mech.* 277 (1994) 109–134.
- [5] Y. Yamamoto, M. Potthoff, T. Tanaka, et al., Large-eddy simulation of turbulent gas-particle flow in a vertical channel: Effect of considering inter-particle collisions, *J. Fluid Mech.* 442 (2001) 303–334.
- [6] A.D. Paris, Turbulence attenuation in a particle-laden channel flow, PhD thesis, Stanford University, USA (2001).
- [7] Y. Tsuji, Y. Morikawa, H. Shiomi, LDV measurements of an air-solid two-phase flow in a vertical pipe, *J. Fluid Mech.* 139 (1984) 417–434.
- [8] R.A. Gore, C.T. Crowe, Effect of particle size on modulating turbulent intensity, *Int. J. Multiph. Flow* 15 (1989) 279–285.
- [9] S. Hosokawa, A. Tomiyama, Influences of relative velocity on turbulent intensity in gas-solid two-phase flow in a vertical pipe. In *Third Int. Conference on Multiphase Flow, ICMF98*, Lyon, France (1998).
- [10] G. Hetsroni, *Particles-turbulence interaction*, *Int. J. Multiph. Flow* 15 (1989) 735–746.
- [11] J. Kussin, M. Sommerfeld, Experimental studies on particle behaviour and turbulence modification in horizontal channel flow with different wall roughness, *Exp. Fluids* 33 (2002) 143–159.
- [12] M. Mandø, Turbulence modulation by non-spherical particles, PhD thesis, Aalborg Universitet, Denmark (2009).
- [13] S. Elghobashi, G.C. Truesdell, On the two-way interaction between homogeneous turbulence and dispersed solid particles. i: Turbulence modification, *Phys. Fluid Fluid Dyn.* 5 (1993) 1790–1801.
- [14] S. Elghobashi, Dns of turbulent flows laden with droplets or bubbles, ArXiv e-prints, April (2018).
- [15] M. Pan, C. Liu, Q. Li, et al., Impact of spray droplets on momentum and heat transport in a turbulent marine atmospheric boundary layer, *Theor. App. Mech. Lett.* 9 (2019) 71–78.
- [16] Y. Sato, U. Fukuichi, K. Hishida, Effect of inter-particle spacing on turbulence modulation by lagrangian PIV, *Int. J. Heat Fluid Fl.* 21 (2000) 554–561.
- [17] R. Clift, J. Grace, M. Weber, *Bubbles, Drops, and Particles*, Academic Press (1978).
- [18] S. Geiss, A. Dreizler, Z. Stojanovic, et al., Investigation of turbulence modification in a non-reactive twophase flow, *Exp. Fluids* 36 (2004) 344–354.
- [19] A. Ferrante, S. Elghobashi, On the physical mechanisms of two-way coupling in particle-laden isotropic turbulence, *Phys. Fluids* 15 (2003) 315–329.
- [20] A. Saber, T. Lundström, J. Hellström, Turbulent modulation in particulate flow: A review of critical variables, *Engineering* 7 (2015) 597–609.
- [21] T. Tanaka, J.K. Eaton, Classification of turbulence modification by dispersed spheres using a novel dimensionless number, *Phys. Rev. Lett.* 101 (2008) 114502.
- [22] K. Luo, J. Fan, K. Cen, Modulations on turbulent characteristics by dispersed particles in gas-solid jets, *Proc. R. Soc. Lond.* 461 (2005) 3279–3295.
- [23] S. Elghobashi, On predicting particle-laden turbulent flows, *Appl. Sci. Res.* 52 (1994) 309–329.

- [24] Y. Wu, H. Wang, Z. Liu, et al., Experimental investigation on turbulence modification in a horizontal channel flow at relatively low mass loading, *Acta Mech. Sinica-PRC* 22 (2006) 99–108.
- [25] J. Li, H. Wang, Z. Liu, et al., An experimental study on turbulence modification in the near-wall boundary layer of a dilute gas-particle channel flow, *Exp. Fluids* 53 (2012) 1385–1403.
- [26] I. Lashgari, F. Picano, L. Brandt, Transition and self-sustained turbulence in dilute suspensions of finite-size particles, *Theor. App. Mech. Lett.* 5 (2015) 121–125.
- [27] A. Berlemont, P. Desjonqueres, G. Gouesbet, Particle lagrangian simulation in turbulent flows, *Int. J. Multiph. Flow* 16 (1990) 19–34.
- [28] C.B. Rogers, J.K. Eaton, The effect of small particles on fluid turbulence in a flat-plate, turbulent boundary layer in air, *Phys. Fluid Fluid Dyn.* 3 (1991) 928–937.
- [29] K. Luo, M. Luo, J. Fan, On turbulence modulation by finite-size particles in dilute gas-solid internal flows, *Powder Technol.* 301 (2016) 1259–1263.
- [30] D. Lohse, Viewpoint: Particles go with the flow, *Physics* 1 (2008) 18.
- [31] J.K. Eaton, Turbulence modulation by particles, *Multiphase Flow Handbook* (ed. C.T. Crowe), CRC, Taylor and Francis (2006). ISBN:9781498701006
- [32] Z. Yuan, E.E. Michaelides, Turbulence modulation in particulate flows—a theoretical approach, *Int. J. Multiph. Flow* 18 (1992) 779–785.
- [33] P. Hutchinson, G.F. Hewitt, A.E. Dukler, Deposition of liquid or solid dispersions from turbulent gas streams: a stochastic model, *Chem. Eng. Sci.* 26 (1971) 419–439.
- [34] L.P. Yarin, G. Hetsroni, Turbulence intensity in dilute two-phase flows-3 the particles-turbulence interaction in dilute two-phase flow, *Int. J. Multiph. Flow* 20 (1994) 27–44.
- [35] R.N. Parthasarathy, G.M. Faeth, Turbulence modulation in homogeneous dilute particle-laden flows, *J. Fluid Mech.* 220 (1990) 485–514.
- [36] M. Mizukami, R.N. Parthasarathy, G.M. Faeth, Particle-generated turbulence in homogeneous dilute dispersed flows, *Int. J. Multiph. Flow* 18 (1992) 397–412.
- [37] C.T. Crowe, On models for turbulence modulation in fluid-particle flows, *Int. J. Multiph. Flow* 26 (2000) 719–727.
- [38] V.M. Kenning, Self-induced turbulence in solid-liquid flow, PhD thesis, Washington University, USA (1996).
- [39] S.L. Lee, F. Durst, On the motion of particles in turbulent duct flows, *Int. J. Multiph. Flow* 8 (1982) 125–146.
- [40] V.M. Kenning, C.T. Crowe, On the effect of particles on carrier phase turbulence in gas-particle flows, *Int. J. Multiph. Flow* 23 (1997) 403–408.
- [41] Y. Levy, F.C. Lockwood, Velocity measurements in a particle laden turbulent free jet, *Combust. Flame* 40 (1981) 333–339.

Section 2: New insights into turbulence statistics of spray-induced turbulent flows
(submitted)

Highlights:

- A spray-induced turbulence phenomenon is numerically investigated using a second-order Reynolds- stress turbulence modeling.
- Numerical results are validated against experimental data based on the DynAsp setup.
- The slip velocity modeling is shown to be an important parameter to correctly predict the spray-turbulence modulation.
- Kenning’s mechanistic model, combined with a slip velocity correlation, is suitable for the prediction of the turbulence characteristics in large-scale simulations.



1 A new methodology for modeling turbulence induced 2 by a particle-laden flow using a mechanistic model

3 Guodong Gai · Sergey Kudriakov · Olivier Thomine ·
4 Stephane Mimouni · Abdellah Hadjadj

5
6 Received: date / Accepted: date

7 **Abstract** In particle-laden flows, a turbulent field can be produced in the carrier phase by the
8 movement of the particle/spray cloud. In this study, the intensity and the integral length scale of the
9 particle-induced turbulence are studied using a simple mechanistic model with comparison to ex-
10 perimental data and numerical simulations for large-scale numerical applications. The experimental
11 results of DynAsp are investigated with numerical simulations based on Neptune_CFD code. Out
12 of the spray nozzle, two regions can be distinguished for the spray dynamics: an inertial zone and
13 an equilibrium zone. It is found that the initial injection velocity of the cloud has little effect on
14 the terminal slip-velocity of the particles in the equilibrium zone far from the injection region.
15 The turbulent kinetic energy is closely related to the particle slip-velocity and shows a maximal
16 value when particles reach their terminal velocity inside the equilibrium zone. The integral length
17 scale depends mainly on three parameters: particle slip-velocity, particle size and volume fraction.
18 Combined with the terminal slip-velocity correlation, the reduced-order mechanistic model can
19 give a reasonable estimation of the turbulent kinetic energy as well as the integral length scale of
20 the particle-laden flow in large-scale configurations.

21 **Keywords** Particle Cloud · Turbulence Modulation · Reduced-order Model

22 1 Introduction

23 Spray systems can be used as emergency devices in gas processing plants or in offshore platforms.
24 The systems are essential for the prevention of unwanted accidental scenarios, such as hydrogen

Guodong Gai
DEN-DM2S-STMF, CEA, Université Paris-Saclay, 91191 Gif-sur-Yvette, France
E-mail: guodong.gai@insa-rouen.fr

Sergey Kudriakov
DEN-DM2S-STMF, CEA, Université Paris-Saclay, 91191 Gif-sur-Yvette, France

Olivier Thomine
DEN-DM2S-STMF, CEA, Université Paris-Saclay, 91191 Gif-sur-Yvette, France

Stephane Mimouni
EDF R&D, Fluid Dynamics Power Generation and Environment, 78401 Chatou, France

Abdellah Hadjadj
University of Normandy, INSA, CORIA UMR - 6614 CNRS, 76000 Rouen, France

25 explosions. In the case of combustion ignition, various regimes can occur depending on the local
26 concentration of hydrogen, air and water steam, as well as pressure and temperature distributions.
27 In most circumstances, spray devices are installed inside industrial buildings and off-shore plat-
28 forms, mainly for fire mitigation purposes. A number of experimental investigations have demon-
29 strated that spray systems can have a mitigating effect on flame propagation [1; 2]. The attenuation
30 relies on the evaporation of small-size water droplets inside the flame [3]. On the contrary, a certain
31 number of experiments [4] resulted in explosion enhancement in the presence of water sprays. It
32 has been established that the main reason for explosion enhancement is the turbulence generated by
33 water sprays in the gas mixture. Depending on the evolution of accident scenarios, ignition might
34 occur before or after the activation of the spray system. Thus, an understanding of the dynamics
35 of water spray in generating turbulence is needed to evaluate its mitigation or enhancement ability
36 during accidental explosions.

37 Spray- or particle-induced turbulence has been investigated for several decades [5–11]. The
38 presence of particles or a second phase in a continuous flow could change the intrinsic turbulence
39 topology of the carrier flow, which is known as turbulence modulation [12]. Several key factors
40 arise from various experimental studies that contribute to the turbulence modulation due to
41 the presence of particles [12; 13]: surface, inertial, response, loading and interaction effects.
42 Some physical parameters are taken as criteria to distinguish between the attenuation and the
43 enhancement effects of the particle cloud on the carrier flow such as the length scale ratio [14],
44 the particle momentum number Pa [15], etc.

45 Several difficulties arise in modeling of phenomenon of turbulence generation by water sprays:
46 *a)* Many factors are involved in the modeling process such as the water flow rate, droplet size,
47 and initial velocity of the droplets. These factors depend on the nozzle type and, in general, are
48 related to each other. Therefore, it is hard to vary each parameter independently. *b)* The industrial
49 sprays have a polydisperse nature. The consequence is that the equilibrium between the gravity and
50 drag forces is reached at different distances from the nozzle, depending on droplet diameter. These
51 distances are short for small-diameter ones, while they could be relatively large for large-diameter
52 droplets. *c)* The nozzles are often placed in linear or circular rows, which leads to an interaction
53 between sprays. This might change not only the droplet size distributions but also the turbulent
54 parameters in the interaction zone.

55 Ideally, one could imagine an experiment where tracer particles are introduced in the gas
56 affected by the water spray and the turbulence statistics is gathered via, for example Particle
57 Image Velocimetry (PIV) techniques. Unfortunately, to our knowledge, such experimental data
58 are scarcely available in the open literature. Instead, a large amount of experimental data exist
59 on turbulence modulation in the carrier phase by using solid particles. Measurements of air and
60 particle velocities of the two-phase flow in a vertical pipe were made by means of a Laser Doppler
61 Velocimetry (LDV) technique [16]. It was noted that the large particles increase the air turbulence
62 throughout the pipe section, while small particles reduce it. In case of turbulence enhancement,
63 the fluctuations were amplified near the pipe centerline and get reduced when approaching the
64 wall [6; 17]. Kulick *et al.* [18] studied the effects of particles on the fully developed turbulent pipe
65 flow for different particles having smaller sizes compared to the Kolmogorov scale η . The small
66 particles were found to attenuate the turbulence, with the increase of the Stokes number, the mass
67 loading and the distance from the wall.

68 A comprehensive research program called DynAsp (Dynamique de l'Aspersion) was carried
69 out in 1996 at CEA in France with aim to build up a series of experiments dealing with exchange

70 of momentum between water spray and ambient gas [19; 20]. To simplify the problem, the water
71 spray was replaced by solid glass particles. Thus, the deformation, break-up or coalescence of the
72 particles is not taken into account. Laser Doppler Velocimeter (LDV) technique was employed
73 to allow direct measurements of gas velocities in the presence of particles. A standard LDV uses
74 very small particles like tracers to measure the carrier phase movement. Larger dispersed particles
75 produce a stronger signal, which can be discriminated from the carrier phase. For the gaseous
76 carrier phase, the tracers typically have diameters of $\mathcal{O}(1) \mu m$, while the dispersed particles have
77 a larger range of diameters of $\mathcal{O}(10 - 1000) \mu m$ [21]. The gas flow velocity was measured by PIV.

78 Several theoretical and modeling approaches have been developed to understand the turbulence
79 modulation associated with dilute particle-laden flows [22–27]. Yuan *et al.* [22] developed a simple
80 mechanistic model for turbulence modulation in particle-laden flows based on the interaction
81 of a single particle with turbulent eddies. Kenning *et al.* proposed another simple mechanistic
82 model on turbulence modulation [28; 29]. Two sources of turbulent energy of the carrier phase are
83 considered: inherent turbulence of the carrier phase and turbulent energy induced by the relative
84 velocity of the two phases. The turbulent statistics has been presented for mono-dispersed solid
85 particles, which reach terminal velocity inside liquid. For a fully developed dilute particle-laden
86 flow in a vertical pipe, Crowe *et al.* [25] simplified the volume averaged turbulent kinetic energy
87 equation by taking into account the turbulence generation via velocity gradients by particle drag
88 and viscous dissipation. However, there is still a lack of a general formulation that can account for
89 most important related factors as stated in [30–32].

90 Given the complexity of the flow, the particle-induced turbulence is difficult to investigate and
91 the direct measurements of the turbulence characteristics are scarcely available in the literature. For
92 the simulations of large-scale configurations in industrial structures, the current existing turbulence
93 models, such as RANS or LES, require an extensive validation and assessment through a series
94 of highly-resolved numerical simulations that are difficult to meet nowadays. These large-scale
95 simulations can be hydrogen explosions in a nuclear confinement building (volume $V = 10^4 \sim 10^5$
96 m^3), or offshore facilities (volume $V = 10^5 \sim 10^6 m^3$). The smallest grid sizes for these problems,
97 for practical reasons, cannot be smaller than $\Delta x \approx \mathcal{O}(10 cm)$, and the direct application of
98 turbulence models such as RANS, involving action of spray and spray-flame interaction, can give
99 erroneous results. The description of spray-induced turbulence in current commercial engineering
100 code is mostly based on empirical correlations. For example, for turbulent combustion simulations
101 in the FLACS code [33], a factor F_1 is used to increase the turbulence intensity if any water sprays
102 are present. On the contrary, a quenching factor, denoted F_2 , is used to reduce the burning rate if
103 the conditions for droplet break-up are satisfied. Both F_1 and F_2 factors are user-defined using a set
104 of experimental data and are strongly case-dependent. In general cases, the validity of the model
105 for burning velocity evaluation is questionable. In this study, we propose another methodology
106 to provide input parameters for large-scale combustion modeling under water spray effects [34].
107 The objective is to assess the performance of a simple mechanistic model for the estimation of
108 turbulence characteristics such as turbulent kinetic energy (TKE) k_t as well as the turbulent length
109 scale L_t in a large-scale particle-laden flow.

110 The current study is organized as follows: Section 2 describes the methodology applied in this
111 study; Section 3 describes briefly the experiments setup DynAsp; Section 4 shows the validation
112 of the Neptune_CFD code using the experimental results of DynAsp; Section 5 discusses the
113 assessment of the mechanistic model of Kenning [28] in the DynAsp configuration using the
114 validated results of Neptune_CFD code. Conclusions are given in Section 6.

115 2 Methodology

In large-scale modeling, the influence of the turbulence on flame acceleration process is usually described through the variation of the turbulent burning velocity s_T . Generally, the turbulent velocity s_T can be expressed as following [34]:

$$s_T = f(s_L, \delta_L, Le, \dots) \times u'^\alpha \times L_t^\beta, \quad (1)$$

116 where $f(s_L, \delta_L, Le, \dots)$ is a function of chemical properties of the gas mixture such as, laminar
 117 flame velocity s_L , laminar flame thickness δ_L , Lewis number Le , etc., u' is the turbulence intensity,
 118 and L_t is the integral turbulence length scale. The last two turbulent parameters resulting from a
 119 spray-gas interaction have to be determined and they will serve as inputs for the flame velocity
 120 in the large-scale combustion code. The following systematic approach is adapted in order to
 121 determine the turbulent characteristics resulting from a spray-gas interaction:

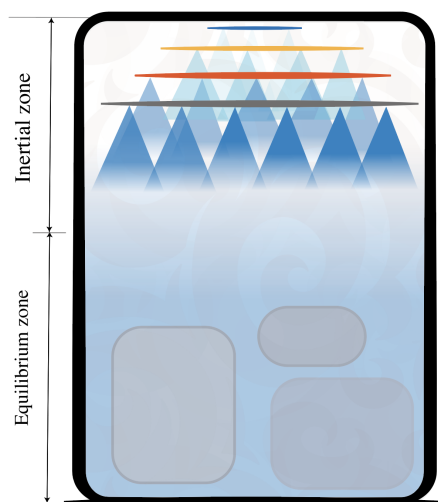


Fig. 1: Industrial spray system containing two regions: inertial zone close to the nozzles and equilibrium zone far from the nozzles.

122 Having a geometry, we can loosely define two zones affected by water spray as shown in Fig.
 123 1. One we shall call, in what follows, the “inertial zone”. In this zone, the steady terminal settling
 124 velocity is not reached for the majority of the spray droplets. The second zone, further called
 125 the “equilibrium zone”, where the terminal settling velocity is reached for the majority of the
 126 droplets. The geometrical characteristics of the two zones depend on the nozzle characteristics and
 127 the geometry of the building where the nozzles are installed. The estimation of the turbulence
 128 parameters in the *inertial zone* will be the subject of the future publications. In this paper, a
 129 methodology for the estimation of turbulent characteristics in the *equilibrium zone* using simple
 130 models is introduced in the following steps:

- 131 1. As a first step, we shall validate the two-phase CFD code Neptune [35] using the DynAsp exper-
 132 imental data. The computed flow variables are compared with their experimental counterparts.
 133 Turbulent characteristics extracted from the computed results are presented and analyzed. Thus

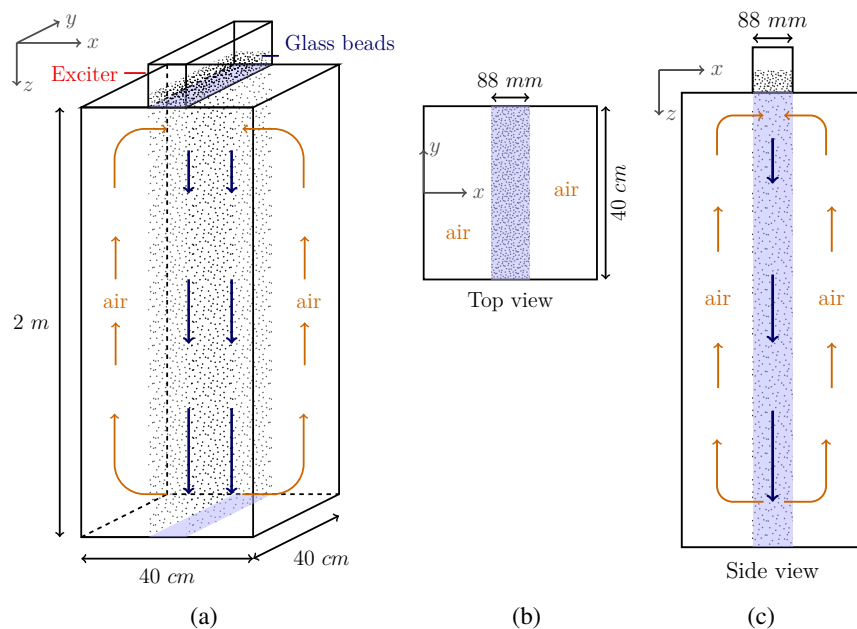


Fig. 2: Dimensions and coordinate system of the experimental setup; (a) main geometry, (b) top view, (c) side view of the setup.

134 validated computer code can be used later in order to find the turbulence parameters inside the
 135 inertial zone.

136 2. Model of Kenning [28] is adapted in order to find the turbulence characteristics inside equilib-
 137 rium zone of the spray-affected volume. The main input parameter, the slip-velocity, which can
 138 be calculated analytically using the Schiller-Naumann drag coefficient correlation [36].

139 3. Kenning's model coupled with the slip-velocity correlation is assessed with numerical simula-
 140 tions of the Neptune_CFD code. The prediction abilities of the simple model on numerical 3D
 141 turbulence characteristics are evaluated and discussed.

142 3 Experimental setup of DynAsp

143 A plexiglas box of dimensions of $(0.4 \times 0.4 \times 2.0) m^3$ was used in the experiment as depicted in
 144 Fig. 2a. A device for injecting glass beads was set on the top of the box. The coordinates system $(x,$
 145 $y, z)$ is defined as shown in Fig. 2b and Fig. 2c, where z is oriented from top to bottom. As shown
 146 in Fig. 2a and Fig. 2b, the injection slot has a size of $(88 \times 400) mm^2$. The injection has different
 147 flow rates of uniform-size particles which are released without initial velocities. Under the effect
 148 of gravity, the particles accelerate during the free fall. After the injection, the measurements are
 149 performed during 30 seconds after a waiting time of 15 seconds.

150 In this study, we consider particles of diameter, $d_p = 500 \mu m$. The numerical results are
 151 firstly validated against experimental data and then used to assess the predictive behavior of the
 152 mechanistic model of Kenning [28]. Particles characteristics are given in the Table 1.

Table 1: Characteristics of the spray particles

d_p (μm)	ρ_p (kg/m^3)	mass flow rate (g/s)	measurement time (s)
200, 500	2450-2550	16-60	30

153 4 Numerical modelling

154 The NEPTUNE_CFD code used in this study, is a three-dimensional multi-fluid Navier-Stokes
 155 solver developed jointly by EDF (Électricité de France) and CEA (Commissariat à l'Énergie
 156 Atomique et aux Énergies Alternatives) [35; 37]. The code relies on a finite volume discretization
 157 and allows the use of various mesh types (tetra or hexahedral element) for different flow regimes:
 158 compressible/incompressible, steady/unsteady, laminar and turbulent.

The two-fluid model used in Neptune_CFD is based on mass, momentum and energy conservation laws. The mass conservation equation is given as [38]:

$$\frac{\partial}{\partial t}(\alpha_k \bar{\rho}_k) + \nabla \cdot (\alpha_k \bar{\rho}_k \bar{V}_k) = \Gamma_k, \quad k = l, g, \quad (2)$$

159 where α_k is the volume fraction, $\bar{\rho}_k$ the mass density, \bar{V}_k the local mean velocity of the phase k , Γ_k
 160 is the interphase mass transfer rate, l and g denote the liquid and the gas phases, respectively.

The momentum balance equation gives:

$$\frac{\partial}{\partial t}(\alpha_k \bar{\rho}_k \bar{V}_k) + \nabla \cdot (\alpha_k \bar{\rho}_k \bar{V}_k^2) = -\alpha_k \nabla \bar{p} + M_k + \alpha_k \bar{\rho}_k f_g + \nabla \cdot [\alpha_k (\bar{\tau}_k + \bar{\tau}_k^T)], \quad k = l, g, \quad (3)$$

161 where \bar{p} is the gas pressure, f_g the gravity acceleration, M_k the interphase momentum transfer term
 162 and $\bar{\tau}_k$, $\bar{\tau}_k^T$ denote the viscous and Reynolds stress tensors, respectively [39].

163 The total enthalpy conservation equation gives:

$$\begin{aligned} \frac{\partial}{\partial t} \left[\alpha_k \bar{\rho}_k \left(\bar{h}_k + \frac{\bar{V}_k^2}{2} \right) \right] + \nabla \cdot \left[\alpha_k \bar{\rho}_k \left(\bar{h}_k + \frac{\bar{V}_k^2}{2} \right) \bar{V}_k \right] = & \alpha_k \frac{\partial \bar{p}}{\partial t} + \alpha_k \bar{\rho}_k f_g \bar{V}_k + \Gamma_k \left(\bar{h}_{k,int} + \frac{\bar{V}_k^2}{2} \right) \\ & + q_k A_{int} + q_{wk} - \nabla \cdot [\alpha_k (\bar{q}_k + \bar{q}_k^T)] \end{aligned} \quad (4)$$

164 where h_k stands for the phase-averaged specific enthalpy for the phase k , $\bar{h}_{k,int}$ the interfacial-
 165 averaged enthalpy; Γ_k and $q_k A_{int}$ denote the interfacial transfer of mass and heat, respectively. The
 166 wall-to-fluid heat transfer flux term is q_{wk} and the molecular and the turbulent heat fluxes in phase
 167 k are \bar{q}_k and \bar{q}_k^T , respectively. The flow quantities are α_k , ρ_k , V_k and h_k . More details about the
 168 model and turbulent closure of other terms can be found in [35; 40].

169 4.1 Geometry and mesh

170 The geometry used in this study is shown in Fig. 2a. The mesh is generated using the SALOME
 171 platform [41]. Two different meshes are used with an averaged cell size $\Delta l_1 = 1$ cm and $\Delta l_2 = 0.5$
 172 cm. Figure 3 shows the axial gas and droplet velocity evolution for the two considered meshes.
 173 We can see that the change of the mesh size has a relatively small effect, especially on the droplet

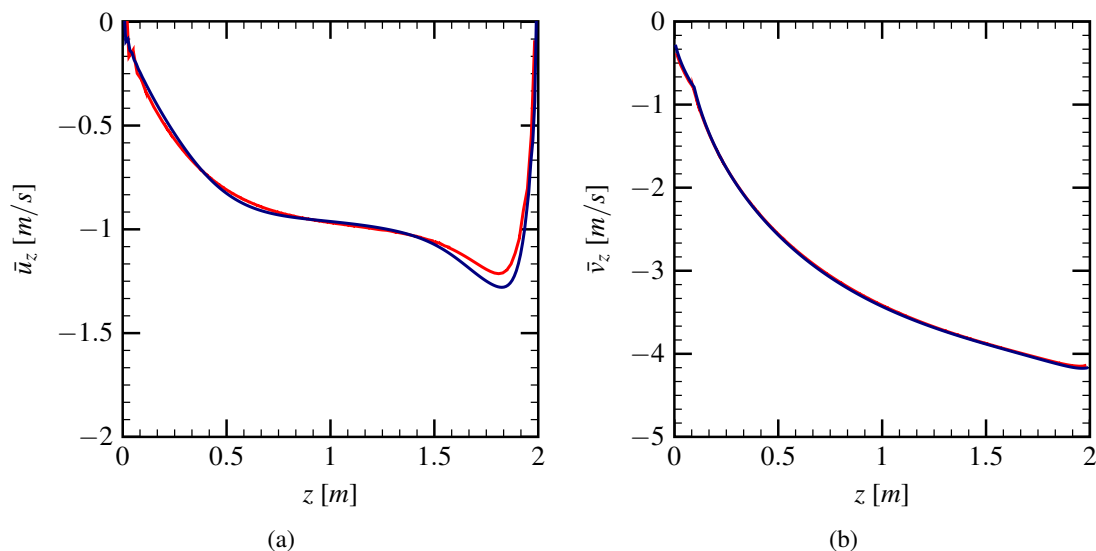


Fig. 3: Spatial distribution of gas and droplet velocities for two different mesh sizes: $\Delta l_1 = 1 \text{ cm}$ (—), $\Delta l_2 = 0.5 \text{ cm}$ (—); (a) axial air velocity, (b) axial droplet velocity.

174 velocity evolution. The numerical solution can therefore be considered to be mesh-independent.
 175 The bottom boundary condition is an outlet for the solid particles and a wall condition for the gas
 176 phase. The wall conditions are set for other geometry surfaces except for the particle inlet at the
 177 top of the box.

178 4.2 RANS Turbulence models for gas and particles

179 Different RANS models are implemented in Neptune_CFD code [37]. For continuous flow fields,
 180 the models range from the simplest one, mixing-length, to a more sophisticated, $R_{i,j} - \epsilon$ SSG
 181 model ($R_{i,j}$ stands for Reynolds stress tensor) involving seven turbulent transport equations [42].
 182 For the dispersed phase, the Tchen model [43] is an algebraic local equilibrium model. The R2-
 183 Q12 model [44] resolves the kinetic stress and fluctuating movement covariance. It is noted that
 184 these four particle turbulence models have to be used with a gas turbulence model predicted by
 185 either $k - \epsilon$ or $R_{i,j} - \epsilon$ turbulence closures. More details regarding the turbulence modeling aspects
 186 can be found in [37].

187 A number of comparative numerical studies are performed using the configuration of the
 188 experiment DynAsp with different turbulent models. The injection rate of the particles of $d_p = 500$
 189 μm is taken as 35 g/s . The numerical results are systematically compared with the experimental
 190 measurements. For the measurement of the gas velocity, 10^5 trace particles were taken into account
 191 for the calculation of vertical component, and 5×10^4 particles for the horizontal component
 192 [19; 20]. The tracer particle distribution has a Gaussian shape. The program selects the velocity
 193 of most counted tracers which is located in the center of the velocity distribution. This velocity is
 194 defined as the instantaneous gas velocity. The mean gas velocity is obtained by superposition of

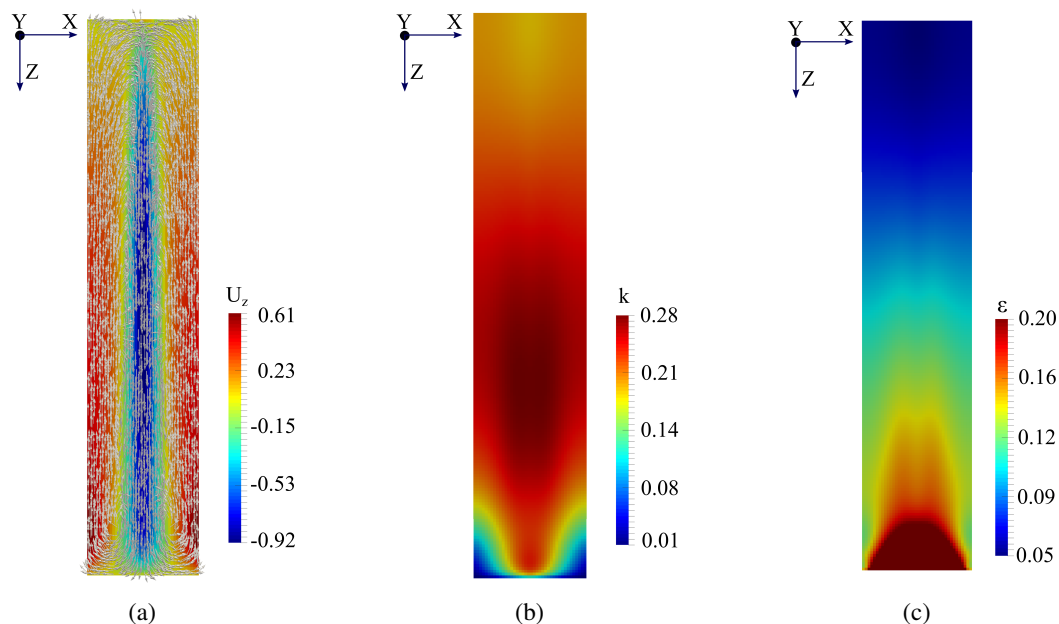


Fig. 4: Numerical simulation showing mean flow quantities: (a) gas velocity (m/s), (b) turbulent kinetic energy (m^2/s^2), (c) turbulent dissipation (m^2/s^3).

195 several measurements. The experimental standard deviations which represents the validity interval
 196 of the measurement are given through error bars (see Fig. 5a).

197 Figure 4a shows the gas velocity field on the central x-z section for an injection rate of 35 g/s.
 198 Two symmetric convective loops can be observed: the gas moves downwards in the central biphasic
 199 region and rises up at the pure gas zone. The distributions of the turbulent kinetic energy (TKE)
 200 and turbulent dissipation are depicted in Figs. 4b and 4c. It can be seen that the TKE has a maximal
 201 value at the lower middle of the biphasic region while the region of high turbulent dissipation rate
 202 is located at the bottom of the box. In fact, at the lower middle part of the particle-laden region,
 203 the particle velocity gradient becomes small and the production and dissipation of the TKE have very
 204 close values.

205 Figure 5a shows the comparison between the numerical results and the experimental data in
 206 terms of axial gas velocity for different combinations of air/particle turbulence models. It can be
 207 noted that the particle turbulence model does not have an influence on the axial air speed. The
 208 $k - \epsilon$ model shows larger errors on the prediction of the air velocity, compared to the second order
 209 $R_{i,j} - SSG$ model, which better reproduce the evolution of the air velocity. Similar results can be
 210 obtained for the mass injection rate of 16 g/s and 60 g/s.

211 The influence of different turbulence models on the computed particle velocity evolutions is
 212 given in Fig. 5b. Contrary to the gas velocity prediction, the $k - \epsilon$ model gives a slightly better
 213 estimation on the particle velocity evolutions. The experimental results for particle velocity vary
 214 little with different injection rates. However, the axial particle velocity seems to increase with the
 215 injection rate in the numerical simulations as depicted in Fig. 6b.

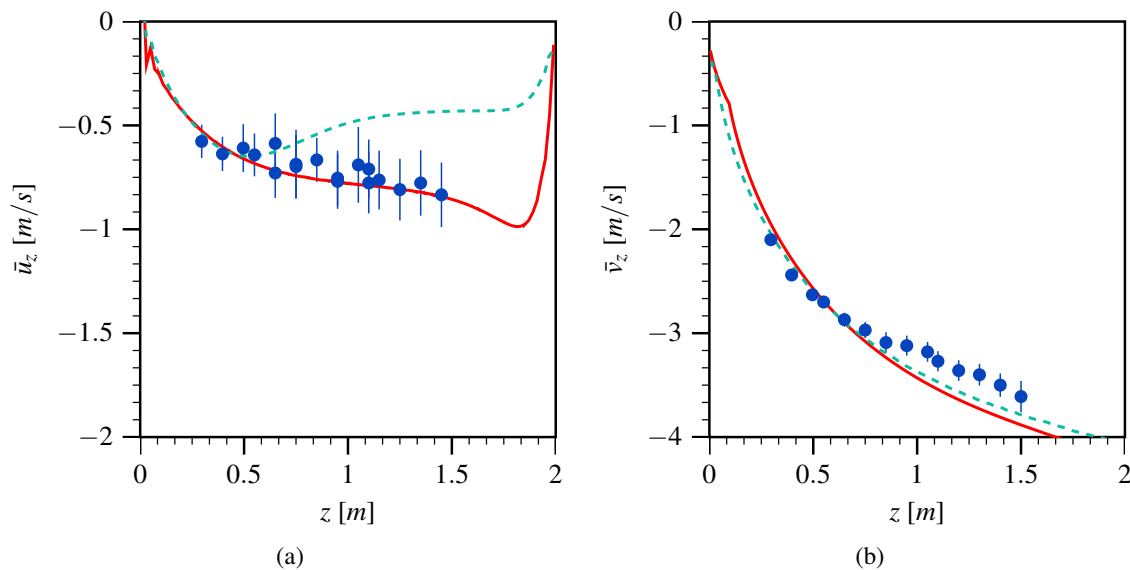


Fig. 5: Comparison of gas (a) and particle (b) axial velocity on the centerline for different turbulence models with an injection rate of 35 g/s; experimental results (\bullet), $R_{i,j} - \epsilon$ SSG model ($—$) and $k - \epsilon$ model ($- - -$).

216 4.3 Numerical validation with Reynolds stress model $R_{i,j} - SSG$

217 In order to study the air flow turbulence modulation by particles, the $R_{i,j} - \epsilon$ SSG model is used
 218 based on the accuracy of the gas velocity prediction. The R2-Q12 model [44] is employed for the
 219 dispersed phase when using $R_{i,j} - \epsilon$ SSG model for the gas phase.

220 Figure 6a shows the axial velocity of air on the centerline of the box as a function of distance
 221 from the injection slot, for two different loading rates: 16 g/s and 60 g/s. The simulation results
 222 of Neptune_CFD are compared to the corresponding experimental data. For all mass injection
 223 rates, the particles accelerate along the vertical direction, which through drag forces create the air
 224 motion. The larger the mass injection rate is, the faster the axial air velocity becomes. The gas
 225 velocity reduces to a small value at the bottom of the domain.

226 The behavior of the particle velocity as a function of distance from injection slot is given in
 227 Fig. 6b. The particles accelerate along the vertical direction. We can see that the height of the
 228 experimental set-up is not sufficient for the particles to reach a terminal velocity. The experiments
 229 show that the particle velocity evolution is not significantly affected by the change of the mass
 230 injection rate. However, the numerical simulation highlights the effects of different mass injection
 231 rate. Intuitively, the more particles appear in the flows, the easier the air accelerates.

232 Generally, we have a good agreement between the numerical and experimental results. The
 233 $R_{i,j} - SSG$ model shows a good performance for the validation of the DynAsp experiments,
 234 especially for the predictions of the axial velocities of the air inside the particle/air two-phase
 235 flow.

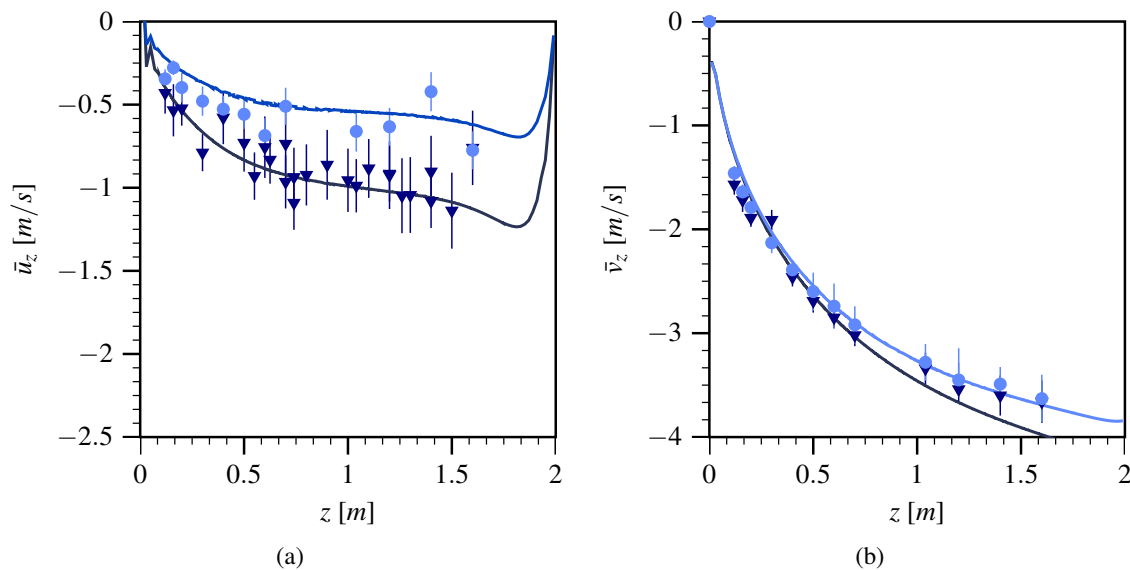


Fig. 6: Comparison of the axial velocity of gas (a) and particles (b) of diameter $500 \mu\text{m}$ on the centerline for different loading rates: DynAsp 60 g/s (▼), 16 g/s (●) and SSG Model 60 g/s (—), 16 g/s (—).

236 4.4 Axial gas velocity near the wall

237 The axial gas velocity at the centerline is shown in Fig. 7, with four different injection mass rates:
 238 23 g/s , 35 g/s , 41 g/s and 60 g/s and compared to the experimental data. The error bars and the
 239 particle-laden flow borders are also added.

240 We can see that the numerical estimations of the axial gas velocity confirm the experimental
 241 trends for all test cases. Some experimental observations can be confirmed by the numerical
 242 simulation, such as the gas velocity increases when approaching the wall. The vertical gas velocity
 243 is negative inside the particle flow, and turns to positive near the wall. It can be noted that the
 244 gas velocities at two vertical position $z = 0.74 \text{ m}$ and $z = 1.26 \text{ m}$ have slight difference. And the
 245 numerical results match well the experimental measurements inside the two-phase region.

246 5 Comparison between numerical simulations and the Kenning model [28]

247 The turbulence modulation by falling solid beads were investigated by [28] using a one-
 248 dimensional energy balance for validation of experimental data. A mechanistic model was
 249 proposed for the estimation of the length scale of the particle-induced turbulence. Initially,
 250 the particles are introduced into a still fluid, when the particles reach their *terminal velocity*, the
 251 motion of the particle cloud is considered to be the only source of turbulence. The loss of energy
 252 of the carrier phase can be divided into two parts: viscous dissipation and particle velocities fluctu-
 253 ations. When the subsequent particles encounter the carrier phase with fluctuating components,
 254 the turbulent energy can be redistributed to the particles (see A for more details).

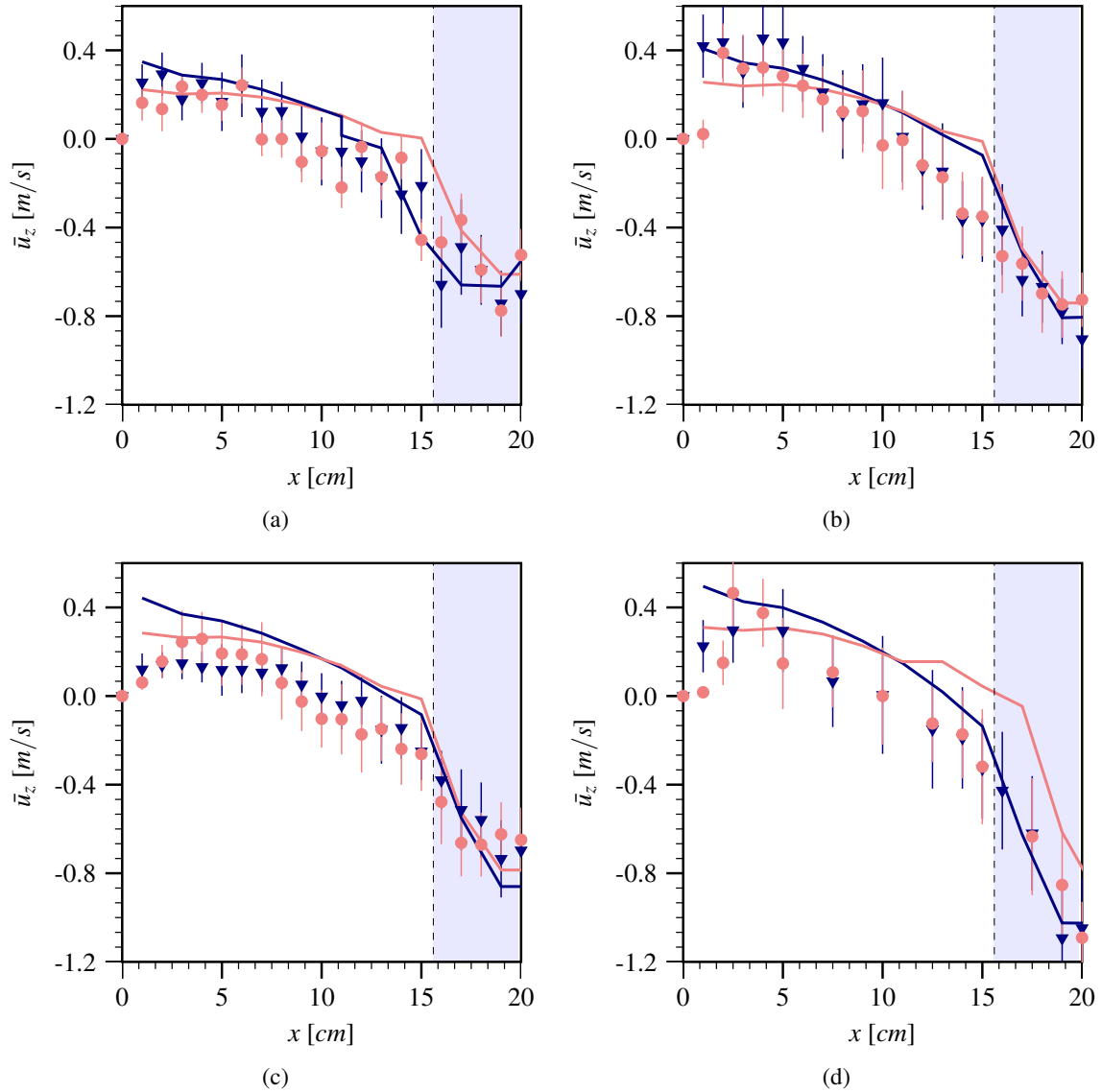


Fig. 7: Axial gas velocity distribution as a function of wall distance; experimental results at $z = 0.74$ m (\blacktriangledown), $z = 1.26$ m (\bullet) and numerical results at $z = 0.74$ m (---), $z = 1.26$ m (---); particle cloud border (---); injection rate (a) 23 g/s, (b) 35 g/s, (c) 41 g/s, (d) 60 g/s. Note that the wall is located at $x = 0$.

255 5.1 Mechanistic model compared to numerical simulations

256 Five axial probes are used to measure the flow velocities inside the two-phase flow domain. The
 257 probe locations are shown in Fig. 8a. The evolution of different parameters such as gas/droplet
 258 velocity, integral length scale and kinetic turbulence energy are estimated by the Neptune_CFD
 259 code.

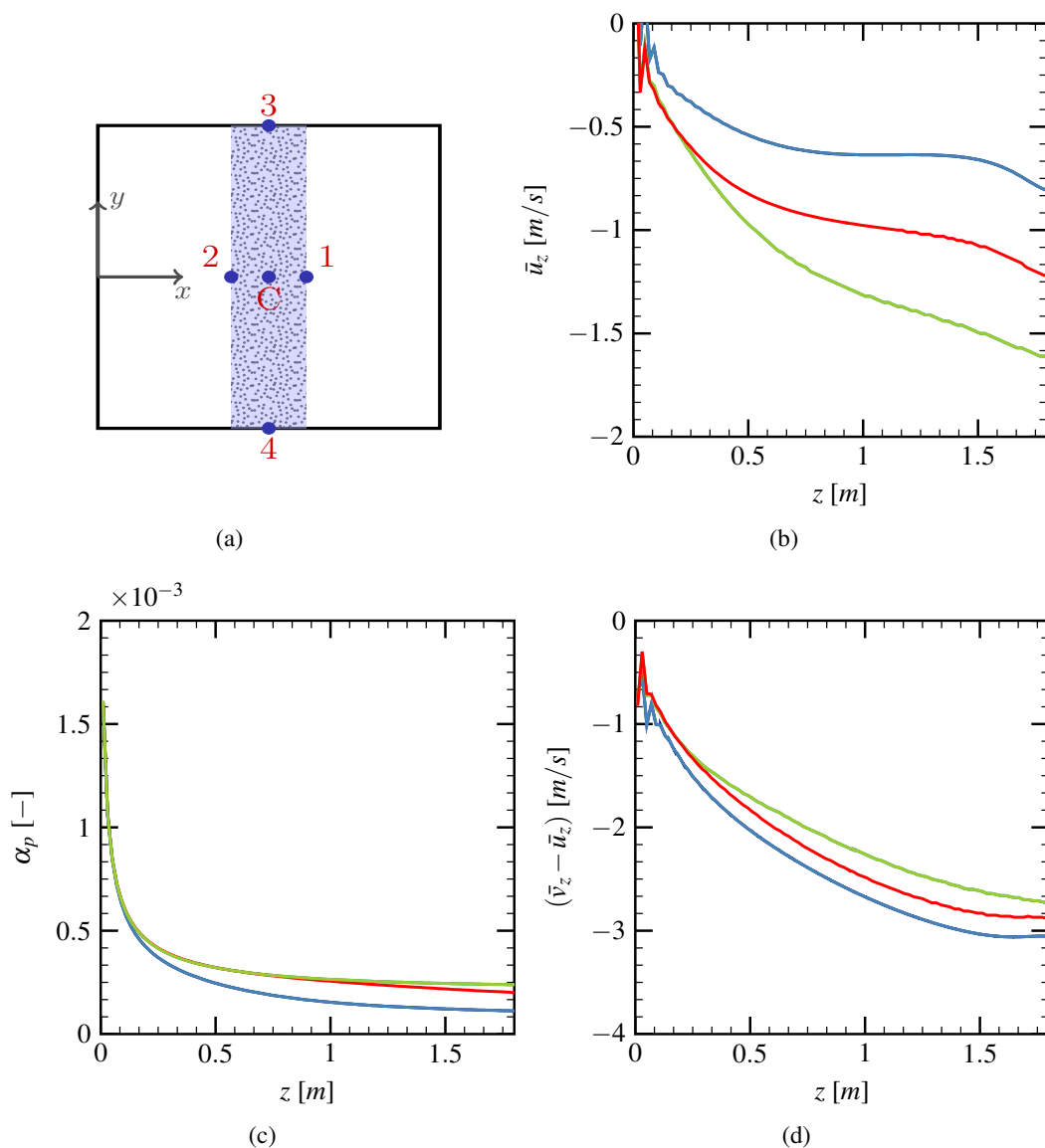


Fig. 8: Numerical results of Neptune_CFD code. (a) Positions of the axial probes. Spatial evolutions of physical properties, (b) axial gas velocity, (c) volume fraction, (d) slip-velocity, for different probes: probe 1 (—), probe 2 (—), probe 3 (—), probe 4 (—), center (—). The numerical results for probes 1, 2 and 3, 4 are fully super-imposed due to symmetry.

260 The mechanistic model of Kenning needs to have three input parameters: gas velocity u_g ,
 261 particle velocity v_p and particle volume fraction α_p , to estimate the kinetic turbulence energy
 262 k_t and the integral length scale L_t (see A for more details). These parameters are space and time
 263 dependent. Figure 8 shows the variation of these three parameters along the z axis at 5 probe
 264 positions.

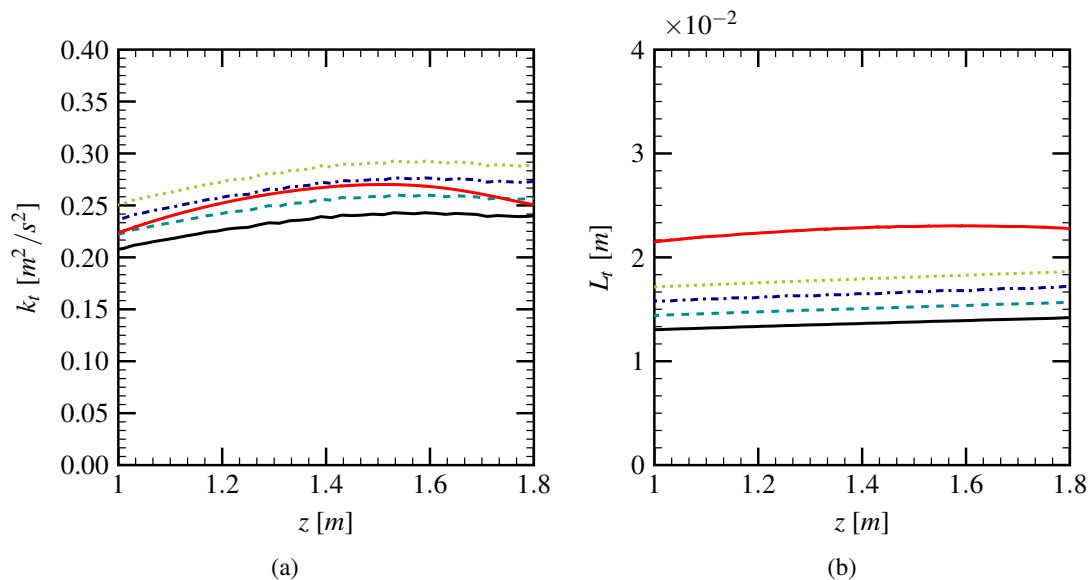


Fig. 9: Kenning's model prediction (—) v.s. numerical results of Neptune_CFD in the centerline (—); the mechanistic model with 1.1λ as inter-particle distance (---), with 1.2λ (-·-·-), with 1.3λ (·····); (a) turbulent kinetic energy, (b) integral length scale.

265 From Fig. 8c we can see that the volume fraction of the droplets decreases with the vertical
 266 distance and reaches a stable value of $\mathcal{O}(10^{-4})$ at the bottom of the geometry. Figs. 8b and 8d
 267 show the evolution of the axial gas velocity and the axial slip-velocity. We can see that the probes
 268 1 and 3 give the same values for gas and slip-velocity since they are symmetric relative to the
 269 center (the same case for probe 2 and 4).

270 Given the values of \bar{u}_z , \bar{v}_z and α_p at the centerline probe as input parameters, we can use the
 271 Kenning model to predict the kinetic turbulence energy and the integral length scale as depicted
 272 in Fig. 9. The calculation results of Neptune_CFD are also given for comparison. The turbulent
 273 kinetic energy k_t extracted directly from the code and the integral length scale L_t is given by the
 274 expression: $L_t = C_\mu^{3/4} k_t / \varepsilon$, where $C_\mu \approx 0.09$ is a constant.

275 Fig. 9 gives the comparison between the numerical simulations and the mechanistic model in
 276 the centerline of the lower-part of the DynAsp experimental setup. It is assumed that in this region,
 277 the turbulence is homogeneous and isotropic. From Fig. 9a, we can see that the mechanistic model
 278 using the input parameters of the central probe can give a good tendency for the kinetic turbulence
 279 energy. The values of k_t for different vertical distances have the same order of magnitude as
 280 Neptune_CFD. Generally, the mechanistic model can be used to estimate the turbulence intensity if
 281 the input values for the volume fraction α_p , gas velocity u_g and especially the slip-velocity $v_p - u_g$
 282 are well estimated.

283 Similar results can be obtained for the integral length scale. The mechanistic model can provide
 284 a prediction of L_t of correct order of magnitude (see Fig. 9b). The difference of the model
 285 estimation and the numerical simulations can be due to the geometrical configurations used in
 286 the DynAsp experiments. From Fig. 2a, we can see that particles are injected in a small section

287 in the middle of the experimental domain. However, the mechanistic model has been validated
 288 for homogeneous particle-laden flows [28]. Given a larger inter-particle distance λ , the difference
 289 between the numerical results and model estimations can be reduced. For example, the model
 290 predictions with 1.1λ , 1.2λ or 1.3λ are given in Fig.9b.

291 The mean volume fraction of the droplets α_p can be referred to the industrial measurements
 292 under the particle injection system. In the study of [28], u_g is the terminal velocity of the free-fall
 293 particles, which plays a minor role on the determination of the kinetic turbulence energy. Thus,
 294 the most important parameter to be determined is the slip-velocity $\bar{v}_p - \bar{u}_g$. For the configuration
 295 of DynAsp, where the initial velocities of the particles are zero, the terminal slip-velocity can be
 296 easily estimated by correlations as discussed in section 5.3.

297 5.2 Turbulent length-scale

It was shown that the turbulence enhancement is mainly driven by the dynamics of large droplets [4]. For instance, in water spray system, the large-scale turbulence generated from the *bulk* flow of water from the nozzles is considered to be the reason for the flame speed increase. To support this idea, Wingerden *et al.* [4] designed an experiment involving spray and premixed flame in interaction, and used the formula proposed by [45], for the estimation of turbulence parameters of the gas mixture affected by a spray:

$$\Lambda_f = (2\pi\nu t_d)^{1/2} \quad (5)$$

298 where Λ_f is the Eulerian integral length scale of turbulence, ν is the kinematic viscosity, and t_d
 299 is the time for turbulence decay. The tests in [4] show that the turbulence exists in the mixture
 300 affecting the flame propagation up to 10 s after switching off the spray system. This decay
 301 time indicates that the length scale of the spray-generated-turbulence would be of the order of
 302 $\Lambda_{spray} = 3 \text{ cm}$.

303 According to the experimental data given in [4], we take, for example, the case of spray
 304 with average droplet size of $500 \mu\text{m}$, with flow rate of 99 l/min . The kinetic viscosity is taken
 305 $\nu = 1.43 \times 10^{-5} \text{ m}^2/\text{s}$. Since the volume fraction of spray droplets was not given in [4], we assume
 306 that $\alpha_p = 1 \times 10^{-4}$. We can therefore calculate the inter-particle spacing $\lambda = 0.00818 \text{ m}$. Taking
 307 the width of the experimental box as the integral dissipation length scale $L_i = 1 \text{ m}$, equation (22)
 308 gives $L_h = 1.62 \text{ cm}$, which matches the order of magnitude of $\Lambda_{spray} = 3 \text{ cm}$. Both estimations are
 309 close to our results as depicted in Fig. 9.

310 5.3 Terminal slip-velocity

In a particle-laden flow, the particle terminal velocity in a cloudy bulk flow is related to the particle volume fraction, which can not be determined analytically. However, the slip-velocity is independent of the injection rate when the particle reaches its terminal velocity. Basing on the force balance, the terminal particle slip-velocity can be calculated by:

$$u_s = \sqrt{\frac{4(\rho_p - \rho_g) d_p g}{3 \rho_g C_d}}, \quad (6)$$

where g is the gravity acceleration, d_p is the particle diameter, ρ_p and ρ_g denote the particle and gas density, respectively. C_d represents the drag coefficient, which can be calculated using the Schiller-Naumann correlation [36]:

$$C_d = \frac{24}{Re_p} \left(1 + 0.15 Re_p^{0.687} \right) \quad \text{with } Re_p = \frac{\rho_g d_p u_s}{\mu_g} \quad (7)$$

311 where Re_p is the particle Reynolds number and μ_g denotes the air viscosity. By combining Eqs.
 312 (6) and (7), one can solve a nonlinear equation to obtain the slip-velocity $u_{s,corr}$. The terminal
 313 slip-velocity is the relative velocity of the solid particles when the viscous resistance of the carrier
 314 phase is equal to the gravity. If the carrier phase is stationary and infinite, the slip-velocity is equal
 315 to the particle terminal velocity.

316 Using similar geometry as the one used in DynAsp tests but having a much larger height $H = 8$
 317 m , the assessment of this correlation using different particle diameters d_p and particle densities ρ_p
 318 is studied. A longer geometry is used to calculate the slip-velocity $u_{s,Neq}$ in Neptune_CFD code.
 319 The comparison between the results for slip-velocity of Neptune_CFD and the correlation is given
 320 in the Table 2. The particles of diameter $d_p = 500 \mu m$ and density $\rho_p = 2550 kg/m^3$ are used in
 321 all these simulations.

Table 2: Validation of the terminal slip-velocity correlation, injection rate 35 g/s.

d_p (μm)	ρ_p (kg/m^3)	$u_{s,Neq}$ (m/s)	$u_{s,corr}$ (m/s)	Error
50	2500	0.21	0.18	14%
100	2500	0.54	0.55	1.9%
200	2500	1.34	1.41	5.2%
300	2500	2.12	2.23	5.2%
400	2500	2.86	2.98	4.2%
500	2500	3.55	3.69	3.9%
50	1000	0.074	0.07	5.4%
100	1000	0.25	0.24	4%
200	1000	0.70	0.71	1.4%
300	1000	1.12	1.17	4.5%
400	1000	1.54	1.61	4.5%
500	1000	1.95	2.02	3.5%

322 We can see that the equation (6) exhibits a good trend of terminal slip-velocity for particles
 323 larger than $50 \mu m$. The relative error is less than 10% for most simulation cases of different droplet
 324 diameter and density. Here calculations are done for droplets less than $500 \mu m$ with particle
 325 Reynolds number equal to $Re_p \approx 1330$. With particles of diameter $100 \mu m$ ($Re_p \approx 266$), the
 326 correlation (7) can give an estimation having the same order of magnitude as the numerical results.

327 For smaller particles such as $d_p = 50 \mu m$, the difference of the slip-velocity estimated can be
 328 more important (14% for the case $d_p = 50 \mu m$ and $\rho_p = 2500 kg/m^3$). First, the droplets are too
 329 small to have a stable terminal slip-velocity while falling down to the bottom of the tube. Moreover,
 330 the droplet velocity approaches the air velocity for these small particles. Therefore, the value of
 331 the terminal slip-velocity becomes small which leads to large relative errors. As a conclusion, the
 332 correlation can be used to estimate the terminal slip-velocity for particles ($d_p > 50 \mu m$). The

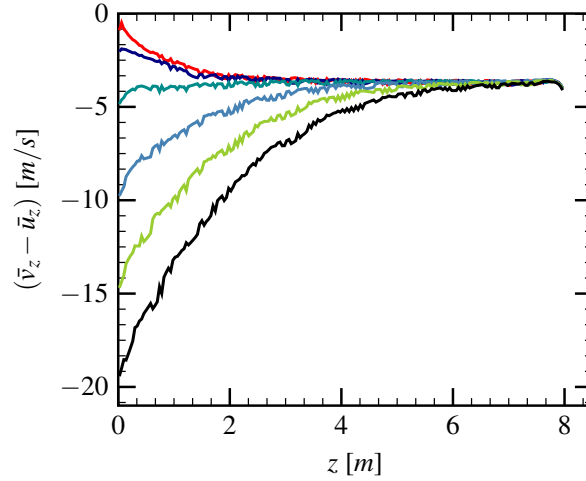


Fig. 10: slip-velocity as a function of the channel height for different initial velocities v_0 ; $v_0 = 0$ m/s (—), $v_0 = 2$ m/s (—), $v_0 = 5$ m/s (—), $v_0 = 10$ m/s (—), $v_0 = 15$ m/s (—), $v_0 = 20$ m/s (—).

333 particles of smaller diameter ($d_p < 50 \mu m$) have a less important influence on the turbulence
 334 generation [4; 46]. It is noted that the mass flow rate has less influence on the terminal slip-velocity.

335 Figure 10 shows the slip-velocity evolutions for different initial injection axial velocities at the
 336 center of the two-phase flow domain. We can see that the difference of the injection velocity has
 337 an influence on the slip-velocity at the first half of the jet. After the stabilization, the slip-velocity
 338 decrease/increase to a constant value which is close to the case of spray without initial injection
 339 velocity. Thus, if the height of the geometry studied is long enough, the initial velocity effect on
 340 the terminal slip-velocity can be neglected for the far field region from injection.

341 6 Conclusions

342 The particle-induced turbulence in a large-scale geometry is investigated numerically by means
 343 of 3D RANS calculations using Neptune_CFD code and a simple predictive model based on
 344 Kenning modeling approach. The obtained results are in good agreements with the experimental
 345 data of DynAsp on the particle velocity and air velocity evolutions. The model is compared to the
 346 Neptune_CFD code and it shows a good capacity to estimate the kinetic turbulence energy and the
 347 integral length scale inside the equilibrium zone.

348 The slip-velocity between the particle and the gas flow is proved to be an important parameter
 349 for the estimation of the turbulence intensity. An empirical correlation is compared to the numerical
 350 simulations, which can be used to provide the terminal slip-velocity for particles of diameters of the
 351 order of $\mathcal{O}(100) \mu m$. Using the Neptune_CFD code, the initial velocity of the injection particles
 352 is noted to have very small influence on the terminal particle slip-velocity in the equilibrium zone
 353 far from the injection region.

354 Using the Kenning model and the terminal slip velocity equation, we can estimate the turbu-
 355 lent kinetic energy and the turbulent length scale inside the equilibrium zone generated by falling

356 particles with a sufficient accuracy for large-scale numerical simulations. The simple mechanistic
 357 model is proved to be capable of providing reasonable estimations of the turbulent characteristics
 358 which can be implemented in large-scale modeling in future studies. This method can be applied to
 359 the simulation of slow flame-spray interaction in industrial scenarios such as nuclear containment
 360 building, offshore facilities, etc. The future work will consist of estimation of the turbulence param-
 361 eters inside the *inertial zone*. This will be done through extensive validation of the Neptune_CFD
 362 code using available experimental data on the near field of the industrial nozzles.

363 Acknowledgements

364 The authors gratefully acknowledge the financial support from Electricité de France (EDF) within
 365 the framework of the Generation II & III reactor research program.

366 Conflict of interest

367 The authors declare that they have no conflict of interest.

368 Appendix

369 A Mechanistic Model of Kenning *et al.* [28]

370 For simplicity, the distribution of the dispersed phase is considered as uniform and the fluctuations induced
 371 in the carrier phase by the particles are assumed to be isotropic, even though the fluctuation in the streamwise
 372 direction is almost twice the fluctuation in the transverse direction [47].

Since both the carrier flow and the dispersed phase exhibit fluctuating behavior, the relative fluctuations are used to investigate the turbulent energy production and dissipation due to the presence of particles. The relative particle velocity fluctuations were described from the spherical-particle motion equation as:

$$\frac{dv'_p}{dt} = \frac{1}{\tau_p}(u' - v'_p) + \frac{1}{2} \frac{\rho_f}{\rho_p} \frac{d(u' - v'_p)}{dt}, \quad (8)$$

373 where ρ_f , ρ_p denote the density of the carrier fluid and the dispersed particle, respectively and u' and v'_p are
 374 the fluid and the particle velocity fluctuations respectively, τ_p is the response time of the particle.

Assuming that the fluctuating velocity components of the fluid and the particle velocity behave as:

$$u' = u_0 e^{i\omega t}, \quad v'_p = u_0 \mathcal{A} e^{i\omega t + \phi}, \quad (9)$$

where u_0 , $\mathcal{A}u_0$ are the amplitudes of the fluid and the particle velocity fluctuations, respectively and ω is the characteristic frequency of the fluid defined as:

$$\omega = \frac{v_{rel}}{\lambda}, \quad (10)$$

375 where v_{rel} and λ denote the relative velocity between the two phases and the mean inter-particle distance of
 376 the dispersed phase, respectively.

377 By introducing (9) into Equation (8), we can have:

$$\begin{aligned} \mathcal{A} \cos\phi - S_t \sin\phi \mathcal{A} \left(1 + \frac{1}{2} \frac{\rho_f}{\rho_p}\right) &= 1, \\ \mathcal{A} \sin\phi + S_t \cos\phi \mathcal{A} \left(1 + \frac{1}{2} \frac{\rho_f}{\rho_p}\right) &= S_t \left(\frac{1}{2} \frac{\rho_f}{\rho_p}\right), \end{aligned} \quad (11)$$

378 where $S_t = \omega \tau_p$ is the Stokes number.

From Equation (11), we can obtain ϕ and \mathcal{A} as:

$$\phi = \arctan \left(\frac{-2S_t}{S_t^2 \frac{\rho_f}{\rho_p} \left(1 + \frac{1}{2} \frac{\rho_f}{\rho_p}\right) + 2} \right), \quad (12)$$

$$\mathcal{A} = \sqrt{\frac{1 + \tan^2 \phi}{\left[1 - S_t \tan \phi \left(1 + \frac{1}{2} \frac{\rho_f}{\rho_p}\right)\right]^2}}, \quad (13)$$

Kenning *et al.* [28] propose a simple expression of the fluctuation amplitude \mathcal{A} using the Stokes number, such as:

$$\mathcal{A} = \sqrt{\frac{S_t^2 \frac{\rho_f^2}{\rho_p^2} + 4}{4S_t^2 + 4S_t^2 \frac{\rho_f}{\rho_p} + S_t^2 \frac{\rho_f^2}{\rho_p^2} + 4}}. \quad (14)$$

379 We can notice from Equation (14) that \mathcal{A} is smaller than unity, which indicates that the particles
380 oscillation magnitude is smaller than that of the fluid fluctuations.

381 A.1 Turbulence generation by particles

Considering the main flow direction, the kinetic energy transfer rate from particles to fluid per unit particle mass due to the velocity difference can be estimated by:

$$P_p = \frac{(u - v_p)^2}{\tau_p}, \quad (15)$$

382 where u and v_p are fluid and particle instantaneous velocity, respectively. τ_p is the mean particle response
383 time. The velocities can be divided into mean and fluctuating parts as:

$$\begin{aligned} u &= \bar{u} + u', \\ v_p &= \bar{v}_p + v'_p, \end{aligned} \quad (16)$$

Considering the expression of Equation (9), we can calculate the averaged energy production rate as:

$$\bar{P}_{p,1} = \frac{1}{2} \left[\frac{2(\bar{u} - \bar{v}_p)^2 + \mathcal{A}^2 u_0^2 - 2u_0^2 \mathcal{A} \cos \phi + u_0^2}{\tau_p} \right], \quad (17)$$

Even though the kinetic energy transfer is mainly due to the velocity in the main flow direction, the fluctuation of the fluid and the particles are basically three-dimensional. Thus, the turbulent energy production from the particle to the fluid should be three-dimensional, leading to a more general formulation of the turbulent production term:

$$\bar{P}_p = \frac{1}{2} \left[\frac{2(\bar{u} - \bar{v}_p)^2 + 3\mathcal{A}^2 u_0^2 - 6u_0^2 \mathcal{A} \cos \phi + 3u_0^2}{\tau_p} \right]. \quad (18)$$

384 A.2 Energy redistributing to particles

Particle fluctuations are mainly due to the fluid flow fluctuations. The presence of dispersed particles dissipates part of the turbulent energy of the carrier phase. The dissipation rate per unit mass of particles is derived from the following particle equation:

$$\varepsilon_p = \frac{d(\frac{1}{2}v_p'^2)}{dt} = \left[\frac{1}{\tau_p}(u' - v_p') + \frac{1}{2} \frac{\rho_f}{\rho_p} \frac{d(u' - v_p')}{dt} \right] v_p', \quad (19)$$

Using Equation (9), a mean dissipation rate over a complete oscillation period results in:

$$\bar{\varepsilon}_p = 3 \times u_0^2 \mathcal{A} \left[\frac{2\cos\phi - 2\mathcal{A} + S_t \sin\phi \frac{\rho_f}{\rho_p}}{4\tau_p} \right]. \quad (20)$$

385 where the factor 3 indicates that the dissipation of the fluctuations account for three dimensional effect,
386 similar to the turbulence generation.

387 A.3 Viscous flow dissipation

The presence of particles in the carrier phase will not generate only turbulence, but also modify the viscous dissipation rate of the fluid. The rate of turbulent dissipation proposed by Kenning is:

$$\varepsilon = \frac{k_t^{3/2}}{L_h}, \quad (21)$$

where L_h is the hybrid length scale which combines the inherent integral length scale L_i and the mean inter-particle distance of the dispersed particles λ .

$$L_h = \frac{2}{\frac{1}{\lambda} + \frac{1}{L_i}} = \frac{2L_i\lambda}{L_i + \lambda}. \quad (22)$$

388 The factor 2 comes from the harmonic average of these two length scales.

Combining (18) and (20), the turbulent kinetic energy rate can be expressed as:

$$\frac{dk_t}{dt} = (\bar{P}_p - \bar{\varepsilon}_p) \left(\frac{\alpha_p}{1 - \alpha_p} \right) \left(\frac{\rho_p}{\rho_f} \right) + (P_i - \varepsilon). \quad (23)$$

389 where α_p denotes the volume fraction of the dispersed phase, and P_i is the inherent turbulence in the carrier
390 fluid for no-stagnant initial conditions.

391 References

- 392 1. K.V. Wingerden and B. Wilkins. The influence of water sprays on gas explosions. Part 2: mitigation. *J. Loss Prevent. Proc.*, 8(2):61–70, 1995.
- 393 2. G.O. Thomas. On the conditions required for explosion mitigation by water sprays. *Process. Saf. Environ.*, 78(5):339–354, 2000.
- 394 3. G. Gai, S. Kudriakov, B. Rogg, A. Hadjadj, E. Studer, and O. Thomine. Numerical study on
395 laminar flame velocity of hydrogen-air combustion under water spray effects. *Int. J. Hydrog. Energy*,
396 44(31):17015 – 17029, 2019.

- 399 4. K.V. Wingerden and B. Wilkins. The influence of water sprays on gas explosions. Part 1: water-spray-
400 generated turbulence. *J. Loss Prevent. Proc.*, 8(2):53–59, 1995.
- 401 5. G. Hetsroni and M. Sokolov. Distribution of mass velocity and intensity of turbulence in a two-phase
402 turbulent jet. *ASME J. Appl. Mech.*, 38(2):315–327, 1971.
- 403 6. G. Hetsroni. Particles-turbulence interaction. *Int. J. Multiph. Flow*, 15(5):735–746, 1989.
- 404 7. R.A. Gore and C.T. Crowe. Modulation of turbulence by a dispersed phase. *ASME J. Fluids Eng.*,
405 113(2):304–307, 1991.
- 406 8. S. Elghobashi. On predicting particle-laden turbulent flows. *Appl. Sci. Res.*, 52(4):309–329, June 1994.
- 407 9. A. Sadiki, M. Chrigui, J. Janicka, and M. R. Maneshkarimi. Modeling and Simulation of Effects of
408 Turbulence on Vaporization, Mixing and Combustion of Liquid-Fuel Sprays. *Flow Turbul Combust*,
409 75(1):105–130, December 2005.
- 410 10. Y. Xu and S. Subramaniam. Effect of Particle Clusters on Carrier Flow Turbulence: A Direct Numerical
411 Simulation Study. *Flow Turbul Combust*, 85(3):735–761, December 2010.
- 412 11. G. Mallouppas, W.K. George, and B.G.M. van Wachem. Dissipation and inter-scale transfer in fully
413 coupled particle and fluid motions in homogeneous isotropic forced turbulence. *Int. J. Heat. Fluid Flow*,
414 67:74 – 85, 2017.
- 415 12. C.T. Crowe, J.D. Schwarzkopf, M. Sommerfeld, and Y. Tsuji. *Multiphase flows with droplets and
416 particles*. CRC, Taylor and Francis, 2012. ISBN 9781439840504.
- 417 13. G. Gai, A. Hadjadj, S. Kudriakov, and O. Thomine. Particles-induced turbulence: A critical review
418 of physical concepts, numerical modelings and experimental investigations. *Theor. App. Mech. Lett.*,
419 10:1–7, 2020.
- 420 14. R.A. Gore and C.T. Crowe. Effect of particle size on modulating turbulent intensity. *Int. J. Multiph.*
421 *Flow*, 15(2):279–285, 1989.
- 422 15. T. Tanaka and J.K. Eaton. Sub-Kolmogorov resolution particle image velocimetry measurements of
423 particle-laden forced turbulence. *J. Fluid Mech.*, 643:177–206, 2010.
- 424 16. Y. Tsuji, Y. Morikawa, and H. Shiomi. LDV measurements of an air-solid two-phase flow in a vertical
425 pipe. *J. Fluid Mech.*, 139:417–434, 1984.
- 426 17. S. Hosokawa and A. Tomiyama. Influences of relative velocity on turbulent intensity in gas-solid two-
427 phase flow in a vertical pipe. In *Third Int. Conference on Multiphase Flow, ICMF98*, Lyon, France,
428 1998.
- 429 18. J.D. Kulick, J.R. Fessler, and J.K. Eaton. Particle response and turbulence modification in fully
430 developed channel flow. *J. Fluid Mech.*, 277:109–134, 1994.
- 431 19. A. Patigniez. Expérience DynAsp - résultats expérimentaux. *Technical Report*, 1996.
- 432 20. L. Herlin, G. Mallet, J.-C. Coche, and P. Dumas. Présentation de l'expérience DynAsp. *Technical
433 Report*, 1996.

- 434 21. S. Balachandar and J.K. Eaton. Turbulent dispersed multiphase flow. *Annu. Rev. Fluid Mech.*,
435 42(1):111–133, 2010.
- 436 22. Z. Yuan and E.E. Michaelides. Turbulence modulation in particulate flows. A theoretical approach. *Int.*
437 *J. Multiph. Flow*, 18(5):779–785, 1992.
- 438 23. L.P. Yarin and G. Hetsroni. Turbulence intensity in dilute two-phase flows-3 the particles-turbulence
439 interaction in dilute two-phase flow. *Int. J. Multiph. Flow*, 20(1):27–44, 1994.
- 440 24. D. Wacks and N. Chakraborty. Flame Structure and Propagation in Turbulent Flame-Droplet Interaction:
441 A Direct Numerical Simulation Analysis. *Flow Turbul Combust*, 96(4):1053–1081, 2016.
- 442 25. C.T. Crowe. On models for turbulence modulation in fluid-particle flows. *Int. J. Multiph. Flow*,
443 26(5):719–727, 2000.
- 444 26. M. Mandø. *Turbulence modulation by non-spherical particles*. PhD thesis, Aalborg Universitet,
445 Denmark, 2009.
- 446 27. M. Mandø, M.F. Lightstone, L. Rosendahl, C. Yin, and H. Sørensen. Turbulence modulation in dilute
447 particle-laden flow. *Int. J. Heat. Fluid Flow*, 30(2):331 – 338, 2009.
- 448 28. V.M. Kenning. *Self-induced turbulence in solid-liquid flow*. PhD thesis, Washington University, USA,
449 1996.
- 450 29. V.M. Kenning and C.T. Crowe. On the effect of particles on carrier phase turbulence in gas-particle
451 flows. *Int. J. Multiph. Flow*, 23(2):403–408, 1997.
- 452 30. J.K. Eaton. *Turbulence modulation by particles, Multiphase Flow Handbook (ed. C.T. Crowe)*. CRC,
453 Taylor and Francis, 2006. ISBN 9781498701006.
- 454 31. A. Saber, T. Lundström, and J. Hellström. Turbulent modulation in particulate flow: A review of critical
455 variables. *Engineering*, 7:597–609, 2015.
- 456 32. S. Elghobashi. DNS of turbulent flows laden with droplets or bubbles. *ArXiv e-prints*, April 2018.
- 457 33. Gexcon AS. FLACS code User Manual, 2020. <http://www3.gexcon.com/files/manual/flacs/html/index.html>.
- 458 34. A. Velikorodny, E. Studer, S. Kudriakov, and A. Beccantini. Combustion modeling in large scale
459 volumes using europlexus code. *J. Loss Prevent. Proc.*, 35:104 – 116, 2015.
- 460 35. S. Mimouni, M. Boucker, J. Laviéville, A. Guelfi, and D. Bestion. Modeling and computation of
461 cavitation and boiling bubbly flows with the neptune_cfd code. *Nucl. Eng. Des.*, 238(3):680–692, 2008.
- 462 36. L. Schiller and A. Naumann. A drag coefficient correlation. *Zeitschrift des Vereins Deutscher*
463 *Ingenieure*, 75:318–320, 1935.
- 464 37. *Neptune_CFD version 4.3.1 Theory Guide*, 2019.
- 465 38. M. Ishii and T. Hibiki. *Thermo-fluid Dynamics of two-phase flow*. Springer, Berlin, 2006.
- 466 39. O. Pironneau and B. Mohammadi. *Analysis of the k-epsilon turbulence model*. Mason, 1994.
- 467 40. S. Mimouni. Modeling and cavitation flows : a two-phase flow approach. *La Houille Blanche*, 6, 2006.

-
- 468 41. A. Ribes and C. Caremoli. Salomé platform component model for numerical simulation. In *31st*
469 *Annual International Computer Software and Applications Conference (COMPSAC 2007)*, volume 2,
470 pages 553–564, July 2007.
- 471 42. C.G. Speziale, S. Sarkar, and T.B. Gatski. Modelling the pressure–strain correlation of turbulence: an
472 invariant dynamical systems approach. *J. Fluid Mech.*, 227:245–272, 1991.
- 473 43. E. Deutsch and O. Simonin. Large eddy simulation applied to the motion of particles in stationary
474 homogeneous fluid turbulence. In *Turbulence Modification in Multiphase Flows*, volume 110, page
475 35–42, 1991.
- 476 44. O. Simonin. Second-moment prediction of dispersed phase turbulence in particle-laden flows. In *8th*
477 *Symposium on Turbulent Shear Flow*, Germany, 1991.
- 478 45. J.O. Hinze. *Turbulence*. McGraw-Hill classic textbook reissue. McGraw-Hill, 1987.
- 479 46. C.T. Crowe, T.R. Troutt, and J.N. Chung. Numerical models for two-phase turbulent flows. *Annu. Rev.*
480 *Fluid Mech.*, 28(1):11–43, 1996.
- 481 47. R.N. Parthasarathy and G.M. Faeth. Turbulence modulation in homogeneous dilute particle-laden flows.
482 *J. Fluid Mech.*, 220:485–514, 1990.

Chapter 6

Conclusions and Perspectives

In this work, reduced-order modeling strategies along with empirical correlations based on conservation laws are developed in order to provide better information on the physics of flow phenomena related to hydrogen explosion evolutions under effects of the water spray system in the context of nuclear accidental scenarios. Special attention is paid to the interactions between premixed hydrogen-air combustion, explosion-induced shock waves, and spray-induced turbulence. One of the objectives of the current study is to include the effects of these interactions in large-scale analysis using simplified modeling approaches.

Fundamental physical phenomena and associated physical models are presented in Chapter 1: combustion properties, water droplet characteristics, planar shock waves and turbulence modulations. The combustion phenomena involved in the accidental explosion scenarios are discussed such as flame acceleration and deflagration-to-detonation transition. Mechanisms of the premixed hydrogen-air combustion are briefly introduced as well as the definition of the laminar flame thickness and burning velocity. Important factors during spray-flame interactions are presented such as droplet evaporation, droplet breakup, droplet size distribution and spray dispersion. etc. The influence of explosion-induced shock waves on spray dispersion and droplet size distribution via droplet breakup is examined. The Eulerian-Lagrangian method is applied for the description of the planar shock wave and the disperse droplets. Two-way formalism is used for the spray-shock interaction by taking into account both the droplet acceleration and the gas deceleration by the droplets. The gas turbulence induced by the movement of the spray bulk flow is noted to be important for the flame acceleration. Two types of RANS turbulence models ($k - \varepsilon$ and $R_{ij} - \varepsilon$ SSG) are introduced which are widely used for the evaluation of the turbulence intensity in large geometries.

Spray-flame interaction

Before the development of reduced-order models, a lumped-parameter study is carried out in Chapter 2. By neglecting the less important physical phenomena, this lumped-element model is developed to evaluate the spray evaporation effect on the asymptotic behavior of the pressure and temperature evolution after an AICC

combustion. Based on the conservation of mass and energy, the model can predict burnt gas properties for combustions with or without droplet evaporation. Different hydrogen-air mixtures are investigated within the flammability limits. CHEMKIN code is used for the assessment of the developed model on the prediction of asymptotic AICC temperature. The limit volume fractions for different gas mixtures are given, under which the liquid phase can totally evaporate during the complete combustion. The spray evaporation is shown to have an efficient mitigation effect on the asymptotic pressure for different initial droplet volume fractions. A methodology is presented to determine the pressure evolutions during turbulent hydrogen combustion in the presence of the water spray in a closed volume. A simplified engineering model serves to provide guideline values for the key parameters such as the flame velocity constant K_0 , the heat transfer coefficient H , and the volumetric evaporation rate $\dot{\alpha}$. Due to the lack of accurate experimental measurements, the estimation of these parameters can only rely on theoretical or other relative experimental parameters available in the literature. Using these estimations, the combustion code CREBCOM is used to determine the transient state of the combustion system, focusing on the evolution of pressure and the flame velocity in the presence of water spray. The DOE method has been employed to perform the sensitivity analysis with respect to these model parameters. Calculation results are shown to collaborate the experimental findings, that the water spray has an effective mitigation influence on the pressure evolution during the turbulent combustion. This methodology provides an approach to identify, estimate and evaluate the important parameters for the determination of the pressure loads due to combustion in the presence of sprays at large scale.

Chapter 3 presents the “Laminar Flame Velocity under Droplet Evaporation Model” (LVDEM) for premixed hydrogen-air combustion which was developed and assessed using the Cosilab code and the experimental results. The main object of this model is to quantify the laminar flame deceleration due to the spray evaporation within the flame thickness. A key ingredient of the LVDEM-model is the single droplet evaporation model which is essential for the determination of the evaporated mass in the flame zone. In general, for all considered droplet diameters, the laminar flame velocity decelerates with increasing water volume fraction. Two critical droplet diameters are noted: (i), $D_{c,1} = 35 \text{ mm}$ above which the droplets do not affect the laminar flame velocity for the droplet volume fraction of $\alpha = 10^{-4}$ and, (ii), $D_{c,2} = 3.9 \text{ mm}$, below which the droplets can totally evaporate for all flammable hydrogen-air mixtures and for droplet volume fractions in the range $0 \leq \alpha \leq 10^{-4}$. The effects of the droplets volume fraction, mixture composition and droplet size on the propagation velocity of the laminar flame velocity and flame thickness are investigated numerically.

Spray-shock wave interaction

Chapter 4 presents two analytical models on the description of the spray dispersion topology after interaction with the explosion-induced shock waves. Small rigid particles are investigated instead of water droplets for simplicity. First, an analytical model is developed to study the cloud topology after the passage of a planar shock wave in the framework of a one-way interaction formalism. The momentum exchange between the shock and particles are studied in order to elucidate the dynamic aspect of the shock-cloud interaction

mechanisms. The assessment of the model is conducted through a comparison with numerical simulations performed using the high accuracy Navier-Stokes solver Asphodele. Small particles of diameter $\mathcal{O}(1) \mu m$ are noted to be sensitive to the drag of the post-shock gas and the presence of piece-wise structures of the shock-cloud interaction is shown. A simple extension of the one-way to the two-way formulation confirms the necessity of using the two-way formalism in the numerical simulation of the shock-cloud interaction. An important shock attenuation effect is noticed for the particle cloud of high volume fractions $\mathcal{O}(10^{-3})$. Various mechanisms such as shock reflection and attenuation can be observed in the two-way simulations which are neglected in the one-way formalism. Then, the problem of shock-wave propagation into a dispersed particle-laden area is investigated both numerically and analytically in a one-dimensional shock tube configuration. A new analytical model is derived to evaluate the particle dispersion topology as well as the post-shock gas properties in the framework of the two-way formalism. The development of the analytical model is based on the observations of the numerical results and assessed using the Navier-Stokes solver Asphodele. Two regimes of shock reflections are revealed by numerical simulations, depending on the initial shock Mach number. The estimation of the spray dispersion topology after the shock passage, characterized by the volume fraction of the particles, mainly depends on the correct estimation of post-shock gas properties. A particle number density peak is predicted for strong Mach numbers ($M_s > 2$) and moderate particle diameter ($D = 10 \mu m$). The appearance of a compressed gas layer at the gas-spray interface is considered to be a key factor for the number density peak. Necessary conditions for the formation of a particle density peak are proposed, and the peak density amplitude is seen to increase when increasing M_s . The predictions of the analytical model show a good agreement with the numerical results, thereby demonstrating the predictive capabilities of the proposed model.

Spray-induced turbulence

Chapter 5 discusses the spray-induced turbulence, beginning with a review of the most important physical concepts and numerical modeling and empirical correlations. In large-scale facilities, such as reactor buildings, the spraying geometry could be subdivided into two zones: one lies immediately below the spray nozzles where the droplets have important initial velocity and their velocity has not reached the terminal one, and the other zone is where the most of the droplets reach the terminal velocity (5 – 10 m below the nozzles). The modeling techniques can be developed differently for each zone. In the “terminal velocity” zone – the mechanistic model of Kenning (or others) can be applied as it has been developed for these range of parameters. The “momentum” zone turbulent parameters, can be extracted from 3D CFD simulations such as Neptue_CFD code.

Several criteria are widely discussed such as the length-scale ratio d_p/l_t , Particles Reynolds number Re_p , Stokes number S_t , and the particle momentum number Pa_{S_t} . However, it is noted that the turbulence modulation cannot be fully characterized by a single parameter. Further experimental and numerical data are needed for the validation and assessment of these criteria. Many theoretical and analytical models have been proposed to predict turbulence modulation. Among them, the mechanistic model of Kenning is easy to

implement and provides reasonable results. It is believed that this simple model can be reasonably used for the turbulence modulation prediction in large-scale simulations of spray systems. A numerical investigation on the particle-induced turbulence is carried out by means of 3D RANS calculations using Neptune_CFD code. Kenning's model is compared to the numerical results and shows a good capacity to estimate the kinetic turbulence energy and the integral length scale. The obtained results are also in good agreements with the experimental data of DynAsp on the particle velocity and air velocity evolutions. Moreover, the slip-velocity between the particle and the gas flow is proved to be an important parameter for the estimation of the turbulence intensity. On the contrary, the initial velocity of the injection particles is noted to have very small influence on the terminal particle slip-velocity. An empirical correlation can be used to provide the slip-velocity values for particles of diameters of the order of $\mathcal{O}(100) \mu m$. By coupling the Kenning model and this empirical slip-velocity correlation, one can estimate the turbulent kinetic energy and the turbulent length scale generated by falling particles with a sufficient accuracy for large-scale numerical simulations. This methodology can be applied to the simulation of slow flame-spray interaction in industrial scenarios such as nuclear containment building, offshore facilities, etc.

Finally, additional information are provided in the Appendix. The mean inter-particle distance is discussed since it is closely related to the particle-induced turbulent length scale. Cosilab, Asphodele and Neptune_CFD are the numerical simulation tools used for the assessment or validation of the simple models developed for the descriptions of different interactions. The introductions of these codes are briefly presented for the completeness of the state-of-art.

In a short summary, we have partially solved the four issues proposed in the Chapter 1. For the spray effects on the accidental premixed hydrogen-air explosion, three main interactions are investigated: spray-flame interaction, spray-shock interaction and the spray-induced turbulence. Dominant phenomena are selected according to the open literature and current studies: spray evaporation for flame deceleration, spray dispersion caused by the shock propagation, and spray-induced turbulence which can accelerate the flame velocity. We propose to use the simple or reduced-order models dedicated to these three types of interactions in order to implement in large-scale numerical simulations.

Perspectives

Even though several dominant phenomena have been talked about in this study, the spray explosion interaction remains complicated since it consists of a number of coupled physical processes. Further work can be envisaged to complete the present study, especially in the following directions:

- Droplet breakup and fragment size distribution as a function of Weber number;
- Spray-shock interaction taking account common droplet size distributions;
- Turbulence modulation by a poly-dispersion spray;
- Coupling of simplified models and their validation at large scale;

- Optimization of spray application strategies for the explosion extinction.

The droplet breakup remains the most important phenomena for the evaluation of the spray system, since it is related simultaneously to the spray evaporation and spray dispersion, thus directly affecting the mitigation capacity of the spray. For now, we have only worked on the one-dimensional shock-spray interaction, while in a finite geometry, the wall-reflected shock waves can change again the post-shock spray topology. It is repeated many times that small particles can mitigate the ambient turbulence while large ones enhance it, while a real industrial spray contains all sizes of droplets, of which the overall consequence of the presence of spray remains unclear. Also, the coupling of the current developed models and their extensions to multi-dimensional geometries are interesting and challenging. Finally, the optimization of spray application strategies is also important for different accidental explosion scenarios, concerning the ignition positions, gas compositions, pressure and temperature conditions, etc.

Appendix A

Appendix of spray flame interaction

A.1 Combustion length scales

For turbulent combustion phenomena in severe accident scenarios, such as LOCA in PWR plants, two kinds of length scales are of major importance: 1) the length scale related to combustion and 2) the length scale related to turbulence. Here, one can take an example of turbulent combustion of hydrogen-air mixture of molar fraction $x_{H_2} = 10\%$ to estimate the magnitude of these length scales. The initial conditions $P^{ini} = 1.013$ bar and $T = 294$ K, in a 1000 m^3 volume ($10\text{ m} \times 10\text{ m} \times 10\text{ m}$) can be considered.

The flame thickness consists of two parts: the thermal thickness of the preheating zone and the chemical thickness of the reaction zone. Experimental and numerical investigations show that the chemical flame thickness is roughly one order of magnitude less than the thermal flame thickness [132]. According to Eq. (1.10), the thermal flame thickness can be estimated by:

$$l_{th} \approx \frac{\lambda_b}{\rho_u c_p S_L} \sim O(10^{-4}\text{ m}) \quad (\text{A.1})$$

Thus the chemical length scale l_{chem} may have the order of magnitude:

$$l_{chem} \sim O(10^{-5}\text{ m}) \quad (\text{A.2})$$

The turbulent integral length scale, l_t , can be estimated by 10% of the geometrical length scale ($L_0 = 10\text{ m}$) [5]:

$$l_t \sim O(1\text{ m}) \quad (\text{A.3})$$

To estimate the length scale of Kolmogorov, η_k , we take the turbulent Reynolds number $Re_t = \frac{u' l_t \rho}{\mu} \approx 10^3$, with u' the magnitude of the velocity fluctuations, taking 1% of an averaged flame velocity of the order of $O(1)\text{m/s}$ [57]), and one can have:

$$\eta_k = \frac{l_t}{Re_t^{3/4}} \sim O(10^{-3}\text{ m}) \quad (\text{A.4})$$

In order to resolve all the above scales one will need about $(L_0/\min\{l_{chem}, l_{th}, \eta_k\})^3 = 10^{18}$ computational cells, which is not realistic for the current computation facilities. Therefore, the development of reduced-order and simple models based on the experimental and numerical simulation results becomes one of the main objects of this study.

A.2 Cosilab code

In this section, we discuss briefly the one-dimensional governing equations for the gas phase implemented in the Cosilab code [51]. Cosilab is a tool for solving complex chemical kinetics problems, which is widely used in research and industry for combustion and chemical processing applications. Its computational capabilities allow us to investigate in details the complex chemical reactions, including intermediate compounds, trace compounds and pollutants for mono-phase or two-phase reactive flows [133]. One-dimensional governing equations are solved to obtain a steady solution of a freely propagating premixed flame. Gas-phase governing equations are the Eulerian conservation equations of overall mass, species mass, momentum, and enthalpy. Liquid-phase is described by tracking the droplets in a Lagrangian manner, monitoring the droplet size, velocity and temperature. The gas- and liquid-phase coupling is inspired by [67; 72], including phase-exchange terms for liquid and gaseous mass, momentum and energy.

First, the overall mass conservation equation is given by the continuity equation:

$$\boxed{\frac{\partial \rho_f}{\partial t} + \frac{\partial}{\partial y}(\rho_f v_g) = S_m} \quad (\text{A.5})$$

where t and y denote the time and space coordinates, ρ_f is the fluid density, v_g is the gas velocity along the y direction and S_m is the gaseous mass per unit time and unit space transferred between two phases.

In a multi-phase (here two phases) et multi-species system, the conservation for gaseous species mass is given by:

$$\frac{\partial \rho_f Y_{g,k}}{\partial t} + \frac{\partial \rho_f v_{g,k} Y_{g,k}}{\partial y} = -\frac{\partial}{\partial y}(\rho_f v_{g,k} Y_{g,k}) + \varepsilon \omega_{g,k} + S_{m,k} \quad (\text{A.6})$$

where $Y_{g,k}$ denotes the mass fraction of the k -th gaseous specie, $v_{g,k}$ denotes its diffusion velocity, $\omega_{g,k}$ represents its mass rate of production per unit volume, $S_{m,k}$ is the mass rate of the k -th gaseous specie transferred between the two phases and ε is the volume fraction of the gaseous phase defined as: $\varepsilon = \frac{V_g}{V_g + V_l}$. One can have for the mixture mass density:

$$\rho_m = \varepsilon \rho_g + (1 - \varepsilon) \rho_l \quad (\text{A.7})$$

where ρ_g and ρ_l denote the gas and liquid phase density, the fluid density is defined $\rho_f = \varepsilon \rho_g$. The mass production rate is defined:

$$\omega_{g,k} = W_k \sum_{i=1}^I v_{j,i} r_i \quad (\text{A.8})$$

where W_k is the molecular weight of k -th specie, r_i is the net reaction rate of i -th reaction and $\nu_{j,i}$ is the stoichiometric coefficient of species j in the i -th reaction. The left hand side (L.H.S.) of equation (A.6) can be expressed:

$$\frac{\partial \rho_f Y_{g,k}}{\partial t} + \frac{\partial \rho_f \nu_g Y_{g,k}}{\partial y} = \rho_f \left(\frac{\partial Y_{g,k}}{\partial t} + \frac{\partial \nu_g Y_{g,k}}{\partial y} \right) + Y_{g,k} \left(\frac{\partial \rho_f}{\partial t} + \frac{\partial}{\partial y} (\rho_f \nu_g) \right), \quad (\text{A.9})$$

By equation (A.5), one can have:

$$\frac{\partial \rho_f Y_{g,k}}{\partial t} + \frac{\partial \rho_f \nu_g Y_{g,k}}{\partial y} = \rho_f \frac{DY_{g,k}}{Dt} + Y_{g,k} S_m, \quad (\text{A.10})$$

Thus the species conservation equation for k -th gaseous specie can be expressed by:

$$\boxed{\rho_f \frac{DY_{g,k}}{Dt} = -\frac{\partial}{\partial y} (\rho_f \nu_g Y_{g,k}) + \epsilon \omega_{g,k} + S_{m,k} - Y_{g,k} S_m \quad k = 1, 2, \dots, K.} \quad (\text{A.11})$$

with K the total number of species exchanged between two phases.

The overall gas phase momentum conservation equation can be written as:

$$\begin{aligned} \frac{\partial \rho_f \nu_g}{\partial t} + \frac{\partial \rho_f \nu_g \nu_g}{\partial y} &= -\epsilon \nabla p + \epsilon \nabla (\mu_g \nabla \nu_g) + S_v \\ &= -\epsilon \frac{\partial p}{\partial y} + \epsilon \frac{4}{3} \frac{\partial}{\partial y} \left(\mu_g \frac{\partial \nu_g}{\partial y} \right) + S_v, \end{aligned} \quad (\text{A.12})$$

where μ_g denotes the gas phase dynamic viscosity, S_v represents a momentum sink(source) due to the presence of the liquid phase. Similar to the species mass conservation equation, by equation (A.5), we can have:

$$\frac{\partial \rho_f \nu_g}{\partial t} + \frac{\partial \rho_f \nu_g \nu_g}{\partial y} = \rho_f \frac{D\nu_g}{Dt} + \nu_{g,k} S_m, \quad (\text{A.13})$$

Alternatively, we can rewrite the momentum conservation equation:

$$\boxed{\rho_f \frac{D\nu_g}{Dt} = -\epsilon \frac{\partial p}{\partial y} + \epsilon \frac{4}{3} \frac{\partial}{\partial y} \left(\mu_g \frac{\partial \nu_g}{\partial y} \right) + S_v - \nu_g S_m.} \quad (\text{A.14})$$

The gas phase mixture enthalpy is defined:

$$h_g = \sum_{k=1}^K Y_{g,k} h_{g,k}, \quad (\text{A.15})$$

with K the total number of species in the gas phase. The gas phase heat-flux vector contains two terms:

$$q_g = \underbrace{-\lambda_g \frac{\partial T_g}{\partial y}}_{\text{diffusion}} + \underbrace{\sum_{k=1}^K j_{g,k} h_{g,k}}_{\text{conduction}}, \quad (\text{A.16})$$

where λ_g is the conductivity of the gas mixture, T_g is the gas temperature and $j_{g,k} = \rho_g v_{g,k}$. The overall energy conservation equation can be written as:

$$\frac{\partial \rho_f h_g}{\partial t} + \frac{\partial \rho_f v_g h_g}{\partial y} = -\varepsilon \frac{\partial q_g}{\partial y} - \underbrace{\varepsilon \sum_{k=1}^K h_{g,k} \omega_{g,k}}_{\text{heat release rate}} + S_e, \quad (\text{A.17})$$

where S_e represents a energy sink (source) due to the liquid phase.

For ideal gas, the caloric equation of state is taken in the form:

$$h_g(T_g) = h_g^0 + \int_{T^0}^{T_g} c_{p,g} dT \quad \text{with} \quad c_{p,g} = \sum_{k=1}^K c_{p,k}, \quad (\text{A.18})$$

Thus the L.H.S. of Eq. (A.17) can be rewritten as:

$$\begin{aligned} \frac{\partial \rho_f h_g}{\partial t} + \frac{\partial \rho_f v_g h_g}{\partial y} &= \rho_f \left(\frac{\partial h_g}{\partial t} + \frac{\partial h_g v_g}{\partial y} \right) + h_g \left(\frac{\partial \rho_f}{\partial t} + \frac{\partial}{\partial y} (\rho_f v_g) \right) \\ &= \rho_f c_{p,g} \left(\frac{\partial T_g}{\partial t} + v_g \frac{\partial T_g}{\partial y} \right) + h_g S_m \\ &= \rho_f c_{p,g} \frac{DT_g}{Dt} + h_g S_m, \end{aligned} \quad (\text{A.19})$$

Finally, the overall conservation equation of energy can be written:

$$\boxed{\rho_f c_{p,g} \frac{DT_g}{Dt} = \varepsilon \frac{\partial}{\partial y} \left(\lambda \frac{\partial T_g}{\partial y} \right) - \varepsilon \frac{\partial T_g}{\partial y} \sum_{k=1}^K c_{p,g,k} j_{g,k} - \varepsilon \sum_{k=1}^K h_{g,k} \omega_{g,k} + S_e - \left(\sum_{k=1}^K Y_{g,k} h_{g,k} \right) S_m.} \quad (\text{A.20})$$

Appendix B

Appendix of spray shock interaction

B.1 Asphodele code

The governing equations for the gaseous phase in Asphodele are the compressible Navier-Stokes equations. In a multi-species flow, the conservation of mass can be established by considering the transport of different species k of the mass fraction Y_k with $\sum Y_k = 1$. The transport equation of the species k is given by:

$$\frac{\partial \rho Y_k}{\partial t} + \frac{\partial \rho u_i Y_k}{\partial x_i} = \frac{\partial}{\partial x_i} \left(\rho D_k \frac{\partial Y_k}{\partial x_i} \right) + \dot{\omega}_k, \quad (\text{B.1})$$

where D_k is the diffusivity of the species k , $\dot{\omega}_k$ is a chemical or evaporation source term of the species k .

The momentum transport equation can be expressed as:

$$\frac{\partial \rho u_i}{\partial t} + \frac{\partial \rho u_i u_j}{\partial x_j} = - \frac{\partial p}{\partial x_i} + \frac{\partial \tau_{ij}}{\partial x_j}, \quad (\text{B.2})$$

with ρ is the density of the gas, u_i the speed gas in the direction i and τ_{ij} the viscous-stress tensor given by [134]:

$$\tau_{ij} = \mu \left[\frac{\partial u_i}{\partial x_j} + \frac{\partial u_j}{\partial x_i} \right] - \frac{2\mu}{3} \frac{\partial u_l}{\partial x_l} \delta_{ij}. \quad (\text{B.3})$$

with μ the dynamic viscosity of the fluid. For the inviscid flow, the viscous stress terms are ignored.

The sensible energy e_s of the fluid is transported by the following equation:

$$\frac{\partial \rho e_s}{\partial t} + \frac{\partial \rho u_i e_s}{\partial x_i} = \frac{\partial}{\partial x_i} \left(\lambda \frac{\partial T}{\partial x_i} \right) - \frac{\partial p u_i}{\partial x_i} + \frac{\partial \tau_{ij} u_i}{\partial x_j} + \dot{\omega}_{e_s}, \quad (\text{B.4})$$

where λ is the thermal conductivity of the medium and $\dot{\omega}_{e_s}$ is the chemical source term.

B.1.1 WENO scheme

The weighted essentially non-oscillatory (WENO) methods are classes of high-resolution schemes which are used in the numerical solution of hyperbolic partial differential equations [109]. Consider the initial problems

of nonlinear hyperbolic differential laws:

$$u_t + \nabla \cdot f(u) = 0 \quad \text{with} \quad u(x, 0) = u_0(x) \quad (\text{B.5})$$

The integration of (B.5) on the cell $I_i = [x_{i-1/2}, x_{i+1/2}]$ gives the semi-discretization scheme:

$$\frac{d}{dt} \bar{u}_i(t) + \frac{1}{\Delta x_i} \left(\hat{f}(u_{i+1/2}^-, u_{i+1/2}^+) - \hat{f}(u_{i-1/2}^-, u_{i-1/2}^+) \right) = 0 \quad (\text{B.6})$$

where \hat{f} is a monotone numerical flux, $u_{i+1/2}^-$ can be reconstructed by WENO method using the following 5-cell stencil:

$$S = \{I_{i-2}, I_{i-1}, I_i, I_{i+1}, I_{i+2}\}$$

This stencil is the union of three third order stencils S_1, S_2 and S_3 . The fifth order approximation of $u_{i+1/2}^-$ based on the large stencil S can be reconstructed as a linear convex combination of the three third order approximations $u_{i+1/2}^{(1)}, u_{i+1/2}^{(2)}$ and $u_{i+1/2}^{(3)}$ based on the three small stencils S_1, S_2 and S_3 , respectively:

$$u_{i+1/2}^- = \gamma_1 u_{i+1/2}^{(1)} + \gamma_2 u_{i+1/2}^{(2)} + \gamma_3 u_{i+1/2}^{(3)}, \quad (\text{B.7})$$

where the linear weight coefficients in this reconstruction case have the values:

$$\gamma_1 = \frac{1}{10}, \quad \gamma_2 = \frac{3}{5}, \quad \gamma_3 = \frac{3}{10}, \quad (\text{B.8})$$

Besides the linear reconstruction, the WENO method propose another approximation as non-linear convex combination of the three order approximations:

$$u_{i+1/2}^- = w_1 u_{i+1/2}^{(1)} + w_2 u_{i+1/2}^{(2)} + w_3 u_{i+1/2}^{(3)}, \quad (\text{B.9})$$

where the nonlinear weights $w_j \leq 0$ ($j = 1, 2, 3$) are determined by:

$$w_j = \frac{\bar{w}_j}{\sum_j \bar{w}_j}, \quad \text{with} \quad \bar{w}_j = \frac{\gamma_j}{\sum_j (\varepsilon + \beta_j)^2} \quad j = 1, 2, 3 \quad (\text{B.10})$$

Here ε is a small positive number to avoid the denominator to become zero and typically can be chosen as $\varepsilon = 10^{-6}$ in calculations. Linear weights are taken as in Eq. (B.8). The choice of nonlinear weights w_j depends on the smoothness indicator β_j , which is a measurement of the relative smoothness of the function $u(x)$ on the stencil S_j .

The most widely chosen smoothness indicator is:

$$\beta_j = \sum_{l=1}^k \Delta x^{2l-1} \int_{x_{i-\frac{1}{2}}}^{x_{i+\frac{1}{2}}} \left(\frac{d^l}{dx^l} p_j(x) \right)^2 dx, \quad (\text{B.11})$$

where $p_j(x)$ is the relevant interpolation polynomial in the interval $[x_{i-1/2}, x_{i+1/2}]$ and k is the polynomial degree. The explicit expression of the smoothness indicator can be obtained:

$$\beta_1 = \frac{13}{12} (u_{i-2} - 2u_{i-1} + u_i)^2 + \frac{1}{4} (u_{i-2} - 4u_{i-1} + 3u_i)^2$$

$$\beta_2 = \frac{13}{12}(u_{i-1} - 2u_i + u_{i+1})^2 + \frac{1}{4}(u_{i-1} - u_{i+1})^2$$

$$\beta_3 = \frac{13}{12}(u_i - 2u_{i+1} + u_{i+2})^2 + \frac{1}{4}(3u_i - 4u_{i+1} + u_{i+2})^2$$

The larger the smoothness indicator β_j is, the less smooth the function $u(x)$ is on the stencil S_j .

Assuming that the cell average values of $u(x)$ over the interval $I_i = [x_{i-1/2}, x_{i+1/2}]$ are known:

$$\bar{u}_i = \int_{x_{i-1/2}}^{x_{i+1/2}} u(x) dx \quad (\text{B.12})$$

The explicit formula for the approximations on the three third order stencils $u_{i+1/2}^{(1)}$, $u_{i+1/2}^{(2)}$ and $u_{i+1/2}^{(3)}$ can be obtained by simple algebra:

$$u_{i+1/2}^{(1)} = p_1(x_{i+1/2}) = \frac{1}{3}\bar{u}_{i-2} - \frac{7}{6}\bar{u}_{i-1} + \frac{11}{6}\bar{u}_i$$

$$u_{i+1/2}^{(2)} = p_2(x_{i+1/2}) = -\frac{1}{6}\bar{u}_{i-1} + \frac{5}{6}\bar{u}_i + \frac{1}{3}\bar{u}_{i+1}$$

$$u_{i+1/2}^{(3)} = p_3(x_{i+1/2}) = \frac{1}{3}\bar{u}_i + \frac{5}{6}\bar{u}_{i+1} - \frac{1}{6}\bar{u}_{i+2}$$

The reconstruction of $u_{i+1/2}^-$ is symmetric with respect to x_i of the above procedures. For conservative Euler equations systems, the reconstructions are performed in local characteristic direction to avoid oscillations.

B.1.2 Minimal storage time-advancement scheme

A third-order Runge-Kutta method is adopted in *Asphodele* for the time discretization. The minimal storage time-advancement scheme has been used to construct the Runge-Kutta method. The main object of the scheme is to find the solution of the vector system:

$$\frac{dy}{dt} = \mathbf{f}(\mathbf{y}, t) \quad (\text{B.13})$$

Some assumptions are considered in the scheme modeling:

- for successive times $t_0, t_1 = t_0 + \Delta t_0, t_2 = t_1 + \Delta t_1, \dots$, the solution $\mathbf{y}(t)$ is approximated to some order as the Taylor series, with the approximations denoted by $\mathbf{y}_0, \mathbf{y}_1, \mathbf{y}_2, \dots$
- only two memory locations are available to store the values of $\mathbf{y}(t)$;
- each computed $\mathbf{f}(\mathbf{y}, t)$ occupies one of the two memory location;
- during each time step, the operation is cyclic, the memory locations contain the updated value during this time step.

Assuming that the solution \mathbf{y}_n at the step n is known, and occupies one of the memory locations. The other memory location is empty at the beginning of the step $n + 1$, which can be denoted as:

$$\mathbf{y}_{n,0} \mid (\mathbf{empty}) \quad (\text{B.14})$$

where the two memory locations are presented at two sides.

Apparently, we can use the value \mathbf{y}_n to calculate the $\mathbf{f}(\mathbf{y}, t)$ and store it in the second memory position as:

$$\mathbf{y}_{n,0} \mid \mathbf{f}(\mathbf{y}_{n,0}, t) \quad (\text{B.15})$$

According to the first condition, using Eq. (B.13) one can propose to update \mathbf{y}_n :

$$\underbrace{\mathbf{y}_{n,0} + a\Delta t\mathbf{f}(\mathbf{y}_{n,0}, t)}_{y_{n,1}} \mid \underbrace{\mathbf{y}_{n,0} + A\Delta t\mathbf{f}(\mathbf{y}_{n,0}, t)}_{y_{n,2}} \quad (\text{B.16})$$

where a and A are two constants, the new values of the two memory positions are denoted as $y_{n,1}$ and $y_{n,2}$. Then \mathbf{f} can be re-calculated for the second memory position:

$$\mathbf{y}_{n,1} \mid \mathbf{f}(\mathbf{y}_{n,2}, t + A\Delta t) \quad (\text{B.17})$$

Thus a new linear composition can be obtained in a similar way:

$$\underbrace{\mathbf{y}_{n,1} + b\Delta t\mathbf{f}(\mathbf{y}_{n,2}, t + A\Delta t)}_{y_{n,3}} \mid \underbrace{\mathbf{y}_{n,1} + B\Delta t\mathbf{f}(\mathbf{y}_{n,2}, t + A\Delta t)}_{y_{n,4}} \quad (\text{B.18})$$

where b and B are also constants to be determined. $y_{n,3}$ and $y_{n,4}$ can be used to estimate the \mathbf{y}_{n+1} , as the situation:

$$\underbrace{\mathbf{y}_{n,3} + c\Delta t\mathbf{f}(\mathbf{y}_{n,3}, t + (a+B)\Delta t)}_{y_{n+1}} \mid (\mathbf{empty}) \quad (\text{B.19})$$

where the second memory position can be considered to be empty for the next time step.

Based on the construction above, the coefficients a , A , b , B and c need to be determined to obtain a third order accuracy. By Taylor expansion, one can have:

$$y_{n+1} = y_n + \Delta t f(y_n, t) + \frac{\Delta t^2}{2} f^{(2)}(y_n, t) + \frac{\Delta t^3}{6} f^{(3)}(y_n, t) + \mathcal{O}(\Delta t^4) \quad (\text{B.20})$$

where

$$f^{(2)}(y_n, t) = \frac{d}{dt}(f(y_n, t)) = \frac{\partial f}{\partial t} + f \frac{\partial f}{\partial y_n} \quad (\text{B.21})$$

and similarly

$$f^{(3)}(y_n, t) = \frac{d}{dt} \left(\frac{\partial f}{\partial t} + f \frac{\partial f}{\partial y_n} \right) = \frac{\partial^2 f}{\partial t^2} + \frac{\partial f}{\partial t} \frac{\partial f}{\partial y_n} + 2f \frac{\partial^2 f}{\partial y_n \partial t} + f \left(\frac{\partial f}{\partial y_n} \right)^2 + f^2 \frac{\partial^2 f}{\partial y_n^2} \quad (\text{B.22})$$

On the other hand, from the situation (B.19), our estimation for y_{n+1} can be explicitly given as:

$$\begin{aligned}
 y_{n+1} = & y_n + (a + b + c)\Delta t f(y_n, t) + ((a + B)c + Ab)\Delta t^2 f^2(y_n, t) \\
 & + \frac{1}{2}(A^2b + (a + B)^2c)f^2\Delta t^2 \frac{\partial^2 f}{\partial y_n^2} + ABc\Delta t^3 f \left(\frac{\partial f}{\partial y_n} \right)^2 + \mathcal{O}(\Delta t^3)
 \end{aligned} \tag{B.23}$$

By comparing the Eqs. (B.20) and (B.23), one can have the relations for the parameters:

$$\begin{aligned}
 a + b + c &= 1 \\
 (a + B)c + Ab &= \frac{1}{2} \\
 A^2b + (a + B)^2c &= \frac{1}{3} \\
 ABc &= \frac{1}{6}
 \end{aligned} \tag{B.24}$$

An estimation of third order for \mathbf{y} can be obtained by resolving this system. One of the particular solution [135] of the system (B.24) is:

$$a = \frac{1}{4}, A = \frac{8}{15}, b = 0, B = \frac{5}{12}, c = \frac{3}{4} \tag{B.25}$$

and this simple particular solution is used in Asphodele for the resolution of time advancement.

Appendix C

Appendix of spray turbulence interaction

C.1 Numerical modelling Neptune_CFD

In order to assess the simple reduced-order models found in the literature, numerical simulations are performed to investigate free-fall particles and industrial nozzle spray. The NEPTUNE_CFD code is a three-dimensional multi-phase Navier-Stokes solver developed jointly by EDF (Électricité de France) and CEA (Commissariat à l'Énergie Atomique et aux Énergies Alternatives) [136; 16]. The solver allows the use of various mesh types (tetra or hexahedral element) for different flow regimes: compressible/incompressible, steady/unsteady, laminar and turbulent.

The multi-fluid Euler-Euler model used in Neptune_CFD is based the resolution of mass, momentum and energy conservations using a finite volume discretization. Two principal methods are used spontaneously for the numerical resolution: the elliptic and the hyperbolic method. First, the prediction of the velocity field is obtained by resolving the conservation of momentum. Then, coupled with the conservation of mass and energy, the other properties are calculated [1].

The mass conservation for the phase k is given as [137]:

$$\frac{\partial}{\partial t}(\alpha_k \bar{\rho}_k) + \nabla \cdot (\alpha_k \bar{\rho}_k \bar{V}_k) = \Gamma_k, \quad k = l, g, \quad (\text{C.1})$$

where α_k is the volume fraction, $\bar{\rho}_k$ the mass density, \bar{V}_k the local mean velocity of the phase k , l and g denote the liquid and the gas phases, Γ_k is the interphase mass transfer rate defined as:

$$\Gamma_k = \sum_{l \neq k} \Gamma_{l \rightarrow k}^c + \Gamma_{wall \rightarrow k}, \quad (\text{C.2})$$

$\Gamma_{l \rightarrow k}^c$ is the interfacial mass transfer from phase l to phase k , $\Gamma_{wall \rightarrow k}$ represents the effects of deposit or

resuspension. From the definitions, one can deduce the following relations:

$$\sum_k \alpha_k = 1, \quad (\text{C.3})$$

$$\sum_k \Gamma_k = 0 \text{ with } \Gamma_{l \rightarrow k}^c + \Gamma_{k \rightarrow l}^c = 0. \quad (\text{C.4})$$

The momentum balance equation for the phase k gives:

$$\frac{\partial}{\partial t} (\alpha_k \bar{\rho}_k \bar{V}_k) + \nabla \cdot (\alpha_k \bar{\rho}_k \bar{V}_k^2) = -\alpha_k \nabla \bar{p} + M_k + \alpha_k \bar{\rho}_k f_g + \nabla \cdot [\alpha_k (\bar{\tau}_k + \bar{\tau}_k^T)], \quad k = l, g, \quad (\text{C.5})$$

where \bar{p} is the gas pressure, f_g the gravity acceleration, M_k the interphase momentum transfer term and $\bar{\tau}_k$, $\bar{\tau}_k^T$ represent the viscous and Reynolds stress tensors, respectively [138]. One can have for the interphase momentum transfer term:

$$\sum_k M_k = 0. \quad (\text{C.6})$$

The enthalpy conservation equation is used in NEPTUNE_CFD instead of internal energy, which gives:

$$\begin{aligned} \frac{\partial}{\partial t} \left[\alpha_k \bar{\rho}_k \left(\bar{h}_k + \frac{\bar{V}_k^2}{2} \right) \right] + \nabla \cdot \left[\alpha_k \bar{\rho}_k \left(\bar{h}_k + \frac{\bar{V}_k^2}{2} \right) \bar{V}_k \right] = \alpha_k \frac{\partial \bar{p}}{\partial t} + \alpha_k \bar{\rho}_k f_g \bar{V}_k + \Gamma_k \left(\bar{h}_{k,int} + \frac{\bar{V}_k^2}{2} \right) \\ + q_k A_{int} + q_{wk} - \nabla \cdot [\alpha_k (\bar{q}_k + \bar{q}_k^T)]. \quad k = l, g. \end{aligned} \quad (\text{C.7})$$

where h_k stands for the phase-averaged specific enthalpy for the phase k defined as:

$$h_k = e_k + \frac{\bar{p}}{\rho_k}. \quad (\text{C.8})$$

$\bar{h}_{k,int}$ is the interfacial-averaged enthalpy. Γ_k and $q_k A_{int}$ denote the interfacial transfer of mass and heat, respectively. The wall-to-fluid heat transfer flux term is q_{wk} and the molecular and the turbulent heat fluxes in phase k are \bar{q}_k and \bar{q}_k^T , respectively. The flow quantities are α_k , ρ_k , V_k and h_k .

Closure laws are need for several terms involved in the conservation laws, such as:

- interfacial transfer terms of mass, momentum and enthalpy: Γ_k , M_k , $q_k A_{int}$
- Reynolds tensor $\bar{\tau}_k^T$
- heat flux density \bar{q}_k and \bar{q}_k^T

More details about the model and turbulent closure of other terms can be found in [136; 139].

C.2 Turbulence modeling

Concerning the turbulence models, different RANS and LES models are implemented in Neptune_CFD code [16] as listed in Tab. C.1.

TABLE C.1: Different turbulent models in Neptune_CFD code [16].

Gas turbulence model	Particle turbulence model
mixing-length	Tchen
$k - \varepsilon$	Q2-Q12
$k - \varepsilon$ "linear production"	R2-Q12
$R_{i,j} - \varepsilon$ SSG	R2-Q12-Tchen
$R_{i,j} - \varepsilon$ EBRSM	

For continuous flow fields, the RANS models contain the mixing-length model, $k - \varepsilon$ model and the $R_{i,j} - \varepsilon$ SSG model ($R_{i,j}$ stands for Reynolds stress tensor) involving seven turbulent transport equations [140]. For the dispersed phase, the Tchen model is an algebraic local equilibrium model [141]. The Q2-Q12 model resolves the kinetic energy transport and fluid/particle fluctuating movement covariance. The R2-Q12 model resolves the kinetic stress and fluctuating movement covariance [142]. It is noted that these particle turbulence models have to be used with a gas turbulence model predicted by either $k - \varepsilon$ or $R_{i,j} - \varepsilon$ turbulence closures. For the phase k , the Reynolds stress tensor is closed by a Boussinesq-like hypothesis:

$$\overline{\rho_k u'_{k,i} u'_{k,j}} = -\mu_{t,k} \left[\frac{\partial u_{k,i}}{\partial x_j} + \frac{\partial u_{k,j}}{\partial x_i} \right] + \frac{2}{3} \delta_{i,j} \left[\rho_k q_k^2 + \mu_{t,k} \frac{\partial u_{k,m}}{\partial x_m} \right], \quad (\text{C.9})$$

where $\mu_{t,k}$ is the turbulent viscosity and q_k^2 denotes the turbulent kinetic energy of the phase k :

$$q_k^2 = \frac{1}{2} \overline{u'_{k,i} u'_{k,i}}. \quad (\text{C.10})$$

C.2.1 Standard $k - \varepsilon$ model

The $k - \varepsilon$ model was first proposed for single-phase turbulence modeling by Launder *et al.* [143], which resolves the turbulent kinetic energy k and the turbulent dissipation rate ε . This turbulence model is widely used in the current industrial applications and academic researches. The k and ε equation of the $k - \varepsilon$ model can be expressed as:

$$\rho \frac{\partial k}{\partial t} + \text{div} \left[\rho \bar{u} k - \left(\mu + \frac{\mu_t}{\sigma_k} \right) \overrightarrow{\text{grad} k} \right] = \mathcal{P} + \mathcal{G} - \rho \varepsilon + k \text{div}(\rho \bar{u}), \quad (\text{C.11})$$

$$\rho \frac{\partial \varepsilon}{\partial t} + \text{div} \left[\rho \bar{u} \varepsilon - \left(\mu + \frac{\mu_t}{\sigma_\varepsilon} \right) \overrightarrow{\text{grad} \varepsilon} \right] = C_{\varepsilon_1} \frac{\varepsilon}{k} [\mathcal{P} + (1 - C_{\varepsilon_3}) \mathcal{G}] - \rho C_{\varepsilon_2} \frac{\varepsilon^2}{k} + \varepsilon \text{div}(\rho \bar{u}), \quad (\text{C.12})$$

where \mathcal{P} is the shear stress production term defined as:

$$\mathcal{P} = -\rho R_{ij} \frac{\partial u_i}{\partial x_j} = \mu_t \left(\frac{\partial u_i}{\partial x_j} + \frac{\partial u_j}{\partial x_i} \right) \frac{\partial u_i}{\partial x_j} - \frac{2}{3} \mu_t (\text{div} \bar{u})^2 - \frac{2}{3} \rho k \text{div}(\bar{u}), \quad (\text{C.13})$$

and \mathcal{G} represents the gravity term:

$$\mathcal{G} = -\frac{1}{\rho} \frac{\mu_t}{\sigma_t} \frac{\partial \rho}{\partial x_i} g_i. \quad (\text{C.14})$$

The eddy turbulent viscosity is given by:

$$\mu_t = \rho C_\mu \frac{k^2}{\varepsilon} \quad (\text{C.15})$$

The constants in the above equations are:

$$C_\mu = 0.09, \quad C_{\varepsilon_1} = 1.44, \quad C_{\varepsilon_2} = 1.92, \quad \sigma_k = 1, \quad \sigma_\varepsilon = 1.3, \quad C_{\varepsilon_3} = 0 \text{ for } \mathcal{G} \geq 0 \quad (C_{\varepsilon_3} = 1 \text{ for } \mathcal{G} \leq 0).$$

C.2.2 $R_{ij} - \varepsilon$ SSG model

Reynolds stress model, also referred to as second moment closures are the most complete classical turbulence model in the RANS models. The eddy-viscosity hypothesis is avoided and the individual components of the Reynolds stress tensor transportations are directly computed. Reynolds stress models offer higher accuracy than $k - \varepsilon$ model, while being computationally cheaper than Direct Numerical Simulations (DNS) and Large Eddy Simulations (LES).

One of the most widely used Reynolds stress models is the $R_{ij} - \varepsilon$ SSG model proposed by Speziale *et al.* [140]. In this model, for each Reynolds stress component R_{ij} , one resolves:

$$\frac{\partial R_{ij}}{\partial t} + v_k \frac{\partial R_{ij}}{\partial x_k} = \mathcal{P}_{ij} - \Pi_{ij} + \frac{2}{3} \varepsilon \delta_{ij} + \mathcal{G}_{ij}, \quad (\text{C.16})$$

where the \mathcal{P}_{ij} is the shear stress production term:

$$\mathcal{P}_{ij} = -R_{ik} \frac{\partial \bar{v}_j}{\partial x_k} - R_{jk} \frac{\partial \bar{v}_i}{\partial x_k} \quad (\text{C.17})$$

Π_{ij} is the pressure-strain term and \mathcal{G} denotes the gravity term.

For the dissipation rate ε , one needs to resolve the advection-dissipation equation:

$$\rho \frac{\partial \varepsilon}{\partial t} + \text{div} \left[\rho \bar{\mathbf{u}} \varepsilon - (\overrightarrow{\mu \text{grad}} \varepsilon) \right] = D_\varepsilon + C_{\varepsilon_1} \frac{\varepsilon}{k} [\mathcal{P} + \mathcal{G}_\varepsilon] - \rho C_{\varepsilon_2} \frac{\varepsilon^2}{k} + \varepsilon \text{div}(\rho \bar{\mathbf{u}}). \quad (\text{C.18})$$

where D_ε is the turbulent diffusion term, \mathcal{P} is the shear stress production term and \mathcal{G}_ε denotes the gravity term:

$$\mathcal{G}_\varepsilon = \max(0, \frac{1}{2} G_k k) \quad (\text{C.19})$$

More details regarding the different gas phase turbulence and particle turbulence modeling aspects can be found in [16].

In the particle-laden flow, the quantity of the dispersed phase inside a given volume is usually characterized by the volume fraction α_d . However, the volume fraction cannot contain all the important informations about the particle cloud. For example, at a given volume fraction, the number density of the particles is reversely proportional to the particle diameter. One important parameter characterizing the particle quantity is the

mean inter-particle distance, which is closely related to the spray-induced turbulence intensity [124]. Besides the particle volume fraction α_d , the mean inter-particle distance depends also on the particle diameter and the particle arrangement in the space. Two different inter-particle distances can be defined based on the volumetric capacity of this arrangement (see Appendix C.3. A general expression can be obtained:

$$\frac{\lambda}{d_p} = \left(\frac{\tau}{\alpha_p} \right)^{\frac{1}{3}} - 1 \quad (\text{C.20})$$

where τ is the volumetric capacity, α_p is the particle volume fraction and d_p denotes the particle diameter.

C.2.3 Turbulence scaling

It is reported that the water spray can have an explosion-enhancing effect as a result of the spray-generated turbulence [28]. The turbulence enhancement is mainly due to the the *bulk* flow of large droplet motions from the nozzles. Large-scale turbulence is considered to be the reason for the flame speed increase and the turbulence length can be related to the geometry size. However, the determination of the integral length scale of turbulence in large geometry has no standard measurement solutions. To resolve this, Wingerden *et al.* designed an interesting experiment according to the formula proposed by [144]:

$$\Lambda_f = (2\pi\nu t)^{1/2} \quad (\text{C.21})$$

where Λ_f is the Eulerian integral length scale of turbulence, ν is the kinematic viscosity, and t is the time for decay of turbulence. The tests in [28] show that the turbulence exists in the mixture affecting the flame propagation up to 10 s after switch off the the spray system. This decay time gives that the length scale of the spray-generated-turbulence would be of the order of:

$$\Lambda_{\text{spray}} = 3 \text{ cm} \quad (\text{C.22})$$

which is very large in comparison with the size of the droplets but small compared to the size of the geometry.

According to [145], the Eulerian integral length scale of turbulence can be defined as:

$$\Lambda_f = \int_0^\infty f(x) dx \quad (\text{C.23})$$

where $f(x)$ is the space correlation in the x -direction between the turbulent intensity of two points, separated by distance x . According to [144], the one-dimension energy spectrum of turbulence can be expressed as:

$$E(k, t) = \frac{2}{\pi} u'^2 \int_0^\infty f(x, t) \cos(kx) dx \quad (\text{C.24})$$

one can deduce the Eulerian integral scale:

$$\Lambda_f = \frac{\pi}{2u'^2} \lim_{k \rightarrow 0} E(k, t) \quad (\text{C.25})$$

Assume that f is the Gaussian error curve:

$$f(x, t) = \exp(-x^2/8\nu t) \quad (\text{C.26})$$

The energy spectrum can be obtained:

$$E(k,t) = u'^2 \sqrt{\frac{8\nu t}{\pi}} \exp(-2k^2 \nu t) \quad (\text{C.27})$$

hence, the equation (C.21).

On the other aspect, one can investigate the integral length scale of turbulence induced by the spray by using reduced-order models to validate this measurement [124]. Kenning *et al.* introduced a new hybride length scale for the turbulent flow with particles. This hybrid length scale depends on both the inherent dissipation length scale L_i , and the mean inter-particle spacing λ , which is in fact the harmonic mean of these two length scales:

$$L_h = \frac{2L_i\lambda}{L_i + \lambda} \quad (\text{C.28})$$

where λ is estimated by Eq. C.34:

$$\frac{\lambda}{d_p} \approx \left(\frac{\pi}{6\alpha_d} \right)^{1/3} - 1 \quad (\text{C.29})$$

in which, d_p is the sphere equivalent diameter of the particles and α_d is the volume fraction of particle phase.

According to the experimental data given in [28], we take, for example, the case of spray with average droplet size of $500 \mu m$, with flow rate of $99 l/min$. The kinetic viscosity is estimated to be $\nu = 1.43 \times 10^{-5} m^2/s$. Unfortunately, the volume fraction of spray droplets was not given in [28], thus we assume that the volume fraction has the same order of magnitude as in industrial applications $\alpha_d = 1 \times 10^{-4}$. Under this assumption, one can calculate the inter-particle spacing $\lambda = 0,00818 m$. Taking the width of the experimental box as the integral dissipation length scale $L_i = 1 m$, the Eq. (C.28) gives:

$$L_h = 1.62 cm \quad (\text{C.30})$$

It is interesting to see that the length scale $L_h = 1.62 cm$ meets the order of magnitude of $\Lambda_{spray} = 3 cm$. This agreement provides a proof for the utilization of simple reduced-order model on the prediction of spray-induced turbulence length scales.

C.3 Mean inter-particle distance

Two different inter-particle distances can be defined based on the volumetric capacity of this arrangement: cubic and tetrahedron case.

C.3.1 Cubic case

Let us consider the regular cubic arrangement of the particles in the carrier phase. The particles are considered to have exactly the same size. We define the symbols:

- r_s distance between the centers of two successive balls

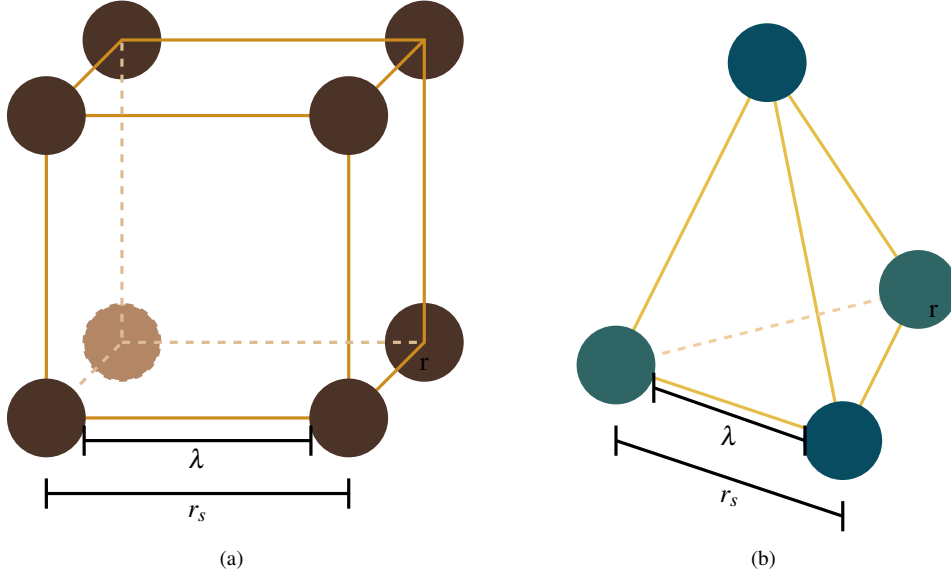


Figure C.1: (a) Regular cubic arrangement of particles in space (b) Regular tetrahedron arrangement of particles.

- r radius of a single ball
- d diameter of a single ball
- α_d volumetric fraction of the particles inside the carrier phase
- τ volumetric capacity of the particles for a compact arrangement in the carrier phase

According to the definition of volumetric fraction α_d , from Fig. C.1a we have:

$$r_s^3 \alpha_d = \frac{4}{3} \pi r^3 = \frac{\pi}{6} d^3 \quad (\text{C.31})$$

which gives:

$$r_s = \left(\frac{\pi}{6\alpha_d} \right)^{\frac{1}{3}} d \quad (\text{C.32})$$

with the definition of λ , we have directly:

$$\lambda = r_s - 2r = r_s - d \quad (\text{C.33})$$

and finally we have the mean inter-particle distance equation [124]

$$\frac{\lambda}{d_p} = \left(\frac{\pi}{6\alpha_d} \right)^{\frac{1}{3}} - 1 \quad (\text{C.34})$$

A simple calculation of volumetric capacity of this arrangement gives: $\tau_c = \frac{\pi}{6}$. Thus, equation (C.34) can be rewritten to:

$$\frac{\lambda}{d_p} = \left(\frac{\tau_c}{\alpha_d} \right)^{\frac{1}{3}} - 1 \quad (\text{C.35})$$

C.3.2 Regular tetrahedron case

Another definition of the inter-particle distance can use the regular tetrahedron arrangement, because all the particles are equidistant and a better volumetric capacity can be reached. Knowing that the volumetric capacity of regular tetrahedron is the maximal capacity that can be reached mathematically, one can have:

$$\tau_t = \tau_{max} \approx 0.74 \quad (\text{C.36})$$

Firstly, assuming that the balls are arranged to touch each other, we have $\tau_t = 0.74$. From Fig. C.1b, one can calculate the volume of balls covered by the tetrahedron:

$$V_{part} = \tau_t V_{tetrahedron} \quad (\text{C.37})$$

Knowing that the volume of the tetrahedron:

$$V_{tetrahedron} = \frac{\sqrt{2}}{12} r_s^3 \quad (\text{C.38})$$

and the volume of a single particle ball (since $r_s = 2r$):

$$V_{ball,0} = \frac{4}{3} \pi \left(\frac{r_s}{2} \right)^3 \quad (\text{C.39})$$

Thus, the solid angel of particle balls inside a tetrahedron is obtained:

$$\Omega_b = \frac{V_{part}}{V_{ball,0}} = \frac{\sqrt{2} \tau_t}{2\pi} \quad (\text{C.40})$$

Now, we consider a more general case that is $r_s > 2r$. According to the definition of volumetric fraction α_d :

$$\alpha_d = \frac{V_{ball} \Omega_b}{V_{tetrahedron}} = \frac{\frac{4}{3} \pi r^3 \frac{\sqrt{2} \tau_t}{2\pi}}{\frac{\sqrt{2}}{12} r_s^3} \quad (\text{C.41})$$

Simple algebra can give:

$$\frac{\lambda}{d} = \left(\frac{\tau_t}{\alpha_d} \right)^{\frac{1}{3}} - 1 \quad (\text{C.42})$$

And we can see that this equation is exactly the same as Eq. (C.34).

Finally at a given a given volumetric fraction, the maximal mean inter-particle distance λ is reached when the volumetric capacity takes the maximal value τ_{max} , which is the case of tetrahedron (or octahedron) arrangement. The mean inter-particle distance is important in the estimation of the particle-induced turbulence length scale in several reduced-order or empirical models [146; 147].

Bibliography

- [1] A. Foissac. *Modélisation des interactions entre gouttes en environnement hostile*. PhD thesis, Université Pierre & Marie Curie, France, 2011. xv, 2, 3, 4, XI
- [2] W. Breitung, C. Chan, S. Dorofeev, A. Eder, B. Gelfand, M. Heitsch, R. Klein, A. Malliakos, E. Shepherd, E. Studer, and P. Thibault. State-of-the-art report on flame acceleration and deflagration-to-detonation transition in nuclear safety. Technical report, NEA, 2000. xv, 5, 6
- [3] B Lewis and G Von Elbe. *Combustion, flames and explosions of gases. Third edition*. Academic Press, 1987. xv, 8
- [4] H.L. Le Chatelier E. Mallard. Sur la vitesse de propagation de la flamme. *Ann. Mines*, 4:379, 1883. xv, 5, 9, 11
- [5] Norbert Peters. *Turbulent Combustion*. Cambridge Monographs on Mechanics. Cambridge University Press, 2000. xv, 11, I
- [6] K.V. Wingerden and B. Wilkins. The influence of water sprays on gas explosions. part 1: water-spray-generated turbulence. *J. Loss Prevent. Proc.*, 8(2):53–59, 1995. xv, 2, 12, 14, 17, 30, 31, 45
- [7] M. Pilch and C.A. Erdman. Use of breakup time data and velocity history data to predict the maximum size of stable fragments for acceleration-induced breakup of a liquid drop. *Int. J. Multiphase Flow*, 13(6):741–757, 1987. xv, 20, 22, 23
- [8] D. Ducret, J. Vendel, and D. Vigla. Etude préliminaire de l’aspersion. Technical report, IPSN/DSU/SERAC/LECEV, 1993. xv, 23
- [9] Linden Gledhill. Shock waves from an hydrogen oxygen explosion, 2020. <https://www.flickr.com/photos/13084997@N03/>. xv, 24
- [10] O. Thomine. *Development of multi-scale methods for the numerical simulation of biphasic reactive flows*. PhD thesis, University of Rouen, France, November 2011. xvi, 26, 27

- [11] J.M. Ingram et al. Suppression of hydrogen-oxygen-nitrogen explosions by fine water mist: Part 1. burning velocity. *Int. J. Hydrog. Energy*, 37:19250–19257, 2012. xvi, 34, 35, 36
- [12] H. Cheikhraovat. *Etude expérimentale de la combustion de l'hydrogène dans une atmosphère inflammable en présence de gouttes d'eau*. PhD thesis, Université d'Orléans, 2009. xvi, 34, 37, 38, 39
- [13] S. Gupta and G. Langer. Experimental research on hydrogen deflagration in multi-compartment geometry and application to nuclear reactor conditions. *Nucl. Eng. Des.*, 343:103–137, 2019. xvi, 33, 34, 40, 41
- [14] UCSD. Ucsd detail hydrogen combustion mechnism, 2020. <http://web.eng.ucsd.edu/mae/groups/combustion/mechanism.html>. xvii, 9, 10
- [15] S. Gupta, E. Schmidt, M. Freitag, G. Langrock, and F. Funke. Experimental investigations on containment spray performance under severe accident conditions. In *8th Conference on Severe Accident Research*, 05 2017. xvii, 40
- [16] *Neptune_CFD version 4.3.1 Theory Guide*, 2019. xvii, XI, XII, XIII, XIV
- [17] International Atomic Energy Agency. *IAEA annual report*, 2018. 1
- [18] IEA, Paris. *Nuclear Power in a Clean Energy System*, 2018. 1
- [19] E. Studer, J.-P. Magnaud, F. Dabbene, and I. Tkatschenko. International standard problem on containment thermal–hydraulics isp47: Step 1—results from the mistra exercise. *Nucl. Eng. Des.*, 237:536–551, 03 2007. 1
- [20] S. Kudriakov, F. Dabbene, E. Studer, A. Beccantini, J.P. Magnaud, H. Paillère, A. Bentaib, A. Bleyer, J. Malet, E. Porcheron, and C. Caroli. The TONUS CFD code for hydrogen risk analysis: Physical models, numerical schemes and validation matrix. *Nucl. Eng. Des.*, 238(3):551 – 565, 2008. Benchmarking of CFD Codes for Application to Nuclear Reactor Safety. 1, 51, 53
- [21] E. Vyazmina, S. Jallais, L. Krumenacker, A. Tripathi, A. Mahon, J. Commanay, S. Kudriakov, E. Studer, T. Vuillez, and F. Rosset. Vented explosion of hydrogen/air mixture: An intercomparison benchmark exercise. *Int. J. Hydrog. Energy*, 44(17):8914 – 8926, 2019. Special issue on The 7th International Conference on Hydrogen Safety (ICHS 2017), 11-13 September 2017, Hamburg, Germany. 1
- [22] IAEA Techdoc. *Mitigation of Hydrogen Hazards in Severe Accidents in Nuclear Power Plants*. Number 1661 in TECDOC Series. INTERNATIONAL ATOMIC ENERGY AGENCY, Vienna, 2011. 1
- [23] X.G. Huang, Y. Yang, X. Cheng, N. Al-Hawshabi, and S.P. Casey. Effect of spray on performance of the hydrogen mitigation system during lb-locas for cpr1000 npp. *Ann. Nucl. Energ.*, 38:1743–1750, 08 2011. 1

BIBLIOGRAPHY

- [24] J. Yanez, M. Kuznetsov, and A. Souto-Iglesias. An analysis of the hydrogen explosion in the fukushima-daiichi accident. *Int. J. Hydrog. Energy*, 40(25):8261 – 8280, 2015. 1, 5
- [25] G.P. Choi, D.Y. Kim, K.H. Yoo, and M.G. Na. Prediction of hydrogen concentration in nuclear power plant containment under severe accidents using cascaded fuzzy neural networks. *Nucl. Eng. Des.*, 300:393 – 402, 2016. 1
- [26] E. Kim, J. Park, J.H. Cho, and I. Moon. Simulation of hydrogen leak and explosion for the safety design of hydrogen fueling station in korea. *Int. J. Hydrog. Energy*, 38(3):1737 – 1743, 2013. 2011 Zing International Hydrogen and Fuel Cells Conference: from Nanomaterials to Demonstrators. 1
- [27] J.W. Yang, Z. Musicki, and S. Nimmual. Hydrogen combustion, control, and value-impact analysis for pwr dry containments. In *NUREG/CR-5662*, 1991. 1
- [28] K.V. Wingerden and B. Wilkins. The influence of water sprays on gas explosions. part 2: mitigation. *J. Loss Prevent. Proc.*, 8(2):61–70, 1995. 2, 12, 14, 30, 31, XV, XVI
- [29] G.O. Thomas. On the conditions required for explosion mitigation by water sprays. *Process Saf. Environ. Prot.*, 78(5):339 – 354, 2000. 2, 14, 30, 45
- [30] Anon. Pwr and bwr containment spray system design criteria. Technical report, American Nuclear Society., 1980. 3
- [31] C. Rabe, J. Malet, and F. Feuillebois. Experimental investigation of water droplet binary collisions and description of outcomes with a symmetric weber number. *Phys. Fluids*, 22(4):047101, 2010. 3
- [32] S. Mimouni, A. Foissac, and J. Lavieville. Cfd modelling of wall steam condensation by a two-phase flow approach. *Nucl. Eng. Des.*, 241(11):4445 – 4455, 2011. 13th International Topical Meeting on Nuclear Reactor Thermal Hydraulics (NURETH-13). 3
- [33] J. Qian and C.K. Law. Regimes of coalescence and separation in droplet collision. *J. Fluid Mech.*, 331:59–80, 1997. 3
- [34] A.H. Lefebvre and V. G. McDonell. *Atomization and sprays*. CRC, Taylor and Francis, 2016. 3, 19, 20, 21, 23
- [35] J. Lavieville, E. Deutsch, and O. Simonin. Large eddy simulation of interactions between colliding particles and a homogeneous isotropic turbulence field. *American Society of Mechanical Engineers, Fluids Engineering Division (Publication) FED*, 228:347–357, 01 1995. 3
- [36] P. Coppolani, N. Hassenboehler, J. Joseph, J.-F. Petetrot, J.-P. Py, and J.-S. Zampa. *La Chaudière des Réacteurs à Eau sous Pression*. EDP Science, Les Ulis, France, 2004. 3
- [37] I.O. Moen, M. Donato, R. Knystautas, and J.H. Lee. Flame acceleration due to turbulence produced by obstacles. *Combust. Flame*, 39(1):21 – 32, 1980. 5

- [38] B. Hjertager, K. Fuhre, S.J. Parker, and J.R. Bakke. Flame acceleration of propane-air in a large-scale obstructed tube. *Prog. Astronaut. Aeronaut.*, 94:504–522, 01 1984. 5
- [39] I.O. Moen, J.H.S. Lee, B.H. Hjertager, K. Fuhre, and R.K. Eckhoff. Pressure development due to turbulent flame propagation in large-scale methane-air explosions. *Combustion and Flame*, 47:31 – 52, 1982. 5
- [40] S.B. Dorofeev, V.P. Sidorov, A.E. Dvoinishnikov, and W. Breitung. Deflagration to detonation transition in large confined volume of lean hydrogen-air mixtures. *Combust. Flame*, 104(1):95 – 110, 1996. 5
- [41] K. Ren, A. Kotchourko, and A. Lelyakin. Local mesh refinement in com3d. In *International Conference on Nuclear Engineering, Proceedings, ICONE*, volume 4, 07 2012. 5
- [42] J.H.S. Lee and I.O. Moen. The mechanics of transition from deflagration to detonation in vapor cloud explosions. *Prog. Energy Combust. Sci.*, 6(4):359 – 389, 1980. 5
- [43] E. Studer, S. Kudriakov, and A. BECCANTINI. Combustion et explosion de prémélanges gazeux et sûreté des installations. Technical Report AF3682 V1, Techniques de l'ingénieur, 2016. 6
- [44] A. Velikorodny, E. Studer, S. Kudriakov, and A. Beccantini. Combustion modeling in large scale volumes using europlexus code. *Journal of Loss Prevention in the Process Industries*, 35:104 – 116, 2015. 7, 30
- [45] V. Zimont, W. Polifke, M. Bettelini, and W. Weisenstein. An efficient computational model for premixed turbulent combustion at high reynolds numbers based on a turbulent flame speed closure. *J. of Gas Turbines Power*, 120:526–532, 1998. 7, 32
- [46] Gexcon AS. Flacs code user manual, 2020. <http://www3.gexcon.com/files/manual/flacs/html/index.html>. 7, 31
- [47] Z. Chen. Combustion basis - chemical reaction dynamics. Note technique, Peking University, Peking University, 2020. 8
- [48] A. Neophytou and E. Mastorakos. Simulations of laminar flame propagation in droplet mists. *Combust. Flame*, 156(8):1627 – 1640, 2009. 9, 45
- [49] Gas Research Institut. Gri mech 3.0, 2020. <http://combustion.berkeley.edu/gri-mech/version30/text30.html>. 9
- [50] P. Boivin. *Reduced-kinetic mechanisms for hydrogen and syngas combustion including autoignition*. PhD thesis, Escuela Politécnica Superior, Spain, 12 2011. 9
- [51] Cosilab[®]. *Two-Phase Flames: Liquid Sprays and Droplet Steams in Flames*. Rotexto GmbH & Co. KG, The Combustion Simulation Laboratory, Bad Zwischenahn (Germany), version 2.0 edition, 2006. 9, 19, II

BIBLIOGRAPHY

- [52] P. Saxena and F.A. Williams. Testing a small detailed chemical-kinetic mechanism for the combustion of hydrogen and carbon monoxide. *Combust. Flame*, 145(1-2):316–323, 2006. 9
- [53] Y.B. Zeldovich and D.A. Frank-Kamenetskii. A theory of thermal propagation of flame. *Acta Physicochim USSR*, 9:341–350, 1938. 9, 11
- [54] I. Glassman. *Combustion*. Academic Press, 1883. 9
- [55] G. Gai, S. Kudriakov, B. Rogg, A. Hadjadj, E. Studer, and O. Thomine. Numerical study on laminar flame velocity of hydrogen-air combustion under water spray effects. *Int. J. Hydrog. Energy*, 44(31):17015 – 17029, 2019. 11, 30
- [56] H. Pitsch. Turbulent premixed combustion. Note technique, RWTH Aachen, CEFRC Combustion Summer School, 2014. 11
- [57] T. Poinso and D. Veynante. *Theoretical and numerical combustion*. Edwards, Philadelphia, 2001. 11, 12, I
- [58] Bruno C. (eds) In: Casci C., editor. *On the Structure and Morphology of Turbulent Premixed Flames*, chapter Recent Advances in the Aerospace Sciences. Springer, Boston, MA, 1985. 12
- [59] M.J. Sapko, A.L. Furno, and J.M. Kuchta. *Quenching methane-air ignitions with water sprays*. Bureau of Mines Report of Investigations., 1977. 12
- [60] R.G. Zalosh and S.N. Bajpai. Water fog inerting of hydrogen-air mixtures. In *Proc. 2nd Int Conf on the Impact of Hydrogen on Water Reactor Safety.*, New Mexico, USA, 1982. 12, 34, 37
- [61] H. Cheikhravat, J. Goulier, A. Bentaib, N. Meynet, N. Chaumeix, and C.-E. Paillard. Effects of water sprays on flame propagation in hydrogen/air/steam mixtures. *Proc. Combust. Inst.*, 35(3):2715 – 2722, 2015. 12, 14
- [62] H. Phillips. On the transmission of an explosion through a gap smaller than the quenching distance. *Combust. Flame*, 7:129 – 135, 1963. 14
- [63] L.W. Carlson, R.M. Knight, and J.O. Henrie. *Flame and detonation initiation and propagation in various hydrogen-air mixtures, with and without spray*. Atomic International DIvision Rockwell International, May 1973. 14, 34, 37
- [64] D.B. Spalding. *Some Fundamentals of Combustion*. Butterworths, 1955. 14, 17
- [65] A.M. Kunary. *Fluid Dynamics And Transport of Droplets And Sprays*. Cambridge university press, 2010. 14, 17
- [66] D.R. Ballal and A.H. Lefebvre. Ignition and flame quenching of flowing heterogeneous fuel-air mixtures. *Combust. Flame*, 35:155 – 168, 1979. 14

-
- [67] W.A. Sirignano. *Fluid Dynamics and Transport of Droplets and Sprays*. Cambridge University Press, 2 edition, 2010. 14, 19, II
- [68] G.A.E. Godsave. Studies of the combustion of drops in a fuel spray—the burning of single drops of fuel. *Symposium (International) on Combustion*, 4(1):818 – 830, 1953. Fourth Symposium (International) on Combustion. 14
- [69] C. K. Law and H. K. Law. A d²-law for multicomponent droplet vaporization and combustion. *AIAA J.*, 20(4):522–527, 1982. 14
- [70] C.K. Law. Unsteady droplet combustion with droplet heating. *Combust. Flame*, 26:17 – 22, 1976. 14
- [71] C.K. Law and W.A. Sirignano. Unsteady droplet combustion with droplet heating—ii: Conduction limit. *Combustion and Flame*, 28:175 – 186, 1977. 17
- [72] B. Abramzon and W.A. Sirignano. Droplet vaporization model for spray combustion calculations. *Int. J. Heat Mass Transfer.*, 32(9):1605 – 1618, 1989. 17, 18, 45, II
- [73] S. Prakash and W.A. Sirignano. Liquid fuel droplet heating with internal circulation. *International Journal of Heat and Mass Transfer*, 21(7):885 – 895, 1978. 17
- [74] S.K. Aggarwal, A.Y. Tong, and W.A. Sirignano. A comparison of vaporization models in spray calculations. *AIAA J.*, 20(10):1448–1457, 1984. 17
- [75] P. J. Sáenz, K. Sefiane, J. Kim, O. K. Matar, and P. Valluri. Evaporation of sessile drops: a three-dimensional approach. *J. Fluid Mech.*, 772:705–739, 2015. 17
- [76] J.C. Meng and Tim Colonius. Numerical simulation of the aerobreakup of a water droplet. *J. Fluid Mech.*, 835:1108–1135, 2018. 20
- [77] T.G. Theofanous, V. Mitkin, and C.-H. Chang. The dynamics of dense particle clouds subjected to shock waves. Part 1. experiments and scaling laws. *J. Fluid Mech.*, 792:658–681, 2016. 20
- [78] H. Zhao, H. Liu, J. Xu, and W. Li. Experimental study of drop size distribution in the bag breakup regime. *Ind. Eng. Chem. Res.*, 50(16):9767–9773, 2011. 20
- [79] A. R. Hanson, E. G. Domich, and H. S. Adams. Shock tube investigation of the breakup of drops by air blasts. *Phys. Fluids*, 6(8):1070–1080, 1963. 20, 21
- [80] W. R. Lane. Shatter of drops in streams of air. *Ind. Eng. Chem.*, 43(6):1312–1317, 1951. 21
- [81] J. O. Hinze. Fundamentals of the hydrodynamic mechanism of splitting in dispersion processes. *AIChE J.*, 1(3):289–295, 1955. 21
- [82] Boris E. Gelfand. Droplet breakup phenomena in flows with velocity lag. *Prog. Energy Combust. Sci.*, 22:201–265, 1996. 21

BIBLIOGRAPHY

- [83] R.A. Brodkey. *The Phenomena of Fluid Motions*. Reading, MA: Addison-Wesley, 1967. 21
- [84] T.G. Theofanous, G.J. Li, and T.N. Dinh. Aerobreakup in rarefied supersonic gas flows. *ASME J. Fluids Eng.*, 126:516–527, 2004. 21
- [85] S. Nukiyama and Y. Tanasawa. Experiments on the atomization of liquids in an airstream. *Trans. Soc. Mech. Eng. Jpn.*, 5:68–75, 1939. 21
- [86] P. Rosin and E. Rammler. The laws governing the fineness of powdered coal. *J. Inst. Fuel*, 7(31):29–36, 1933. 21, 22
- [87] N.K. Rizk and A.H. Lefebvre. Drop-size distribution characteristics of spill-return atomizers. *AIAA J. Propul. Power*, 1(3):16–22, 1985. 21
- [88] R. Mugele and H.D. Evans. Droplet size distributions in sprays. *Ind. Eng. Chem.*, 43(6):153–164, 1951. 21
- [89] S.W. Lee and H.C. No. Droplet size prediction model based on the upper limit log-normal distribution function in venturie scrubber. *Nucl. Eng. Technol.*, 51:1261–1271, 2019. 22
- [90] R.W. Johnson. *Handbook of Fluid Dynamics*. CRC, Taylor and Francis, 2016. 23
- [91] G.F. Carrier. Shock waves in a dusty gas. *J. Fluid Mech.*, 4(4):376–382, 1958. 24
- [92] G. Rudinger. Some properties of shock relaxation in gas flows carrying small particles. *Phys. Fluids*, 7(5):658–663, 1964. 24
- [93] M. Olim, G. Ben-Dor, M. Mond, and O. Igra. A general attenuation law of moderate planar shock waves propagating into dusty gases with relatively high loading ratios of solid particles. *Fluid Dyn. Res.*, 6(3):185 – 199, 1990. 24
- [94] J.H. Geng, A. Van de Ven, Q. Yu, F. Zhang, and H. Grönig. Interaction of a shock wave with a two-phase interface. *Shock Waves*, 3(3):193–199, 1994. 24
- [95] Y. Ling, L. Wagner, S.J. Beresh, S.P. Kearney, and S. Balachandar. Interaction of a planar shock wave with a dense particle curtain: Modeling and experiments. *Phys. Fluids*, 24(11):113301, 2012. 24
- [96] G. Gai, O. Thomine, A. Hadjadj, and S. Kudriakov. Modeling of particle cloud dispersion in compressible gas flows with shock waves. *Phys. Fluids*, 32(2):023301, 2020. 24
- [97] G. Jourdan, L. Biamino, C. Mariani, C. Blanchot, E. Daniel, J. Massoni, L. Houas, R. Tosello, and D. Praguine. Attenuation of a shock wave passing through a cloud of water droplets. *Shock Waves*, 20(4):285–296, 2010. 24
- [98] J. Kersey, E. Loth, and D. Lankford. Effect of evaporating droplets on shock waves. *AIAA J.*, 48(9):1975–1986, 2010. 24

- [99] G.O. Thomas. On the conditions required for explosion mitigation by water sprays. *Process Saf. Environ.*, 78(5):339 – 354, 2000. 24
- [100] G. Gai, S. Kudriakov, A. Hadjadj, E. Studer, and O. Thomine. Modeling pressure loads during a premixed hydrogen combustion in the presence of water spray. *Int. J. Hydrog. Energy*, 44(10):4592 – 4607, 2019. 24, 45
- [101] T.C. Hanson, D.F. Davidson, and R.K. Hanson. Shock-induced behavior in micron-sized water aerosols. *Phys. Fluids*, 19(5):056104, 2007. 24
- [102] A. Chauvin, G. Jourdan, E. Daniel, L. Houas, and R. Tosello. Experimental investigation of the propagation of a planar shock wave through a two-phase gas-liquid medium. *Phys. Fluids*, 23(11):113301, 2011. 24
- [103] B.E. Gelfand. Droplet break-up phenomena in flows with velocity lag. *Prog. Energy Combust. Sci.*, 22(3):201–265, 1996. 24
- [104] M. Pilch and C.A. Erdman. Use of breakup time data and velocity history data to predict the maximum size of stable fragments for acceleration-induced breakup of a liquid drop. *Int. J. Multiph. Flow*, 13(6):741 – 757, 1987. 24
- [105] D.R. Gueldenbecher, C. Lopez-Rivera, and P.E. Sojka. Secondary atomization. *Exp. Fluids*, 46:371–402, 2009. 24
- [106] Geum-Su Yeom and Keun-Shik Chang. Dissipation of shock wave in a gas-droplet mixture by droplet fragmentation. *Int. J. Heat Mass Transf.*, 55(4):941 – 957, 2012. 24
- [107] F.M. White. *Fluid Mechanics*. McGraw-Hill series in mechanical engineering. McGraw Hill, 2011. 25
- [108] S. Elghobashi, S. Balachandar, and A. Prosperetti. An updated classification map of particle-laden turbulent flows. *IUTAM Symposium on Computational Approaches to Multiphase Flow*, 81:3–10, 2006. 26
- [109] G.-S. Jiang and C.-W. Shu. Efficient implementation of weighted eno schemes. *J. Comput. Phys.*, 126(1):202 – 228, 1996. 26, V
- [110] A.A. Wray. Minimal storage time-advancement schemes for spectral methods. Technical report, NASA Ames Research Center, 1991. 26
- [111] S. Mimouni, J.-S. Lamy, J. Lavieville, S. Guieu, and M. Martin. Modelling of sprays in containment applications with a cmfd code. *Nucl. Eng. Des.*, 240(9):2260–2270, 2010. 27
- [112] S. Elghobashi. On predicting particle-laden turbulent flows. *Appl. Sci. Res.*, 52(4):309–329, June 1994. 27, 30

BIBLIOGRAPHY

- [113] C.T. Crowe, J.D. Schwarzkopf, M. Sommerfeld, and Y. Tsuji. *Multiphase flows with droplets and particles*. CRC, Taylor and Francis, 2012. ISBN= 9781439840504. 30
- [114] G. Hetsroni and M. Sokolov. Distribution of mass velocity and intensity of turbulence in a two-phase turbulent jet. *ASME J. Appl. Mech.*, 38(2):315–327, 1971. 30
- [115] Y. Tsuji, Y. Morikawa, and H. Shiomi. LDV measurements of an air-solid two-phase flow in a vertical pipe. *J. Fluid Mech.*, 139:417–434, 1984. 30
- [116] G. Hetsroni. Particles-turbulence interaction. *Int. J. Multiph. Flow*, 15(5):735–746, 1989. 30
- [117] R.A. Gore and C.T. Crowe. Modulation of turbulence by a dispersed phase. *ASME J. Fluids Eng.*, 113(2):304–307, 1991. 30
- [118] T. Tanaka and J.K. Eaton. Sub-Kolmogorov resolution particle image velocimetry measurements of particle-laden forced turbulence. *J. Fluid Mech.*, 643:177–206, 2010. 30
- [119] G. Mallouppas, W.K. George, and B.G.M. van Wachem. Dissipation and inter-scale transfer in fully coupled particle and fluid motions in homogeneous isotropic forced turbulence. *Int. J. Heat. Fluid Fl.*, 67:74 – 85, 2017. Symposium on Experiments and Simulations in Fluid Dynamics Research. 30
- [120] S. Balachandar and J.K. Eaton. Turbulent dispersed multiphase flow. *Ann. Rev. Fluid Mech.*, 42(1):111–133, 2010. 30
- [121] R.A. Gore and C.T. Crowe. Effect of particle size on modulating turbulent intensity. *Int. J. Multiph. Flow*, 15(2):279–285, 1989. 30
- [122] E.K. Dale. Simulation and modelling of water spray in the 3d explosion simulation program flacs. Master’s thesis, University of Bergen, 2004. 31
- [123] Inc Ansys. Fluent website, 2020. https://www.afs.enea.it/project/neptunius/docs/fluent/html/ug/main_pre.htm. 32
- [124] V.M. Kenning. *Self-induced turbulence in solid-liquid flow*. PhD thesis, Washington University, USA, 1996. 33, XV, XVI, XVII
- [125] L.B. Thompson, J.J. Haugh, and B.R. Sehgal. Large scale hydrogen combustion experiments. In *ANS Int. Conference on Containment Design*, Toronto Canada, 1984. 33, 34, 40
- [126] T.K. Blanchat and D.W. Stamps. Deliberate ignition of hydrogen-air-steam mixtures in condensing steam environments. Technical report, Report NUREG/CR-6530, SAND94-1676, 1007. 33, 34, 40
- [127] P.N. Battersby et al. Suppression of hydrogen-oxygen-nitrogen explosions by fine water mist: Part 2. mitigation of vented deflagrations. *Int. J. Hydrog. Energy*, 37:19258–19267, 2012. 34, 37

- [128] J.R. Butz, P. French, and M. Plooster. Application of fine water mists to hydrogen deflagrations. In *Halon Alternatives Technical Working Conference*, pages 345–356, 1993. 34, 37
- [129] Jr. Malcolm W. Chase. *NIST-JANAF Thermochemical Tables*. American Institute of Physics for the National Institute of Standards and Technology, Washington, DC : New York : American Chemical Society, 1998. 49
- [130] CEA. Classification des cas tests, 2020. <http://www-cast3m.cea.fr/>. 51
- [131] Reaction Design. Chemkin, 2020. [http://www.wikipedia.fr/CHEMKIN\(Chemical Kinetics\)](http://www.wikipedia.fr/CHEMKIN(Chemical Kinetics)). 51
- [132] Aurélie Faix-Gantier. *Acceleration of flames in the presence of obstacles. Application to the safety hydrogen code*. PhD thesis, University of Poitiers, 2001. I
- [133] Cosilab[®]. *User manual two-phase flames*. Rotexto GmbH & Co. KG, 2018. II
- [134] S. Chandrasekhar. Hydrodynamic and hydromagnetic stability. *Oxford University Press.*, pages 11–14, 1961. V
- [135] A.A. Wray. Minimal storage time-advancement schemes for spectral methods. Technical report, NASA Ames Research Center, 1991. IX
- [136] S. Mimouni, M. Boucker, J. Laviéville, A. Guelfi, and D. Bestion. Modeling and computation of cavitation and boiling bubbly flows with the neptune_cfd code. *Nucl. Eng. Des.*, 238(3):680–692, 2008. XI, XII
- [137] M. Ishii and T. Hibiki. *Thermo-fluid Dynamics of two-phase flow*. Springer, Berlin, 2006. XI
- [138] O. Pironneau and B. Mohammadi. *Analysis of the k-epsilon turbulence model*. Mason, 1994. XII
- [139] S. Mimouni. Modeling and cavitation flows : a two-phase flow approach. *La Houille Blanche*, 6, 2006. XII
- [140] Charles G. Speziale, Sutanu Sarkar, and Thomas B. Gatski. Modelling the pressure–strain correlation of turbulence: an invariant dynamical systems approach. *J. Fluid Mech.*, 227:245–272, 1991. XIII, XIV
- [141] E. Deutsch and O. Simonin. Large eddy simulation applied to the motion of particles in stationary homogeneous fluid turbulence. In *Turbulence Modification in Multiphase Flows*, volume 110, pages 35–42, 1991. XIII
- [142] O. Simonin. Second-moment prediction of dispersed phase turbulence in particle-laden flows. In *8th Symposium on Turbulent Shear Flow*, Germany, 1991. XIII
- [143] B.E. Launder and D.B. Spalding. The numerical computation of turbulent flows. *Comput. Methods Appl. Mech. Eng.*, 3:269–289, 1974. XIII

BIBLIOGRAPHY

- [144] J.O. Hinze. *Turbulence*. McGraw-Hill classic textbook reissue. McGraw-Hill, 1987. XV
- [145] P.J.H. Bultjes. Determination of the eulerian longitudinal integral length scale in a turbulent boundary layer. *Appl. Sci. Res.*, 31, 1975. XV
- [146] V.M. Kenning and C.T. Crowe. On the effect of particles on carrier phase turbulence in gas-particle flows. *Int. J. Multiph. Flow*, 23(2):403–408, 1997. XVIII
- [147] C.T. Crowe. On models for turbulence modulation in fluid-particle flows. *Int. J. Multiph. Flow*, 26(5):719–727, 2000. XVIII